ROLE OF PLASTICITY ON FRETTING
FATIGUE BEHAVIOR OF Ti-6Al-4V

DISSERTATION

Kisu Shin, Major, ROKAF

AFIT/DS/ENY/04-05

DEPARTMENT OF THE AIR FORCE
AIR UNIVERSITY

AIR FORCE INSTITUTE OF TECHNOLOGY

Wright-Patterson Air Force Base, Ohio

The views expressed in this dissertation are those of the author and do not reflect the official policy or position of the United States Air Force, Department of Defense, or the United States Government.

AFIT/DS/ENY/04-05

ROLE OF PLASTICITY ON FRETTING FATIGUE BEHAVIOR OF Ti-6Al-4V

DISSERTATION

Presented to the Faculty

Graduate School of Engineering and Management

Air Force Institute of Technology

Air University

Air Education and Training Command

in Partial Fulfillment of the Requirements for the

Degree of Doctor of Philosophy

Kisu Shin, BS, MS

Major, ROKAF

September 2004

AFIT/DS/ENY/04-05

ROLE OF PLASTICITY ON FRETTING FATIGUE BEHAVIOR OF Ti-6Al-4V

Kisu Shin, BS, MS
Major, ROKAF

Approved:

<u>Date</u>

_____   _____
Dr. Shankar Mall (Chairman)

_____   _____
Dr. Vinod Jain (Member)

_____   _____
Dr. Yung Kee Yeo (Member)

_____   _____
Dr. Henry B. Potoczny (Dean's Representative)

Accepted:

_____   _____
Robert A. Calico, Jr.   Date
Dean, Graduate School of Engineering and Management

AFIT/DS/ENY/04-05

Abstract

Fretting fatigue leads to the degradation of the fatigue strength of a material due to cyclic micro-slip between two contacting materials. Since fatigue life reduction caused by fretting fatigue occurs in various mechanical components, such as bolted connections and blade/disk dovetail joints etc., fretting fatigue is regarded as an important issue in the design of aerospace structures. Consequently, a number of studies have been performed to predict the behavior of fretting fatigue. However, while many studies have evaluated fretting fatigue behavior under elastic deformation conditions, few studies have focused on fretting fatigue behavior under elastic-plastic deformation conditions. Due to the fact that plastic deformation is an integral part of crack nucleation, the role of plastic deformation in crack initiation should be considered, especially when a large plastic zone is presented. The primary goal of this study was to characterize the fretting fatigue crack initiation behavior in the presence of plasticity.

Experimental tests were performed using pad configurations involving elastic-plastic deformations. A total of eight different configurations of fretting pads were used for this dissertation. Five of the eight geometries were intended to generate the elastic deformation, i.e. 50.8 mm, 101.6 mm and 304.8 mm radius pads with normal contact load of 1.334 N, 2.224, and 4.003 kN respectively and two flat with rounded edge pads with normal contact load of 1.334 and 4.003 kN. In order to replicate the elastic-plastic deformation conditions, the smaller radii of the cylindrical pads, i.e. 5.08 mm radius pads, and flat pad type3 (FP3) with smaller edge radius, were included in this study. Two different contact loads were applied with the 5.08 mm radius cylindrical pad, i.e. 1.334 and 1.779 kN, while one contact load was applied with the flat pad type3, i.e. 4.003 kN. The crack initiation location was found near the trailing edge under both elastic and

elastic-plastic fretting fatigue conditions. The crack initiation orientation was also measured and found to have similar angles for all pad configurations involving both elastic and elastic-plastic deformation.

In order to calculate stress distributions under elastic-plastic fretting fatigue conditions, finite element analysis (FEA) was also performed. In order to obtain accurate stress and strain results, the mesh size was determined through comparison with FEA and analytical solution, i.e. Ruiz Program. The applied loading conditions obtained during experimental works were utilized in the FEA. Several parametric approaches of crack initiation, i.e. effective stress/strain, modified shear stress range (MSSR) and second modified shear stress range (SMSSR), were used to predict fretting fatigue life using stress distribution obtained from FEA. However, those parameters using contact surface stresses were unable to establish equivalence between elastic fretting fatigue data and elastic-plastic fretting fatigue data. Based on this observation, the critical distance methods, which are commonly used in notch analysis, were applied to the fretting fatigue problem. Among of the critical distance methods applied in this study, the effective strain range method, when used in conjunction with the SMSSR parameter, showed a comparatively good correlation of data points between the pad configurations involving elastic and elastic plastic deformations.

Acknowledgments

Kisu Shin

Table of Contents

List of Figures

List of Tables

ROLE OF PLASTICITY ON FRETTING FATIGUE BEHAVIOR OF Ti-6Al-4V

I. Introduction

Fretting fatigue occurs where the contacting surfaces of mechanical parts are subjected to normal pressure and oscillatory micro-slip. Stress distribution within the contact region is intensified due to the combination of contact stresses and remote loadings. The presence of increased stress fields in the contact area often promotes rapid crack initiation and accelerates crack propagation. A number of researchers [1, 2, 3] have demonstrated the reduction of fatigue life under fretting fatigue as compared to plain fatigue conditions. Fretting fatigue is therefore one of the most important considerations in designing engineering structures or machine components.

The subject of fretting fatigue is important to the United States Air Force because fretting fatigue has been attributed to the failure of turbine engines. Specifically, fretting fatigue has been found to occur in dovetail joints between the turbine blade and turbine rotor interface, as seen in Figure 1. The vibration of the turbine engine imposes cyclic loading on the rotor-to-blade interface joint and induces the conditions for fretting fatigue. Failure of this joint due to fretting fatigue cannot currently be predicted nor is there currently an accepted technique to account for fretting in the initial design. Therefore, designers must over-compensate for the potential of fretting by making these dovetail joints more robust than may actually be necessary. Yet, such over-compensation in the design of the joint leads to heavier, less efficient and more costly engines. Moreover, due to the inability to accurately predict failure caused by fretting fatigue, periodic maintenance inspections must be performed to ensure cracks do not propagate and lead to catastrophic failure. Such inspections increase maintenance time and cost. A better understanding of the failure mechanisms induced by fretting would allow engineers to better design for, prevent, and predict fretting in future engine designs as well as in

engines currently in the Air Force's fleet. Better designed engines will also increase engine efficiency and reliability, reduce maintenance time and cost, and improve safety for pilots, crews, and passengers
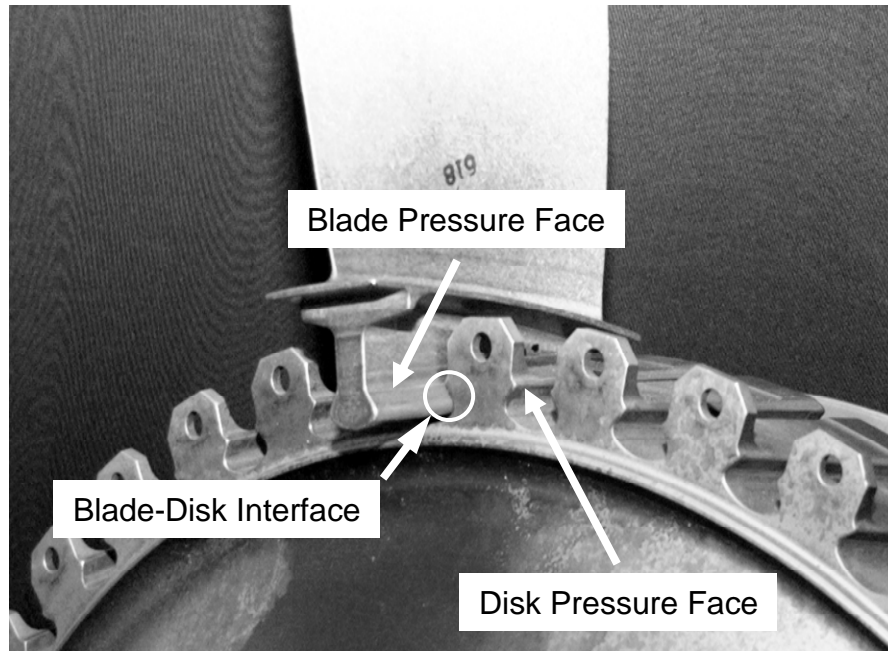
Figure 1. Turbine Engine Dovetail Joint

Consequently, a number of studies [4 - 10] have been performed to predict the behavior of fretting fatigue. Generally in fatigue analysis, crack nucleation and propagation are characterized by parameters which are based on the state of cyclic stress, strain or any combination of these. One of the most commonly used approaches to describe the fretting fatigue behaviors is the critical plane parameter. The critical plane parameter has been developed based on observations that fatigue cracks often nucleate on a particular plane. In critical plane approaches, crack nucleation, initiation and growth can be modeled by the combination of normal and shear stresses or strains on the critical plane. Normal stresses and strains are postulated to open the crack in this approach.

Shear stresses and strains are supposed to induce dislocation movement along slip lines, causing nucleation and growth of cracks.

The critical plane approach for fretting fatigue was initially proposed by Szolwinski and Farris [4]. They used a facsimile of a plain fatigue approach developed by Smith et al. [5], which was formulated to account for the stress ratio or mean stress effects. Szolwinski and Farris [4] modified this approach for the analysis of fretting fatigue crack initiation. This modified parameter assumed that the crack initiates on the location where the product of normal strain amplitude, ε_a, and maximum normal stress, σ_{max}, is maximum. There are a number of similar parameters that have been widely used in the critical plane approach, such as Smith-Watshon-Topper (SWT) [5] and Fatemi-Socie (FS) [6], etc.

Neu et al. [7] examined the fretting fatigue behavior of stainless steel, PH 13-8 Mo, by using two critical plane parameters: Smith-Watshon-Topper (SWT) [5] and Fatemi-Socie (FS) [6]. They demonstrated that the SWT parameter predicted the crack location well, but were not successful in predicting the crack orientation. However, they also showed that the Fatemi-Socie (FS) parameter predicts both the location and orientation of the primary fretting fatigue crack. Similar observations have been made by Lykins et al. [8] for the SWT parameter using titanium alloy, Ti-6Al-4V. So Lykins et al. [8] proposed a shear stress based critical plane parameter called shear stress range (SSR) as a better parameter than SWT. This SSR parameter involves the maximum shear stress range along with the local shear stress ratio on the critical plane. This parameter successfully characterized fretting fatigue crack initiation location as well as orientation, unlike the SWT parameter. The FS and SSR parameters proposed by Fatemi-Socie and Lykins et al. respectively are shear-cracking models where shear stress plays a dominant role. It has been observed that both shear and normal stresses may play an important role in the multi-axial fatigue loading condition. [9].

Recently, Namjoshi et al. [10] proposed another parameter which was called Modified Shear Stress Range Parameter (MSSR). This modified parameter explicitly included the effects of shear stress as well as normal stress. They showed that the MSSR parameter predicted the angle of crack location and orientation in agreement with corresponding experimental counterparts. The MSSR also predicted the number of cycles for the failure of specimen. An important characteristic of the MSSR parameter is that it was independent of fretting contact configuration. In spite of numerous studies devoted to the characterization of fretting fatigue behavior, most endeavors have been focused on the elastic stress and strain environment. However, plastic deformation is an essential part of the crack nucleation mechanism in general during fatigue. In fretting fatigue, there is a concentration of stress near the trailing edge in the contact region. The stresses in this location are generally very close to the yield point of the material. However, when large normal and tangential forces are present, they generate a significant plastic deformation and this deformation acts as a major role for crack nucleation. As illustrated in Figures 2 and 3, the effective stress (i.e. von Mises stress) on the contact surface calculated from finite element analysis (FEA) exceeds the yield stress value where the normal load on pad, $P = 1,334$ N, the shear force on pad, $Q = 627$ N and bulk load, $F = 6854$ N were applied. As these applied load values increase, the size of the plastic zone will be expanded also and the effect of the plastic deformation on crack nucleation must not be disregarded.
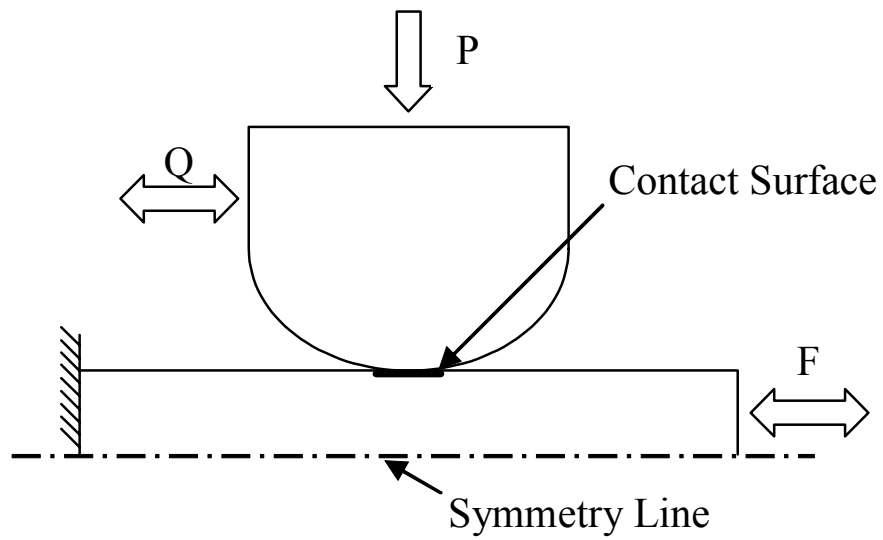
Figure 2. Typical Fretting Fatigue Condition
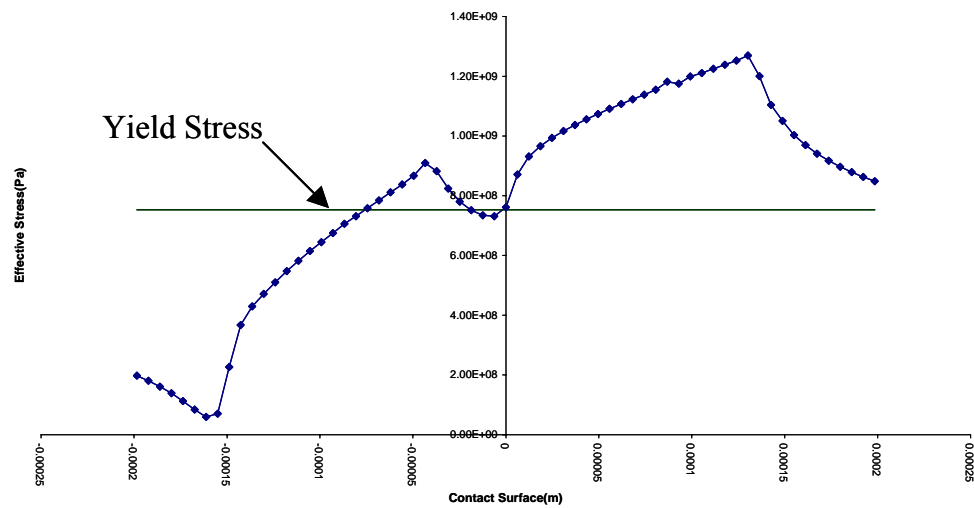
Figure 3. von Mises Stress along the Contact Surface

There are various examples of mechanical parts that have geometries causing stress concentrations including plastic deformation similar to conditions at the trailing edge of the contact region. Also, numerous methods that can elucidate the behavior of the fatigue mechanism under such situations have been introduced by a number of researchers. One common example that exhibits large concentrated stress effects is the notch problem. In the notch problem, where the maximum stress generally occurs at the end of notch, the stress life approach is considered as a simple method which assumes that fatigue behavior could be characterized by the maximum stress found at the notch root. This maximum stress is often called hot-spot stress. The hot-spot stress approach works perfectly well for blunt notches. However, for sharper notches, this approach gives a prediction that becomes increasingly inaccurate as the radius of the notch tip becomes smaller. The cause of this inaccuracy is generally assumed to be that sharp notches generate larger peak stress than do blunt notches.

Several methods have therefore been attempted to acquire the reliable prediction of fatigue failure for sharp notch problems. Historically, the initial methods developed to deal with the sharp-notch problem were based on the concept of a process zone, a small volume of material around the notch, and the assumption that volume size was a material constant. It was proposed by Peterson [11], Neuber [12] etc, that fatigue should be characterized not only by the maximum stress at the notch root, but by the stress at the designated point or averaged stress over the process zone. Peterson used point stress that was located at a critical distance from the notch root. Neuber instead used the averaged stress along a line of critical length, starting at the root. Peterson's and Neuber's approaches are often called point and line methods respectively. These approaches gave a good prediction of notch effects on the fatigue failure once the value of the critical distance was known.

However, since the critical distance concept does not account for the geometry of the notch and diverse loading conditions, some researchers abandoned the concept of critical distance as a material constant. Instead of assuming critical distance as a fixed value for each material, they used a stress gradient approach, which accounts for the state of stress distribution around the notch root. Qylafku et al. [13] and Kadi [14] utilized the stress gradient method for the notch problem. Qylafku et al. showed that this method works for elastic-plastic stress distribution too. In the stress gradient approach, the stress variation near the notch along the specimen depth was investigated. The effective stress and distance was calculated for each geometry and loading condition. This approach provided good agreement with the fatigue test results. From the results of Kadi's work, the stress gradient approach was shown to be as a method that was independent of the geometry of the notch size and shapes for fatigue failure prediction.

In the fretting fatigue studies, a number of researchers have utilized volume procedures that were commonly used in notch problems. Araujo and Nowell [15] calculated analytical fatigue life using critical distance and demonstrated good agreements with corresponding test results. Furthermore, they concluded that the dimension of the critical distance is not a material constant in the fretting fatigue condition. Other researchers who investigated the critical plane parameters in conjunction with the process volume are Swalla and Neu [16] and Namjoshi et al. [17]. Swalla and Neu examined the relationship between the dimensions of process volume and several critical plane parameters for predicting the angle of crack orientation. To generate a reliable prediction of the crack orientation, they found that different critical plane parameters, i.e. Fatemi-Socie-Kurath (FSK) [6] and Smith-Watson-Topper (SWT) [5] parameters, require small and large volume of the process zone, respectively.

Namjoshi et al. [17] also studied size effects of process volume in fretting fatigue using Smith-Watson-Topper (SWT), Findley (FP), Shear Stress Range (SSR) and

Modified Shear Stress Range (MSSR) parameters. They showed that the values of all critical plane parameters had an inverse relationship with the size of the process volume. In addition, they demonstrated that the MSSR parameter was the only parameter that satisfactorily predicted the crack initiation location, orientation angle and the number of cycles to fretting fatigue crack initiation.

As mentioned above, there have been a number of studies involving the critical distance and process volume approaches on fretting fatigue. However these investigations have been conducted under elastic stress distribution condition. Since crack initiation involves the plastic deformation at any rate in fretting fatigue, such as in the notch case, it is important that the plastic effects are considered in the investigation of fretting fatigue crack initiation. The focus of this study is in this direction, especially in the presence of the large plastic deformation.

A few researchers have investigated the behavior of the plastic deformation under fretting conditions. Ambrico and Begley [18] analyzed the fretting problem of a cyclically loaded cylinder on a flat elastic-plastic surface. From the detailed numerical analyses, they created shakedown maps and cyclic plastic strain behavior maps to describe the relative contribution of cyclic plasticity, ratcheting and shakedown as a function of loading. Several plasticity models were considered: elastic/perfectly-plastic, isotropic strain and kinematic strain hardening. Their results showed that the amount of plastic deformation was not much affected by the selection of material plasticity models. The results also demonstrated that the escalating tangential load increased the amount and severity of plasticity. Ambrico and Begley also studied the role of plastic deformation in fretting fatigue life predictions using fretting conditions similar to those mentioned above [19]. From this endeavor, they found that purely elastic analyses might not be adequate to predict the fretting fatigue life correctly over the entire load range. The analysis presented by this study also showed that the plastic ratcheting contributes towards the

8

increase in fretting fatigue life and residual stress created by plastic deformation causes decrease in life. However, no experimental studies were conducted by them or others where plasticity has been included explicitly.

In summary, a number of studies have been conducted to investigate fretting fatigue behavior. However, most of the works have been performed in situations in which the stress state in the contact region is within elastic regime. Even though some works have been done by considering plastic deformation, those efforts were mainly involved the analytical approach. The objective of this study is therefore to characterize the fretting fatigue crack initiation behavior in the presence of plasticity. This study will involve both experiments and analyses. The specific tasks will be the following:

1. To conduct the fretting fatigue tests with several contact configurations and with loading conditions which would generate plasticity or yielding of the material in the contact region.

2. To analyze the experiments by using finite element analysis in order to characterize the fretting fatigue damage mechanisms in the presence of plasticity.

3. To develop the fretting fatigue crack initiation parameter/model/criterion in the presence of plasticity. Further attempt will be made that this parameter/model/criterion is also applicable to the elastic regime as well as to different contact configurations.

II. Background

This chapter will review previous works on fretting and notch fatigue analyses that dealt with the effects of stress concentration. Stress concentrations exist in almost all mechanical components due to geometrical and loading discontinuities. Fretting and notch are common examples of these discontinuity configurations. For fretting fatigue, the contact mechanics will be reviewed first, and then the various parameters which have been utilized to attempt to predict fretting fatigue life are discussed. For the notch case, several methods which are related to process volume approaches will be reviewed. These methods were developed to overcome the difficulty of using only the peak stress value to measure the fatigue strength reduction in sharp notch configurations.

2.1. The Sphere on Flat Plane Contact Mechanics

In order to understand the effect of applied loading conditions on the fretting fatigue problem, it is helpful to examine the surface stresses on the contact surface. Therefore, it is necessary to discuss the contact mechanics of a cylindrical body and a flat body in contact. The analytical solution of stress state in the contact region has been discussed in detail by Hills and Nowell [20]. They introduced the elastic stress state solution for the fretting contact condition. The solution can be divided into three categories: first, solving the plane problem with no contact condition; second, solving the contact problem of cylinders called the Hertz problem; finally, solving the surface traction distribution for the contact of cylinders under partial slip.

2.1.1. Plane Problems

Figure 4 shows a half-plane subject to normal force, P, and shear force, Q. In this case, stress and strain formulas are obtained by inserting an Airy stress function into the biharmonic equation and using Hooke's Law, respectively as follows:

$$\sigma_{rr} = -\frac{2}{\pi r}(P\cos\theta - Q\sin\theta)$$

$$\sigma_{\theta\theta} = \tau_{r\theta} = 0 \tag{1}$$

$$\varepsilon_{rr} = \frac{1}{8\mu}\{\sigma_{rr}(1+\kappa) + \sigma_{\theta\theta}(\kappa-3)\}$$

$$\varepsilon_{\theta\theta} = \frac{1}{8\mu}\{\sigma_{\theta\theta}(1+\kappa) + \sigma_{rr}(\kappa-3)\} \tag{2}$$

$$\gamma_{r\theta} = \frac{\tau_{r\theta}}{\mu}$$

where $\kappa = 3 - 4\nu$ under the plane strain condition. The derivatives of surface displacement, $u(x)$ and $\upsilon(x)$, equations can be found by integration of strain equations and replacing the line forces with the distributed tractions as can be seen below:

$$\frac{\partial u}{\partial x} = \frac{\kappa-1}{4\mu}p(x) + \frac{\kappa+1}{4\pi\mu}\int\frac{q(\xi)}{x-\xi}d\xi$$

$$\frac{\partial \upsilon}{\partial x} = -\frac{\kappa-1}{4\mu}q(x) + \frac{\kappa+1}{4\pi\mu}\int\frac{p(\xi)}{x-\xi}d\xi \tag{3}$$
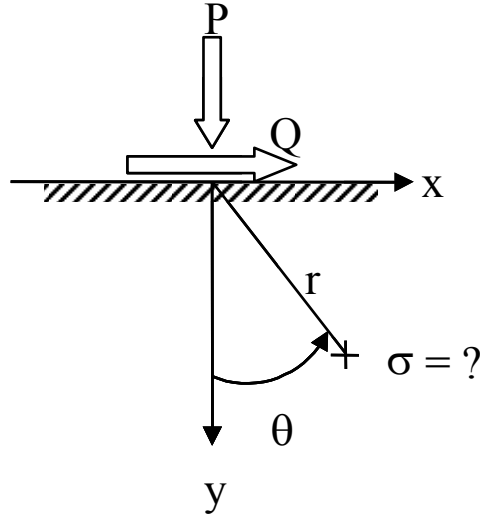
Figure 4. A Half Plane Subject to Normal and Tangential Forces

If we consider a condition which two bodies are to be brought into contact by the applied normal and shearing forces P, Q, then two corresponding points on the surface will have a relative displacement component. The relative displacement component can be written as $h(x) = \upsilon_1(x) - \upsilon_2(x)$ and $g(x) = u_1(x) - u_2(x)$ in the y and x-direction respectively. For the conditions in which the transverse plane strain and two contact bodies are the same material, the equations in terms of the $h(x)$ and $g(x)$ derivations will be

$$\frac{1}{A}\frac{\partial h}{\partial x} = \frac{1}{\pi}\int_{-a}^{a}\frac{p(\xi)}{x-\xi}d\xi$$

$$\frac{1}{A}\frac{\partial g}{\partial x} = \frac{1}{\pi}\int_{-a}^{a}\frac{q(\xi)}{x-\xi}d\xi$$

(4)

where the contact region extends from $x = -a$ to $x = a$ and $A = 4\left(1 - v^2/E\right)$ is called the composite compliance. The normal force along the contact area, p(x), at given $h(x)$ can be found by the inversion of this equation

12

$$p(x) = -\frac{w(x)}{A\pi} \int_{-a}^{a} \frac{h'(\xi)d\xi}{w(\xi)(\xi - x)} + Cw(x) \tag{5}$$

where $h'(x) \equiv \partial h/\partial x$ and $w(x) = \sqrt{a^2 - x^2}$

2.1.2. Hertz Problem

The explicit solution of the $p(x)$ can be obtained when the simple form of the $h'(x)$ is used in equation (5). To derive the simple form of $h(x)$, consider the circular bodies which have large radii of curvature, R_1 and R_2, in comparison with the contact width, a, as shown in figure 5. In the condition depicted in figure 5, the two contacted bodies can be approximated as half-plane and the local relative displacement component at the point of contact may be derived by a parabolic equation such as

$$h'(x) = \frac{dh}{dx} = -kx \tag{6}$$

where $k = (1/R_1) + (1/R_2)$ represents the relative curvature. However, in the sphere on the flat plane condition, one of contact bodies is considered as an infinite value of R that leads to the relative curvature form expressed by the equation $k = 1/R$.
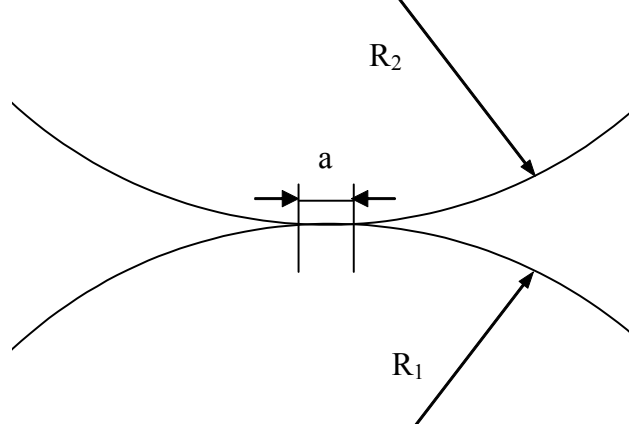
Figure 5. Radius, R_1 and R_2, and Contact Width, a

Since one of the contact bodies has circular geometry, the contact pressure will be zero at both ends of the contact and with these boundary conditions, equation (5) can be simplified as

$$p(x) = -\frac{k}{A}\sqrt{a^2 - x^2} \qquad (7)$$

Furthermore, using the relation between total normal force, P, and the $p(x)$ which can expressed by

$$P = -\int_{-a}^{a} p(\xi)d\xi = \frac{\pi k a^2}{2A} \qquad (8)$$

The simple form of the contact area, a, can be found as

$$a = \sqrt{\frac{2PA}{\pi k}} \qquad (9)$$

Using this simple equation of the contact area, a, the convenient formulation of $p(x)$, which is called Hertzian pressure, can be obtained as follows:

14

$$p(x) = -p_o \sqrt{1-(x/a)^2} \qquad\qquad (10)$$

where $p_o = \dfrac{2P}{\pi a}$ is the peak contact pressure.

Once the Muskhelishvili potential [21] is correlated with the sliding contacts condition, $|q(x, y)| = -fp(x, y)$, and Hertzian pressure equation, the stress state on the contact surface can be written as follows, where f is the coefficient of friction.

$$
\begin{aligned}
&\frac{\sigma_{xx}^n}{p_o} = \frac{\sigma_{yy}^n}{p_o} = \frac{\tau_{xy}^t}{fp_o} = -\frac{\sqrt{a^2 - x^2}}{a} \\[2mm]
&\frac{\sigma_{xx}^t}{p_o} = -2\frac{x}{a} \\[2mm]
&\frac{\sigma_{yy}^t}{fp_o} = \frac{\tau_{xy}^n}{p_o} = 0 \qquad\qquad\qquad (11)\\[2mm]
&\frac{\sigma_{zz}^n}{p_o} = -2v\frac{\sqrt{a^2 - x^2}}{a} \\[2mm]
&\frac{\sigma_{zz}^t}{fp_o} = -2v\frac{x}{a}
\end{aligned}
$$

2.1.3. Contact of Cylinders Under Partial Slip

In the previous section, only the contact load was considered when the cylinders or a cylinder and a half-plane were pressed against each other. If there are no tangential forces, then there are no shear tractions and relative motions between the contacted surfaces. In this condition, the derivative of the tangential relative displacement can be assumed as zero and expressed as $\partial g / \partial x = 0$. The $q(x)$ value is derived from an equation (4) using the formulation $\int_{-a}^{a} q(x)dx = Q$ as follows:

$$q(x) = \frac{Q}{\pi\sqrt{a^2 - x^2}} \tag{12}$$

However, as long as the shear force, Q, is nonzero, the quantity of the $q(x)$ goes to an infinite value where x approaches $\pm a$. This means that slip will occur no matter what the value of the coefficient of friction is at this point. If the tangential force increases monotonically where Q<fP is applied, then a stick and slip zone will occur in the contact area as shown in figure 6.
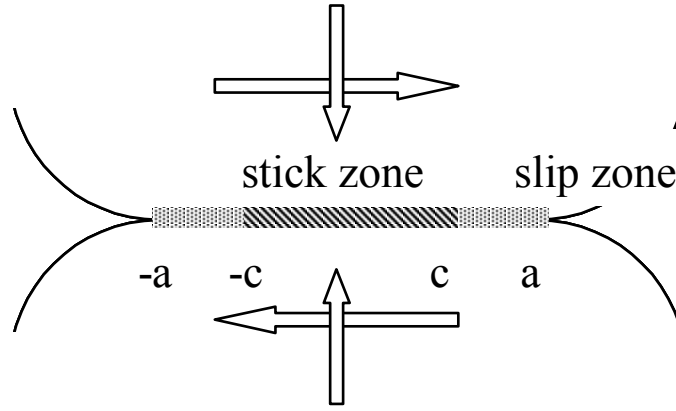
Figure 6. Stick and Slip Regions for the Contact of Cylinders in Partial Slip

Since in the slip zone the $q(x)$ can be expressed as $q(x) = fp(x) = fp_o\sqrt{1-(x/a)^2}$. the shear tractions between $-a \langle x \langle +a$ can be modeled as follows:

$$q(x) = fp_o\sqrt{1-(x/a)^2} + q'(x) \tag{13}$$

where $q'(x) \neq 0$ in the stick zone, which means there is a small change in the tangential load. Using the condition of $g(x)' = 0$ at the stick zone, the $q'(x)$ can be solved as

$$q'(t) = -fp_o \left(\frac{c}{a}\right)\sqrt{1-t^2} \quad -1 < t < 1 \tag{14}$$

where $v = \xi/c$ and $t = x/c$. Also, considering the relation of $q(x)$ and Q, the equation of shear force can be generated without difficulty.

$$Q = \frac{fp_o\pi}{2a_o}\left(a^2 - c^2\right) \tag{15}$$

A convenient form, which is called the Mindlin solution, of this relation can be derived by using $p_o = \dfrac{2P}{\pi a}$ such as:

$$c/a = \sqrt{1 - |Q/fP|} \tag{16}$$

Using the Mindlin solution, the distribution of shear tractions on the surface can be solved at the given Q/fP value.

The stress field on the contact surface can be obtained using shear traction distribution. The surface traction can be thought of as a superposition of three elliptical distributions:

a) A distribution of normal pressure of peak magnitude $-p_o$ acting between $x = \pm a$

b) A distribution of shear traction of peak magnitude fp_o acting between $x = \pm a$

c) A second shear traction distribution of peak magnitude $-fp_o(c/a)$ between

$x = \pm c$

For example, to calculate the $\sigma_{xx}(x, y)$ component of stresses at a point (x, y) in un-normalized coordinates for a contact transmitting normal and shear tractions and for

which the stick zone semi-width is c, it is simply necessary to superimpose three results to give

$$\sigma_{xx}(x,y) = p_o\left[\sigma_{xx}^n\left(\tfrac{x}{a},\tfrac{y}{a}\right)\right] + fp_o\left[\sigma_{xx}^t\left(\tfrac{x}{a},\tfrac{y}{a}\right)\right] - fp_o\frac{c}{a}\left[\sigma_{xx}^t\left(\tfrac{x}{c},\tfrac{y}{c}\right)\right] \tag{17}$$

Chan and Lee [22] wrote a program named "Ruiz Program" which calculates the numerical solution of equation 17. In this study, the analytical result was compared to the numerical solution which was derived by Finite Element Analysis for the fretting condition. This comparison was performed for verification of the FEA model for the cylindrical pad geometry.

2.2. Previous Work on Critical Plane Approach for Fretting Fatigue

The simplest parameter to represent the fatigue life data is the applied bulk stress range ($\Delta\sigma$), i.e. the stress applied to the substrate, or a variation thereof. However, due to the multi-axial stress state nature of contact surface, the bulk stress approach is inadequate in fretting fatigue condition, especially for predicting the crack initiation location and orientation. For this reason, a number of different approaches have been introduced to predict the crack initiation location and/or orientation for fretting environments. Most of the endeavors have concentrated on empirical approaches that are correlated with combinations of macroscopic variables such as stress and strain. As an example, Ruiz et al. [23] assumed that damage from fretting fatigue depends on the effects of the frictional force between contacting bodies. Furthermore, they also found that crack nucleation in the fretting fatigue depends on the maximum tangential stress, σ_τ. With these assumptions, they proposed the parameter $k = \sigma_\tau\tau\delta$ where τ is shear stress and δ is slip amplitude at the contact surface between two bodies. The location of crack

initiation was found where the value of k was maximum. Some studies have shown that Ruiz's approach can successfully predict the location of the fretting fatigue crack along the interface; however, no evidence has been reported that the parameter can predict the orientation of the nucleated crack.

In the past, a number of critical plane parameters, which are based on similar assumptions as Ruiz et al.'s method, have been introduced by various researchers. The fundamental conception of the critical plane parameters is to find a critical plane that has the maximum principal stress or strain levels. This critical plane can be regarded as the crack propagation path from the contact surface. The major benefit of using these critical plane parameters is acquiring information concerning the crack location and orientation along with the fatigue life.

Recently, Namjoshi et al. [10] worked on verifying previously developed critical plane parameters for predicting the fretting fatigue life using Ti-6Al-4V material, i.e. Smith-Watson-Topper (SWT), shear stress range (SSR) and Findley Parameter (FS). They also evaluated these critical parameters as a potential fretting fatigue parameter which can predict crack initiation location and orientation. Further, these researchers proposed a new parameter called modified shear stress range (MSSR). In this section, Namjoshi et al.'s [10] efforts will be reviewed. In order to evaluate the critical plane parameters, Namjoshi et al. [10] used five different configurations of fretting pads. Three of these pads were cylindrical pads and the other two were flat geometries. The details of the geometry of specimen and pads used by Namjoshi et al. [10] are illustrated in Figures 7 and 8 respectively.
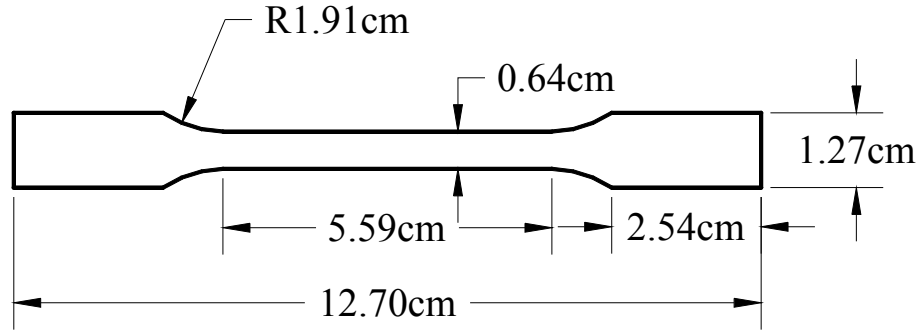
Figure 7. Geometry of the Specimen Used by Namjoshi et al.
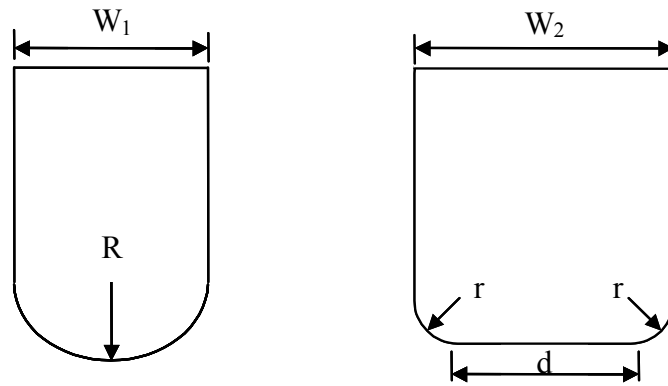
	R(mm)	w_1(mm)
Cylindrical Pad - 1	50.8	9.53
Cylindrical Pad - 2	101.6	9.53
Cylindrical Pad - 3	304.8	9.53

	r(mm)	d(mm)	w_2(mm)
Flat Pad - 1	5.08	5.08	9.53
Flat Pad - 2	2.54	13.97	19.05

Figure 8. Geometry of the Pads Used by Namjoshi et al.

2.2.1. Smith-Watson-Topper (SWT) Parameter

A number of researchers have used the SWT parameter [5] to predict fatigue life in steel and aluminum alloys subjected to multi-axial fatigue loading conditions [9]. In 1996, Szolwinski and Farris [4] modified the SWT parameter to be applicable to the same fretting fatigue conditions. This modified parameter is defined as the product of the normal strain amplitude, ε_a, and the maximum normal stress, σ_{max}, as shown below:

$$SWT = \varepsilon_a \sigma_{max} \qquad (18)$$

In this parameter, the critical plane was defined as the plane where the modified SWT parameter is a maximum. Thus, the critical plane approach using this parameter provided the location and the orientation of the crack initiation in fretting fatigue. In Namjoshi et al.'s [10] work, the modified SWT critical plane parameter was calculated in steps of $0.1°$ at angles ranging from $-90° \leq \theta \leq 90°$ from the perpendicular to the applied bulk stress, using the computed stresses and strains from the finite element analysis of the fretting fatigue experiments. Through the comparison SWT versus fretting fatigue life, Namjoshi et al. [10] found that the fretting fatigue lives resulting from the SWT parameter are dependent on the fretting pad geometry. Further, they also noted that the relationship between this parameter and fatigue life seems to be somewhat proportional to the applied Hertzian peak pressure.

The crack location and the angle of initiation are also two important considerations in the evaluation of any parameter. The SWT parameter's prediction of the crack location matched the experimental observation of the crack location, which was near the trailing edge in all tested fretting pad geometries. However, the SWT parameter

predicted the angle of crack orientation at the contact surface as within +5°to +8° of the perpendicular to the applied loading direction. This was not in agreement with the experimental observation of the crack initiation angle of ~ 45°. Therefore, to summarize, the fretting fatigue data based on SWT parameter showed a strong dependence on the pad geometry and/or the peak Hertzian pressure, and did not predict the orientation of the crack initiation satisfactorily in any pad geometry.

2.2.2. Shear Stress Range (SSR) Parameter

Namjoshi et al. [10] considered another parameter which is based on the shear stress, τ, on a critical plane, i.e. the shear stress range (SSR), $\Delta\tau$. The SSR is expressed as below:

$$\Delta\tau = \tau_{max} - \tau_{min} \tag{19}$$

where, τ_{max} and τ_{min} are the shear stress values resulting from the maximum and minimum applied axial loading conditions respectively.

From attempting to calculate the shear stress range on the critical plane, they noted that the effect of the mean axial/shear stress on the fretting fatigue is not included in the SSR parameter. However, it is well known that the magnitude of mean stress also affects the fretting fatigue behavior. Therefore, the mean shear stress ratio effect on the critical plane was included by incorporating a technique proposed by Walker [24], and is expressed as:

$$\Delta\tau_{crit,effective} = \tau_{max}\left(1 - R_\tau\right)^m \tag{20}$$

where τ_{max} is the maximum shear stress on the critical plane, R_τ is the shear stress ratio on the critical plane, and *m* is a fitting parameter. The value of *m* was determined as 0.45 from the plain fatigue tests performed by Lykins, Mall and Jain [8] for Ti-6Al-4V material. The method of calculating the SSR parameter was similar to the SWT parameter. As was done in the SWT parametric approach, the maximum shear stress range was also computed on all planes ranging from -90° ≤ θ ≤ 90° by increasing of 0.1°. The computed stresses and strains obtained from the finite element analysis (FEA) were utilized for this calculation.

From the applied results of the SSR parameter, it was shown that this parameter generates fretting fatigue life dependent on the fretting pad configurations included by Namjoshi et al. [10]. As in the results from the SWT parameter, the SSR critical plane parameter's prediction matched the experimental observation of the crack location near the trailing edge. Further, the orientation of primary cracks at the contact surface for all pad geometries predicted from this approach, was either from +45° to +50° or from -45° to -50°, which correlated well with the experimental observations.

Therefore, to summarize, the SSR critical plane parameter, based on the shear stress or the shear-cracking approach, also shows a dependence on the pad geometry in predicting fatigue life. However, it does predict the location and orientation of the crack initiation satisfactorily.

2.2.3. Findley Parameter (FP) Parameter

Some of the fatigue parameters involved both the shear and maximum stresses instead of using only one factor. One of the parameters which used both of the components was proposed by Findley [25] in the 1960's. Findley used the shear stress amplitude, $\tau_a = (\tau_{max} - \tau_{min}) / 2$, and the maximum normal stress, σ_{max}. The maximum

normal stress was combined with the shear amplitude through a fretting parameter, $k = 0.45$, as shown by the following:

$$FP = \tau_a + k\sigma_{max} \tag{21}$$

The critical plane was defined where the value of FP is maximum. As before, the value of FP was examined at all the planes by changing angle from $-90° \leq \theta \leq 90°$ in steps of $0.1°$ using the computed stresses and strains obtained from the finite element analysis. The Findley parameter does not show a strong dependency on pad geometry and predicts the crack location satisfactorily. Further, the predicted location of crack initiation was matched with test results near the trailing edge. However, it does not predict the crack orientation satisfactorily. The orientation of the critical plane, indicating the crack initiation angle from the contact surface, predicted by the FP was within $+5°$ to $+25°$ that did not correspond with experimental results.

To summarize, this approach pointed to the fact that the inclusion of the effect of normal stress seems to eliminate the effect of pad geometry. Therefore, a combination of shear and normal stresses in a different form may be able to satisfactorily fit all the experimentally obtained data.

2.2.4. Modified Shear Stress Range (MSSR) Parameter

As discussed in previous section, Namjoshi et al. [10] evaluated the previously developed critical plane parameters, i.e. SWT, SSR and FP parameters. From these efforts, Namjoshi et al. [10] found that the SSR parameter is the only parameter which satisfactorily predicts both the location and orientation of the crack in fretting fatigue condition. Further, they also revealed that the Findley parameter, FP, is independent of

the various pad geometries. If one looks at these parameters in detail, it can be noted that the SSR parameter is primarily included the shear stress effect while, FP includes the normal stress as well as the shear stress. From these observations, Namjoshi et al. [10] suggested the modified SSR parameter. This modification was accomplished to account for the normal stress in SSR parameter. This was because the FP which includes normal stress effects generated independent data on the predicted fretting fatigue life on pad configurations. Furthermore, normal stress was also expected to contribute towards crack initiation.

This modified version of the shear stress range critical plane parameter has been called modified shear stress range (MSSR) and is expressed as follows:

$$\text{MSSR} = A\Delta\tau_{crit,effective}^{B} + C\sigma_{max}^{D} \tag{22}$$

where the values of A, B, C, and D are determined as 0.75, 0.5, 0.75 and 0.5 respectively. These values have been determined by empirically providing a good fit to all the experimental data.

In this parameter, the first term, $\Delta\tau_{crit,effective}$, is the same as the SSR parameter, i.e. $\Delta\tau_{crit,effective} = \tau_{max}(1-R_r)^m$ and the second term is the maximum normal stress, σ_{max}, on the plane at maximum loading condition. The difference between the FP and the MSSR approaches to finding the critical plane should be mentioned here. The FP approach with a combination of the normal stress and the shear stress amplitude determined the critical plane at the maximum value of FP; however, in the MSSR parameter, the critical plane was selected by the maximum value of the $\Delta\tau_{crit,effective}$ first, and then the MSSR value was calculated using the maximum value of σ_{max} on the critical plane. The use of the MSSR parameter showed that this parameter was independent from the pad geometries. Furthermore, this modified parameter satisfactorily predicted the angle of crack

orientation and crack location in agreement with the results from experimental works. In conclusion, since the MSSR parameter explicitly included the effects of shear stress as well as those of normal stress, the MSSR parameter is a proper parameter to be used for predicting all of the fretting fatigue behaviors, such as the fatigue life, crack initiation location and orientation angle.

2.3. Various Averaging Methods

In the previous section, different types of critical plane parameters were discussed for the fretting fatigue condition. However, these parameters were evaluated mainly on the fretting fatigue condition involving elastic deformation. If the radii of the pads are smaller or applied loads to the pads and the specimens are increased, the state of stress on the contact surface will be greater than those in previous studied references, and possibly increased beyond yield stress. Further, the size of the plastic zone will be larger and should not be disregarded. Moreover, the increased maximum stress on the contact surface also leads to change stress distribution near the contact surface. With these increased maximum stress condition, using only the peak stress on the contact surface for predicting fretting fatigue life can be inappropriate.

The similar condition can be finding from the notch problem. In the notch problem, the maximum stress usually occurs at the root of the notch. This maximum stress increase as the radius of the notch root decrease. Consequently, many attempts have been made to develop methods which can measure the fatigue limit reduction factor incorporated with both sharp and blunt notch cases. In this section, several methods which have been developed to correlate fatigue life to the shape of notch roots will be

reviewed. Further, some efforts which apply these methods developed for the sharp

notch problem to the fretting fatigue condition will be mentioned.

2.3.1. Critical Distance Method in Notch Problems

Generally, notches are considered as the one of the typical geometric stress

concentrators in mechanical components. Historically, various methods have been

proposed by a number of researchers to deal with the excessive stress concentration

condition which frequently occurs in sharp notch cases. The quantity of this maximum

stress is dependent on the notch radius and acts to reduce fatigue limits as compared with

plane fatigue, i.e. the specimen without a notch. Generally, these maximum stresses,

σ_{max}, resulted by local stress concentrations, are greater than the nominal stress of the

member, S. In elastic stress state, the ratio of these stresses is defined as K_t, the

theoretical stress concentration factor [26].

$$K_t = \frac{\sigma_{max}}{S} \tag{23}$$

This theoretical stress concentration factor, K_t, is entirely dependent on geometry

and loading conditions. The value of K_t is calculated by static loading conditions.

However, in the study of fatigue behavior, especially in the stress-life approach, the effect

of notches is elucidated by the fatigue notch factor, K_f. This value reveals the

relationship between the unnotched fatigue strength, S_{eu}, to notched fatigue strength, S_{en},

of any given material. This relationship can be written as follows:

$$K_f = \frac{S_{eu}}{S_{en}} \tag{24}$$

Considerable efforts have been made to link the quantities of K_f and K_t. The simplest approach to correlate these factors is regarding the fatigue notch factor as same as the stress concentration factor which can be found at the notch root. This approach is suitable for blunt notches. However, for sharper notches, this approach gives an inaccurate prediction which becomes increasingly unreliable as the notches become sharper [27]. The reason for impropriety is due to the fact that adopting the maximum stress, σ_{max}, at the notch root only does not serve to describe the gradient of the stress field along the depth of specimen, especially in sharp notch cases.

In the past, various methods have been developed to deal with the sharp notch problem. Most of these approaches were based on the concept of a process zone which contains a small volume of material around the notch. Also, the size of the volume was assumed to be a material constant. The process zone method can be classified by the point, line and area methods.

The point method was proposed by Peterson [11]. He related the quantity of K_f to K_t using the radius of the notch, r, and the material constant, a, as described below:

$$K_f = 1 + \frac{K_t - 1}{1 + \dfrac{a}{r}} \tag{25}$$

The constant a depended on material strength and ductility which was can be obtained from long life fatigue tests for notched and unnotched specimens. This method was based directly on the stress gradient effect and the assumption that failure occurs when the stress equals the fatigue strength at a constant distance beneath the notch tip for

28

a given material. An empirical relationship between a and the material tensile strength has been found by a number of researchers [28].

Another well known averaging approach, the line method, was suggested by Neuber [12] in 1949. He proposed using average stress on the line of a critical length starting at the notch roots. Neuber developed a formulation for converting any given theoretical factor K_t into a fatigue notch factor, K_f. This formulation is

$$K_f = 1 + \frac{(K_t - 1)}{1 + \sqrt{\dfrac{\rho}{r}}} \tag{26}$$

where r represents the radius at the root of the notch and ρ is the material. These r and ρ constants are essentially of the same units as those of the point method. However, the material constant, ρ, in the line method is related to the grain size of the material.

It is should be mentioned here that if the material constants, a and ρ, which are used in the point and line method respectively, are zero, then the value of K_f is equal to the K_t value, meaning that the material has 100% notch sensitivity. If these constants become very large, then $K_f = 1$ regardless of the value of K_f and this indicates that the material is completely insensitive to notches. Another interesting factor is that, when r is a very large value, there are no notch effects and $K_f = K_t$, so it is similar to the blunt notch case mentioned before.

Kuhn and Hardraht's study [29] mentioned an additional explanation of the Neuber constant, ρ. Conventionally, the engineering materials were considered as a continuum structure in the theory of elasticity. However, since most materials have a granular structure in reality, this assumption is inappropriate when a stress gradient occurs. Neuber suggested the concept that the material is an aggregate of the building blocks instead of a continuum structure. He also presumed that no stress gradients occur across such a block and the quantity of ρ is the half-length of a block.

As an example, generally large scale specimens which contain an enormous number of grains have been used to determine the property of a given material. With these test conditions, most materials are considered as homogenous. However, if the test specimens were made smaller to contain only a single grain, the measured properties would be varied among test specimens and will depend on the property of the individual grain. Then, it is evident that the assumption of homogeneity becomes incorrect.

With this consideration, the building block could be interpreted as the minimum volume of material which has an acceptable quantity of accuracy with the standard engineering properties of the material. Neuber's building block is a conceptual entity that can be determined only by calculation from tests data. As an example, tests results of the Neuber constant for steel and aluminum can be found in Juvinall's work [30]. Furthermore, it should be mentioned that the preceding interpretation implies the Neuber constant, ρ, may have different values for a given material, depending on test conditions, such as strain, yield stress, static strength, or fatigue strength, etc.

Many researchers have worked on the point and line methods to quantity the fatigue reduction factor on the notch cases, especially for the sharp notch. Recently, Taylor [27] applied the point and line methods to predict the decrease of the fatigue limit for various notch radii. Figure 9 illustrates the difference between these approaches.
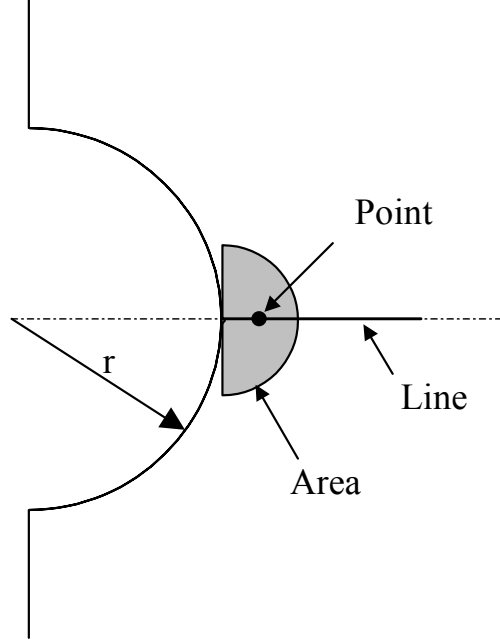
Figure 9. Illustration of the Point, Line and Area methods

Taylor showed that the critical distance, which has been determined by fatigue tests and has been considered as the material constant, can be replaced with the El Haddad et al.'s [31] effective crack length, a_o. The effective crack length is the modification parameter for the classical fatigue limit of a cracked specimen $\Delta\sigma_{oc}$ such as

$$\Delta\sigma_{oc} = \frac{\Delta K_{th}}{\sqrt{\pi a_c}} \tag{27}$$

El Haddad proposed an empirical equation that is a modified form of $\Delta\sigma_{oc}$ by introducing a material constant a_o thus:

$$\Delta\sigma_{oc} = \frac{\Delta K_{th}}{\sqrt{\pi(a_c + a_o)}} \tag{28}$$

and a_o is calculated as follows:

$$a_o = \left(\frac{1}{\pi}\right)\left(\frac{\Delta K_{th}}{\Delta\sigma_o}\right)^2 \qquad\qquad (29)$$

where $\Delta\sigma_o$ is the fatigue limit of the material.

In order to avoid the empirical methods suggested by Paterson and Neuber for finding the critical distance, Taylor correlated this a_o value to the critical distance for crack cases and attempted to use the same concept for the notch problem. Using this process zone approach, that the local stresses of the cracked (or notched) specimens must exceed the plain fatigue limit not only at the hot spot but also within some region ahead of the stress concentrators, Taylor attempted to find the value of critical distance for the specimen with a crack. If a large crack is considered in the elastic stress range, the stress state along the crack direction can be described by the following equation:

$$\Delta\sigma(r) = \Delta\sigma\left(a_c/2r\right)^{1/2} \qquad\qquad (30)$$

where r represents the distance measured on the crack plane and a_c is the crack length. Using equations 29 and 30, he found that when $\Delta K = \Delta K_{th}$ the stress value is the same as the plain fatigue limit value. With this observation, he picked a value of stress at $r = a_o/2$ that is the regarded as the critical distance for the point method. Using a similar approach, he showed that the value of stress averaged along the line, which had a length of $r = 2a_o$ (line method), and over the half circle where the radius $r = a_o$ (area method) are also exactly or about equal to the plain fatigue limit value.

The formulas for the above relationships can be written for the point, line and area methods respectively as follows:

$$\Delta\sigma\big|_{(r=a_o/2)} = \Delta\sigma_o \tag{31}$$

$$\Delta\sigma_{av}\big|_{(r=0-2a_o)} = \frac{1}{2a_o}\int_0^{2a_o}\Delta\sigma\sqrt{\frac{a_c}{2r}}dr = \Delta\sigma_o \tag{32}$$

$$\Delta\sigma_{av}\big|_{(Area=a_o)} = \frac{4}{\pi a_o^2}\int_0^{\pi/2}\int_0^{a_o}\Delta\sigma\sqrt{\frac{a_c}{2r}}\left(\cos\frac{\theta}{2}\right)\left(1+\sin\frac{\theta}{2}\sin\frac{3\theta}{2}\right)rdrd\theta = 1.1\Delta\sigma_o \tag{33}$$

With reasonable results from long crack cases, Taylor was encouraged to extend this concept to short crack cases. Using the stress state equation of a short crack condition, he assumed the point stress equal to the plain fatigue limit, $\Delta\sigma_o$, at the $r = a_o/2$ for the point method. He also presumed that the values of stress, averaged along the line ($r = 2a_o$) and over the half circle ($r = a_o$), are equal to the plain fatigue limit for the line and area methods respectively, using the stress state for the short crack case as follows:

$$\Delta\sigma(r) = \Delta\sigma\Big/\left[1-\left(a_c/(a_c+r)\right)^2\right]^{1/2} \tag{34}$$

the fatigue limit of the cracked body, $\Delta\sigma_{oc}$, for the point and line methods can be written respectively as follows:

$$\Delta\sigma_{oc-\text{point}} = \Delta\sigma_o\left[1-\left(a_c/(a_c+a_o/2)\right)^2\right]^{1/2} \tag{35}$$

$$\Delta\sigma_{oc-\text{line}} = \Delta\sigma_o\left[a_c/(a_c+a_o/2)\right]^{1/2} \tag{36}$$

For the area method, he used numerical results to average the stresses over the given area since no simple analytical solution was available. With this approach, he demonstrated that all three methods follow the general format of El Haddad's solution, meaning that they would also give reasonable approximations of the experimental data.

In the notch problem, he used exactly the same assumptions. Using the stresses in the region of a circular hole in an infinite plate with remote tensile stress, σ, the fatigue limit for a body containing a notch, $\Delta\sigma_{on}$, can be written as follows:

$$\Delta\sigma_{on-\text{point}} = 2\Delta\sigma_o \Big/ \Big[2 + \big(a_n/(a_n + a_o/2)\big)^2 + 3\big(a_n/(a_n + a_o/2)\big)^4 \Big] \tag{37}$$

$$\Delta\sigma_{on-\text{line}} = 2a_o\Delta\sigma_o \Big/ \Big[2a_o + a_n - 0.5a_n^2 \big/ (a_n + 2a_o) - 0.5a_n^4 \big/ (a_n + 2a_o)^3 \Big] \tag{38}$$

Again, the averaged stress value over the given area was calculated numerically since no simple analytical solution could be identified. The averaged stress was evaluated using maximum principal stress at all points in the chosen semi-circular area. By comparing the experimental data for four different hole diameters at $R = -1$, all prediction lines, including Peterson's point method, show the same general features, approaching the plane fatigue limit as the notch size tends to zero. There is somewhat more variation among the three different methods than was found for cracks, but all three give reasonable predictions of data. The area method gives the best estimate of the experimental results.

It should be mentioned here that the a_o value can be varied by the loading ratio R and the geometry of the specimen. This means the basis of the critical distance has changed from the original concept that the critical distance is the material constant as proposed by Paterson and Neuber.

2.3.2. Volumetric Approach

Another approach, called the volumetric approach, was introduced to surmount some deficiencies evident in the traditional critical distance concept. Qylafku et al. [13] pointed out that most of the historical critical distance methods, which had been

suggested by Peterson [11] and Neuber [12], contain constants, called critical distance or material parameters. These constants are mostly empirical values depending on a given material. However, these parameters also depend very much on test conditions and geometries, so it is difficult to generalize them for any other loading cases and specimen geometries. Also, in these critical distance methods, only the fatigue limits were correlated with the notch radius by the value of K_f. However, besides the fatigue limit, the prediction of fatigue failure for any given load is also the most important part of the fatigue phenomenon in fatigue life analysis. Furthermore, considering that most critical distance methods are mainly focused on an elastic stress distribution, the conventional damage models in the notch problem cannot represent the actual situations.

From various recent works on the fatigue failure mechanism using macroscopic and microscopic approaches, it has been shown that the fatigue failure of structures depends not only on the peak stress at the notch root, but also on the stress field in the damaged zone. In view of the fatigue mechanism, crack initiation generally occurs within the local region near the notch surface. However, it has not been possible to quantitatively determine the size of the region, either through macro-mechanical, or micro-mechanical studies.

Kadi [14] also showed an example of the deficiencies of traditional methods in determining fatigue life duration. Since traditional methods contain the stress concentration factor, K_t, and the notch radius, r, two specimens with the same values of K_t and r should have the same fatigue life duration. Figure 10 illustrates an example of specimens which are composed of the same material with $K_t = 2.72$, $r = 0.3$. Nevertheless, the fatigue life duration is different for one than for the other. The reason for this discrepancy can be assumed to be the difference in the stress distribution near the notch tip.

$d_a = 8$ mm, $D_a = 10$ mm $\qquad$ $d_b = 7.2$ mm, $D_b = 15$ mm
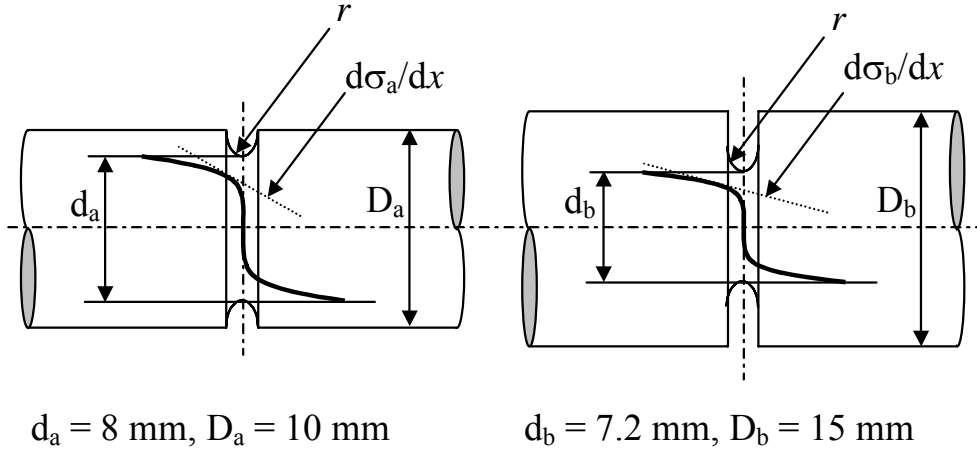
Figure 10. Stress Distributions for Two Specimens with the Same K_f and r

For these reason, they used the volumetric approach to predict fatigue life for the different stress concentrators such as notch and key seat. Qylafku et al. [13] modified the stress field intensity model [32] for fatigue life prediction on notches and key-seat problems. The stress field intensity function, σ_{FI}, can be written as follows:

$$\sigma_{FI} = \frac{1}{V} \int_{\Omega} f(\sigma_{ij}) \varphi(\vec{r}) dv \tag{39}$$

where Ω is fatigue failure region and V is the volume of Ω. The fatigue failure region was assumed to be a circle or a sphere and its size was determined by the fitting of experimental results for each given material. The stress equivalent function, $f(\sigma_{ij})$, is Von Mises equivalent stress for elastic-plastic stress distribution.

The effects of each stress component within a given volume depended on the relative stress gradient. Further, the relative stress gradient was dependent on the distance between the peak stress due to the stress concentrator and the location of the stress which used to predict fatigue life. Therefore, the relative stress gradient takes into

account the influence of the loading mode and geometry effect. This is expressed by the following formulation:

$$\chi = \frac{1}{\sigma_{ij}} \frac{d\sigma_{ij}}{dr} \tag{40}$$

The role of the stress is related to the distance from the stress concentrator and is decreased as the distance increases. The weight function, $\varphi(\vec{r})$, is introduced to contain these two parameters. It can be analytically or numerically obtained and has the following characteristics:

1. $0 \le \varphi(r) \le 1$
2. $\varphi(0) \equiv 1$
3. when $\chi = 0$, $\varphi(r) \equiv 1$

The proper weight function that describes above condition is:

$$\varphi(\vec{r}) = 1 - \chi \cdot |\vec{r}| \tag{41}$$

Although the stress field intensity approach is good for predicting the fatigue life, Qylafku et al. [13] mentioned that it is not yet clear how to quantify the size of the damage zone, Ω. For these reasons, He proposed a new model in which the damage zone was bounded by the effective distance, χ_{ef}. Figure 11 shows the location of the relative gradient and χ_{ef} on a typical elastic-plastic stress distribution in bi-logarithmic coordinates for a notch specimen.
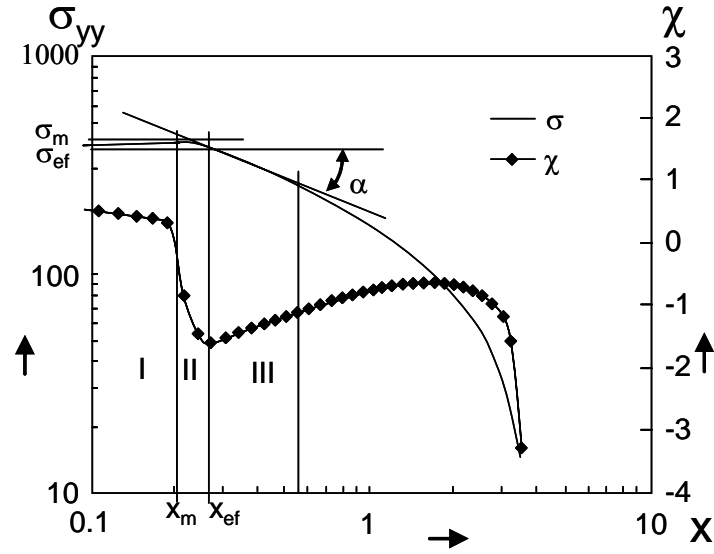
Figure 11. Elastic-plastic Stress Distribution of σ_{yy} and Relative Gradient for Notch

From Figure 11, it can be seen that the elastic–plastic stress distribution shows first a peak point and then decrease as the distance from the notch tip increase. The stress distribution near the notch root can be broken down into three zones: The first zone includes the maximum stress that in the case of elastic–plastic behavior represents a maximum point with respective coordinates, x_m and σ_m. The second zone is an intermediate zone between the first and the third part of the diagram. The third zone is where the stress distribution might be considered as nearly a straight line. Behind the third zone, the stress values are quite small, so this part is not important in the fatigue failure process.

The effective distance, χ_{ef}, was selected at a point where the relative stress gradient has a minimum value. In this case, the minimum value of the gradient occurred at the boundary of second and third zones. Using this effective distance, Qylafku et al. [13] modified the stress field intensity formulation as follows:

$$\sigma_{FI}^* = \frac{1}{x_{ex}} \int_0^{x_{ef}} \sigma_{yy} \left(1 - \chi x\right) \tag{42}$$

Qylafku et al. applied this new method for the elastic-plastic stress distribution on the smooth, notch and key-seat specimens to predict fatigue life. Geometries of specimens were shown as in figure 12. A comparison of the stress field intensity values computed for the notched specimens and the specimens with key-seats, together with the reference curves, is shown as in figure 13.
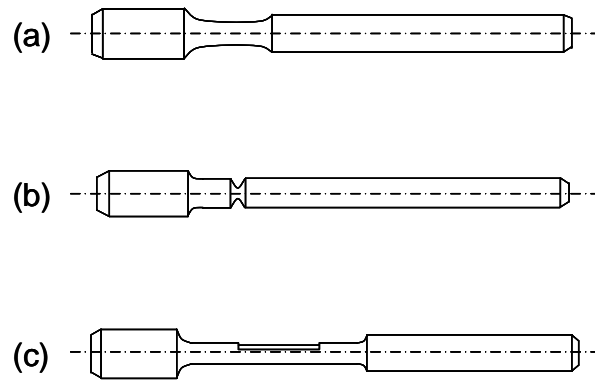
Figure 12. Test Specimens used by Qylafku et al.: (a) smooth specimen, (b) notched specimen, (c) specimen with a key-seat
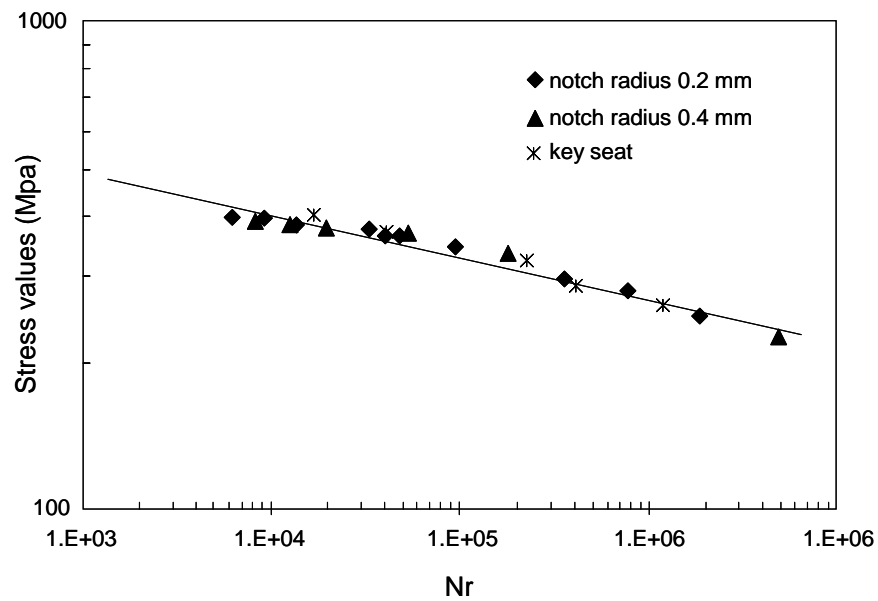
Figure 13. Comparison of the Stress Field Intensity Values for Various Specimens

Qylafku et al. reported that the hot spot, point stress and average stress models are not adequate to describe fatigue failure. The results also showed that the modified stress field intensity approach, based on the intrinsic fatigue strength curve and the elastic-plastic stress distribution, provides good agreement with the experimental data.

Kadi [14] also demonstrated that the volumetric approach gives a good estimate of fatigue life duration in the case of shafts with various geometries of key-seats. The principal concept of this approach is the same as Qylafku et al.'s method in that the fatigue failure is dependent on a specific physical volume. He specified the physical volume by the minimum relative stress gradient, and assumed that all the stresses in this volume were involved in the fatigue failure mechanism. Kadi applied this approach for fatigue testing under a rotating bending loading condition. The smooth specimens were used to obtain a reference curve and two types of key-seat specimens were also tested to compare with the reference curve. Figure 14 shows the two types of key-seat specimens.

For the various test conditions, finite element analysis was conducted to calculate effective stress, σ_{ef}, which has the same meaning as the stress field intensity in Qylafku et al.'s work. From the results, he found that the effective stress gave the same number of cycles to failure as the experimental results. Also, the results demonstrated that the plot of effective stress versus number of cycles to failure was independent of the key seat geometries.

Semi-circular End   Sled Runner R = 5 and 7.5 mm
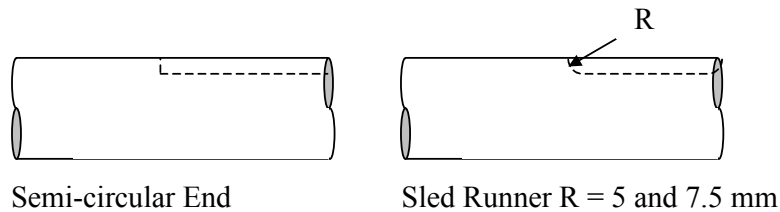
Figure 14. Key-seated Specimens Tested by N. Kadi

It should be mentioned that it was not possible to apply other critical distance models on the specimens with key-seats. This is because almost all of these models refer to notch radius, which cannot be determined in the case of the specimens with key-seats. Therefore, some researchers referred to this new approach as the volumetric approach.

2.3.2. Averaging Methods in Fretting Fatigue

In the previous sections, it was illustrated that the volumetric approach was successfully applied for predicting fatigue life in the notch condition due to the stress gradient effects. Since stress gradient effects also occur in the fretting fatigue condition, some efforts to incorporate the effects of the volume process approach on fretting fatigue problems have been also made.

Recently, Araujo and Nowell [15] had calculated total fatigue lives analytically and compared them with experimental values under fretting fatigue conditions using averaging methods. To obtain the total fatigue life experimentally, they used a cylindrical pad on a flat plane fretting test condition. Two high strength alloys, Al4%Cu and Ti-6Al-4V, were used for both the pads and specimens. However, the radii, R, of pads and the normal load, P, were varied to keep the magnitude of the stress field constant as contact width, a, was changed. The total fatigue life was evaluated analytically using two critical plane models. The first model is the Smith, Watson and Topper (SWT) parameter that was proposed for the cracks that grow in planes of high tensile strain and it can be expressed as follows:

$$SWT = \sigma_{max}\left(\frac{\Delta\varepsilon}{2}\right) \tag{43}$$

where $\Delta\varepsilon$ is the difference of the maximum and minimum strain and σ_{max} is the maximum value of the stress component during the cycle. The directions of both $\Delta\varepsilon$ and σ_{max} are perpendicular to the plane.

Secondly, the FS parameter, which was suggested by Fatemi and Socie [6] for situations in which cracks grow on planes of high shear strain, was used as shown below:

$$FS = \frac{\Delta\gamma}{2}\left(1 + \alpha\frac{\sigma_{max}}{\sigma_y}\right) \tag{44}$$

where $\Delta\gamma$ is the difference of maximum and minimum values of shear strain experienced during the cycle, σ_{max} is the maximum value of the stress normal to the chosen plane, σ_y is the yield strength, and α is a constant which approaches unity during long lives and is reduced during shorter lives. For a fully reversed uniaxial test, it is possible to estimate the crack initiation life by the use of the SWT and FS models. In such a test condition, the stress-life and strain-life curves can be modeled satisfactorily by the Basquin and Coffin-Manson laws and can be written as follows:

$$\frac{\Delta\sigma}{2} = \sigma_{max} = \sigma_f'\left(2N_f\right)^b \tag{45}$$

$$\frac{\Delta\varepsilon}{2} = \frac{\sigma_f'}{E}\left(2N_f\right)^b + \varepsilon_f'\left(2N_f\right)^c \tag{46}$$

where σ_f' and b are the fatigue strength coefficient and exponent, ε_f' and c are the fatigue ductility coefficient and exponents, E is Young's modulus and N_f is the number of cycles to initiate a crack of a given length.

Using the above equations, the crack initiation fatigue lives can be correlated with the SWT and FS parameters as shown below:

$$SWT = \sigma_{max}\left(\frac{\Delta\varepsilon}{2}\right) = \frac{\left(\sigma_f'\right)^2}{E}\left(2N_f\right)^{2b} + \sigma_f'\varepsilon_f'\left(2N_f\right)^{b+c} \tag{47}$$

$$FS = \frac{\Delta\gamma}{2}\left(1 + \alpha\frac{\sigma_{max}}{\sigma_y}\right) = \frac{\tau_f'}{G}\left(2N_f\right)^b + \gamma_f'\left(2N_f\right)^c \tag{48}$$

where E is Young's modulus, G is the shear modulus and τ_f', γ_f', b, and c are constants. These equations are used to obtain the analytical cycle of crack initiation using the maximum value of SWT and FS parameters on the contact surface. To choose the initiated crack size, b_i, within the range of sizes for which LEFM is applicable, they determined the $b_i = 1$ *mm*. The propagation life was calculated by integration of the Paris law:

$$N_p = \int_{b_i}^{b_f} \frac{db}{C\left(\Delta K\right)^m} \tag{49}$$

where the final crack size, b_f, was set to equal the specimen thickness. By comparing analytical total fatigue lives with experimental results, they found that the predicted lives agreed reasonably well with the experimental data for large contact width cases. However, for small contact width conditions, predicted lives were overly conservative for both given materials. The reason of this inaccuracy was assumed to be a result of the steeper stress gradient present at smaller contacts.

These results suggest that these methods will not be adequate for evaluating fretting fatigue life with different geometries, especially in the presence of a high stress

gradient condition. Araujo and Nowell [15] attempted critical distance and volume averaging methods similar to that used for the notch problem to account for stress gradient effects. Even though an averaging dimension is assumed as the material constant value in notch cases, they tried to seek the quantity of the distance or volume that would generate the best fit for the set of experimental data presented. The critical distance method is illustrated in figure 15. As can be seen in the figure, the crack location and angle were determined by the maximum value of SWT or FS on the surface, then the averaged value of SWT or FS was calculated for the arbitrary dimension of depth, d_c.

$$SWT_{AVERAGE} = \frac{1}{N}\sum_{i=1}^{N} SWT_i$$

$$FS_{AVERAGE} = \frac{1}{N}\sum_{i=1}^{N} FS_i$$
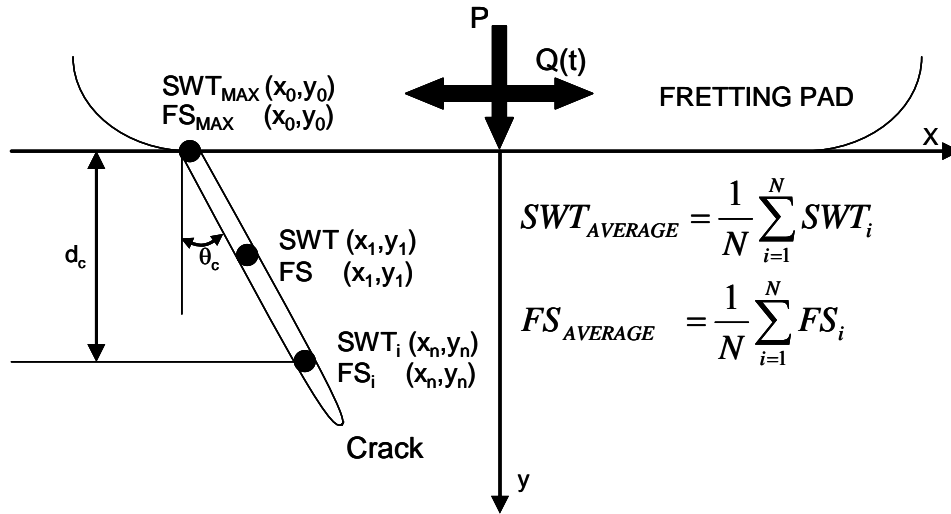
Figure 15. Critical Distance Method Used by Araujo and Nowell

Figure 16 shows the procedure used in the volume method. The volume method was based on the concept in which a crack is initiated by high stresses over a critical volume. Araujo and Nowell [15] averaged stress over the particular volume (or area) and evaluated the fatigue parameter at different planes. Once the global maximum was

45

determined by the average stress, the corresponding location of the crack initiation and critical plane orientation, θc, was selected for the predicted crack behaviors.
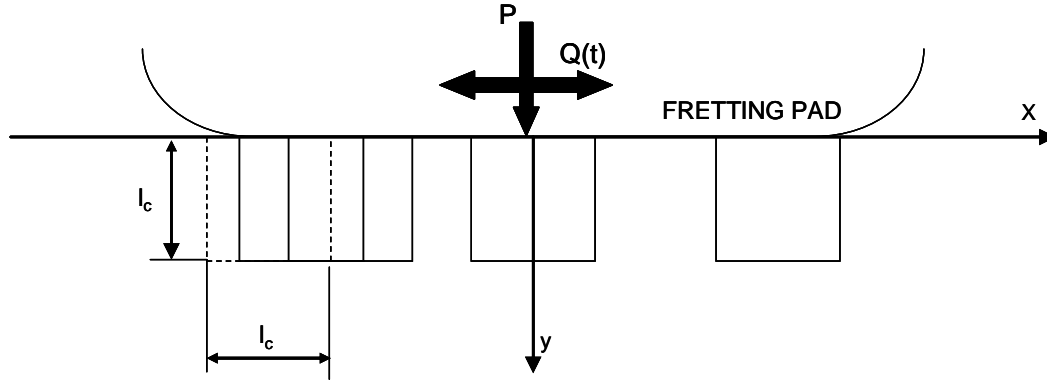
Figure 16. Volume Method Used by Araujo and Nowell

It was concluded from the application of two averaging methods that there was no single averaging dimension or volume that could precisely predict the effect of the stress gradient on the fatigue life. These results imply that the dimensions depended on the geometries and loading factors instead of a true material constant. Even though the dimension of the averaging methods may not be a material constant, Araujo and Nowell [15] found the range of critical depth, d_c, or volumes, l_c, which would give a well-predicted fatigue life for the Hertzian contact geometry across a range of loading conditions for both materials such as: d_c=20-80μm or l_c=20-80μm for Al4%Cu and d_c=5-20μm or l_c=5-20μm for Ti-6Al-4V. Since the suggested dimensions depended on the material instead of averaging methods, they concluded that the life estimates are more sensitive to the characteristic dimension than to the averaging method itself.

Swalla and Neu [16] demonstrated an effect of averaged stresses and strains for predicting the crack nucleation in the fretting fatigue condition as changing the length of

a critical distance. PH 13-8 Mo stainless steel was used for cylindrical-on-the flat contact

fretting fatigue testing under the test conditions of contact load, P = 343.4 N, remote

fatigue stress amplitude, σ_a = 217 MPa, with a stress ratio, R = 0.1. The tested

specimens showed that the direction of the fretting fatigue crack changed as it grew

further into the specimen. Following the angle changes of crack direction, there are three

regimes that can be categorized. The first regime, called the crack nucleation regime, is

extended within a depth approximately 50 μm from the surface. In this regime, the crack

angle was changed from about 65° ± 50° to about 55° ± 5°. The second regime is located

between 50 μm and 200 μm from the surface and the crack angle is near 25° ± 5°. This

regime can be called an intermediate region, which is still strongly influenced by the

frictional force. Finally, the third regime starts at the 200 μm distance from the surface

where the crack angle gradually tends to 0°, normal direction to the fatigue loading. In

this regime, the frictional force by the pad is considered diminished

From these observations, Swalla and Neu [16] assumed there was a critical

volume of material near the contact that is highly influenced by the fretting loads. This

critical volume is referred to as the Fretting Fatigue Process Volume (FFPV). To study

the reliability of some critical plane approaches with changing depth of the FFPV, they

used two multi-axial fatigue models, i.e. Fatemi-Socie-Kurath (FSK) [6] and

Smith-Watson-Topper (SWT) [5]. The value of the FSK model is predominated by shear

stresses. The formulation can be written as follows:

$$FSK = \frac{\Delta \gamma}{2}\left(1 + k\frac{\sigma_{n,\max}}{\sigma_y}\right) \tag{50}$$

where Δγ/2 is the maximum cyclic shear strain amplitude, k is a material dependent

constant, σ_y is the cyclic yield strength and $\sigma_{n,max}$ is maximum normal stress.

However, the quantity of the SWT is mainly varied by tensile stress shown as

follows:

$$SWT = \frac{\Delta\varepsilon}{2}\sigma_{n,max} \tag{51}$$

where Δε/2 is the maximum principal strain amplitude on a plane and $\sigma_{n,max}$ is the

maximum normal stress on this plane during the cycle. They also computed critical

values of maximum average shear strain ($\Delta\bar{\gamma}_c / 2$), maximum average normal strain

($\Delta\bar{\varepsilon}_N / 2$), and average maximum normal stress ($\Delta\bar{\sigma}_{N,max}$), as well as the FSK and SWT.

Figure 17 illustrates the line averaging method that was used to find the critical

plane. For each arbitrary line that has a particular length, L, and angle, θ, the stress/strain

values are transformed at the points on the selected line using the same angular value,

then calculate the averaged value of these stress/strain values. The angle of the predicted

critical plane orientation was determined where the averaged stress/strain or combined

parameters (FSK, SWT) are maximum.
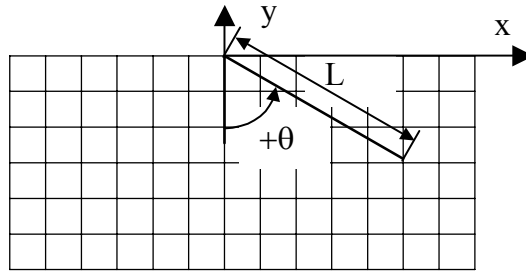
Figure 17. Line Averaging Method Used by Swalla and Neu [17]

From the results, Swalla and Neu [16] found that the parameters were affected by the length L. For L < 40 μm, predicted angles by the $\Delta\bar{\gamma}_c/2$ or FSK parameters are more reliable than the $\Delta\bar{\varepsilon}_N/2$ or SWT parameters to predict the angle of the critical plane orientation. When the depth of the FFPV was between L = 40 to 100 μm, the normal stress/strains became increasingly dominant, so this zone can be regarded as a transitional region. In this zone, it should be reasonable that both the shear and normal stress/strain factors can be used to predict the crack initiation angle. Finally, the normal stress or SWT model appears to be more appropriate when L > 100 μm. Based on these results, they concluded that the most appropriate multi-axial fatigue models for fretting fatigue damage prediction are dependent on the size of the FFPV considered in the analysis.

Namjoshi et al. [17] also investigated the specific character of critical plane parameters under alternative dimensions of the process volume and coefficient of friction in fretting fatigue. The Smith-Watson-Topper (SWT), Shear Stress Range (SSR), Findley (FP) and Modified Shear Stress Range (MSSR) parameters were chosen for the examination. Finite element analysis was accomplished to generate the stress distribution for each fretting condition. Once the averaged stress values were calculated over the arbitrary length of the critical plane, the critical plane parameters were evaluated using these mean stress values. The detail of the volume averaging method is illustrated in Figure 18. The averaged value of the critical plane parameter was calculated at a given angle, θ, and distance, R_{FFPV}, from a chosen point on the contact surface. The critical plane parameters were calculated for all orientations ranging from −90° ≤ θ ≤ 90° with a step increase of 0.1°. For each angle, the value of R_{FFPV} was changed from 0 to 100 μm in steps of 10 μm. Namjoshi et al. [17] determined 15 points as an optimum number to collect the stress values over the chosen line. Once a maximum averaged value for a parameter was calculated, the angle of orientation and length of volume were determined at this condition. The same procedures were conducted for the different points on the

contact surface. Consequently, they predicted crack initiation location and angle by comparing the calculated averaged values of all points for the various dimensions of the process volume.
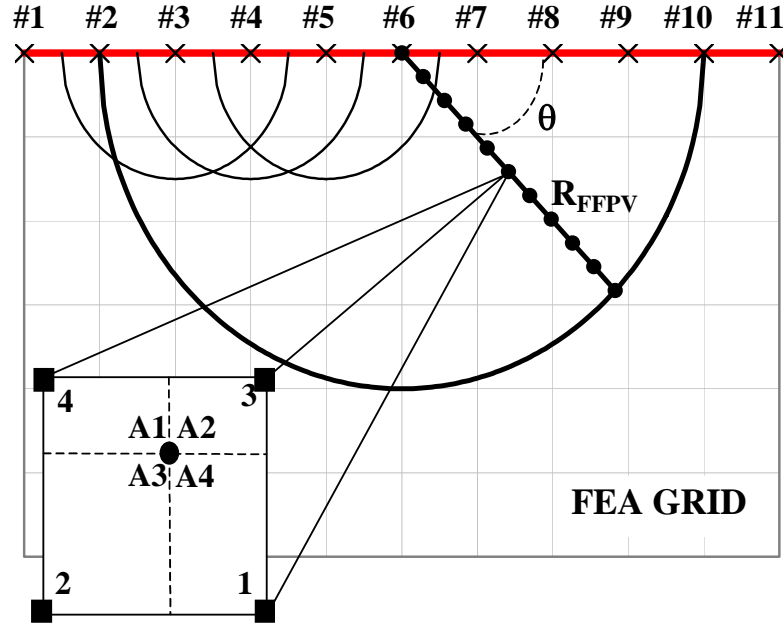
Figure 18. Algorithm of FFPV Used by Namjoshi et al.

Namjoshi et al. [17] showed that the quantity of all critical plane parameters (SWT, SSR, FS and MSSR) have an inverse relationship with the dimension of process volume for all tested pad geometries. For example, the values of the critical plane parameters decreased as the size of process volume increased. They also found that the predicted crack initiation location by the critical plane parameters was not affected by the variation of the process volume size. However, the orientation of crack initiation changed slightly for the flat pad geometries as the radius of a process volume changed.

Finally they asserted that the MSSR parameter, unlike the other three critical plane parameters, was the unique parameter that could satisfactorily predict the crack

initiation location, orientation angle, and the number of cycles to fretting fatigue crack initiation for any size process volume and coefficient of friction.

2.4. Elastic-plastic Considerations in Fretting Fatigue

In addition to the investigations involving fretting fatigue under elastic analysis, there are a few efforts which have studied fretting behavior under elastic-plastic stress distribution. Some of these endeavors are related to the proposed work and will, therefore, be discussed here.

Ambrico and Begley [18] analyzed the behavior of plastic deformations under various fretting loading conditions. To study how plastic deformation evolves under fretting conditions, they employed an idealized model; a rigid cylindrical indenter was employed in which the indenter pressed against a flat substrate with a constant normal load and cyclic tangential load. The rigid pad represented contact condition and the contacting bodies had different elastic properties. Also, analysis was performed under plane strain conditions.

In addition to studying the effects of loading conditions, they considered influences of the different material plasticity models such as elastic perfectly-plastic, kinematic strain hardening and isotropic strain hardening. The plastic zone was broken down into three areas: shakedown, cyclic plasticity, and ratcheting. Shakedown refers to regions where the plastic straining was generated during initial load cycles and experienced no further changes in plastic straining upon continuously applied cyclic loadings. The term cyclic plasticity is applied to the zone where the reversed plastic straining occurred repeatedly and the magnitude of the maximum plastic strain preserved. On the other hand, ratcheting represents regions where the plastic strains increase continually with a number of loading cycles.

Their results indicated that the quantity of plastic deformation was not much affected by the selection of material plasticity models. However, when using the isotropic strain hardening, the ratcheting area in plastic strain zone was notably decreased in comparison to that of other material plasticity models. Ambrico and Begley [18] also showed increasing tangential load increase the amount and severity of plasticity. The steady state was determined by examining the cyclic plastic strain, since ratcheting strains apparently usually shake down and thus are probably not as important for high cycle fatigue considerations. Also, the cyclic plastic straining is rather insensitive to extended cyclic loading and strain hardening, whereas ratcheting often shows opposite trends. These observations led the researchers to determine that three plate tangential load cycles is a sufficient number to capture steady state response. By examining the effect of plasticity on the shear tractions, they showed that contact shear stress on the contact surface was qualitatively similar in elastic and elastic-plastic results. However, the significance of applying plasticity effects in analysis arose from the strain distributions in the direction parallel to the surface; it was demonstrated that the strain distributions on the surface of substrate were remarkably different between two analysis approaches, particularly near the edge of contact. They assumed that this might have important implications for predicting the number of cycles required to nucleate a surface crack. Moreover, by comparison of the magnitude of strain between surface and very near the surface, they showed that large strain gradients exist near the surface that may require more sophisticated material models and more detailed handling of the surface topology. They also investigated the utility of one of fretting fatigue parameters, Ruiz parameter, which was suggested by Ruiz et al. [23] to predict crack nucleation behavior for the fretting fatigue. Since the results using elastic and elastic plastic analysis were similar, they concluded that the elastic analysis fairly accurately predicted nucleation sites relative to the contact area. Finally, since it is possible that certain contact

geometries lead to crack nucleation caused by plastic rupture driven by ratcheting while others lead to nucleation via reversed cyclic plastic straining, it would be difficult (if not impossible) to successfully predict nucleation for different geometries using elastic analyses, as they are obviously incapable of partitioning ratcheting and cyclic plastic strain components.

Ambrico and Begley also studied the role of plastic deformation in fretting fatigue life predictions [19]. They employed similar fretting conditions as those mentioned above in order to investigate the variation of the fatigue life predictions between purely elastic and elastic-plastic analyses. The life predictions were accomplished by using a Coffin-Manson equation and the maximum tensile principal total strain range. They demonstrated some features of predicted fatigue life as can be seen as follows: For small tangential loads, less then 25% of the gross sliding load, an elastic analysis predicted a conservative lifetime. However, for larger tangential loads, elastic analyses provided significantly over-estimated fatigue lives. Because of this transition, it may be difficult to accurately correlate purely elastic analyses with experimental fatigue data over the entire load range using a single methodology. Some of features of cyclic contact deformation that must be considered for accurate nucleation or lifetime prediction were suggested by their efforts. They concluded that plastic ratcheting may be beneficial because it rearranges material to limit strain ranges, while the residual stress fields created by plastic deformation tend to increase strain ranges. The calculations presented in their study demonstrate a potential competition between increased life due to plastic ratcheting and decreased life due to residual stresses.

2.5. Summary and Proposed Work

2.5.1. Summary

As discussed in the previous sections, there have been a number of efforts to predict fatigue behavior of the fretting fatigue condition using critical plane approaches. Namjoshi et al. [10] looked into various critical plane parameters, such as the Smith-Watson-Topper (SWT), Shear Stress Range (SSR) and Findley Parameter (FP), for fretting fatigue life prediction using Ti-6Al-4V material. They also proposed a new parameter called Modified Shear Stress Range (MSSR). Among these parameters, the MSSR was demonstrated as an appropriate parameter for predicting all of the fretting fatigue behaviors such as fatigue life, crack initiation location and growth angle. Additionally, the most beneficial feature of the MSSR was that this parameter was found to be independent of pad geometries for predicting fretting fatigue lives.

Even though there have been several efforts to find parameters that can describe the fretting fatigue behavior effectively, most of the applications of these critical plane parameters have been accomplished under elastic stress conditions. Since the effects of the plastic deformation have not been included in previous works, these analyses may not be applicable in the presence of large plastic deformation. Generally, a large plastic zone is generated by the stresses, which exceed the material yield stress. In this situation, the stress gradient from the spot of peak stress is also very steep. Frequently, a high stress gradient is developed in notch problems especially from a sharp radius of the root tip. To account for the effect of stress concentration in the notch roots, various critical distance methods have been introduced. One of the critical distance methods was the point method proposed by Peterson [11]. This method was based on the assumption that the failure occurs when the stress equals the fatigue strength at a constant distance beneath the notch tip for a given material. Another well known averaging approach was the line

method that was suggested by Neuber [12]. Neuber formulated an equation, which relates the stress concentration factor, K_t, into a fatigue notch factor, K_f, using a critical distance from the peak stress area. Both methods need critical distance that was assumed as a material property.

However, since these critical distance parameters are very dependent on the test conditions and geometries, it is hard to generalize them for any other loading conditions and specimen geometries. Due to these restrictions on the application of critical distance, some researchers, such as Qylafku et al. [13] and Kadi [14], introduced a different approach called the volumetric approach. This approach did not include the fixed critical distance concept for each material. Instead of regarding the critical distance as material constants, they used the damage zone concept to find effective stress by investigating the stress gradient. Using this approach, they demonstrated that the computed stress field intensity values are independent for the notched specimens and the specimens with key-seats.

Recently, Araujo and Nowell [15] calculated total fatigue lives analytically and compared them with experimental values under fretting fatigue conditions. From the analytical calculations using Smith-Watson-Topper (SWT) and Fatemi and Socie (FS) parameters, they demonstrated that the analytically calculated fatigue lives using surface stress distribution only was not adequate for predicting the fatigue lives, especially in the presence of a high stress gradient condition. However, using the critical distance method and the volume method, which has a different approach to calculate the average stress, they successfully predicted the fretting fatigue lives.

Swalla and Neu [16] demonstrated the effect of averaged stresses and strains by changing the length of a critical distance to the prediction of the crack nucleation in the fretting fatigue condition. They investigated the Smith-Watson-Topper (SWT) and Fatemi-Socie-Kurath (FSK) parameters as changing the length for averaged stress and

strain. As a result, they showed that the FSK parameter gave a reliably predicted angle where length was less then 40 μm. However, when the length was grater then 100 μm, the SWT parameter was considered as a better parameter. The reason for these results was assumed to be the difference of dominant stress for each parameter. The FSK parameter was largely affected by shear stresses; however, the SWT parameter varied by tensile stress mainly. Namjoshi et al. [17], also investigated the variation of critical plane parameters as (a cause of) changing the length of volume. By testing the SWT, SSR, FS and MSSR parameters, they claimed that the MSSR parameter was the only parameter which can predict the behavior of the fretting fatigue reasonably.

In addition to the studies discussed above which were performed under elastic conditions, Ambrico and Begley [18] analyzed the behavior of plastic deformation under various loading conditions. They showed that the plastic zone was composed of three areas: shakedown, cyclic plasticity, and ratcheting. In another paper [19], Ambrico and Begley also demonstrated that it was not suitable to predict fretting fatigue lives by using purely elastic analyses only. Furthermore, they claimed that plastic ratcheting acted to increase fatigue life and residual stresses created by the plastic deformation decreased the fatigue life.

From the literature study noted above, it was found that a number of efforts have been made to analyze fretting fatigue. However, most studies were performed under the elastic condition. Many more studies of the plastic effect on fatigue life at the notch problems were found. In notch studies, various averaging methods were introduced to surmount steep stress gradient condition and plastic deformation. The objective of this proposed work is to expand on previous work in the area of fretting fatigue to the elastic-plastic condition using the averaging methods that have been used in notch problems.

2.5.2. Proposed Work

As mentioned in the previous chapter, there have been no studies to investigate fretting fatigue behavior when the stress state in the contact region is greater then the yield stress of material. Therefore the objective of the proposed study is to characterize the fretting fatigue crack initiation behavior in the presence of plasticity. This study will involve both experiments and analyses. The specific tasks will be the following:

1. To conduct the fretting fatigue tests with several contact configurations with loading conditions which would generate the plasticity or yielding of the material in the contact region.

2. To analyze the experiments by using finite element analysis in order to characterize the fretting fatigue damage mechanism under the presence of plasticity.

3. To develop the fretting fatigue crack initiation parameter/model/criterion under the presence of plasticity.

III. Experiments

As mentioned in the background chapter, Namjoshi et al.[10, 17] have studied the fretting fatigue behavior of Ti-6Al-4V. They employed the test data conducted by Lykins [8]. Since the Namjoshi et al's work was focused on elastic fretting fatigue environment, they employed pad configurations and loading conditions which generated elastic stress state and deformations. These were three cylindrical pads with radii of 50.8 mm, 101.6 mm, 304.8 mm and two flat pads of type 1 (FP1), type 2 (FP2). However, in this study, Namjoshi's work will be extended to include elastic-plastic fretting conditions. In order to obtain elastic-plastic deformation conditions, the smaller radii of the cylindrical and flat pad were included in this study. Three configurations of pad geometries were added in this study, i.e. 5.08 mm radius cylindrical pads and one flat pad type3 (FP3). In addition to the changing of pad radii configuration, the normal load on fretting pad was also increased to generate large plastic deformation under fretting fatigue condition. Two different contact loads were applied for the 5.08 mm radius cylindrical pad, i.e. 1,334 and 1,779 N. The flat pad was included for the understanding of the behavior of the fretting fatigue under the turbine blades configuration. The details of the experimental works will be discussed in the following sections.

3.1. Material and Specimen

Both the specimens and pads were machined from Ti-6Al-4V forged plates by the wire electrical discharge method. These forged plates had been preheated and solution treated at 935°C for 105 minutes, cooled under flowing air, vacuum annealed at 705°C for 2 hours, and then cooled under flowing argon. Once these processes were accomplished, this material had a duplex microstructure consisting of 60% (volume) of

58

primary-α (hcp) and 40% (volume) of transformed-β (α platelets in a β matrix - bcc) phases with a grain size of about 10 μm. The longitudinal tensile properties (along the loading axis) were determined, i.e. the elastic modulus was 116 GPa and yield strength was 753 MPa. Figure 19 shows schematics of the dog-bone specimen and the shapes of two different pad geometries (cylindrical and flat pads). Table 1 shows the dimensions of all the pad geometries and normal load applied to the fretting pads.
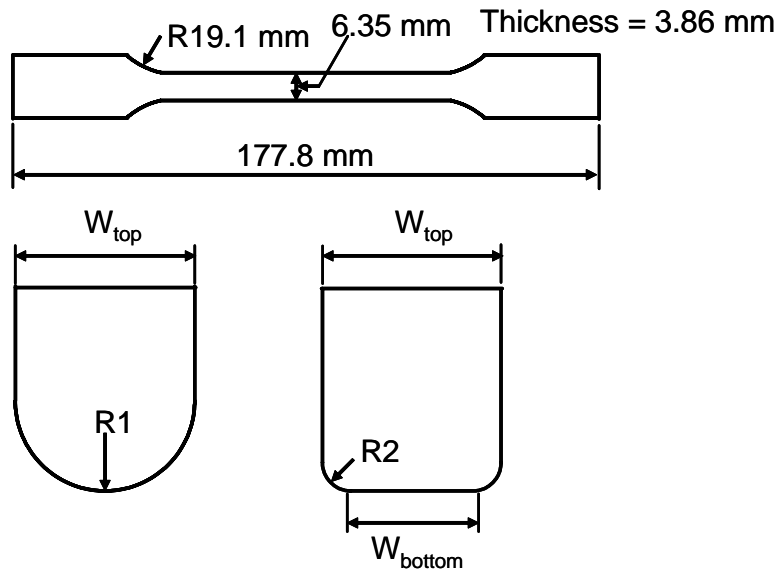
Figure 19. Geometries of the Specimen and Fretting Pads

Table 1. Pad Configurations and Normal Loads

Pad Name	W_{top} (mm)	W_{bottom} (mm)	R (mm)	Normal Load (N)
Cyl. 50.8 mm	9.53	N/A	50.8	1334
Cyl. 101.6 mm	9.53	N/A	101.6	2224
Cyl. 304.8 mm	9.53	N/A	304.8	4003
Cyl. 5.08 mm(1)	9.53	N/A	5.08	1334
Cyl. 5.08 mm(2)	9.53	N/A	5.08	1779
Flat. FP1	9.53	5.08	5.08	1334
Flat. FP2	19.05	13.97	2.54	4003
Flat. FP3	9.53	2.54	2.54	4003

3.2. Test Setup and Procedure

The fretting fatigue tests were conducted on a 22.2 kN servo-hydraulic uniaxial test machine at ambient temperature in a laboratory environment as shown in Figure 20. Figure 21 shows the rigidly mounted fretting fixture on a servo-hydraulic fatigue test machine used in this work. Two load cells, one on each side of the specimen, were used to measure the normal load. A load cell, attached to the servo-hydraulic load frame on the top side of the specimen, measured the axial load above the pads. A lightweight pressure transducer was used to measure the axial load at the bottom of the specimen. This system allowed the user to vary the axial load by controlling the displacement in the axial direction. The displacement was applied in the axial direction at constant amplitude to allow the specimen to be adequately exposed to the prescribed loading conditions. The control system of the test equipment maintained the frequency and the amplitude of the

applied axial displacement constant during the duration of the test. In this study, the displacement was applied in the axial direction at a frequency of 50 Hz.

Figure 20. Servo-Hydraulic Uniaxial Test Machine
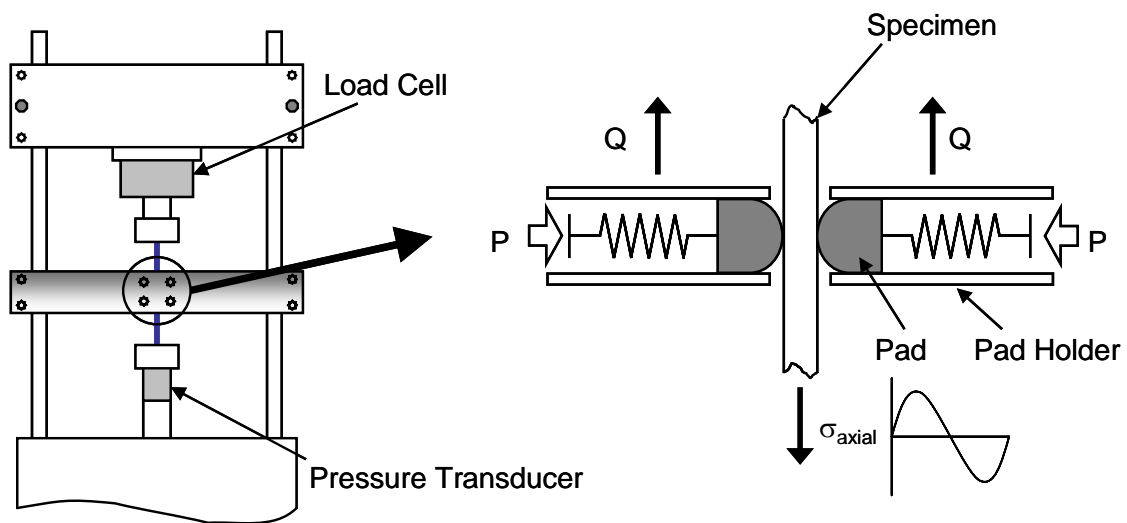
Figure 21. Schematic of the Fretting Fatigue Configuration

Constant amplitude fretting fatigue tests were conducted over a wide range of applied axial force by servo-actuator on the bottom side of the specimen. The normal loads on the pads were applied with the aid of two lateral springs. This load was held constant for the duration of the test and was monitored with a load cell. The normal loads were either 1334 N or 4003 N for each pad configuration as shown in Table 1. Higher normal loads were applied to generate the large plastic deformations. In order to perform finite element analysis (FEA) in chapter four, the axial and tangential loads must be determined as each represents input data for FEA. As previously mentioned, a load cell was attached to the servo-hydraulic load frame on the top of the specimen to monitor the axial load. The tangential load can be determined by the equation:

$$Q = \frac{V - W}{2} \tag{52}$$

where Q is the tangential load on each side of the specimen, V is the axial load applied on the bottom side of the specimen, and W is the applied axial load on the top side of the specimen.

3.3. Test Results

As mentioned above, the applied axial stress, σ_{axial}, and tangential load, Q, were measured during the tests. Appendix A shows the number of cycles to failures for all pad configurations tested in this study along with all loads.

The prediction of crack location is one of the several measures of a predictive fatigue parameter; therefore, the crack location was determined for the each experimental test. As mentioned before, Namjoshi et al. [10] evaluated fretting fatigue life of Ti-6Al-4V for the pad configurations involving elastic deformations, i.e. cylindrical pads with

radii of 50.8 mm, 101.6 mm, 304.8 mm and flat pad type 1 (FP1), type 2 (FP2). They reported that the failure of all specimens with pad configuration involving elastic deformation occurred due to crack growth that initiated at the contact surface and near the trailing edge of contact. The similar results were found for the pad configurations involving elastic-plastic deformations included in this study, i.e. two 5.08 mm radius cylindrical pads with 1334 N and 1779 N normal loads and flat pad type 3 (FP3). Figure 22 shows scar from the 5.08 mm cylindrical pad with 1779 N normal load while Figure 23 shows the typical scar from the flat pad type3 (FP3). As can be seen from figures, the crack initiation location was found near the trailing edge between specimens and pad configurations involving elastic-plastic deformations.

Namjoshi et al. [10] also reported that there were several small secondary cracks observed besides the primary crack which mainly caused the failure of the specimen. These secondary cracks were also observed from the specimen with pad configurations involving elastic-plastic deformations. As an example, Figure 24 shows the typical secondary cracks observed from the specimen with flat pad type 3 (FP3).

Crack initiation orientation was determined by mounting a sectioned specimen which had been made by grinding the specimen. The mounting of specimen also had been polished to ensure the sectioned surface was at the center of the crack initiation zone. Once the specimens polished, they were examined under a scanning electron microscope, SEM [38]. A schematic of the sectioning procedure of specimen and taking SEM photo of the crack initiation orientation can be seen in Figure 25. Namjoshi et al. [10] reported that the experimentally observed primary crack orientations angles under elastic fretting conditions were either -45^0 or $+45^0$ with a variation of $\pm15^0$ from a perpendicular to the loading direction. They presented SEM photographs, as shown in Figures 26 – 28, which show the typical crack initiation orientation and propagation path of the primary crack for the cylindrical and flat pads involving elastic deformations.

Figure 26 shows a specimen used with a cylindrical pad with a 50.8 mm radius, Figure 27 shows a cylindrical pad with a 304.8 mm radius and Figure 28 shows Flat pad type 2 (FP2). As can be seen from the Figures 26 – 28, the typical crack initiation angles resulting from the pad configurations involving elastic deformations are measured about −45°. The angles of the crack initiation observed from specimen under elastic-plastic fretting fatigue conditions are similar to the specimen under elastic fretting fatigue conditions. Figure 29 shows the typical crack orientation of the 5.08 mm radius cylindrical pad with normal load 1,779 N, while Figure 30 shows the crack orientation of the flat pad type 3 (FP3). From the figures, it can be seen the crack orientations resulting from the pad configurations involving elastic-plastic deformation also have around −45° from a perpendicular to the loading direction. This is in agreement with a previous study by Namjoshi el al. [10].
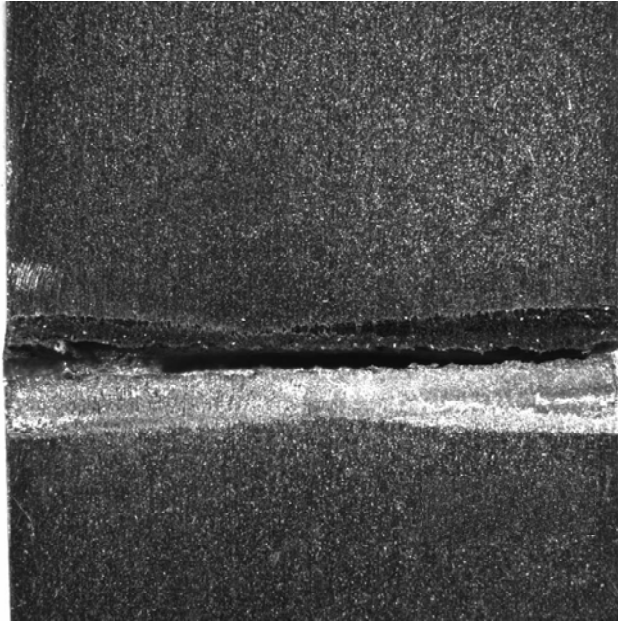
Figure 22. Fretting Scar from the 5.08 mm Radius Cylindrical Pad
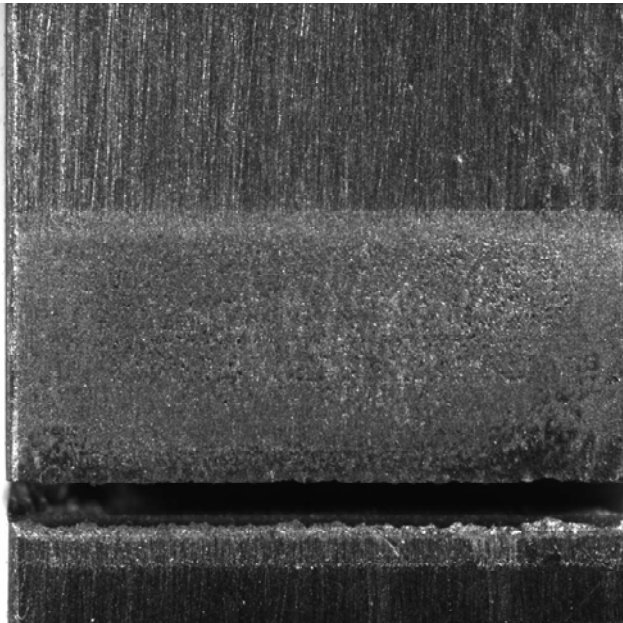
Figure 23. Fretting Scar from the Flat Pad Type 3 (FP3)
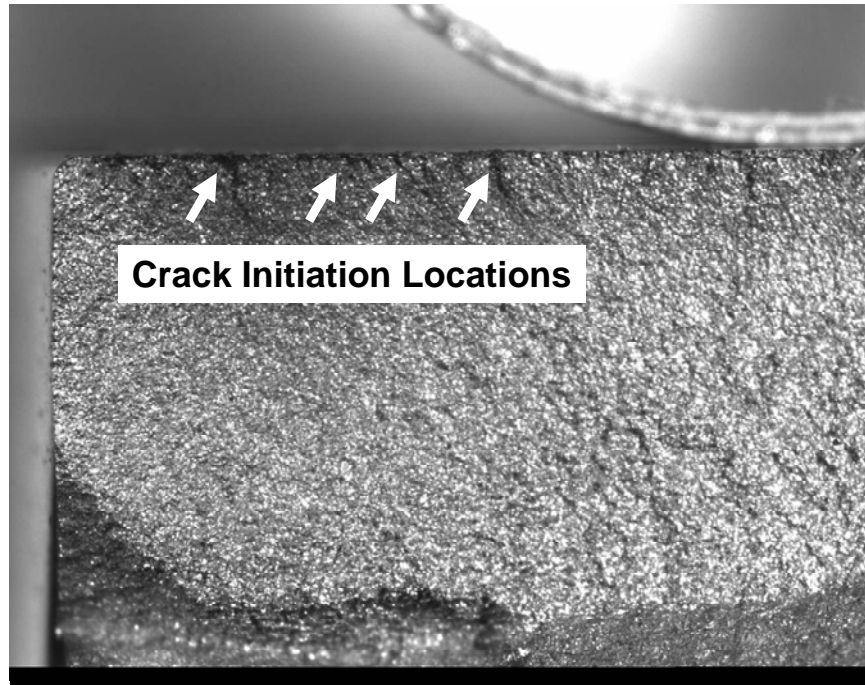
Figure 24. Crack Locations from the Flat Pad Type 3 (FP3)
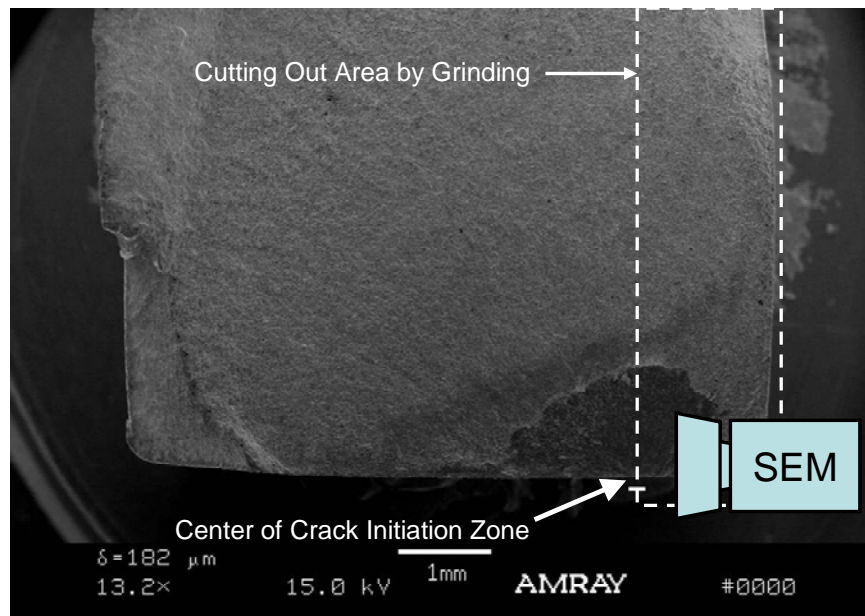
Figure 25. Procedure of the Sectioning and taking SEM Photo
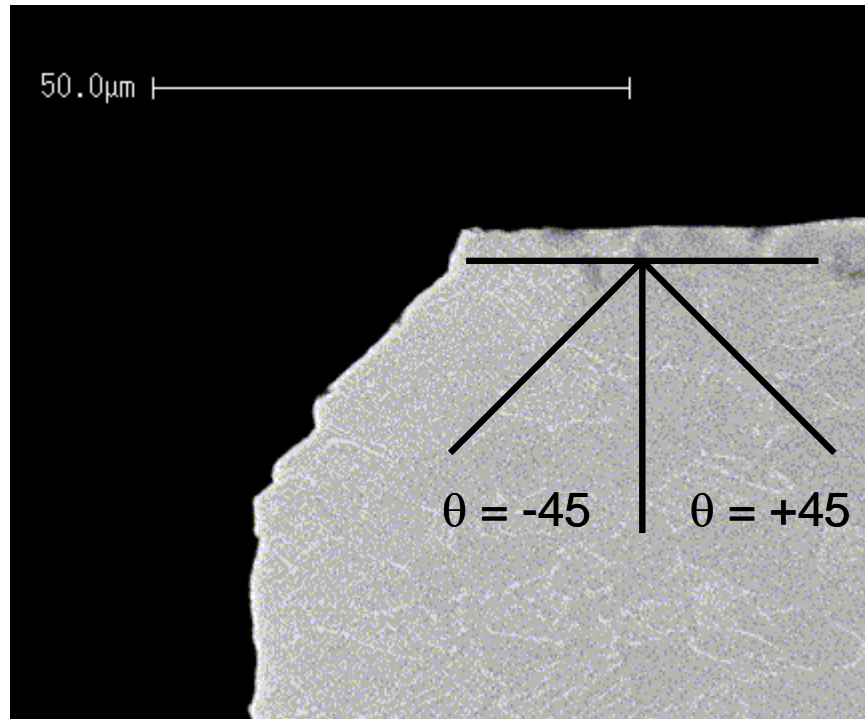
Figure 26. Crack Orientation of the 50.8 mm Radius Cylindrical Pad
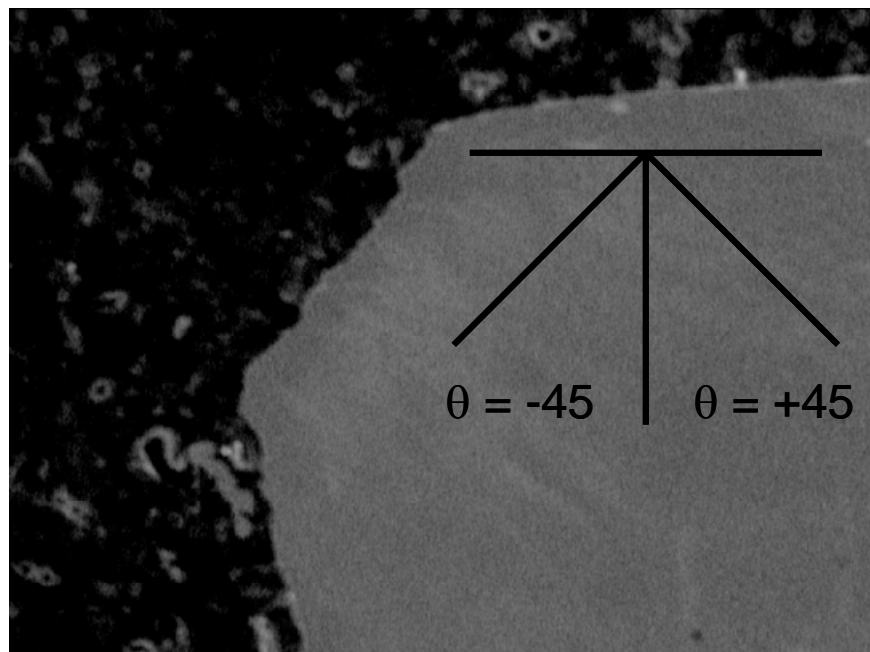
Figure 27. Crack Orientation of the 304.8 mm Radius Cylindrical Pad
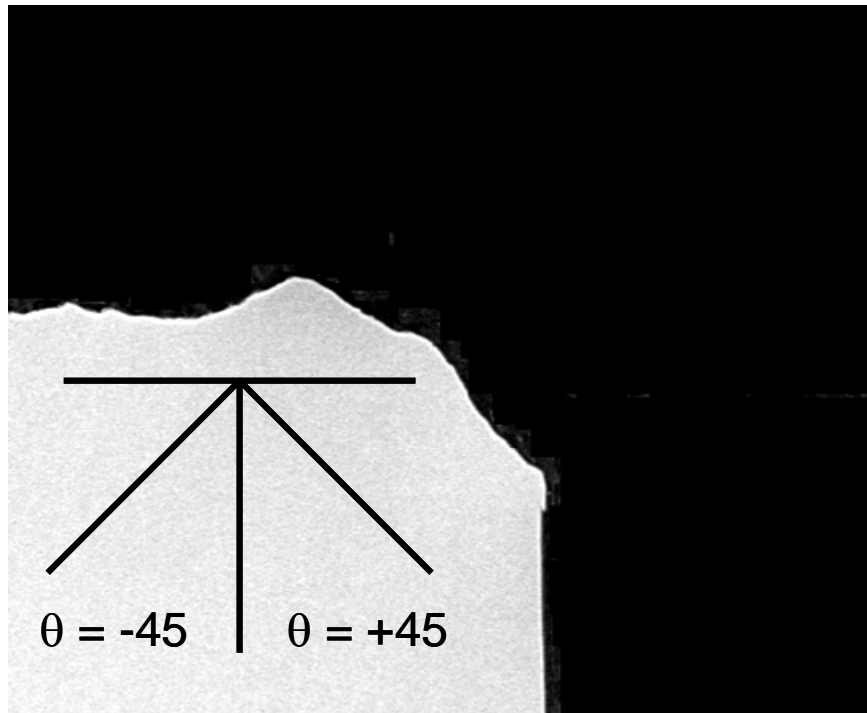
Figure 28. Crack Orientation of the Flat Pad Type 2 (FP2)
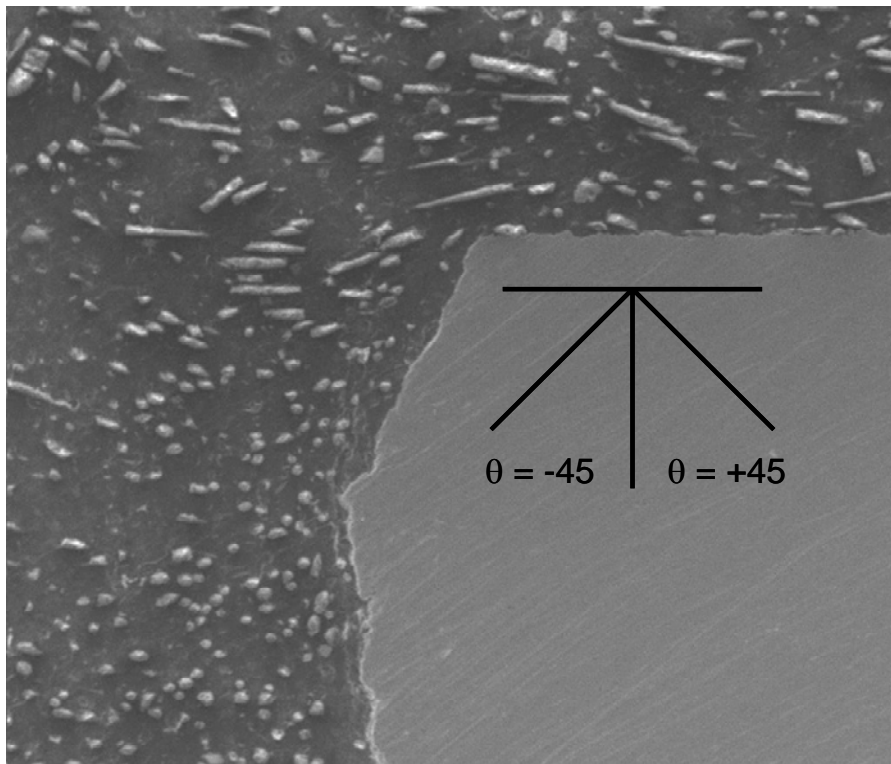
Figure 29. Crack Orientation of the 5.08 mm Radius Cylindrical Pad
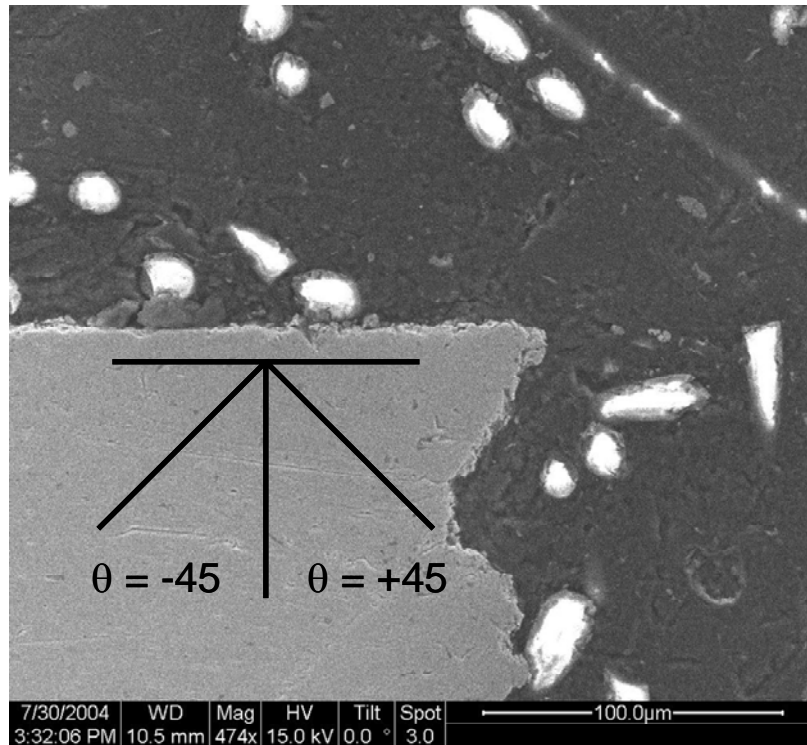
Figure 30. Crack Orientation of the Flat Pad Type 3 (FP3)

IV. Finite Element Analysis

The finite element analysis (FEA) was performed to calculate stress and strain distributions under cyclic fretting conditions. In this study, the finite element solutions were generated by using the commercial code ABAQUS. Since this study was concentrated on investigation of the effects of large plastic deformation on the fretting fatigue, the elastic-plastic analysis was included during the finite element analysis. However, the elastic analysis was also accomplished for purposes of comparison to verify the FEA model with the existing analytical solution, i.e. Ruiz solution [22]. In order to obtain accurate stress and strain results, the mesh size of the FEA model will be determined through a comparison with FEA and Ruiz solution. In order to analyze the FEA results, the effect of the coefficient of friction (COF) on the contact stresses will be discussed. The effects of the plastic deformation on the stress and strain distributions will be also evaluated.

4.1. Finite Element Model Description

In this section, the material property which was used in the elastic-plastic analysis will be discussed. The applied loads used for simulating experimental cyclic loading conditions also will be presented. Finally, the effective mesh size and the validation of the FEA results will be reported.

4.1.1. Material Property and Loading Condition

As mentioned previously, the Ti-6Al-4V alloy was selected for this study. The same material was used to manufacture the pad and specimen. Therefore, the material properties for pad and specimen were identical, i.e. an Elastic Modulus of 116 GPa and

71

Poisson's ratio of $\nu = 0.35$. For the elastic-plastic FEA analysis, the non-linearity of the material was also used where the yield strain was $\varepsilon_Y = \sigma_Y/E = 0.006474$. There are three generally accepted methods to represent the elastic-plastic material behavior as shown in Figure 31. However, the elastic/perfectly-plastic property has been demonstrated as an efficient material property for the Ti-6Al-4V alloy by the several previous studies [18, 33, 34].
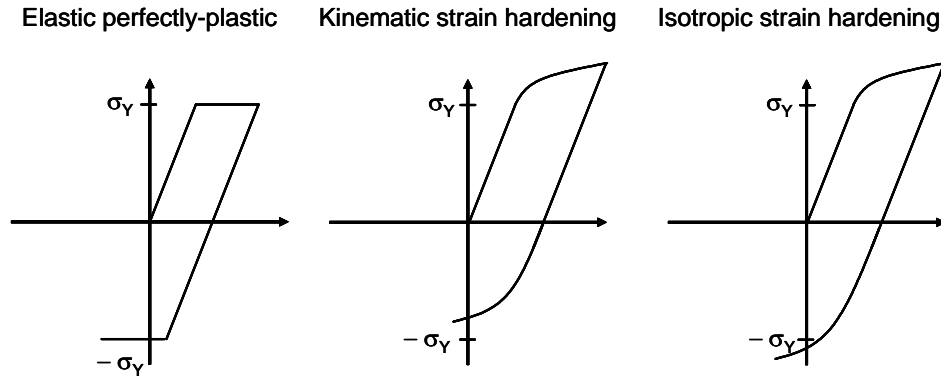
Figure 31. Three Different Properties of the Plasticity

Furthermore, the experimental result also shows the elastic/perfectly-plastic property of the test material, Ti-6Al-4V. Figure 32 shows the tested material's data, i.e. Ti-6Al-4V stress versus strain relation for Ti-6Al-4V. From the figure, it is shown that the stress value has an upper limit created by the yield stress value and then stress values are maintained almost constant as strain values are increased. For these reasons, in this study, the elastic/perfectly-plastic description has been considered and characterized by the von Mises yield criterion.
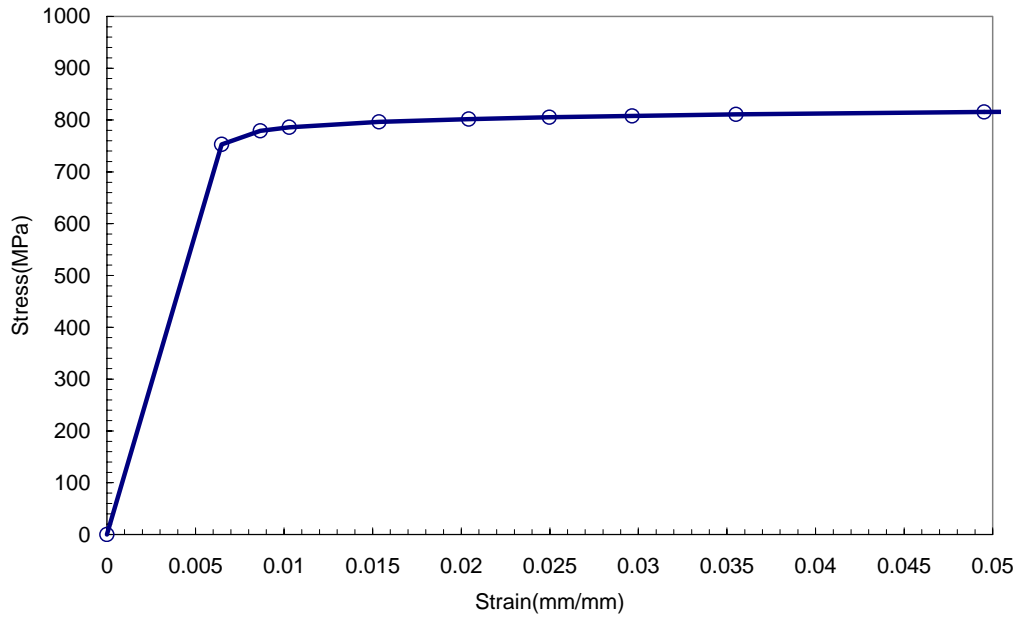
Figure 32. Stress-Strain Curve for Ti-6Al-4V

Figure 33 illustrates a FEA model of the cylindrical pad with radii of 50.8 mm as an example. The FEA model consisted of three bodies: the fretted specimen, the fretting pad and fretting pad holder. As seen in Figure 33, the specimen is fixed at its far end in the negative x-direction, restricted from vertical movement along its bottom surface and free to roll in the x-direction and along its bottom edge. Only half of the experimental setup needs to be modeled using finite elements because ideally the experimental setup is symmetric along the axial centerline of the specimen. Therefore, the finite element model of the specimen has a thickness b = 1.905 mm. The length of the specimen is 12.7 mm in both the positive and negative x-direction from the center of contact. The cylindrical pad is rigidly fixed to the pad holder with the pad holder being free to roll in the y-direction along the side opposite to the fretting pad. All of the three bodies, the fretting pad, fatigue specimen and pad holder, have a depth of 6.35 mm. As has been mentioned, the fretting pad and fatigue specimen share the same material properties with each other as well as with their experimental counterpart, i.e. an Elastic Modulus of 116

GPa and a Poisson's ratio of 0.35. However, the material properties of the pad holder differ from the other two bodies. The primary purpose of the pad holder in the finite element model is to restrain the pad in the x and y-direction prior to the application of load. Therefore, the material properties of the lateral spring are purposely low so that the pad holder has a minimal effect on the interaction between the pad and specimen. The pad holder has an Elastic Modulus and a Poison's Ratio of 0.03 MPa and 0.3 respectively.

The Coefficient of Friction (COF) is one of the main factors that can influence the stress and strain distribution in the contact region resulting from the FEA. In this study, the COF value has been determined based on previous experimental work. Iyer and Mall [35] measured the static COF as $f = 0.5$, for the 50.8 mm pad configuration with the same material. In this study the same value was used for all pad geometries. However, the effects of various COF values on stress and strain distributions will be discussed in more detail in the following section.
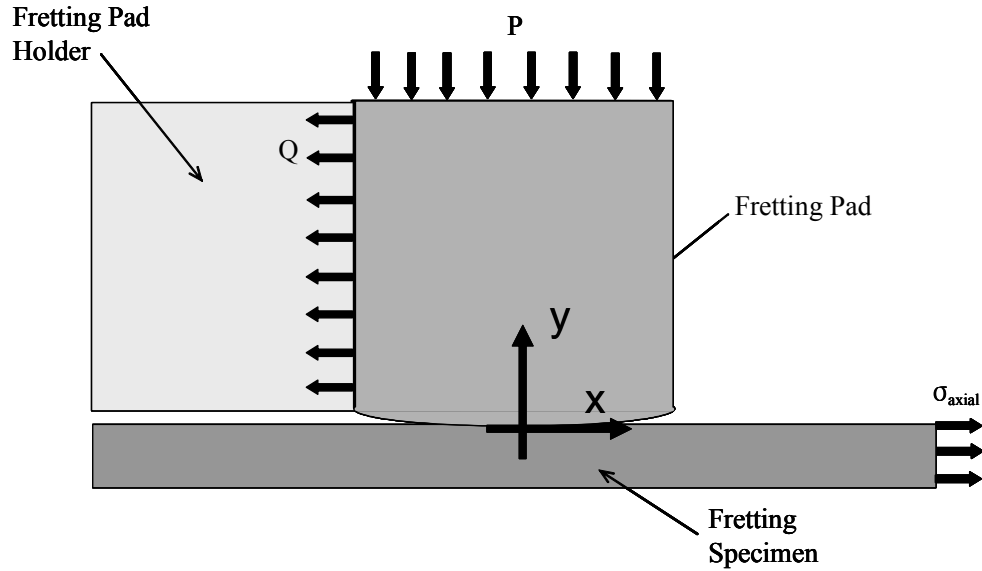
Figure 33. Illustration of the Boundary Conditions for Finite Element Analysis

The measured loads during experimental works were applied to the FEA models. Some of the studies [18, 33] reported that the plastic zone indicated no further plastic strain increments after the first or second cycle. Therefore, in this study, three cyclic loads were utilized to simulate the actual plastic zone size for each experimental condition. The normal load (P) was applied in the first step. This applied normal load was held constant while the tangential load, Q, and axial applied stress, σ_{axial}, varied over the second and third steps. In the second step, the minimum tangential, Q_{min}, and axial applied stress, $\sigma_{axial,min}$, were applied simultaneously. Finally, in the third step, the maximum tangential, Q_{max}, and axial applied stress, $\sigma_{axial,max}$, were added to represent experimental cyclic loading conditions. The combinations of the minimum and maximum loadings were applied three times, and thus a total of three steps were accomplished for FEA.

4.1.2. Mesh Modeling and Verification of Results

4-node, plane strain elements were used in all three bodies of the finite element model. 4-noded elements (bilinear) were chosen instead of 8-noded elements (serendipity), because the mid side node in the 8-noded element introduces an oscillation in the stress state along the contact surfaces as reported by Lykins [8]. The contact between the pad and the specimen was defined using the master-slave algorithm in ABAQUS for contact between two surfaces. The master surface is on the fretting pad and the slave surface is on the fretting fatigue specimen. The ABAQUS master-slave algorithm determines which segments on the master surface and which nodes on the slave surface interact. These master segment/slave node relationships are then used to establish the contact algorithm for how loads are transferred between the two contacting surfaces.

In this study, the FEA model used in Lykins [8] has been modified for the analysis of elastic-plastic fretting fatigue phenomenon. This FEA model has been refined for the purpose of analyzing local stresses and strains along and near the contact surface between pad and specimen. Figure 34 shows the mesh model of 50.8 mm radius cylindrical pad as an example. As seen in Figure 34, the darker regions of the mesh, such as the area near the contact surface, indicate where the mesh is more refined to aid in determining stresses within the contact region. The mesh was less refined in the regions where the values of stresses were not of interest in this study. This is done to decrease the time required to analyze the model. A multi-point constraint (MPC) was applied at the top of the pad to prevent it from rotating due to the application of loads. The top nodes of the pad were forced to move in unison in the y-direction. Also, the MPC was applied to the boundary between regions where the mesh size of the elements differed. The MPC prevented the free nodes from penetrating the larger adjoining elements. An enlarged picture of the refined mesh areas is shown for the cylindrical and flat pads in

76

Figures 35 and 36 respectively. The dimension of the area of the most refined mesh near

the contact surface is shown in Figure 37. As will be discussed in the following section,

in this study, the critical distance methods will be used to find averaged value and end

point of stress and strain along the critical plane near the contact zone. For this reason,

the modification of the FEA model has been done to generate refined mesh area under

contact surface. In order to acquire sufficient range and accuracy of the stress and strain

distributions near the contact surface which was calculated by FEA, the depth of the fine

mesh area from the surface was selected as about 500 μm for all tested pad

configurations. However, the widths of the fine mesh area were dependent on each pad

configuration. This is because the widths were determined to be more than 500 μm from

the edge of fretting pads which vary according to pad configurations.
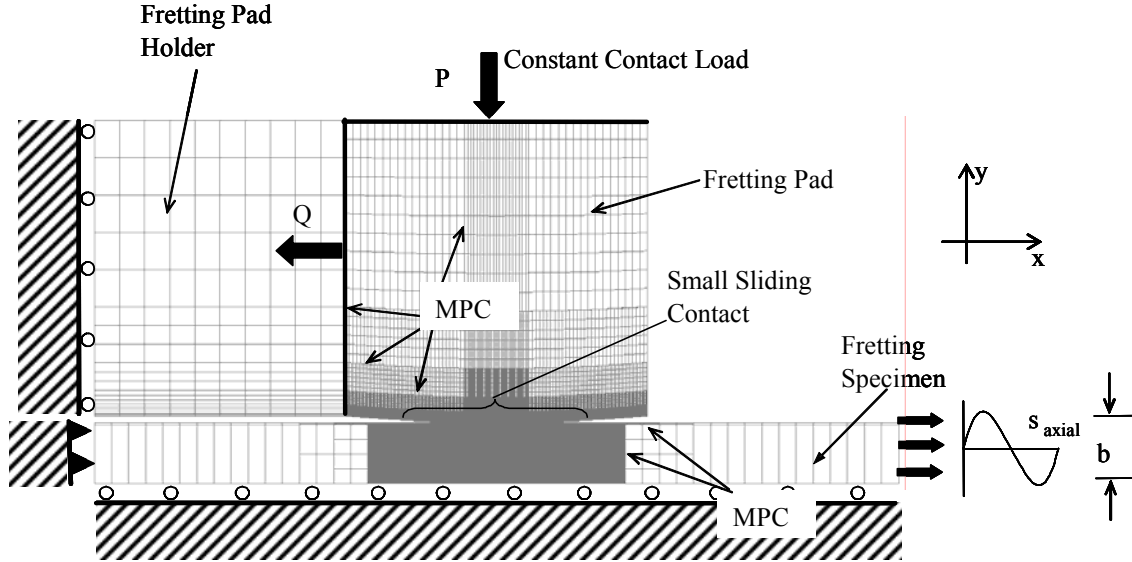
Figure 34. Illustration of the Typical Finite Element Model Mesh
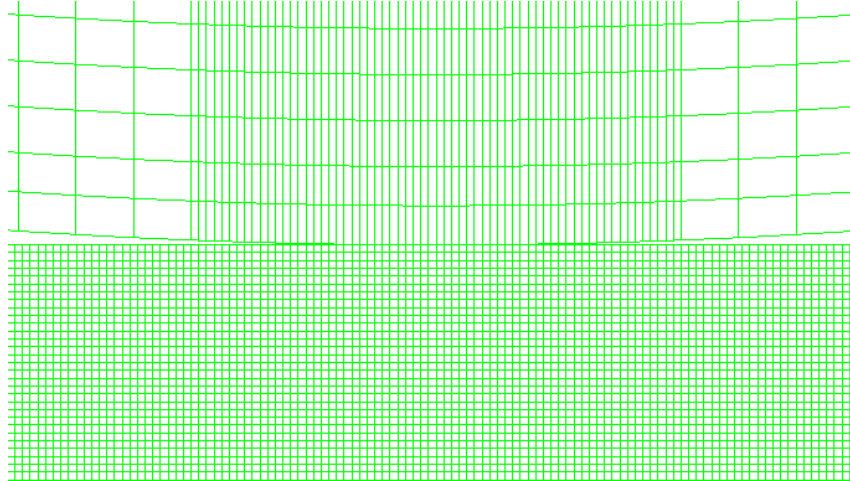
Figure 35. Fine Mesh Area for Cylindrical Pad
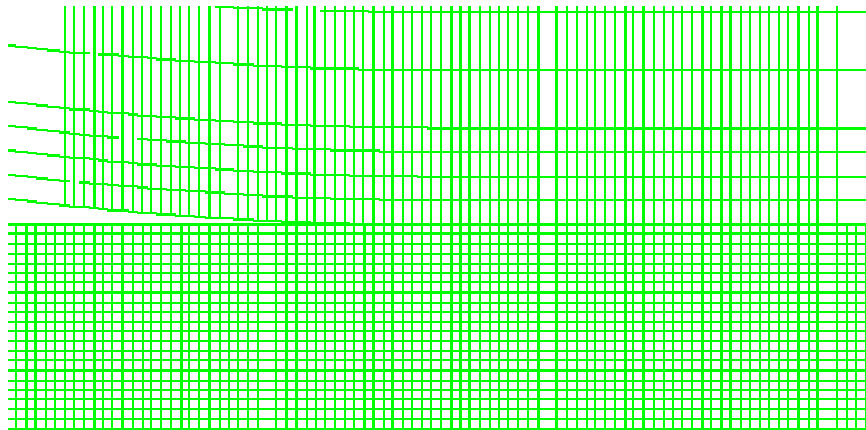
Figure 36. Fine Mesh for the Round Edge Flat Pad
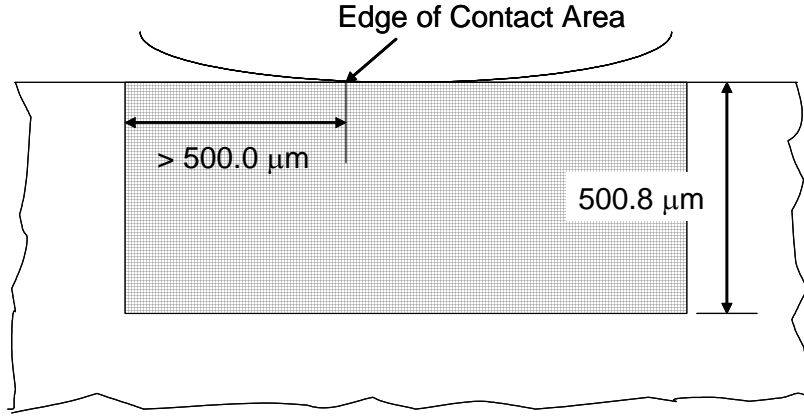
Figure 37. Dimension of the Fine Mesh Area Near the Contact Surface

The mesh size within the fine mesh area was determined by comparison of the results between the FEA and analytical solutions. In this study, a FORTRAN program called "Ruiz", written by Chan and Lee [22], has been carried out as an analytical solution for the fretting fatigue condition. Since the analytical solution was based on the elastic condition, the FEA was performed with the elastic solution also. In this study, the 50.8 mm cylindrical pad configuration was selected for the comparison between FEA and analytical results. The following loading conditions were used for the verification of the proper mesh size: normal load, P = 1.33 kN, tangential load, Q = 0.3 kN, axial stress, σ_{axial} = 55.2 MPa, coefficient of friction, COF = 0.5. These loading conditions are obtained from Lykins's dissertation [8], since it has already been utilized for verification of the mesh model. Figure 28 shows the results of the comparison between the normalized σ_{xx} from the Ruiz program and the FEA calculation for the varied mesh sizes of the 50.8 mm cylindrical pad. As seen in this figure, agreements between FEA and Ruiz calculations were improved as the mesh size decreased.   For the square mesh with 6.35 μm for each side, the predicted contact half width, a, varied by 1.87% between FEA and Ruiz results, where a_{FEA} = 444 μm and a_{Ruiz} = 453 μm. The maximum pressure, P_o, predicted by the FEA model also agreed with the Ruiz program with a 0.4% difference;

79

P_{o-FEA} = 296.49 MPa versus P_{o-Ruiz} = 295.3 MPa. The normalized maximum value of the longitudinal normal stress, σ_{xx}, varied by 6.1% between FEA and Ruiz results, where σ_{xx-FEA} = 1.42 MPa and $\sigma_{xx-Ruiz}$ = 1.32 MPa. The detailed results of verifications for the mesh sizes between the cylindrical and flat pad configurations were accomplished by Lykins's dissertation [8]. Therefore, in this study, the same mesh sizes were utilized for all pad geometries as used by Lykins. The details of all FEA models for analyzed pad configurations are illustrated in the Appendix B. Table 2 illustrates the resultant values of the half width of contact, a, and maximum normal pressure, P_o, which were calculated by FEA for all of the tested pad configurations in this study.
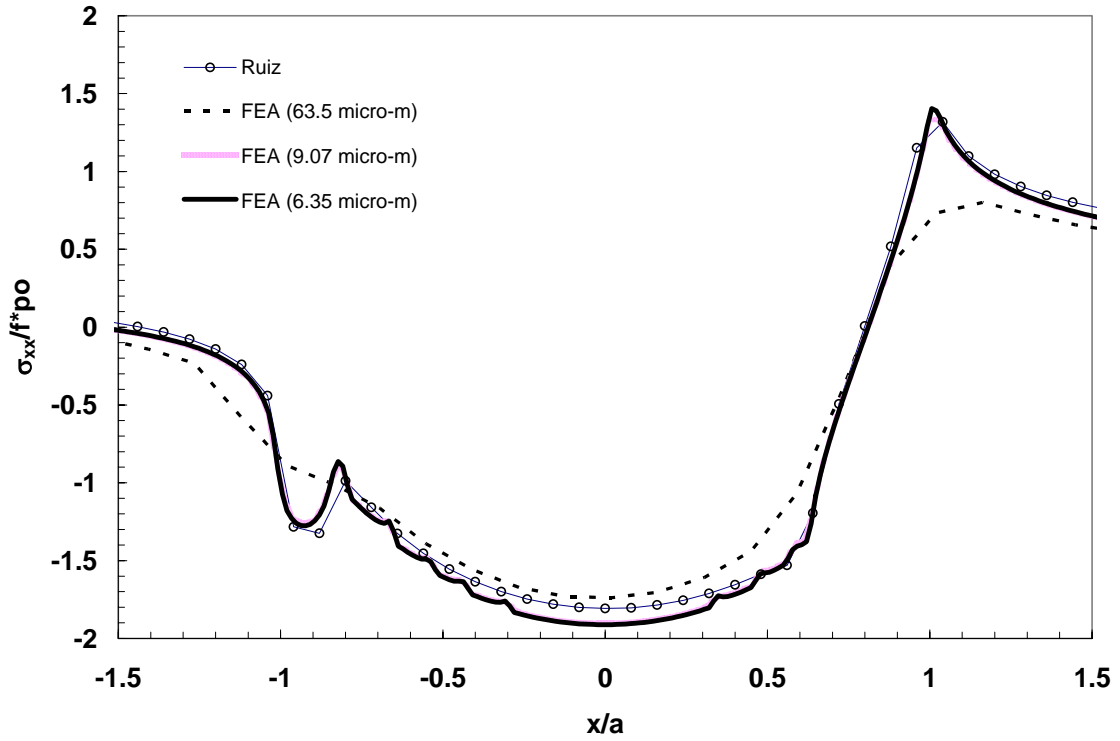
Figure 38. The Comparison of Values σ_{xx} Between Ruiz and FEA Results

Table 2. The Computed Half Contact Width and Maximum Normal Pressures

Pad Configuration	a (µm)	P_o (MPa)
Cyl. 50.8 mm	463.55	304
Cyl. 101.6 mm	819.15	278
Cyl. 304.8 mm	1771.65	213
Cyl. 5.08 mm (1)	152.40	923
Cyl. 5.08 mm (2)	177.80	1068
Flat. FP1	2603.50	250
Flat. FP2	7112.00	110
Flat. FP3	1352.55	719

4.2. Analysis on the Effect of Coefficient of Friction

As mentioned in a previous section, the COF can influence the magnitude of the stress and strain values from FEA. In this study, 0.5 has been used as the COF for the FEA. However, Iyer and Mall [35] reported that the range of COF could be varied from 0.45 to 0.6 under fretting fatigue test conditions. For this reason, the effects of the COF on the FEA results will be investigated in detail. The results of the investigation will be discussed independently for both elastic and elastic-plastic analysis conditions.

4.2.1. The Effects of the COF on the Elastic Analysis

In order to study the effect of COF on elastic analysis, the 50.8 mm radius cylindrical pad with 1334 N normal load condition will be analyzed, because negligible plastic zone sizes have been detected in this pad configuration and thereby the 50.8 mm radius cylindrical pad could be regarded as the elastic behavior case. The loading

condition was selected from one of the applied loading data measured during the experimental works. The selected loading condition was obtained from the middle of fatigue test. This was done to avoid the lowest and highest number of cycles to failure and thereby apply the typical loading condition for investigation of COF effects on elastic fretting condition. The fatigue life of the selected loading condition is 0.12E+6 cycles. The selected loading conditions are as follows:

- The maximum normal stress (σ_{max}) : 416 MPa

- The minimum normal stress (σ_{min}) : 28.70 MPa

- The maximum tangential load (Q_{max}) : 0.46 kN

- The minimum tangential load (Q_{min}) : -0.51 kN

The range of the tested COF was taken from 0.4 to 0.6 because this was the range that Iyer and Mall [44] observed when they studied the coefficient of friction on fretting fatigue using Ti-6Al-4V. In order to compare the effects of COF, the value of the COF has been increased by 0.05. Figure 39 shows the normalized stress, σ_{yy}, values by the maximum pressure, P_o, at different COF values. As shown in the figure, the same distributions of the σ_{yy} are obtained along the contact surface as the COF values increased. This result indicates that the σ_{yy} value is independent to the variation of the COF.
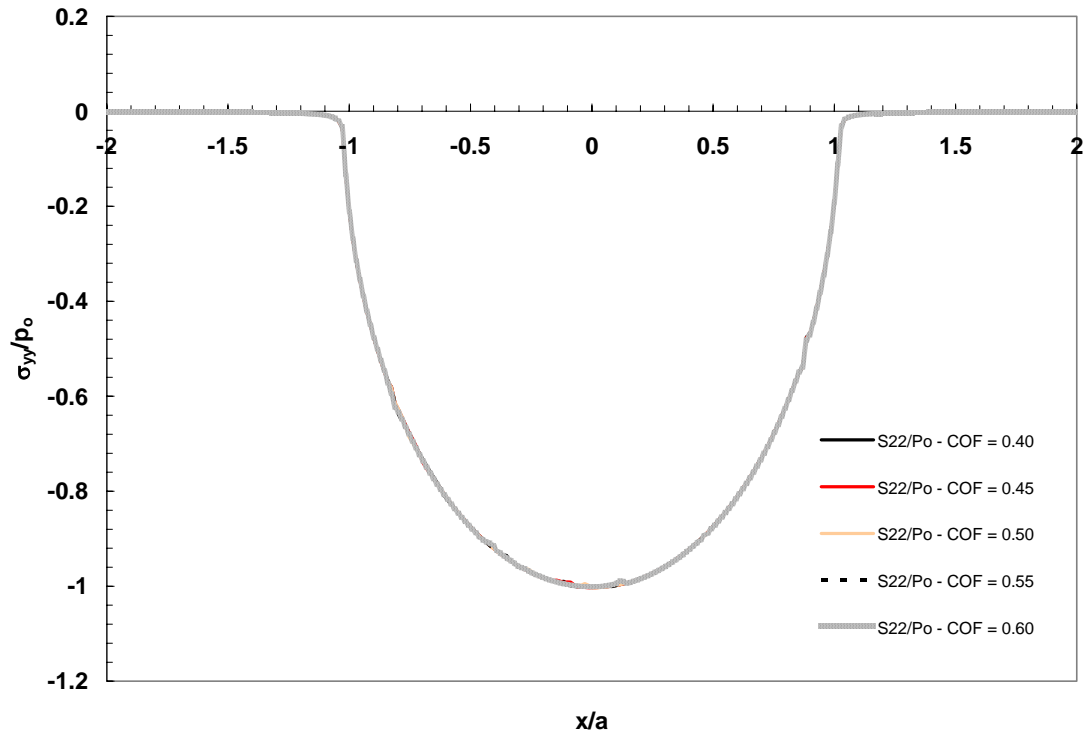
Figure 39. Normalized Pressure for the 50.8 mm cylindrical pad with different COF

Figure 40 presents the effects of the COF on the normalized maximum normal stress on the surface, σ_{xx}/Po, versus the normalized location on the surface, x/a. As shown in Figure 40, the normalized σ_{xx} values at the maximum loading conditions were increased as the COF was increased. The σ_{xx} values were increased at both leading and trailing edges. In general, parametric approaches (i.e. critical plane model/parameter) have been used for analyzing the fatigue life of the fretting fatigue problem. Furthermore, the parametric approaches commonly use the maximum value of stress components. Therefore, the increase of magnitude of the stress components due to increase of COF could alter the parameter values resulting from the parametric approaches.

Other than increasing the maximum σ_{xx} stress values, the increasing COF also leads to the change of the stick and slip zone. As shown in Figure 40, the stick zone increased as the COF values increased. This is because the increased COF caused

enhanced adherence between pad and specimen in the contact surface. Figure 41 illustrates the variation of the normalized von Mises stress curves with different COF values. As shown in this figure, the maximum values of the von Mises stress were increased as the COF value was increased. This result is similar to the σ_{xx} values from Figure 40. However, at the middle of the contact surface, there is difference between von Mises stress and σ_{xx} values. The σ_{xx} values are calculated as a flat line (i.e. constant value) while the von Mises stress shows valley shapes of minimum values as the COF increased. In other word, the minimum value of von Mises at the middle of the contact surface decreased as the maximum value of von Mises increased with increase of COF.
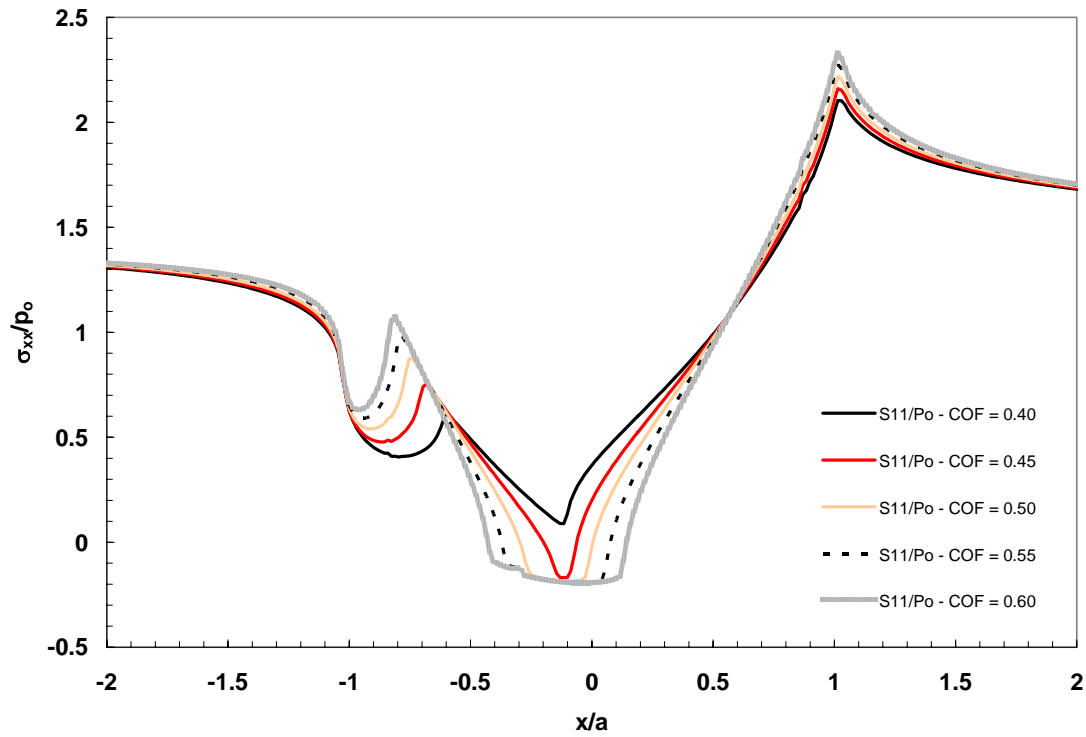
Figure 40. The Effects of COF on σ_{xx} Under Elastic Condition
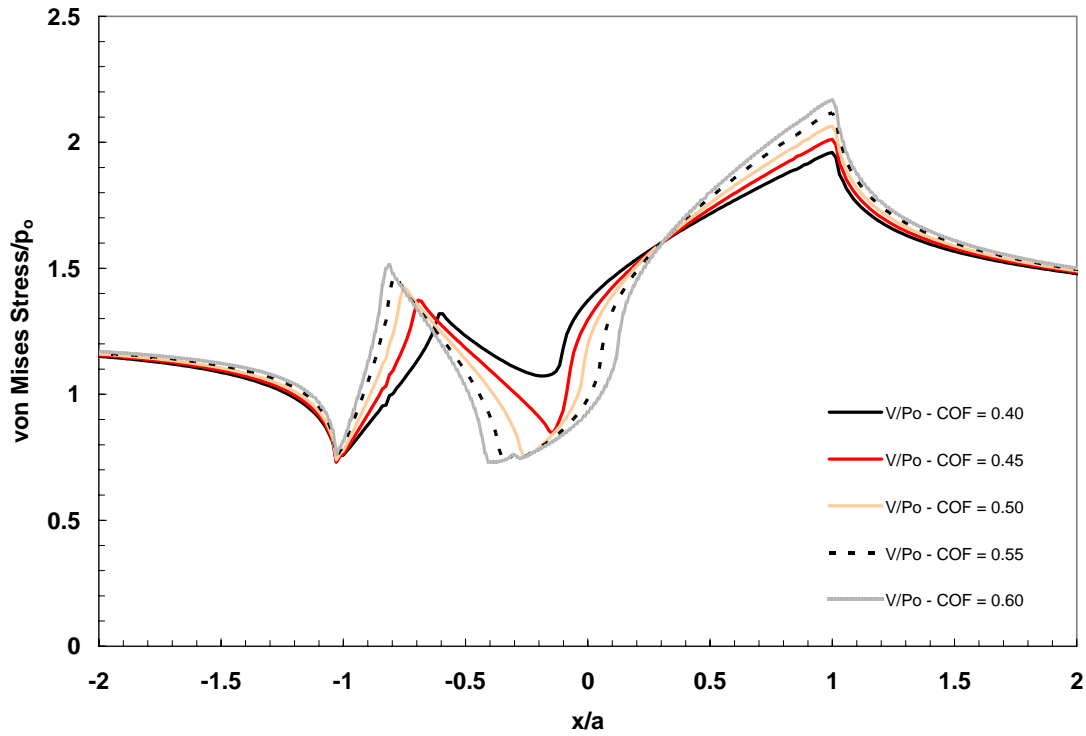
Figure 41. The Effects of the COF on the von Mises Stress under Elastic Condition

4.2.2. The Effects of the COF on the Stress from Elastic-Plastic Analysis

In this section, the effects of the COF on the elastic-plastic condition are discussed. The 5.08 mm radius cylindrical pad with 1779 N normal load condition was selected as an example for this investigation. This is because large plastic deformation occurred in this pad configuration during experimental works. The applied load conditions that generate large plastic deformation was also selected. The fatigue life at the selected applied loading conditions is 1.09E+6 cycles. The details of the applied loading conditions are as follows:

- The applied maximum normal stress (σ_{max}) : 547.59 MPa
- The applied minimum normal stress (σ_{min}) : 374.04 MPa

- The applied maximum normal stress (Q_{max}) : 667.23 N

- The applied minimum normal stress (Q_{min}) : 324.72 N

The FEA was performed with three cycles of maximum and minimum applied load cycles using the elastic-perfectly plastic material property. The resulting stress values were normalized by the maximum normal stress, Po, and half contact width, a.
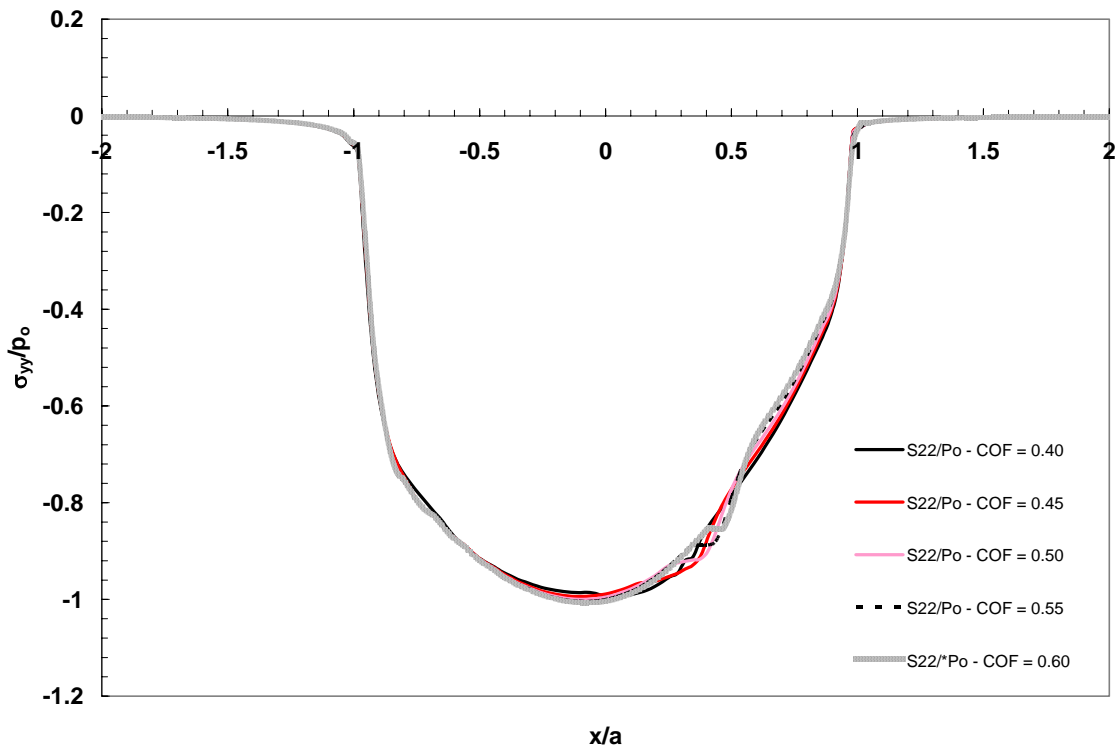
Figure 42. Normalized σ_{yy} for the 5.08 mm Cylindrical Pad with 1.8 kN Normal Load

Figure 42 illustrates the normalized σ_{yy} for the 5.08 mm radius cylindrical pad with 1779 N normal load. The σ_{yy} curves show different shapes with the elastic analysis results as shown in Figure 39. The shapes of σ_{yy} values along the contact surface were not smooth lines as shown in the elastic analysis results. These different curves occurred due to the large plastic zone in the 5.08 mm radius cylindrical pad. The large plastic zone

is caused by accumulation of stresses during cyclic applied loading condition. In comparison with elastic condition, the variation of the σ_{yy} with the change of COF is seen to be the same as in elastic-plastic conditions. In both elastic and elastic-plastic conditions, the variation of the σ_{yy} with the change of COF is negligible.
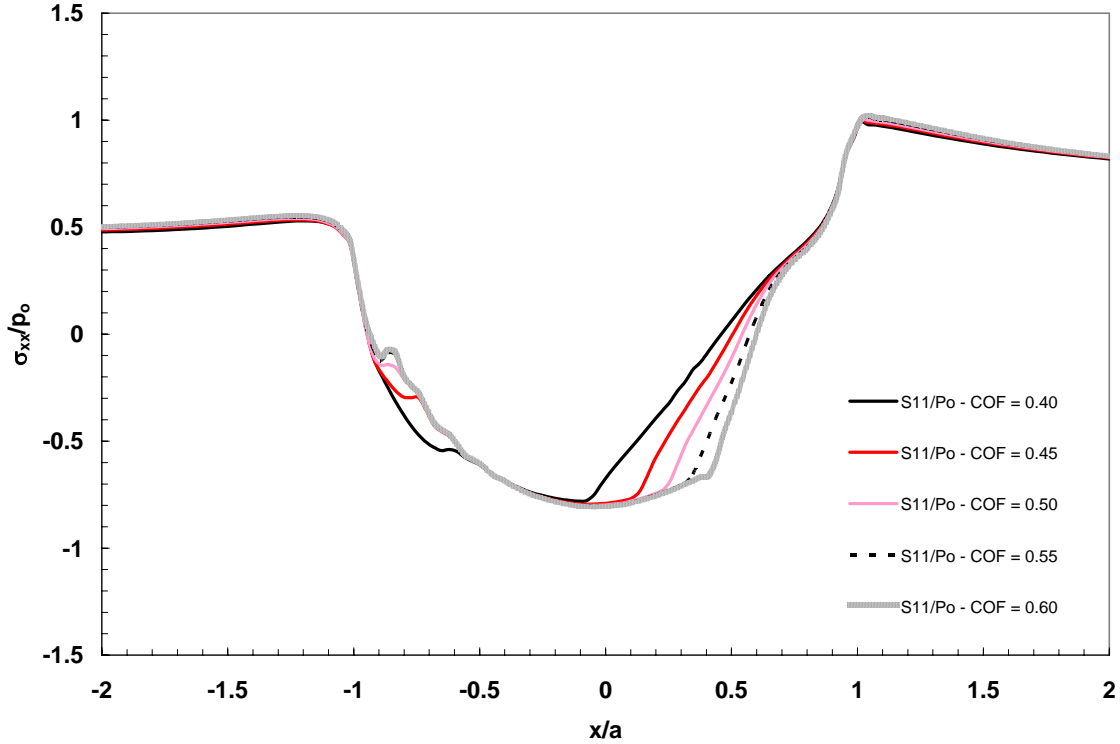
Figure 43. Normalized σ_{xx} for the Various COF on the Elastic-plastic Analysis

Figure 43 illustrates the normalized values of σ_{xx} versus normalized distance, x, for various COF. In Figure 40, the σ_{xx} values from elastic analysis have increased as the COF value is increased. However, from the Figure 43, the maximum normalized value of σ_{xx} did not change as the value of the COF increased. This is because the maximum σ_{xx} values were limited by yield stress value, σ_Y. If the center area of the contact surface is considered, similar features can be found between elastic and elastic-plastic conditions.

In both conditions, the ranges of the minimum value increases as the COF increases. This is because the stick region is increased as the COF increases.
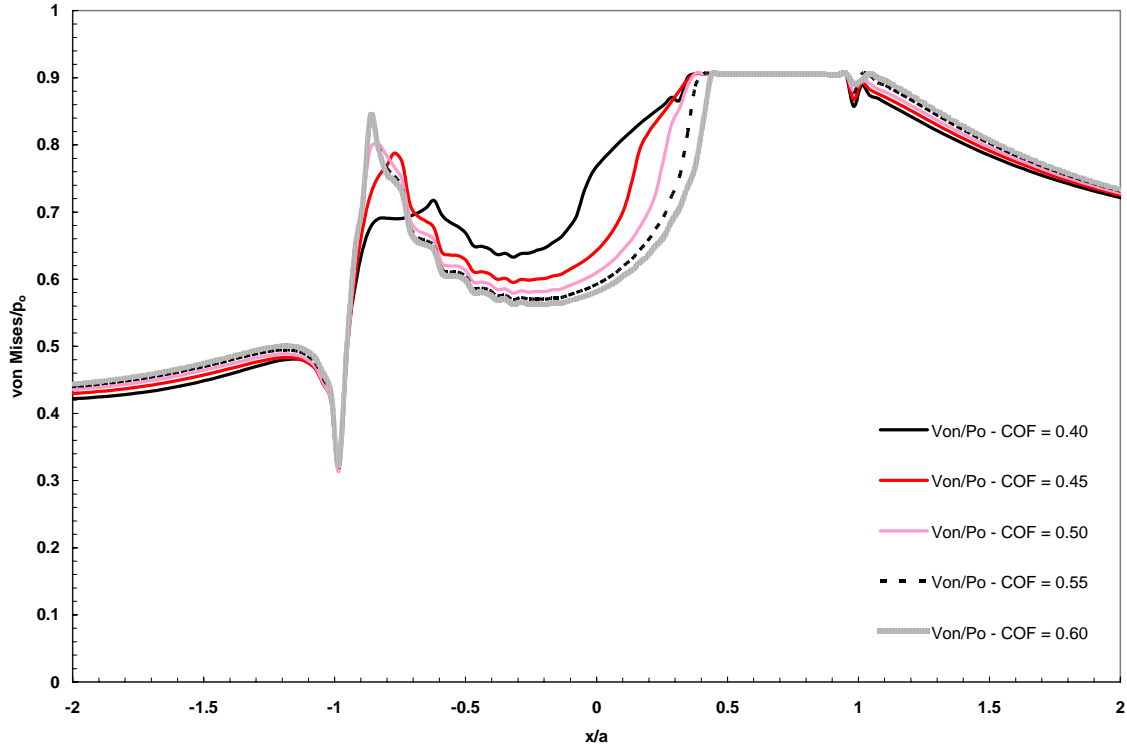
Figure 44. The von Mises for the Various COF Values of the 5.08 mm Cylindrical Pad

Figure 44 shows the normalized von Mises curves for various COF under elastic-plastic condition. Since these calculations were conducted in elastic-plastic analysis conditions, the maximum values of the von Mises stresses were limited by the yield stress, σ_y, value at trailing edge due to plastic deformation. However, the difference is noted in leading edge area. The von Mises values increased in the leading edge area with the increase of COF where the plastic deformation did not occur. Further, the minimum values decreased as the von Mises stresses increased in the leading edge. This is also similar to results of the elastic condition in Figure 41. From the Figure 44, it is can be

noted that the variation of COF is not a significant factor for the maximum value of the von Mises stress as much as it is for the elastic analysis.

As a summary, the change in the normalized σ_{yy} values was negligible as the COF increased in both elastic and elastic-plastic conditions. However, the peak value of the σ_{xx} and von Mises stresses increased as the COF increased in the elastic condition, while these increases were limited by yield stress value in the elastic-plastic condition. In general, the parametric approaches in fretting fatigue analysis use the maximum values of the stress components. Therefore, the output of those parametric approaches could be affected by using elastic or elastic-plastic material properties, especially in the large plastic deformation condition.

4.3. Study of the Stress and Strain Distributions

In this study, FEA was conducted to calculate the stress and strain distributions along and near the contact surface of the fretting fatigue specimen. The calculated stress and strain fields were used in the parametric studies for the behavior of fretting fatigue problems. The FEA was conducted by using the elastic-plastic analysis for all of the tested pad cases. In this section, stress and strain distributions are discussed in detail for all tested pad configurations (cylindrical pads with radii of 50.8 mm, 101.6 mm, 304.8 mm, 5.08 mm and three flat pad type 1 (FP1), type 2 (FP2) , type 3 (FP3)). For comparison of the various pad case results, the same loading conditions were applied as given below and the COF value was equal to 0.5:

- The applied maximum normal stress (σ_{max}) : 577.11 MPa
- The applied minimum normal stress (σ_{min}) : 272.36 MPa
- The applied maximum tangential load (Q_{max}) : 0.20 kN
- The applied minimum tangential load (Q_{min}) : -0.24 kN

89

4.3.1. Comparison of the Stress Distributions

Figure 45 shows the normalized σ_{xx} values for all pad configurations tested in this study, i.e. five cylindrical pads with radii of 50.8 mm, 101.6 mm, 304.8 mm, 5.08 mm (with normal load of 1334 N and 1779 N) and three flat pad type 1 (FP1), type 2 (FP2), type 3 (FP3). The figure has been plotted using FEA results obtained under the same loading conditions. For all of the cylindrical and flat pad configurations, the peak stress values were layered in an inverse relationship to the maximum normal pressure, Po, values. As mentioned previously, the ascending order of Hertzian peak pressure for the tested pad geometries is FP2, 304.8 mm, FP1, 101.6 mm, 50.8 mm, FP3, 5.08 mm with normal load 1334 N and 5.08 mm with normal load 1779 N. Since stresses in Figure 45 was plotted using normalized value by dividing it with Hertzian peak pressure, the pad configuration which has greater Hertzian peak pressure is located in the bottom. For all pad configurations, the maximum peak stress, i.e. σ_{xx}, occurred on the trailing edge where the location, x, is equal to the half of contact width, a.

Appendix C illustrates 3-dimensional stress distributions near the contact surface for all tested pad configurations. By comparing the three cylindrical pads involving elastic deformation (three cylindrical pads with radii of 50.0 mm, 101.6 mm and 304.8 mm), the peak stress of the 304.8 mm cylindrical pad are decreasing slower along the y direction (i.e. away from the contact surface) than the other two pad geometries (cylindrical pads with radii of 50.8 mm, 101.6 mm). Further, if only the two 5.08 mm radius cylindrical pads and three flat pads (FP1, FP2 and FP3) are considered, this decrease is more pronounced.

As has been discussed, similar trend was found in notch problem. In the notch case, the bigger radius of the notch has slower stress gradient or decrease from peak value

at the notch root [13]. Similar results have been found from fretting fatigue conditions.
In the fretting fatigue, the smaller radius of cylindrical pad show faster decrease or more
gradient of stress distribution near the contact surface.
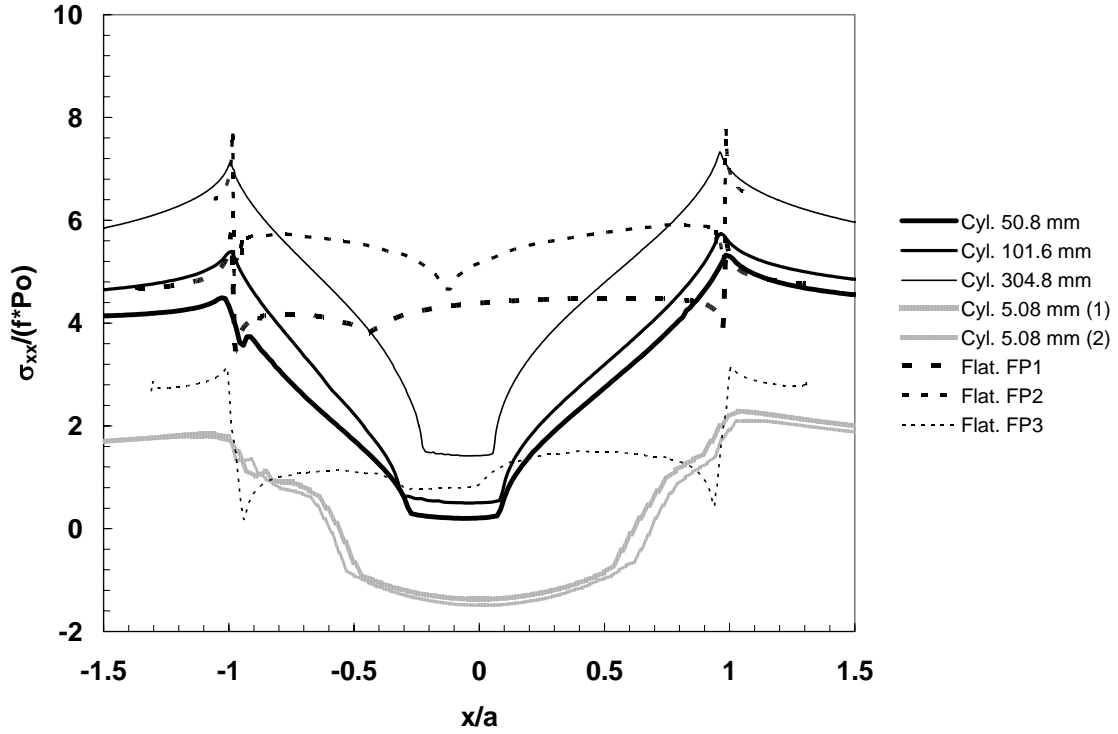
Figure 45. The Normalized σ_{xx} Values for Different Pads under the Same Loading
Condition; Cyl. 5.08 mm (1) represents where normal load was 1334 N, and Cyl 5.08 (2)
had normal load of 1779 N
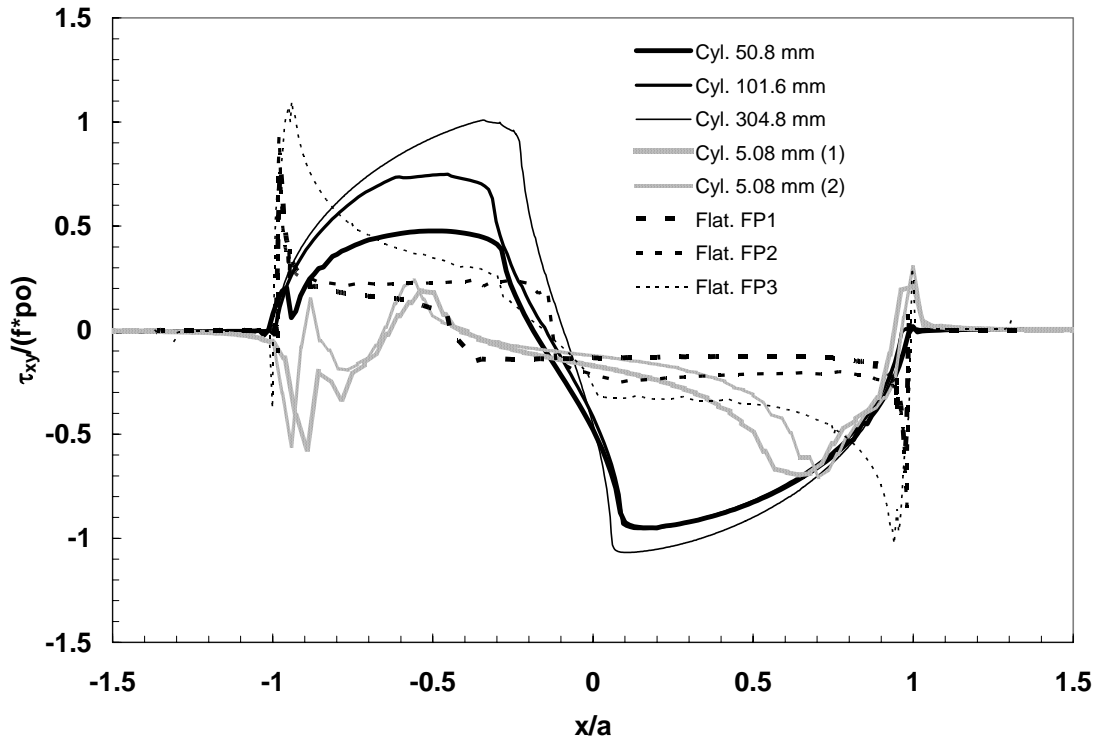
Figure 46. Normalized τ_{xy} Values for the Different Pad Configurations

Figure 46 shows the normalized shear stress, τ_{xy}, curves along the contact surface for all pad configurations tested in this study. By comparing the cylindrical pad configurations with radii of 50.8 mm, 101.6 mm, 304.8 mm and 5.08 mm with two normal loads, it can be seen that the maximum shear stress increases as the Hertzian peak pressure increases. For these five cylindrical pad configurations, trends can be categorized into the elastic fretting conditions (three cylindrical pads with radii of 50.8 mm, 101.6 mm, 304.8 mm) and elastic-plastic fretting fatigue conditions (two cylindrical pads with radii of 5.08 mm under different normal loads). The cylindrical pads involving elastic deformations show the smooth curves of stress values along the contact surface. However, the cylindrical pads involving elastic-plastic deformations show an irregular shape in stress curves. This is because the cylindrical pads involving elastic-plastic deformation show the large plastic deformation.

From the above comparison between cylindrical and flat pad configurations, it can be seen that the locations of the peak shear stress are dependent of the pad configuration. The cylindrical pads have the peak shear stress near the center of the contact surface than the flat pads. This is because the flat pads have greater contact pressure at the edge than the cylindrical pads. As has been explained by Hills and Nowell [20], if the flat-ended pad is pressed into an elastic plane, the size of the contact is independent of the magnitude of the normal load. This contact condition can be called "complete contact condition". In complete contact condition, the surface of the elastic plane is not continuous at the edge of flat pad and thereby the corresponding contact pressure is singular. In this study, in order to replicate the flat pad condition in an experimental configuration and avoid the singular contact pressure at the edge of flat pad, the flat with rounded edges are used instead of the flat-ended pad. However, rounded edges are designed with the small radii, i.e. 5.08 mm and 2.54 mm, and these small edge radii lead to the maximum stress at the edge of the flat pads.
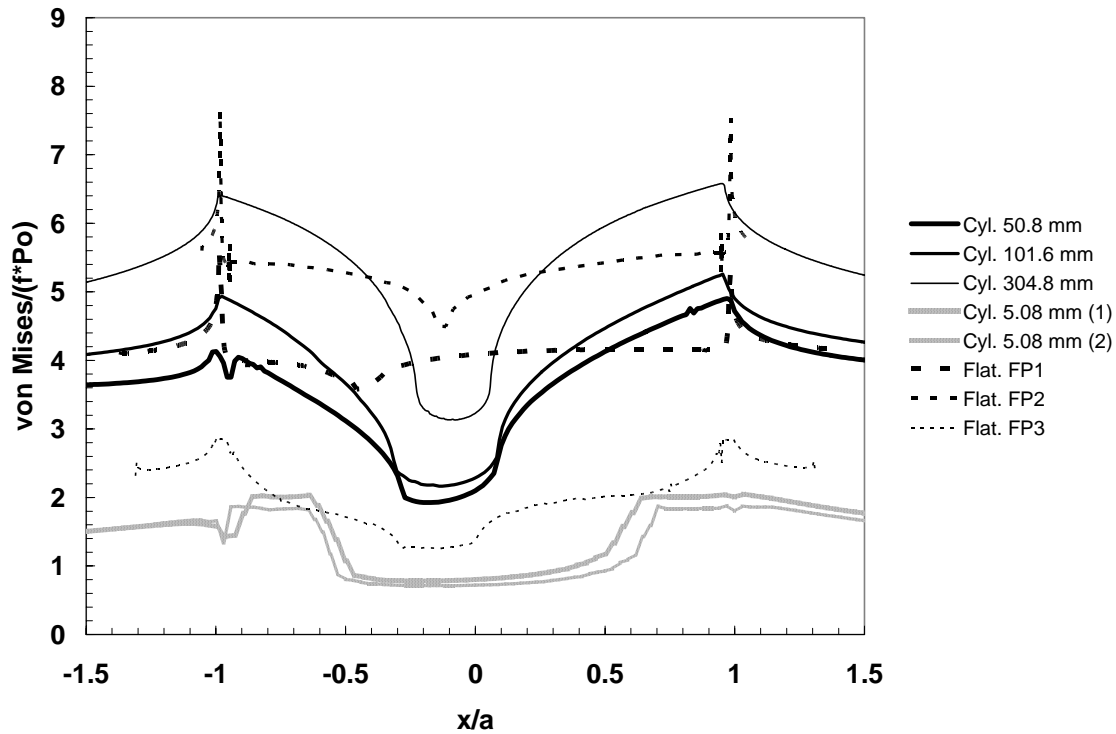
Figure 47. Normalized von Mises Stresses

Figure 47 shows the normalized von Mises stresses on the contact surface for the entire pad configurations tested in this study. The orders of curves followed that of maximum normal pressure similar to the σ_{xx} values in figure 45. As can be seen from Figure 47, the three cylindrical pads with radii of 50.8 mm, 101.6 mm, 304.8 mm and two flat pads of type 1 (FP1), type 2 (FP2) had lower values than the yield stress value. However, two 5.08 mm radius cylindrical pad and flat pad type 1 (FP3) configurations reached the yield stress value, σ_Y, and had plastic deformed area on the surface and show a flat line at the peak stress. Appendix D shows the 3-dementional von Mises stress fields for all pad configurations tested in this study. The Appendix D also shows that two 5.08 mm radius cylindrical pads and one flat pad type 3 (FP3) have plastic deformed region. The cylindrical pad shows a larger plastic deformed region than did the flat pad configuration.

94

4.3.3. Comparison of the Strain Distribution

The von Mises stress distributions for all tested pad configurations were discussed in the preceding section. In this section, the effective plastic strain will be discussed to determine the size of the plastic zone. The plastic zone size of the tested pad configurations can be visualized using post-process tool of the commercial program ABAQUS [37]. For the cyclic loading condition, the ABAQUS determines the size of plastic zone with the equivalent plastic strain, $\bar{\varepsilon}_e^{pl}$. Using von Mises criterion for yield, the effective plastic strain can be expressed as follows:

$$\dot{\bar{\varepsilon}}^{pl} = \sqrt{\frac{2}{3}\dot{\varepsilon}^{pl}\dot{\varepsilon}^{pl}} \tag{53}$$

Also, the equivalent plastic strain after the cyclic loads was defined as:

$$\bar{\varepsilon}_e^{pl} = \bar{\varepsilon}^{pl}\Big|_0 + \int_0^t \dot{\bar{\varepsilon}}^{pl} dt \tag{54}$$

where $\bar{\varepsilon}^{pl}\big|_0$ is the initial equivalent plastic strain at t = 0.

Figures 48 and 49 show the plastic zone using ABAQUS post-process. The sizes of the plastic zone in these figures were calculated by the cumulative effective plastic strain after three cyclic loadings. This is because, as mentioned previously, some of the studies [18, 33] reported that the plastic zone indicated no further plastic strain increments after the first or second cycle. Figure 48 shows the plastic zone of the 5.08 mm radius cylindrical pad configuration while Figure 49 shows the plastic deformation shape of the flat pad type 3 (FP3). The 5.08 mm cylindrical pads generate larger plastic

zone size than the flat pad type 3 (FP3) conditions. The flat pad type 3 (FP3) also shows a narrow shape for the plastic zone near the pad edge. No plastic zones have been found for the five pad configurations (three cylindrical pads with radii of 50.8 mm, 101.6 mm, 304.8 mm cylindrical pads and two flat pads of FP1, FP2) under the applied loading conditions. Since the plastic deformation has a major role in crack nucleation, this plastic deformation could not be ignored in the analysis of fretting crack initiation.

The Appendix E also illustrates the effective strain for the all tested pad configurations. The figures, in Appendix E, are plotted using the normalized total effective strain, ε_e, values by yield strain, ε_Y, value. The total effective strain, ε_e, in multi-axial loading condition is given by the equation [36]

$$\varepsilon_e = \frac{\sqrt{(\varepsilon_1 - \varepsilon_2)^2 + (\varepsilon_2 - \varepsilon_3)^2 + (\varepsilon_3 - \varepsilon_1)^2}}{\sqrt{2}(1+\upsilon)} \tag{55}$$

where υ is Poisson's ratio and ε_1, ε_2 and ε_3 are the three principal strains, with $\varepsilon_1 > \varepsilon_2 > \varepsilon_3$.

As can be seen from figures in Appendix E, for the elastic fretting conditions (three cylindrical pads with radii of 50.8 mm, 101.6 mm, 304.8 mm cylindrical pads and two flat pads of FP1, FP2), the shape of the distribution is similar to the von Mises stress distributions in Appendix D. However for the elastic-plastic deformation conditions (5.08 mm radius cylindrical pads with 1334 N and 1779 N normal loads, and flat pad type 3 (FP3)), different effective strain distributions can be observed. This is because the effective strain can show the magnitude of the plastic deformation within the plastic zone while the von Mises stress can not.
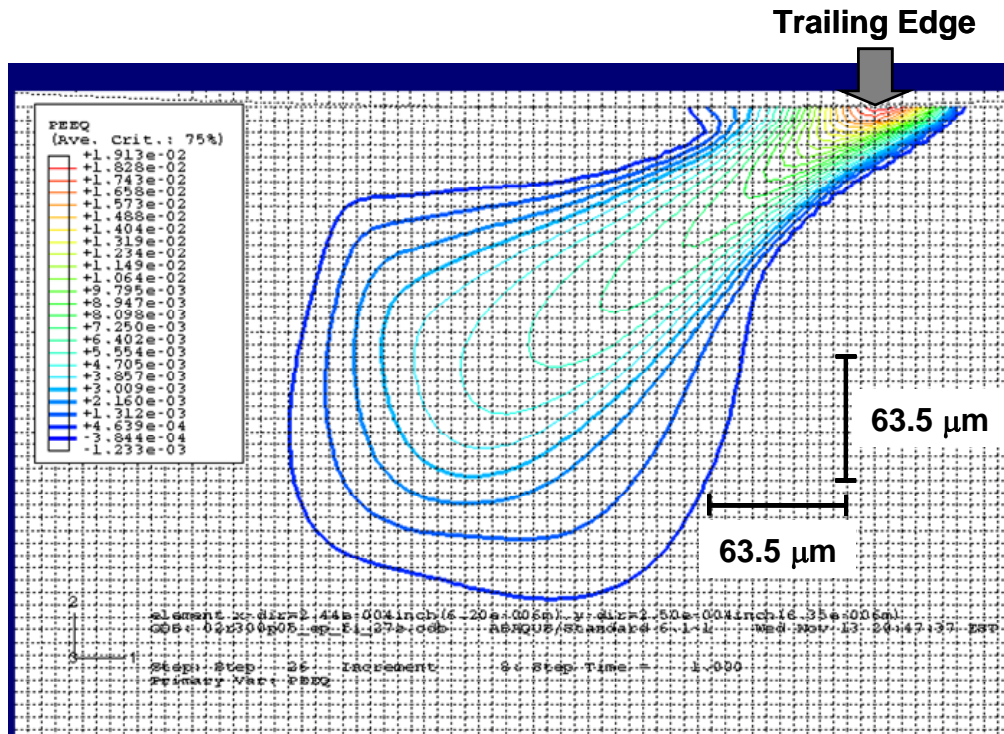
Figure 48. Typical Effective Plastic Strain of the 5.08 mm Radius Pad Configuration
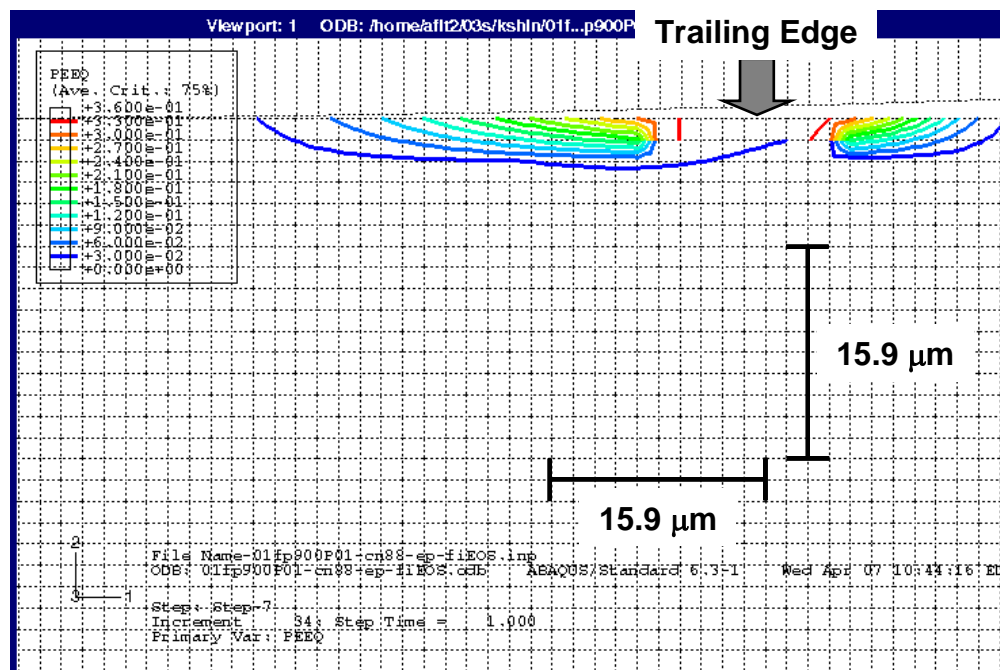
Figure 49. Typical Effective Plastic Strain of the Flat Pad Type 3 (FP3)

97

V. Analyses of Fretting Fatigue

Historically, the total fatigue life of the structures or components under the cyclic loading condition has been characterized as a function of the variables, such as applied stress range and strain range. Typically, the stress-life approach is the most common analytical method to predict fatigue life under elastic strain conditions. Since the stress-life approach does not account for inelastic behaviors, the strain-life method has been frequently used for those situations which induce the elastic-plastic deformation conditions. In this study, both the elastic and elastic-plastic deformation states were present during the fretting tests. Therefore, both stress-life and strain-life approaches will be initially investigated. As mentioned in the background chapter, the critical plane parameters have also been used for the fretting fatigue analysis. As one of the critical plane parameters, the MSSR parameter has been suggested by Namjoshi et al. [10]. In this study, the same parameter will be adapted to analyze the fretting fatigue condition, because this parameter has been shown to be as an effective approach with various contact geometries under elastic fretting fatigue conditions. The application of the MSSR parameter will be extended to the data from elastic-plastic fretting conditions. This will be done to investigate the possibility of the application of this parameter in the contact geometries involving elastic-plastic deformations.

In addition to the application of the MSSR parameter, the author has modified the original formula of the MSSR parameter. The modification was made by employing the local maximum normal stress range, $\Delta\sigma_{xx}$, instead of maximum normal stress value, σ_{max}, on the critical plane as a new approach for analyzing the fretting fatigue behavior involving both elastic and elastic-plastic deformation conditions. The stress distributions for each experimental fretting fatigue test were calculated from the FEA by using an elastic/perfectly-plastic material property as discussed previously.

5.1. Effective Stress versus Life Approach

There are several parametric approaches to account for the effect of the applied bulk stress range, $\Delta\sigma$, or variations thereof on the fatigue life in the literature. In this study, the effective stress, $\sigma_{effective}$, was evaluated as a stress-life approach. This parameter, based on the method suggested by Walker [24] and employed by Lykins et al. [8], is expressed by the equation:

$$\sigma_{effective} = \sigma_{max}(1-R)^m \tag{56}$$

where $\sigma_{effective}$ is the effective stress which takes into account the effects of the stress ratio, R, and σ_{max} is the maximum bulk stress applied to the specimen during a cyclic loading. The fitting parameter, m, was determined to be 0.45 by Lykins et al. [8].

The resulting fretting fatigue data, i.e. the applied effective stress, $\sigma_{effective}$, versus fatigue life, N, from different pad geometries are plotted in Figure 50. For the five pad configurations involving elastic deformations (three cylindrical pads with radii of 50.8 mm, 101.6 mm, 304.8 mm, and two flat pads type 1 (FP1), type2 (FP2)), it can clearly be seen from the Figure 50 that the fretting fatigue life data shows a strong dependence on pad geometries. Further, it can be also observed that the relationships between effective stress and fretting fatigue life from these five geometries are generally layered according to the applied Hertzian peak pressure. As mentioned previously, the ascending order of Hertzian peak pressure for the pad geometries involving elastic deformation is flat pad type 2 (FP2), 304.8 mm radius cylindrical pad, flat pad type 1 (FP1), 101.6 mm radius cylindrical pad, and 50.8 mm radius cylindrical pad. These five pad geometries could be categorized into two groups by amplitude of Hertzian peak pressure: the group with

higher Hertzian peak pressure, i.e. greater than 230 MPa (cylindrical pad with radii of 50.8 mm, 101.6 mm and flat pad type 1 (FP1)) and those with lower Hertzian peak pressure, i.e. less than 230 MPa (304.8 mm radius cylindrical pad and flat pad type 2 (FP2)). The data points from lower Hertzian peak pressure group lie below their counterpart from the other three pad geometries with higher Hertzian peak pressures. This behavior is similar to that in the previous study [35] with one pad geometry.

Figure 50 also shows the data points from pad geometries involving elastic-plastic deformations (two cylindrical pads with radius of 5.08 mm with different normal loads and flat pad type 3 (FP3)). From the figure, the distinctive features of the $\sigma_{effective}$ data points can be observed from elastic and elastic-plastic fretting fatigue conditions. In the elastic fretting conditions, the $\sigma_{effective}$ values have been layered approximately according to the Hertzian peak pressure. However, in the elastic plastic fretting conditions, those values do not follow the order of the Hertzian peak pressure. As mentioned previously, pad configurations involving elastic plastic deformations generated greater Hertzian peak pressures than have the pad geometries involving elastic deformation. However, Figure 50 shows that the $\sigma_{effective}$ values from pad configurations involving elastic-plastic deformations do not layer above the data points from elastic fretting fatigue conditions. Therefore, if the data points from elastic fretting conditions with higher Hertzian peak pressure (cylindrical pads with radii of 50.8 mm, 101.6 mm and flat pad type 1 (FP1)) and elastic-plastic fretting conditions (two 5.08 mm radius cylindrical pads with different normal loads and flat pad type 3 (FP3)) are considered, it can be assumed that the equivalence between elastic and elastic-plastic fretting fatigue conditions could be established, particularly in the low fatigue life regime. However, this is especially true only when the pad configurations involving high Hertzian peak pressure are considered. As shown in Figure 50, the equivalence between data points from all of the tested pad configurations is not established due to the $\sigma_{effective}$ values from the lower Hertzian peak

pressure conditions (304.8 mm radius cylindrical pad and flat pad type 2 (FP2)). As a summary, the $\sigma_{effective}$ approach do not appear to collapse data points into a narrow scatter band, thus indicating that the equivalence among fretting fatigue life from different test pad geometries is not established on the basis of $\sigma_{effective}$.
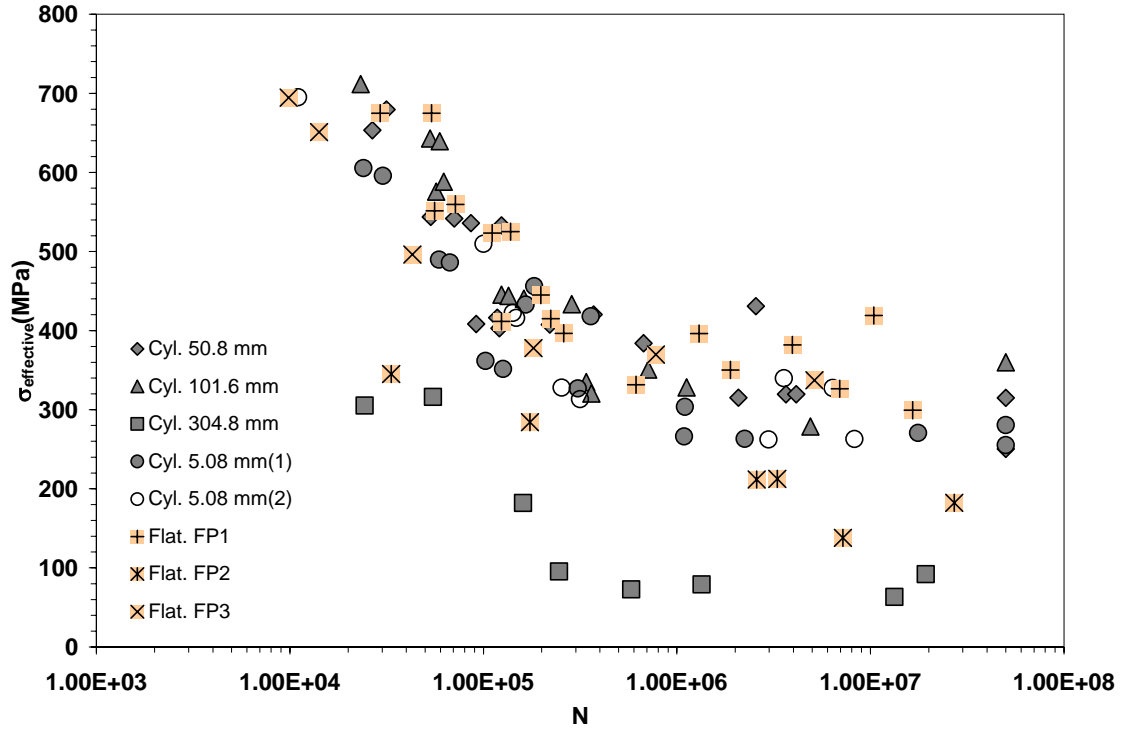
Figure 50. Effective Stress, $\sigma_{effective}$, versus Fretting Fatigue Life

5.2. Effective Strain versus Life Approach

In the previous section, the effective stress, $\sigma_{effective}$, versus fretting fatigue life relationship was evaluated to determine its potential as a fretting fatigue parameter for Ti-6Al-4V under both elastic and elastic-plastic fretting fatigue conditions. However, that attempt resulted in an inappropriate approach due to its strong dependence on different pad configurations. In this section, the effective strain, $\varepsilon_{effective}$, approach will be utilized

for characterizing the fretting fatigue life involving elastic and elastic-plastic deformations. It is well known that the fretting fatigue crack initiation occurs at the stress/strain concentration site. For this reason, it has also been suggested that the effective strain approach could be applied to predict the total fatigue life, especially when elastic-plastic deformation exists [36]. The effective strain, $\varepsilon_{effective}$, in multi-axial loading conditions can be determined from equation (55) in Chapter IV. Figure 51 shows the maximum effective strain, $\varepsilon_{effective-max}$, versus fretting fatigue life data from all eight pad configurations tested in this study. From the comparison of the effective strain versus life approach to the stress versus life approach in Figure 50, three similar observations can be made: first, increased maximum effective strain and stress values are found under the lower fatigue life regime; second, the fretting fatigue life data shows a strong dependence on geometry; finally, the relationships between fretting fatigue life data points from elastic fretting conditions are layered approximately according to the applied Hertzian peak pressure.

However, the distinct trends of results between effective stress and effective strain versus fatigue life approaches can be observed. In the effective stress versus life approach, the data points from elastic fretting conditions under higher Hertzian peak pressure (cylindrical pads with radii of 50.8 mm, 101.6 mm and one flat pad type 2 (FP2)) and elastic-plastic deformation conditions (two cylindrical pads with radii of 5.08 mm and flat pad type 3 (FP3)) were located within the scatter band. However, from the effective strain versus life approach, the data points from elastic-plastic fretting conditions show larger values than of strains those from elastic fretting conditions at a given fatigue life. These differences are due to local plastic deformation, particularly in the low cycle fatigue regime. In the effective stress versus life approach, the applied bulk stress could not account for the effect of the local stress/strain which plays a role in fretting fatigue crack nucleation. However, in the effective strain versus fatigue life

102

approach in Figure 51, the local maximum effective strain is utilized to estimate the number of cycles to failure. Therefore, this approach is able to depict the distinct strain values in the stress concentration area. Figure 51 shows the relatively a smaller scatter range between data points from elastic and elastic-plastic fretting conditions as the number of cycles to failure increases. In other words, the scatter band of the data points between elastic and elastic-plastic fretting conditions decreases as the size of the elastic-plastic deformation diminished under the lower applied stress levels. For this reason, the difference between elastic and elastic-plastic deformation cases is decreased as the number of cycles of failure increases.

As shown in Figures 50 and 51, the data points from the effective stress and effective strain versus fretting fatigue life relationship, obtained from different contact configurations, do not appear to collapse into a narrow scatter range over the entire range of life for elastic and elastic-plastic fretting conditions. However, establishing an equivalence among fretting fatigue life data obtained from different pad geometries is always desirable since it would eliminate or reduce the fretting fatigue experiments which are significantly time consuming and relatively expensive to conduct. An analysis of fatigue life data to establish this equivalence would require consideration of at least two very important factors; a) the continuum variables (i.e. stress/strain state) in the contact region and b) the multi-axial loading effects under the fretting condition. Therefore, it may be appropriate to consider multi-axial fatigue parameters based on stresses/strains in the contact region.
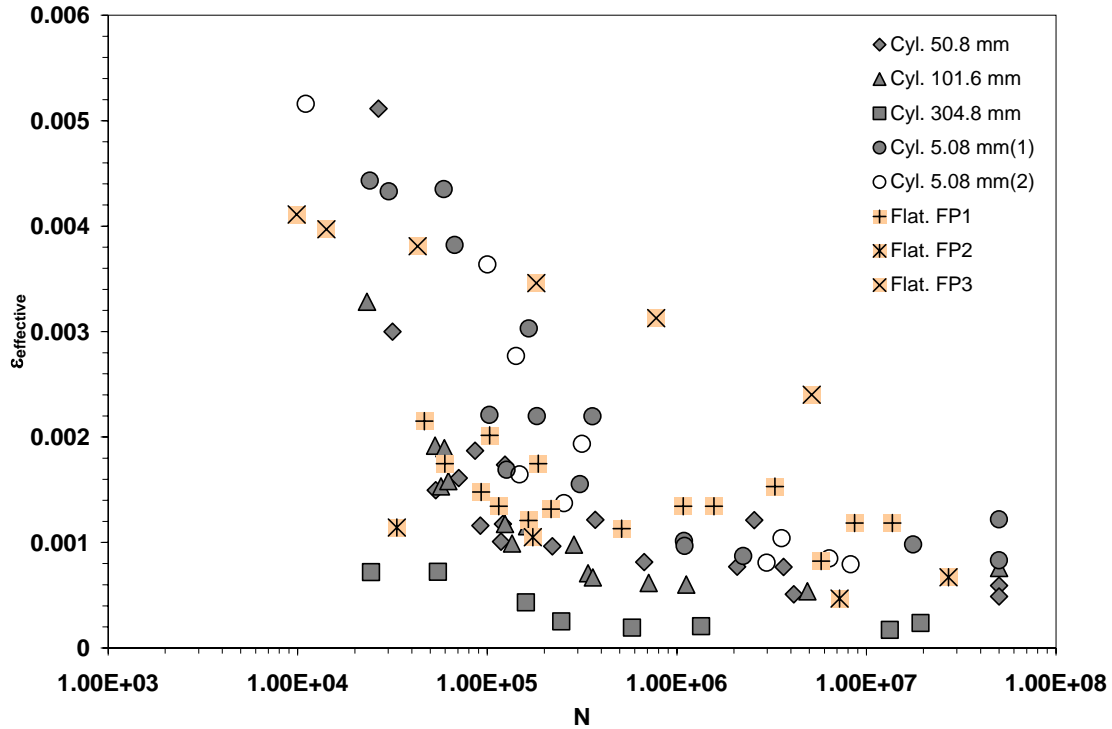
Figure 51. Effective Strain, $\varepsilon_{effective}$, versus Fretting Fatigue Life

5.3. Critical Plane Parameter Using Contact Surface Stress

In previous sections, the stress-life and strain-life approaches were evaluated to determine their potential as fretting fatigue parameters. However, the results indicated that equivalence could not be established between elastic and elastic plastic fretting fatigue conditions from these approaches. As discussed in the background chapter, numerous multi-axial fatigue models/criteria/parameters have been proposed for fretting fatigue analysis [5, 10, 25]. These parameters have been evaluated based on their ability to predict the crack initiation location, crack orientation angle along the contact surface, and fatigue life under fretting fatigue conditions. Of the many multi-axial parameters available, Namjoshi et al. [10] have shown the MSSR to be most effective at predicting

the fretting fatigue life of Ti-6Al-4V. The MSSR incorporates a combination of shear and normal stresses that are encountered in multi-axial fatigue loading and emphasizes the high stress concentration that occurs at the trailing edge of contact.

Although the MSSR has been demonstrated to be an effective parameter for analyzing fretting fatigue conditions, previous works concerning it were limited to the elastic fretting fatigue conditions. For this reason, in this study, the MSSR parameter has been evaluated for experimental data from both elastic and elastic plastic fretting fatigue conditions. However, as it will be shown that this MSSR parameter was not able to effectively correlate the fatigue life data obtained from elastic-plastic fretting fatigue with those from elastic fretting fatigue conditions. For this reason, the author has made a modification to the formulation of the MSSR to make it an effective parameter. As mentioned previously, the MSSR parameter proposed by Namjoshi et al. [10] is based on the shear stress range (SSR) parameter proposed by Walker [24] but is modified to include effects of normal stress. In this study, the author has made a second version of the modified shear stress range (MSSR) parameter and named it the secondly modified shear stress range (SMSSR) parameter. This can be also considered as the second version of MSSR. This modification has been made to predict the fretting fatigue life of elastic-plastic deformation conditions from the elastic fretting fatigue data and to establish equivalence between them independent of fretting pad geometry.

5.3.1. MSSR Parameter versus Fretting Fatigue Life

Firstly, Namjoshi's MSSR parameter is evaluated to determine if it can predict elastic-plastic fretting fatigue life from elastic fretting fatigue life data by using contact surface stresses. The contact surface stress data collected from the FEA was inputted into the FORTRAN program to calculate the MSSR parameter for both elastic and elastic-

105

plastic fretting fatigue conditions. Once the MSSR parameters were calculated, the results were plotted against the number of cycles to failure, N, as shown in Figure 52. As shown in this figure, if only five pad geometries involving elastic deformation (three cylindrical pads with radii of 50.8 mm, 101.6 mm, 304.8 mm, and two flat pads type 1 (FP1) and type 2 (FP2)) were considered, the different scatter bands were observed as the number of cycles to failure increased. In the low fatigue cycle regime, a large range of data occurs, especially where the fretting fatigue life is less than $\sim 5\times10^5$ cycles. However, the MSSR data points fall within a small scatter band under a high cycle fatigue regime. This small scatter band indicates that the resulting fretting fatigue data could be used to predict the fretting fatigue behavior when the MSSR parameter is utilized for the high cycle fatigue life region. Ideally, a parameter describing the fretting fatigue behavior should be able to provide similar behavior among various pad configurations over the entire range of life. However, the authors of previous work [10] proposed that a parameter based on a combination of shear and normal stresses, like the MSSR, can be used to predict the fretting fatigue life for the pad geometries involving elastic deformation.

If three additional pad configurations involving elastic-plastic deformations (two cylindrical pads with radii of 5.08 mm and flat pad type 3 (FP3)) are considered, it can be seen that data points from those pad configurations generate a larger scatter band than five pad geometries involving elastic deformations (three cylindrical pad with radii of 50.8 mm, 101.6 mm, 304.8 mm, and two flat pads type 1 (FP1) and type 2 (FP2)). Most data points from the pad configurations involving elastic-plastic deformation lie above those from the pad geometries involving elastic deformations. Although adding the three pad geometries involving elastic-plastic deformation have acted to increase the scatter band more than elastic deformation conditions only, Figure 52 still shows a considerably smaller scatter band than those from effective stress and strain versus fatigue life

106

relations as shown in Figures 50 and 51 respectively. This means the MSSR critical plane parameter provides a basis that could be utilized to develop a parameter to predict the fretting fatigue life of elastic-plastic fretting fatigue conditions from fatigue data provided by elastic fretting fatigue conditions.

However, from a magnified view of the inside of scatter bands resulting from MSSR as shown in Figure 53, it can be noted that the data points are approximately layered by elastic and elastic-plastic deformation conditions. Further, the data from elastic-plastic fretting fatigue conditions tend to increase the scatter band and, thereby, weaken its accuracy in utilizing elastic fretting conditions to predict the fatigue life of elastic-plastic fretting conditions. In order to better establish the equivalence between elastic and elastic-plastic fretting fatigue life data, the author has suggested the secondly modified shear stress range (SMSSR) parameter. The evaluated result of the SMSSR parameter will be present in the following sections.
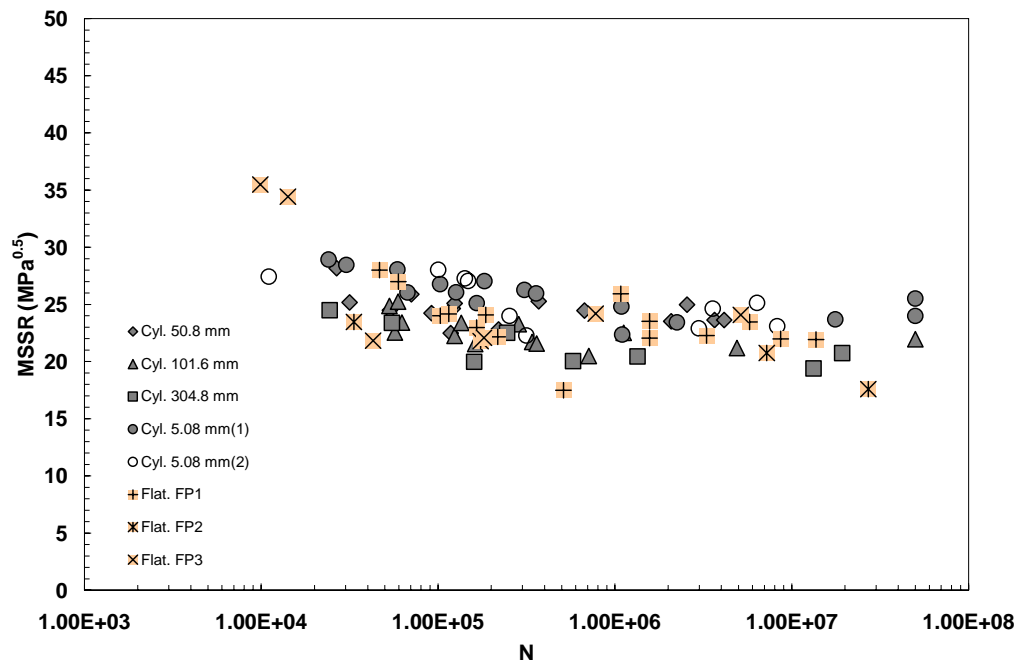
Figure 52. MSSR Parameter versus Fretting Fatigue Life Using Contact Surface Stresses
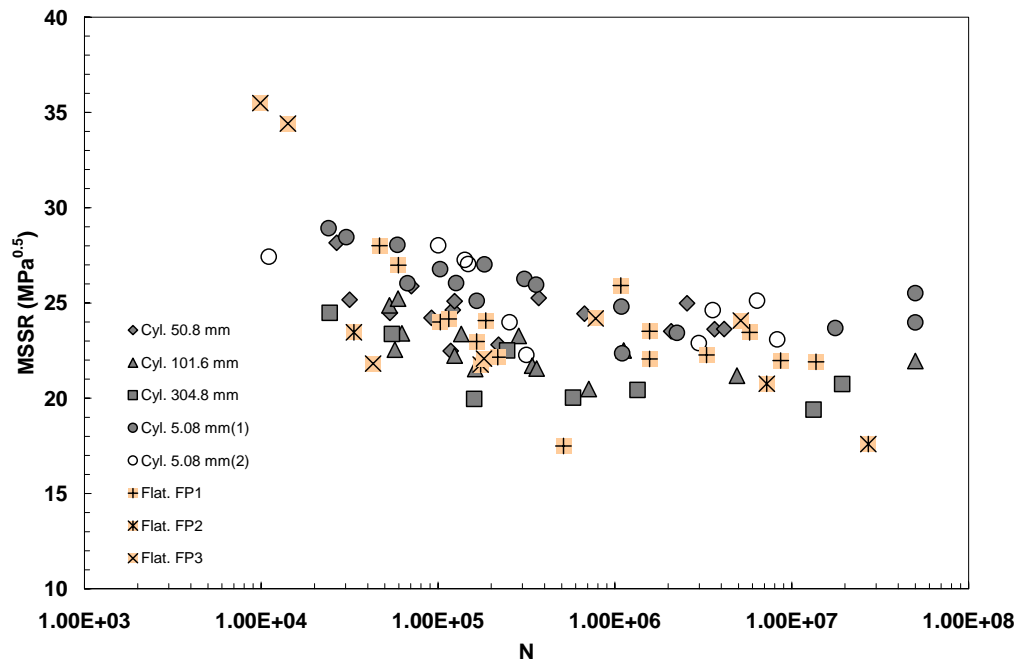
Figure 53. MSSR Parameter versus Fretting Fatigue Life Using Contact Surface Stresses with Smaller Range

5.3.2. SMSSR Parameter versus Fretting Fatigue Life

In order to establish the equivalence between both elastic and elastic-plastic fretting fatigue conditions, a modification is to the MSSR formulation as suggested by Namjoshi et al. [10]. This new version of the MSSR has been named second modified shear stress range (SMSSR) in this study. The MSSR parameter explicitly includes the effects of the effective shear stress range, $\Delta\tau_{crit,effective}$, as well as maximum normal stress amplitude, σ_{max}, to characterize the multi-axial fatigue loading conditions. In the MSSR parameter, the maximum normal stress amplitude, σ_{max}, is utilized to account for the normal stress effects on the crack nucleation and propagation that generally aids in opening the crack surfaces. However, in the SMSSR parameter, the normal stress range, $\Delta\sigma_{normal}$, is utilized instead of the maximum normal stress amplitude, σ_{max} in original MSSR formulation. The SMSSR can be expressed as follows:

$$\text{MSSR} = A\Delta\tau_{crit,effective}^{B} + C\Delta\sigma_{normal}^{D} \tag{57}$$

where $\Delta\tau_{crit,effective} = \tau_{max}(1-R_\tau)^m$, τ_{max} is the maximum shear stress on the critical plane, R_τ is the shear stress ratio on the critical plane, m is a curve fitting parameter determined to be 0.45 for Ti-6Al-4V [8], $\Delta\sigma_{normal}$ is the normal stress range on the critical plane where $\Delta\sigma_{normal} = abs(\sigma_{max}-\sigma_{min})$, and A, B, C, D are curve fitting parameters determined to be 0.75, 0.5, 0.75, and 0.5 respectively for Ti-6Al-4V by Namjoshi et al. [10].

As mentioned above, the modification is made in order to account for the normal stress range, $\Delta\sigma_{normal}$, on the critical plane against the number of cycles to failure. This is done because the fretting fatigue life depends on the minimum loading conditions as well as the maximum loading conditions. The normal stress range is hypothesized to open the

crack and reduce the friction between the crack surfaces while the shear stress causes crack nucleation and growth due to dislocation movement along slip lines. Figure 54 shows results from both the elastic and elastic-plastic fretting fatigue data expressed as the SMSSR parameter versus the number of cycles to failure, N. From the figure, it can be seen that the fretting fatigue life data show a strong dependence on pad geometries. This dependency has been expressed as the layered data points corresponding approximately to the applied Hertzian peak pressure. As mentioned earlier, the ascending order of all tested pad geometries in Hertzian peak pressure is flat pad type 2 (FP2), 304.8 mm radius cylindrical pad, flat pad type 1 (FP1), 101.6 mm radius cylindrical pad, 50.8 mm radius cylindrical pad, flat pad type 3 (FP3), 5.08 mm radius cylindrical pad with 1.33 kN normal load and 5.08 mm radius cylindrical pad with 1.78 kN normal load. The largest amount of deviation occurs between pad configurations involving elastic and elastic-plastic deformation conditions over the entire range of life. Therefore, from the application of the SMSSR parameter, the majority of these data points can be categorized into two groups: a) elastic deformation conditions (three cylindrical pads with radii of 50.8 mm, 101.6 mm, 304.8 mm and two flat pad type 1 (FP1), type 2 (FP2)), and b) elastic-plastic deformation conditions (two cylindrical pads with radii of 5.08 mm and one flat pad type 3 (FP3)).

In the previous section, the MSSR parameter has shown the largest scatter band in low cycle fatigue regime, particularly where the fretting fatigue life is less than $\sim 5\mathrm{x}10^5$ cycles. In high cycle fatigue regime, the scatter band resulting from of MSSR parametric approach was very small. Therefore, it has been concluded that the MSSR can be utilized to predict fretting fatigue behavior within the high cycle fatigue regime. However, the calculated data points from the SMSSR parameter versus fatigue life shows that this parameter can not be utilized to predict the fretting fatigue life due to its strong dependence on pad geometry over the entire fatigue life range.

Although the result from SMSSR shows a considerably strong dependence on pad geometry, one advantage can be noted from these results using SMSSR parameter. The data points from SMSSR parameter show faster descending curves than those from the MSSR parameter as the fatigue life increases for all tested pad geometries. These steeper gradients of data points could provide a clear relationship between applied parameters and the number of cycles to failure, instead of almost flat relationship in the case of MSSR as shown in Figure 52.

From the applications of the MSSR and SMSSR parameters using surface stresses, it can be concluded that these two parameters did not effectively predict the fatigue life of the elastic-plastic fretting fatigue condition from that of the elastic fretting fatigue condition. In other words, the MSSR and SMSSR parameters using contact surface stresses, resulted in approaches inadequate to characterize fretting fatigue life for both elastic and elastic-plastic deformation conditions. As it has been previously mentioned, the purpose of this study is to characterize the fretting fatigue behavior in both elastic and elastic-plastic conditions. One of the typical approaches to achieve this aim is to take into account stress gradients near the contact surface. This is commonly known as the "critical distance method" in the notch problem which has been elaborated in the background chapter. In this study, a similar concept will be applied to establish the equivalence for the test pad configurations involving elastic and elastic-plastic deformation conditions and will be discussed in the following chapter.
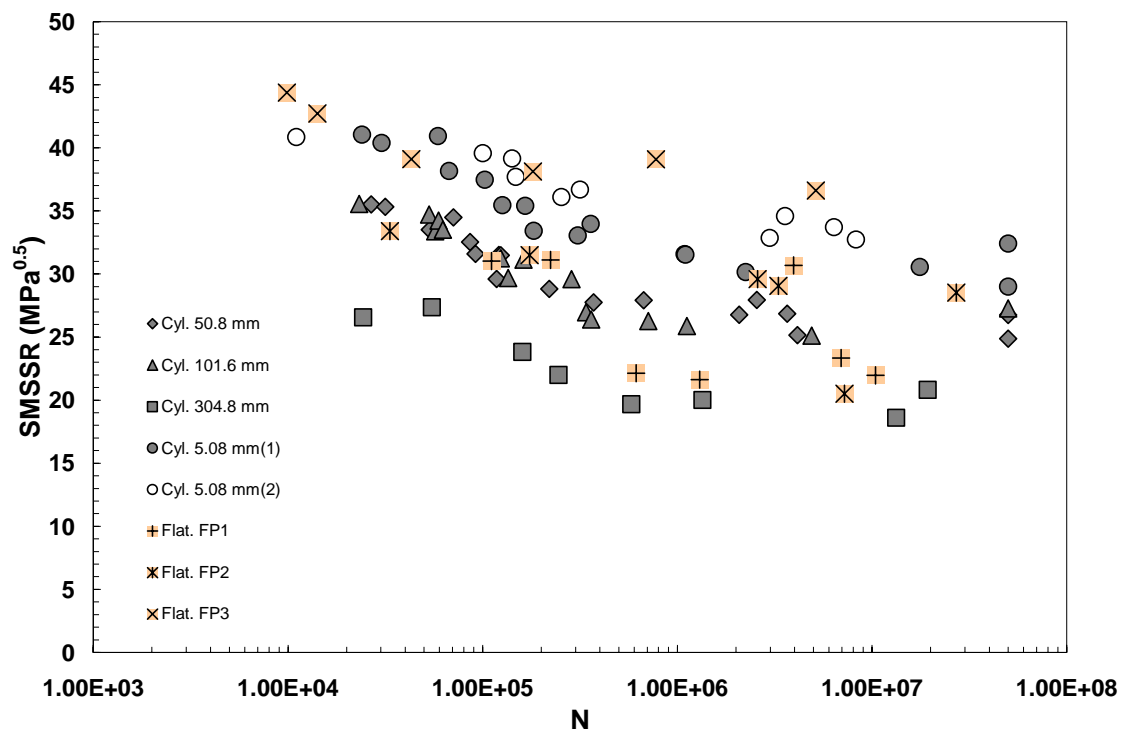
Figure 54. SMSSR Parameter versus Fretting Fatigue Life using Contact Surface Stresses

VI. Methods to Determine the Effective Critical Distance

In the previous chapter, the MSSR and SMSSR parameters were calculated using surface stresses. The results have indicated that these two critical plane parameters using contact surface stresses did not effectively predict the fretting fatigue life of pad configurations involving both elastic and elastic-plastic deformation conditions. For this reason, the application of the critical distance methods will be considered.

As mentioned earlier, the notch problem is a common example of the application of various critical distance methods. In the notch problem, the maximum stress at the notch root has been commonly utilized to predict fatigue life [26]. This maximum stress approach works perfectly well for blunt notches. However, for sharper notches, this approach gives a prediction that becomes increasingly inaccurate as the radius of the notch tip becomes smaller. This is because the sharp notches generate larger peak stress than blunt notches at notch roots. These different radii of notches also produce different stress gradients along the critical plane. In order to account for the effect of the stress gradient in fatigue life prediction, various critical distance methods have been used in the notch problem.

In order to apply the critical distance methods, the critical plane should be first determined to measure the critical distance from the crack initiation location. In the notch problem, the critical plane has been assumed to be perpendicular to the applied loading direction [18, 27] due to its uniaxial stress state nature. However, in the fretting fatigue condition, the critical plane could vary by the contact surface stress state in a fretting fatigue cycle due to its multi-axial stress state nature in the contact region.

Furthermore, in the notch problem, the calculated stress values, i.e. σ_{yy}, along the critical plane were utilized as a parameter to predict the fatigue life. However, in the fretting fatigue problem, the critical plane parameters will be utilized to predict fretting

fatigue life. This is because critical plane parameters have been demonstrated to be effective at predicting the multi-axial fatigue loading conditions, i.e. fretting fatigue condition [5, 10, 25]. As previously discussed, out of the many multi-axial parameters available, the MSSR and SMSSR will be employed as the critical plane parameter for fretting fatigue of Ti-6Al-4V in this study. Therefore, these two parameters will also be evaluated along with the critical distance methods to determine if the equivalence between elastic and elastic-plastic deformation conditions can be established.

The process of determining the critical distance in the fretting fatigue problem can be broken down into three steps: predicting crack initiation location on contact surface, determining crack orientation angle and finally measuring the effective critical distance. The critical plane is determined by crack initiation location and orientation on contact surface. Once the critical plane has been determined, the effective critical distance can be measured from the origin of critical plane. This effective critical distance is the length, which provides the equivalence among the data points calculated from critical plane parameters, i.e. MSSR and SMSSR. In this chapter, these three steps will be demonstrated in detail. Figure 55 illustrates the crack initiation location, orientation and critical plane. Figure 56 illustrates the typical example of the critical plane located on strain distribution for 5.08 mm radius cylindrical pad with 1334 N normal load condition.
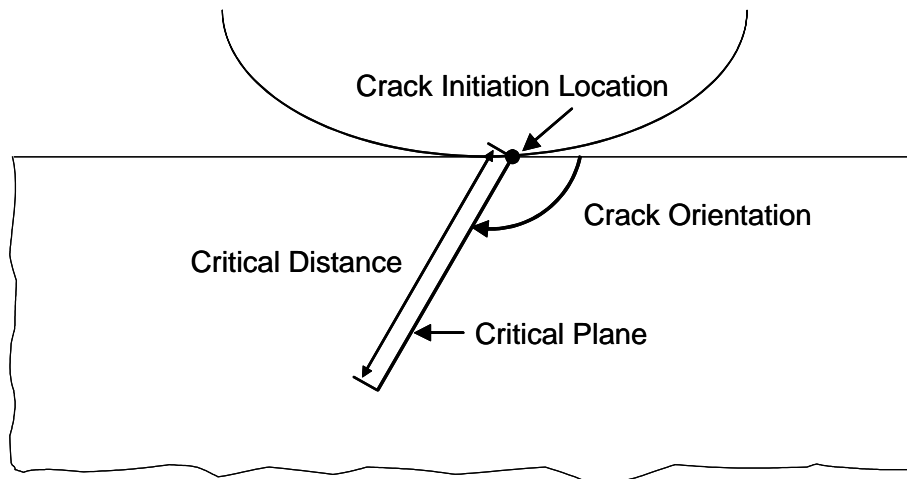
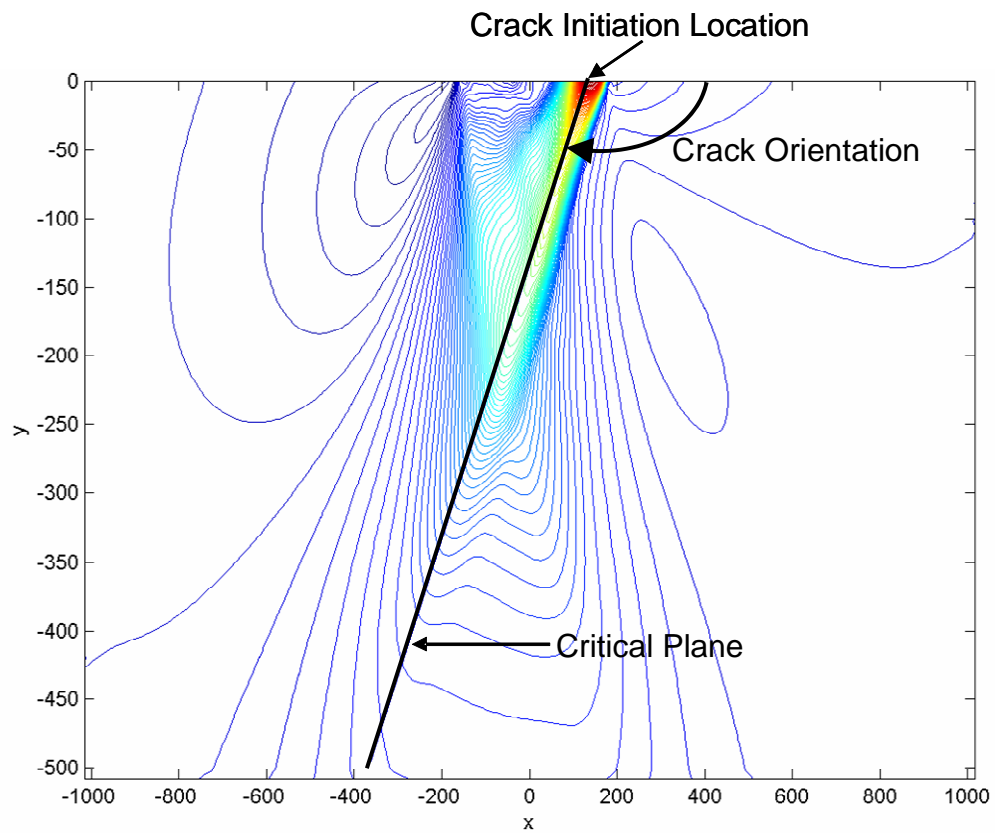Figure 55. Illustration of the Critical Distance along the Critical Plane

Figure 56. Critical Plane Calculated by FORTRAN Program

To determine the crack initiation and orientation, a similar method was used as with MSSR approach by Namjoshi et al. [10]. The crack initiation and orientation were determined by the maximum value of shear stress range, $\Delta\tau_{crit,effective}$, on the contact surface. Once the crack initiation location and angle were predicted, the critical plane was determined using this crack initiation location and orientation information. For the application of the critical distance method, the length of the effective critical distance along the critical plane was also required. In this study, several different approaches will be evaluated to determine the effective critical distance. The methods of finding effective critical distances used in this study can be categorized into three methods: arbitrary critical distance method, effective stress range and effective strain range methods. The arbitrary critical distance method is the simplest method used in this study. This method involves the application of the same distance for all tested pad configurations. After the value of the parameter is calculated, the effective critical distance which generates the smallest scatter band of resulted parameters from all pad configurations tested in this study will be determined. However, in the effective stress and strain range methods, the critical distances are determined by observing the stress and strain gradient along the critical plane; therefore, the critical distance could be different for each pad configuration and loading condition.

In this chapter, a detailed discussion of these three methods will be presented. In order to demonstrate that the difference among these methods, the test loading condition was applied to all pad configurations. This applied loading condition is similar to those used for investigating the stress and strain distribution in previous section. Further, the loading condition was selected over a range between low and high cycle fatigue regimes to apply the typical loading condition. The detail of loading conditions is as follows:

- The applied maximum normal stress (σ_{max}): 577.11 MPa
- The applied minimum normal stress (σ_{min}): 272.36 MPa

- The applied maximum tangential load (Q_{max}): 0.20 kN

- The applied minimum tangential load (Q_{min}): -0.24 kN

In order to demonstrate the role of the critical distance methods used in this study, the different approaches will be applied for each critical distance method. For the arbitrary critical distance method, the calculated critical plane parameter values from each pad configuration will be observed as the critical distance is increased. However, for the effective stress and strain range methods, the effective critical distances, calculated from each pad configuration under same loading condition, will be compared. From the comparison of the calculated effective critical distances, which are dependent on pad configurations, the role of the effective stress and effective strain range methods will be investigated. The coefficient of friction (COF) value was 0.5 for all pad configurations [35]. For the evaluation of three methods, a FORTRAN program, which was written for this study, has been utilized. This FORTRAN program calculates the crack initiation point and predicts crack orientation using contact surface stresses. This program has also been designed to calculate the interpolated values of the stress and strain values along the critical plane using stress and strain distribution fields determined from FEA. Further, this program can calculate the MSSR and SMSSR along the critical plane using the interpolated stress values. The MSSR and SMSSR parameter values have been calculated in two ways, i.e. averaged over a prescribed distance and end point values at the given distance. A detailed discussion for each method will be presented separately in the following sections.

6.1. Arbitrary Critical Distance Method

As mentioned above, the arbitrary critical distance method is the simplest method to determine the critical distance for all pad configurations tested in this study. This method involves the determination of a distance that will provide the best equivalence of experimental fretting fatigue data. In this approach, the crack initiation location and orientation are determined using a method similar to that used in the MSSR parametric approach by Namjoshi el al [10]. This is because the MSSR has effectively predicted both crack initiation location and orientation of fretting fatigue in Ti-6Al-4V [10, 17]. As discussed previously, in the MSSR parametric approach, the location and orientation of fretting fatigue crack initiation have been determined by a maximum value of $\Delta\tau_{crit,effective}$ on the contact surface.

Figure 57 shows the MSSR parameter values versus critical distance while Figure 58 illustrates the variation of the SMSSR as the critical distance increases. As shown in the figure, on the contact surface, where the critical distance is equal to zero, the MSSR data show a relatively smaller scatter band than that from the SMSSR parameter. These different scatter ranges between MSSR and SMSSR are in agreement with the result using the contact surface stresses in Figures 52 and 54. However, both the MSSR and SMSSR parameter values are decreased as the critical distance increases. Although both parameters show decreased values at the longer critical distance, different features of decrement are observed between pad configurations involving the elastic and elastic-plastic deformations. From the pad configurations involving the elastic deformations (three cylindrical pads with radii of 50.8 mm, 101.6 mm, 304.8 mm and two flat pad type 1 (FP1), type 2 (FP2)), both the MSSR and SMSSR approaches show slow decrease as the critical distance increases. However, from the pad geometries involving the elastic-plastic deformations (two cylindrical pads with radii of 5.08 mm and one flat pad type 3

(FP3)), different rates of decrease are seen between the MSSR and SMSSR parameters. For the cylindrical pad configurations involving elastic-plastic deformation, irregular rates of decrease are found in the MSSR while smooth decrease rates are observed in the SMSSR. These differences are caused by the distinctive variations of the maximum normal stress amplitude, σ_{max}, values and the normal stress range, $\Delta\sigma_{normal}$, which are used in the MSSR and SMSSR respectively. These σ_{max} and $\Delta\sigma_{normal}$ show similar variation for the pad configurations involving elastic deformation. However, for the pad configurations involving elastic-plastic deformation, the σ_{max} values show irregular variation while the $\Delta\sigma_{normal}$ values are decreased smoothly as the critical distance increases. The irregular decrease rate of the MSSR causes a wider scatter band as the critical distance increases along the critical plane. However, from the data of the SMSSR parameter, it can be seen that the scatter band is narrowed as the critical distance is increased. Furthermore, from result of the SMSSR parameter, the different slopes are found under the elastic and elastic-plastic fretting fatigue conditions. The elastic fretting conditions cause a slow decrease while the elastic-plastic fretting fatigue conditions result in rapid decrease from the crack initiation location on the surface up to the certain critical distance. These contrasting decrease rates lead to a narrow scatter range as the critical distance increases between data points under elastic versus elastic-plastic fretting conditions. As discussed previously, a similar phenomenon has been observed in the notch problem by several researchers [18, 27]. In the notch problem, the higher peak stresses at the notch roots lead to the high stress gradient along the critical plane. In the fretting fatigue conditions, higher Hertzian peak pressure on a contact surface also generates a high stress gradient along the critical plane. By considering the similarity of the stress gradients between notch and fretting fatigue conditions, it can be assumed that the critical distance method will be an effective approach for establishing the equivalence

among data from various pad configurations which generate elastic and elastic-plastic deformations.
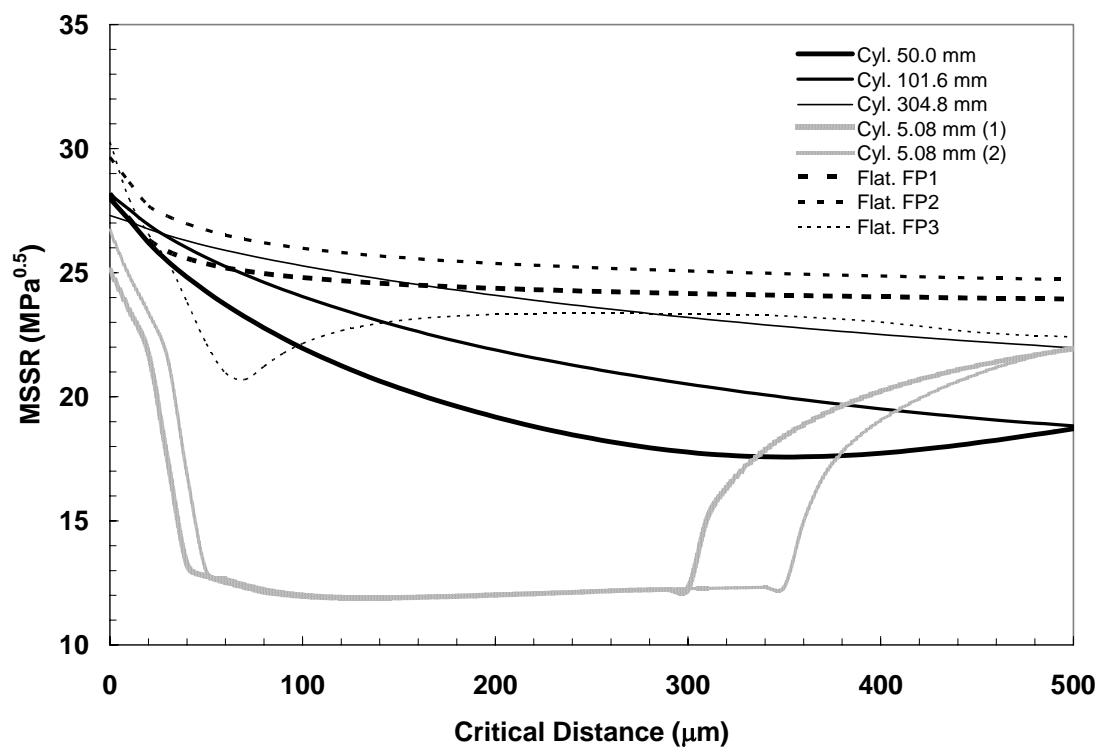

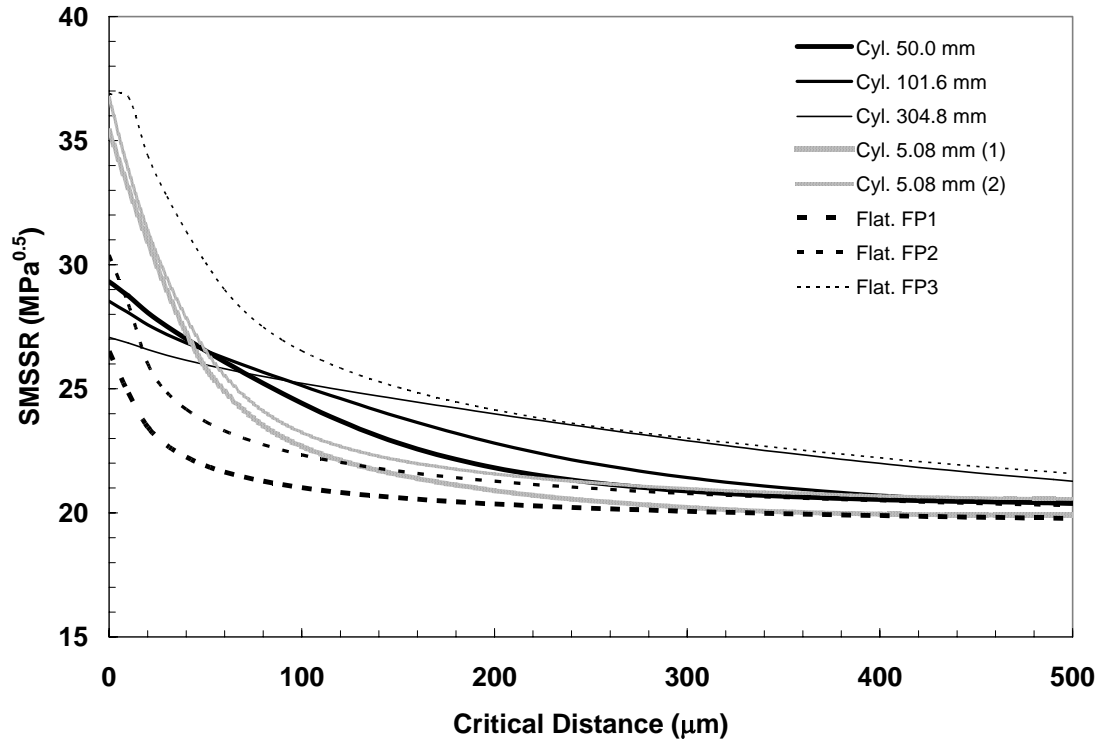Figure 57. Point Values of MSSR on the Critical Plane

Figure 58. Point Values of SMSSR on the Critical Plane

6.2. The Effective Stress Range Method

As mentioned previously, in the notch problems, the normal stress, σ_{yy}, variation has been used along with critical distance methods to determine the effective critical distance from the notch root [18]. In this section, similar approaches will be applied to the fretting fatigue problems; thus the stress values along the critical plane will be utilized to determine effective critical distance. However, the von Mises stress will be utilized instead of the normal stress, σ_{yy}, along with critical distance methods due to the multi-axial nature of the stress distribution in fretting fatigue condition. The critical distance methods used in this study can be broken down into two methods: the von Mises stress range and the modified relative stress gradient method.

121

6.2.1. von Mises Stress Range Method

In general, effective stresses have been utilized to analyze fatigue life under multi-axial loading conditions, i.e. fretting fatigue [36]. As mentioned previously, three pad geometries (two 5.08 mm radius cylindrical pads with different normal loads and one flat pad type 3 (FP3)) have involved the elastic-plastic deformation under the maximum loading condition. Therefore, in order to account for the multi-axial cyclic stress state and characterize the elastic-plastic deformation of the material under fretting fatigue loading condition, the effective stress resulting from von Mises criterion will be utilized. As an example, Figure 59 shows the variation of the von Mises stress at maximum and minimum applied loading conditions. The figure also illustrates the von Mises stress range, Δvon Mises, values versus critical distances along the critical plane. These values have been calculated from one of the 5.08 mm radius cylindrical pad geometries under 1779 N normal load. This is because this pad configuration generates the large elastic-plastic deformation. As shown in Figure 59, the von Mises stress value under the maximum loading condition demonstrates little variation as critical distance increases. As it has been mentioned, in this study, the elastic/perfectly-plastic material property was used. For this reason, within the plastic zone area, the von Mises stresses calculated at maximum loading condition show relatively constant values along the critical plane. However, the von Mises stress at minimum loading condition shows more variation than at maximum loading condition along the same critical plane. Generally, in fatigue problem, the number of cycles to failure depends on both maximum and minimum loading conditions. For this reason, in this study, the von Mises stress range, Δvon Mises, will be utilized as a stress basis for determining the effective critical distance and

this critical distance will be utilized for analyzing the fatigue life along with critical plane parameters, i.e. MSSR and SMSSR.
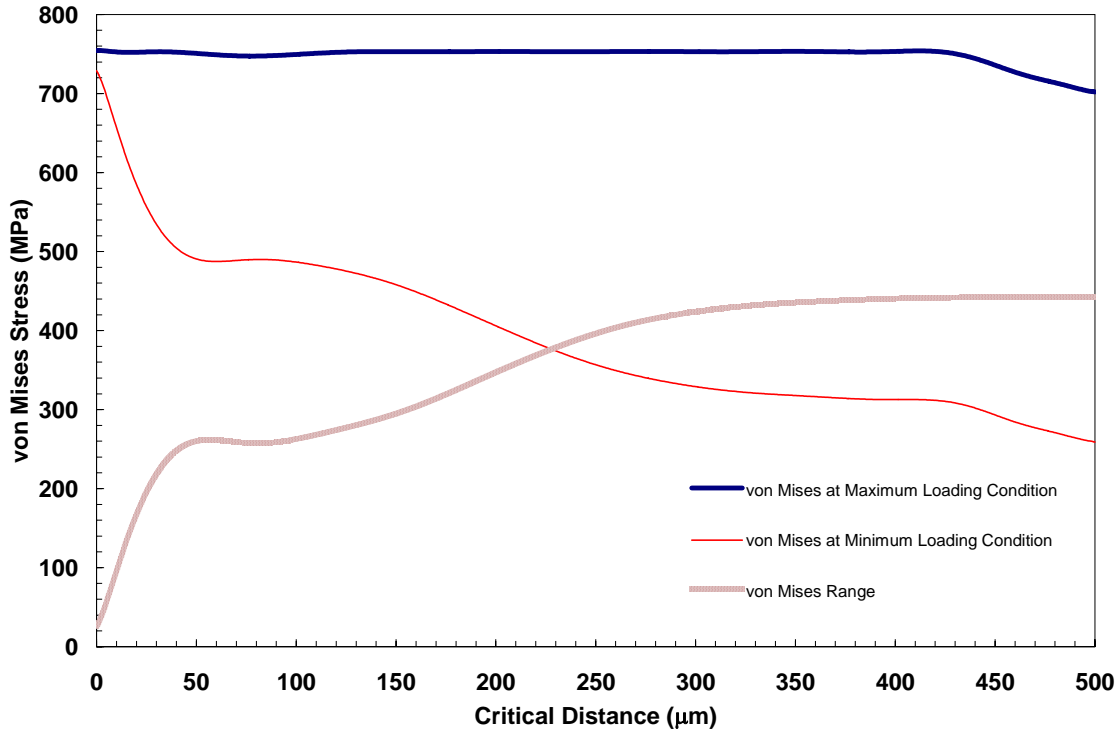

Figure 59. Typical von Mises Stresses at Maximum and Minimum Loading Conditions for 5.08 mm Radius Cylindrical Pads with 1334 N Normal Load

In the von Mises stress range, Δvon Mises, method, the crack initiation location and orientation on the contact surface was determined by a method similar to the MSSR parametric approach [10]; the location and orientation of fretting fatigue crack initiation were determined by the maximum value of $\Delta\tau_{crit,effective}$ value on the contact surface. The critical plane was also determined by crack initiation location and orientation information on the contact surface. Once the critical plane was determined, the magnitude of the von Mises stress range, Δvon Mises, was calculated along the critical plane. The computed stress distribution near the contact surface obtained from the FEA was inputted into the FORTRAN program written for this study. This FORTRAN program was written to

calculate the interpolated value of the von Mises stress range along the critical plane. In the von Mises stress range method, the effective critical distance, d_c, was determined by observing the variation of the von Mises stress ranges. In other words, the effective critical distance was determined by measuring the distance from the origin of the critical plane at the contact surface to the location where the first minimum value of von Mises range value occurs. Figure 60 demonstrates the effective critical distance, d_c, calculated by the von Mises stress range method for the elastic fretting condition, i.e. 50.8 mm radius cylindrical pad case. In order to determine the critical distance, the first derivative of the von Mises stress range, $\Delta V'$, was calculated. Once the values of the first derivation of the von Mises stress range was calculated, the effective critical distance was identified by measuring the distance from the origin of the critical plane to location where the value of the first derivative was equal to zero. To confirm the location that had a minimum value of the von Mises stress range, it was also necessary to observe the second derivative for a positive value. Figure 61 shows the result of the one of elastic-plastic fretting conditions, i.e. 5.08 mm radius cylindrical pad under 1334 N normal load. From the two figures, it was observed that the elastic-plastic deformation condition result shows a shorter effective critical distance than does the elastic deformation condition.

Figure 62 shows the effective critical distance, d_c, calculated by the von Mises stress range method for all pad configurations under same loading condition while Figure 63 shows results of pad configurations involving elastic deformation only. As shown in Figure 62, the variation of the von Mises range can be grouped into the pad configurations involving elastic deformation (three cylindrical pads with radii of 50.8 mm, 101.6 mm, 304.8 mm and two flat pad type 1 (FP1), type 2 (FP2)) and pad configurations involving elastic-plastic deformation (two cylindrical pads with radii of 5.08 mm and flat pad type 3 (FP3)) from observing the trends of curves. On the contact surface, the pad configurations involving elastic deformations have a greater value of von

Mises stress range, ΔV, than that in the pad configurations involving elastic-plastic deformation. This is because the greater local von Mises stress ranges are calculated on the contact surface for the pad configurations involving elastic deformation. Another dissimilar feature between pad configurations involving elastic and elastic-plastic deformations was found in the measured effective critical distances. Most pad configurations involving elastic deformation have the larger effective critical distance than have the pad configurations involving elastic-plastic deformation. This is because the pad configurations involving elastic deformation has a slower decrease of von Mises stress range along the critical plane from the crack initiation location than do the pad configurations involving elastic-plastic deformation. Also, this slower decrease leads to longer distance from the location where the minimum value of the von Mises stress range occurs. Observation of the von Mises stress range method indicates that it can be summarized as follows:

- On the surface, the pad configurations involving elastic deformation show larger von Mises stress range values than do the pad configurations involving elastic-plastic deformation cases.

- The elastic fretting condition cases show longer effective critical distances than do the elastic-plastic fretting conditions.
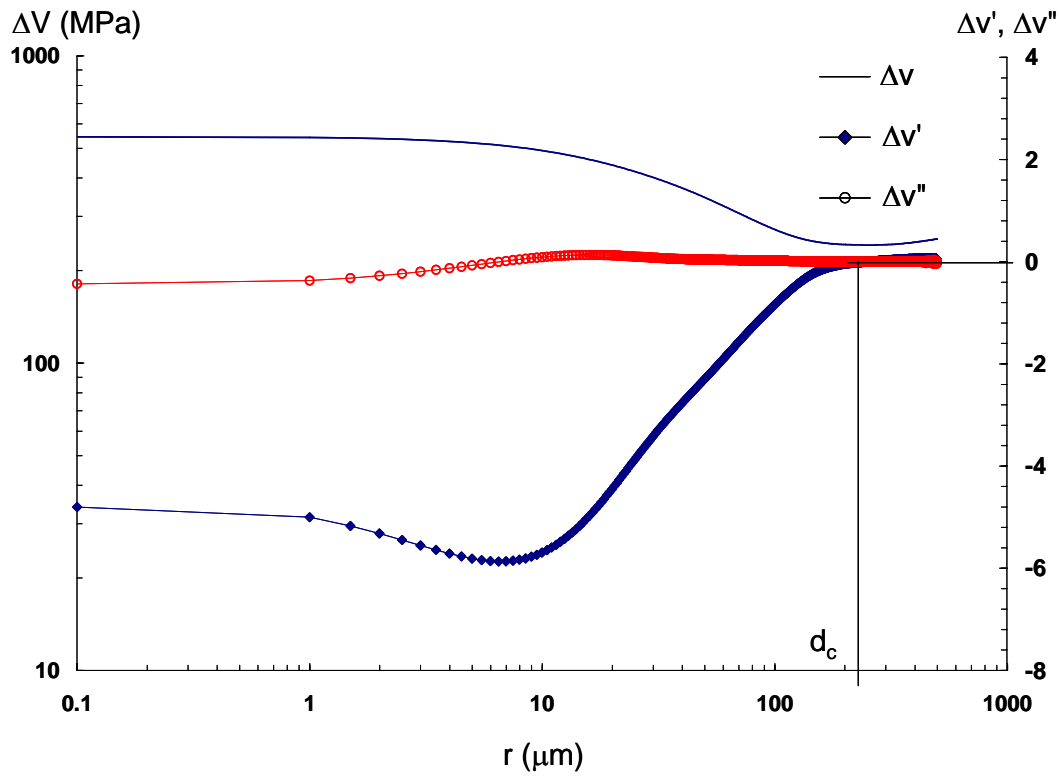
Figure 60. Typical Effective Critical Distance for 50.8 mm Radius Cylindrical Pad von Mises Stress Range Method; ΔV = von Mises Stress Range, ΔV′ = the first derivative of ΔV and ΔV″ = the second derivative of ΔV
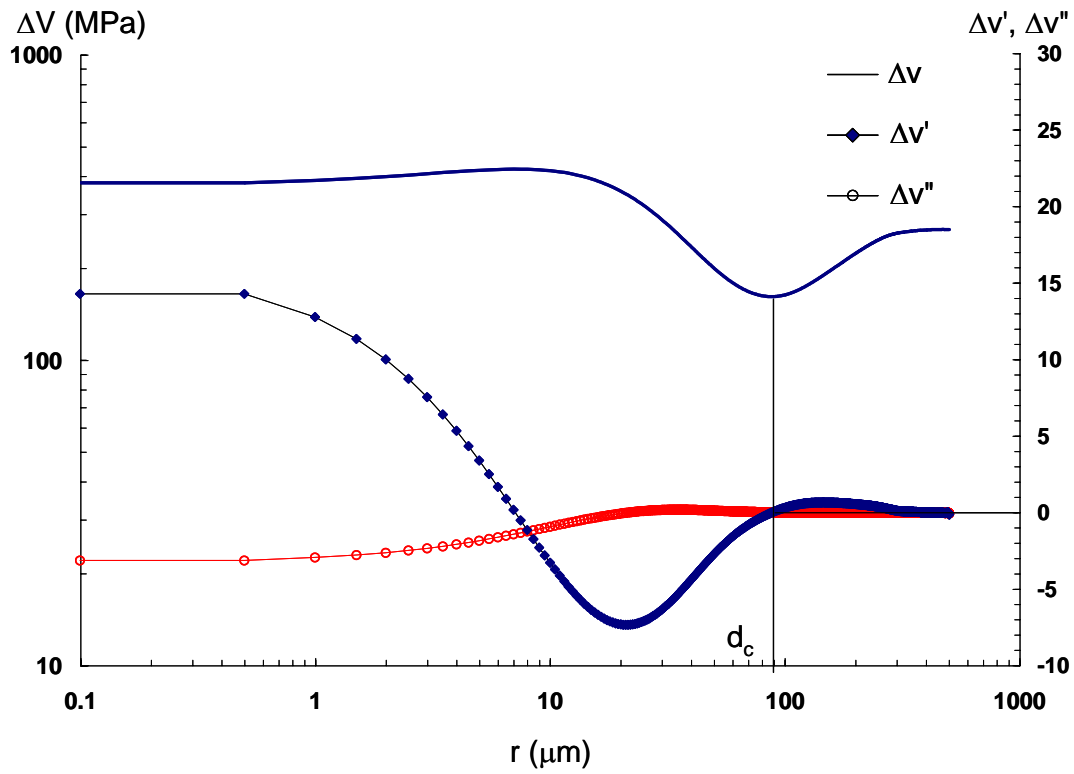
Figure 61. Typical Effective Critical Distance for 5.08 mm Radius Cylindrical Pad with 1334 N Normal Load using von Mises Stress Range Method; ΔV = von Mises Stress Range, ΔV′ = the first derivative of ΔV and ΔV″ = the second derivative of ΔV

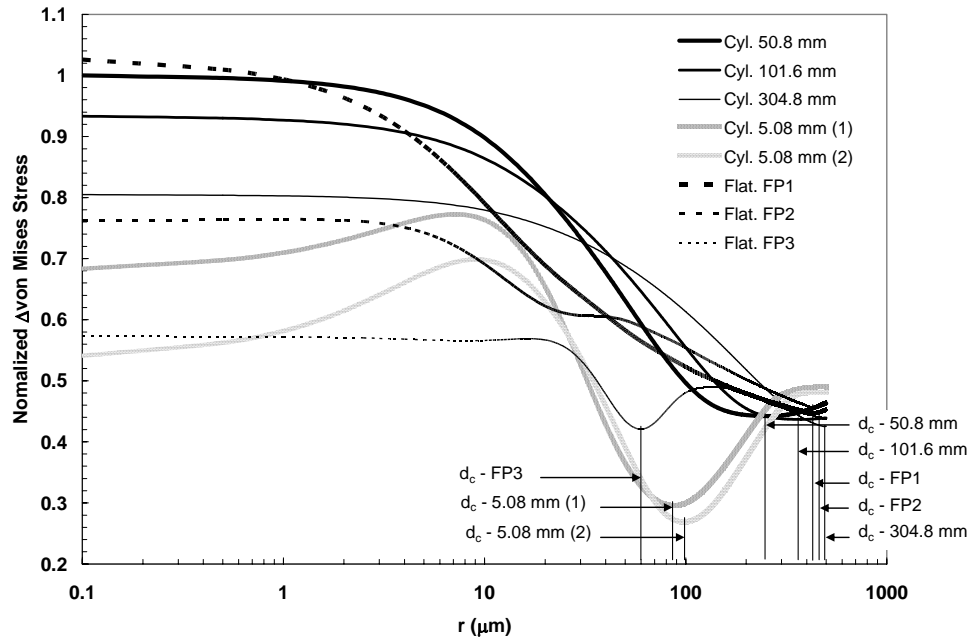Figure 62. Typical Effective Critical Distances using von Mises Stress Range Method for all Tested Pad Configurations; von Mises stress range values was normalized by using 50.8 mm radius pad data
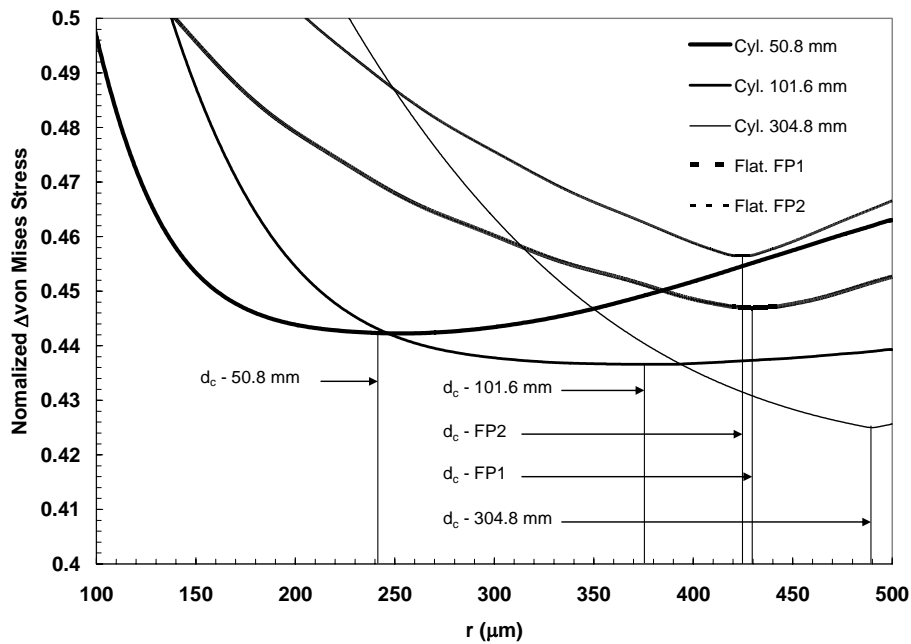

Figure 63. Typical Effective Critical Distances using von Mises Stress Range Method for Pad Configurations Involving Elastic Deformation; von Mises stress range values was normalized by using 50.8 mm radius pad data

6.2.2. Relative Stress Gradient Method

Qylafku et al. [13] suggested the relative stress gradient method for the notch fatigue problem including the elastic-plastic fatigue conditions. In the present study, a similar method will be attempted for the fretting fatigue problem involving elastic and elastic-plastic deformation. Qylafku et al. [13] utilized the σ_{yy} values for the relative stress gradient formula, χ, as given in equation (40). However, in this study, the von Mises stress range, ΔV, was utilized for the stress gradient approach due to its multi-axial stress state nature of fretting fatigue. The von Mises stress range will be used to account for the minimum loading condition as well as maximum loading condition on fatigue life. The modified formula based on Qylafku's original formula (40) involving von Mises stress range can be expressed as follows:

$$\chi = \frac{1}{\Delta V(r)} \frac{d\Delta V(r)}{dr} \tag{58}$$

where r is the distance from the crack initiation location on the surface along the critical plane and ΔV is the von Mises stress range.

In this approach, the crack initiation location and orientation were determined by observing the maximum value of the $\Delta\tau_{crit,effective}$ on the surface. This is the same method of finding the crack initiation location and orientation in the MSSR parametric study by Namjoshi et al. [10]. Figure 64 demonstrates the result of the χ for the pad configuration involving elastic deformation, i.e. 50.8 mm radius cylindrical pad. As shown in the figure, the effective critical distance, d_c, is determined by measuring the distance from the crack initiation location on the surface to the location where the minimum χ value occurs along the critical plane. Figure 65 also shows the result for the 5.08 mm radius cylindrical pad which produces elastic-plastic deformation. Figures 64 and 65, it

demonstrate that the pad configuration involving elastic-plastic deformation has longer effective critical distance than does the pad geometry involving elastic deformation.

Figure 66 shows the effective critical distances calculated from all pad configurations tested in this study. As shown in figure, the three pad configurations involving elastic-plastic deformation (two cylindrical pads with radii of 5.08 mm and flat pad type 3 (FP3)) show increased χ values near the surface and then the χ values are decreased as the critical distance is increased. However, most of the pad configurations involving elastic deformation (three cylindrical pads with radii of 50.8 mm, 101.6 mm, 304.8 mm and two flat pad type 1 (FP1), type 2 (FP2)) show an increasing value of χ as the critical distance increases. These different variations of the χ values lead to different effective critical distances between elastic and elastic-plastic fretting fatigue condition. Most of the pad configurations involving elastic-plastic deformation show longer effective critical distances than do the pad geometries involving elastic deformation. These results are in agreement with Qylafku et al's work [13]. They also reported longer effective critical distance as the plastic deformation zone size enlarged. Comparing the relative stress gradient method to the von Mises stress range method for measuring critical distances, a reverse relationship is obtained. As discussed previously, in the von Mises stress range method, longer effective critical distances were calculated from elastic fretting fatigue conditions. However, in the relative stress gradient method, shorter effective critical distances were calculated under same conditions. Additionally, the von Mises stress method calculated longer effective critical distances than did the stress gradient approach for both elastic and elastic-plastic fretting fatigue conditions.
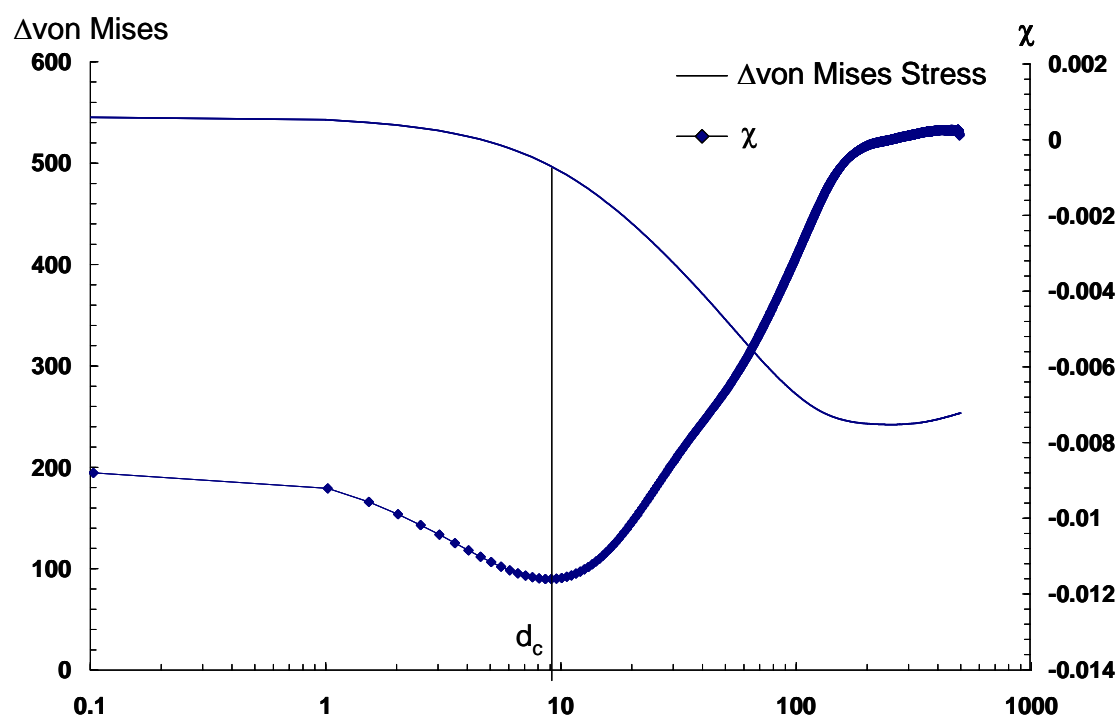
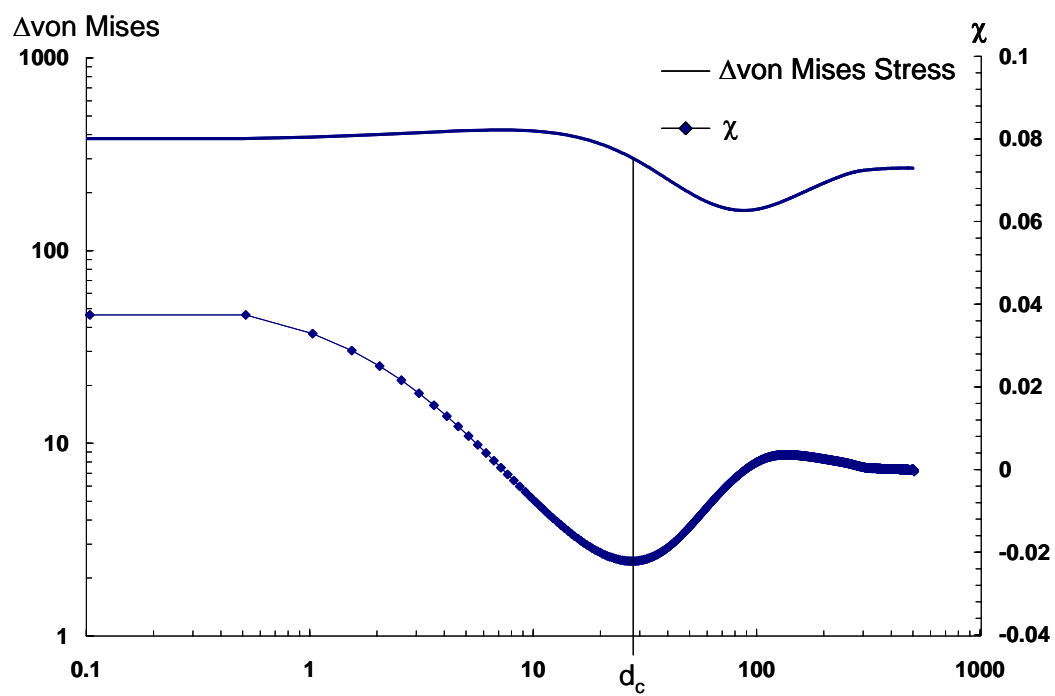Figure 64. Typical Trend of χ for 50.8 mm Radius Cylindrical Pad

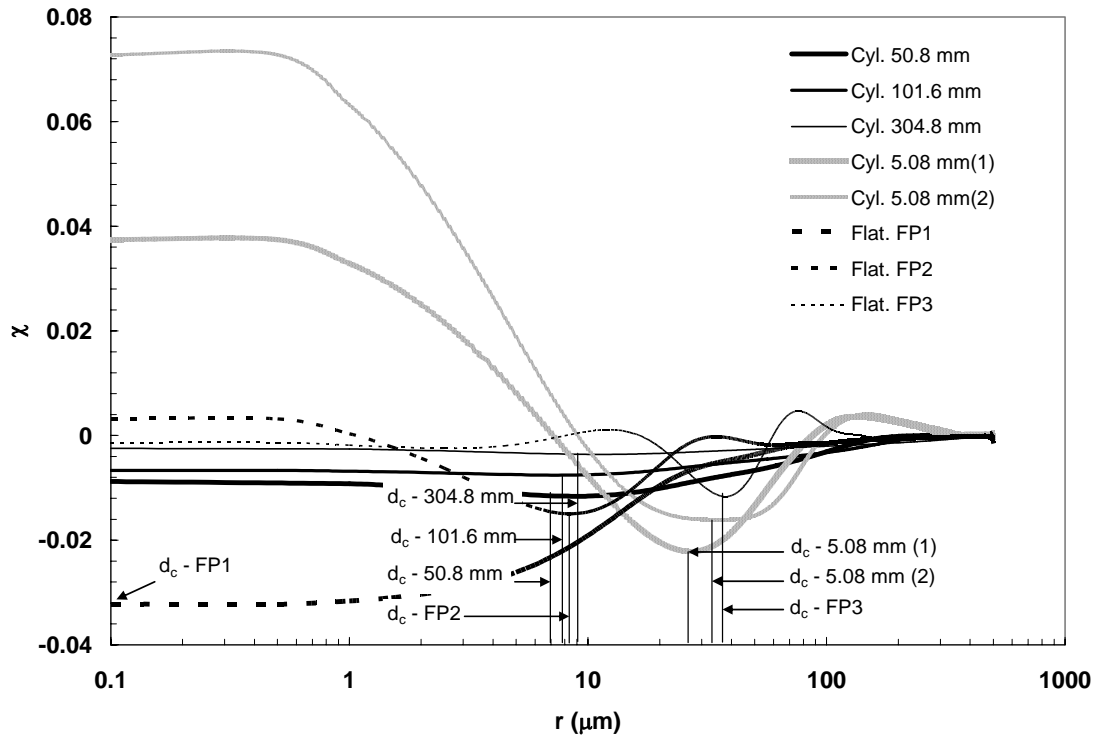Figure 65. Typical Trend of χ for 5.08 mm Radius Cylindrical Pad

Figure 66. Typical Critical Distances for all Tested Pad Configurations using χ

6.3. Effective Strain Range Method

In general, the strain-fatigue life approach has been commonly used for the elastic-plastic fatigue problem due to its capability to measure the large plastic deformation effects on fatigue life [36]. In this study, the total effective strain range, $\Delta\varepsilon_{effective}$, approach has been suggested as one method of finding effective critical distances, d_c, under the fretting fatigue condition. The formula of the total effective strain, $\varepsilon_{effective}$, can be found in the equation (55). While, in the effective stress range methods, i.e. the von Mises stress range method and relative stress gradient method, were utilized the von Mises stress range values to find the effective critical distance, in the effective strain range method, the effective strain range, $\Delta\varepsilon_{effecitive}$, is utilized to determine the effective critical distance.

133

In this effective strain range method, the crack initiation locations were determined by the maximum value of $\Delta\varepsilon_{effecitive}$ on the contact surface. The crack orientations in this approach were assumed to be -45° where the negative angle was measured in the clockwise direction from the perpendicular to the direction of the applied axial stress. This is because the effective strain range values are independent to the orientation angle. In previous works, the experimentally observed primary crack orientations angles were either –45° or 45° with a variation of ±15° from the perpendicular to the direction of the applied loading [10]. For this reason, -45° has been used for the crack orientation. The effective critical distance was determined at the location of a minimum value of $\Delta\varepsilon_{effective}$ along the critical plane. In order to find effective critical distance, a process similar to the von Mises stress range method was utilized; the first and second derivatives of the effective strain range curves were calculated to find minimum value.

Figure 67 demonstrates the typical curves of total effective strain and its derivatives which were used to determine the effective critical distance in the relative strain gradient method. This figure was plotted for one of the elastic fretting conditions, i.e. the 50.0 mm radius cylindrical pad case. Figure 68 shows the variation of the effective strain and calculated effective critical distances for the pad configuration involving elastic-plastic deformation, i.e. 5.08 mm radius cylindrical pad with 1779 N normal load. From the comparison between pad configurations involving elastic and elastic-plastic deformations, it is seen that a longer effective critical distance was determined under the elastic fretting condition than under the elastic-plastic fretting condition. This result is similar to the result from the von Mises stress range method in Figures 60 and 61.
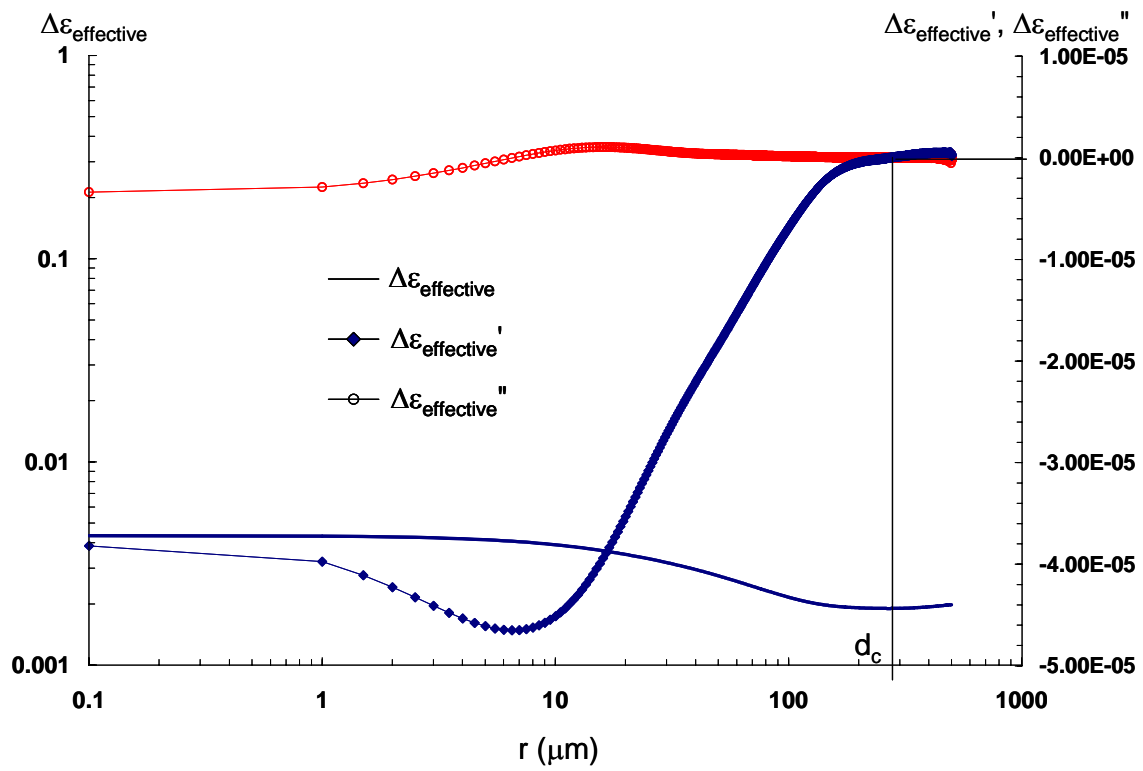
Figure 67. Typical Trend of $\Delta\varepsilon_{\text{effective}}$ for 50.8 mm Radius Cylindrical Pad
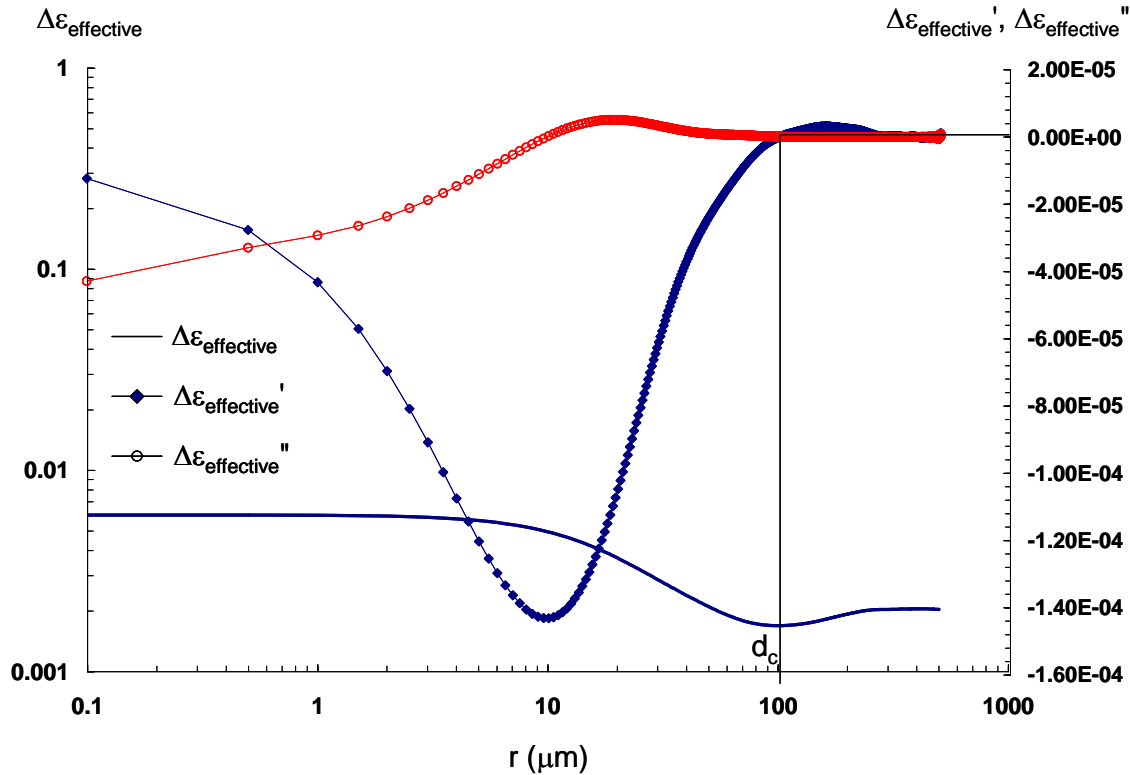
Figure 68. Typical Trend of $\Delta\varepsilon_{effective}$ for 5.08 mm Radius Cylindrical Pad

Figure 69 shows all of the effective strain range, $\Delta\varepsilon_{effective}$, curves for the entire pad geometries under the same loading conditions while Figure 70 shows the results of pad configurations involving elastic deformation only. From the figure, it can be noted that the $\Delta\varepsilon_{effective}$ curves resulting from the elastic fretting fatigue conditions (three cylindrical pads with radii of 50.8 mm, 101.6 mm, 304.8 mm and two flat pad type 1 (FP1), type 2 (FP2)) were similar to the Δvon Mises curves shown in Figure 62. This is because these geometries of pads were deformed in the elastic zone only and, therefore, the variations of the effective strains and von Mises stress are similar to each other. However, for the pad configurations involving elastic-plastic deformations (two cylindrical pads with radii of 5.08 mm and flat pad type 3 (FP3)), differing variations were found between effective stress curves and von Mises stress curves. In the contact surface, the pad configurations involving elastic-plastic deformation show greater

effective strain range, $\Delta\varepsilon_{effective}$, values than do the pad configurations involving elastic-plastic deformations.

However, the main difference between effective strain range method and von Mises stress range method is the orientation of the critical plain. The effective strain range approach uses -45° for all of the tested pad configurations while the von Mises stress range method calculates critical plane orientation using contact surface stresses. The effects of those different crack orientations will be presented with the test data in the next chapter.
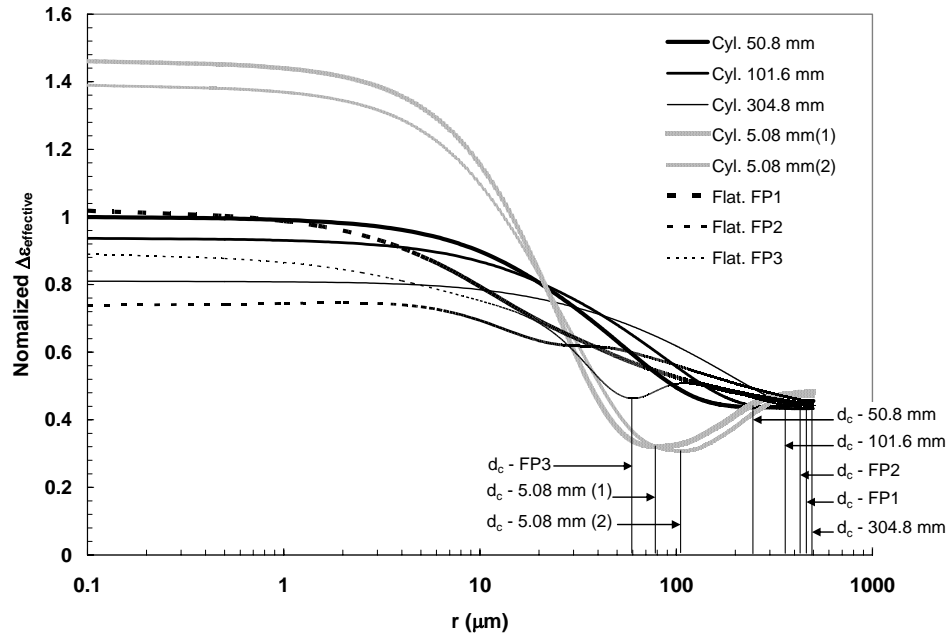
Figure 69. Typical Effective Critical Distances using Effective Strain Range Method for all Tested Pad Configurations; Effective Strain Range values was normalized by using 50.8 mm radius pad data
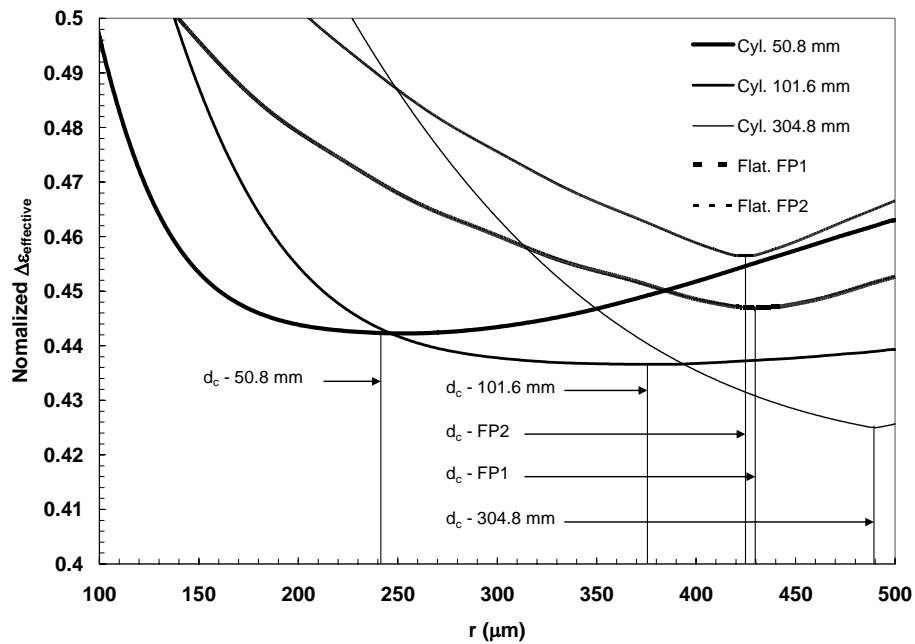

Figure 70. Typical Effective Critical Distances using Effective Strain Range Method for Tested Pad Configurations Involving Elastic Deformation; Effective Strain Range values was normalized by using 50.8 mm radius pad data

VII. Results of the Application of the Critical Distance Approach

In Chapter VI, the four critical distance methods were proposed and demonstrated as different approaches to determine effective critical distances, i.e. the arbitrary critical distance method, the effective stress range methods (von Mises stress range and relative stress gradient method) and the effective strain range method. In this chapter, these methods will be validated through a comparison with results obtained from MSSR and SMSSR parameters. The validation will be principally accomplished by considering the size of scatter bands obtained from MSSR and SMSSR along with critical distance methods. The MSSR and SMSSR parametric values will be calculated in two ways, i.e. averaged value up to the effective critical distance and as the end point value at the effective critical distance on the critical plane.

7.1. Results of the Arbitrary Critical Distance Method

The arbitrary critical distance method will be evaluated for all pad geometries tested in this study. As mentioned previously, in this method, the crack initiation location and orientation are determined using a method similar to that which was used in the MSSR parametric approach on the contact surface by Namjoshi et al. [10]. The arbitrary critical distances were applied from 50 to 500 μm. As an example, Figures 71 and 72 show the result of the MSSR parameter at the critical distance $d_c = 100$ μm for all pad geometries tested in this study. While Figure 71 shows the averaged values of MSSR, Figure 72 shows the end point values of same parameter at $d_c = 100$ μm. As shown in Figure 71, the data points at $d_c = 100$ μm show a larger scatter band than do those using contact surface stresses in Figure 52. This expanded scatter band is mainly caused by the pad geometries involving elastic-plastic deformation (two 5.08 mm cylindrical pads and flat pad type 3 (FP3)) because these pad configurations generate lower values of MSSR

than those from the pad configurations involving elastic deformation (cylindrical pads with radii of 50.8 mm, 101.6 mm and 304.8 mm). These differences in results between elastic and elastic-plastic fretting conditions at critical distance d_c = 100 μm are caused by the different magnitude of maximum normal stresses, σ_{xx}, resulting from pad configurations involving elastic and elastic-plastic deformation at the same distance. As shown in Appendix C, the various pad configurations had different peak normal stress, σ_{xx}, and also produce a different rate of decrease near the contact surface. In the notch problem, the peak stress is dependent on the radius of notch roots. A small radius generates higher peak stress. This greater peak stress also has faster decrease of stress than lower peak stress condition from the notch root. The similar phenomenon can be seen under the fretting fatigue condition. In the fretting fatigue problem, the rates of different stress gradients are dependent on the geometries of pads. In general, the cylindrical pads with smaller radius generate the higher peak stress on the trailing edge than those with larger radius. Furthermore, the cylindrical pads with smaller radius frequently produce the elastic-plastic deformation on the contact area. Therefore, the pad geometries involving large elastic-plastic deformation have higher peak stresses on the surface than that in the pad configurations involving elastic deformation. For this reason, the elastic-plastic fretting fatigue condition shows greater rate of decrease of normal stress values than does the elastic fretting fatigue condition at the same distance. Since the MSSR parameter includes normal stress as one factor in the formulation, the pad configurations involving elastic-plastic deformation generate lower MSSR values than that from the pad configurations involving elastic deformation at d_c = 100 μm. Figure 72 shows the results of the end point values of the MSSR parameter at the d_c = 100 μm. From Figures 71 and 72, it can be seen that the 5.08 mm radius cylindrical pads, i.e. Cyl. 5.08 mm (1) and Cyl. 5.08 mm (2), show relatively greater difference between the averaged and end point values of MSSR than that from other pads. However, for the flat

140

pad type 3 (FP3), the averaged and end point values of MSSR show almost the same results. This is because the 5.08 mm radius cylindrical pads have a larger elastic-plastic zone size than does flat pad type 3 (FP3). Within the plastic zone, the rate of decrease of the normal stress, σ_{xx}, is greater than within the elastic zone. Therefore, the 5.08 mm radius cylindrical pads produce smaller end point values than those from flat pads.

Appendix F illustrates the averaged values of the MSSR parameter as the critical distances increase from 50 to 500 μm. From these figures in Appendix F, it is seen that the scatter band using arbitrary critical distance is bigger than the contact surface result even at a small critical distance, i.e. d_c = 50 μm. This is because the averaged MSSR of three cylindrical pad with radii of 50.8 mm, 101.6 mm and 304.8 mm maintain nearly the same values, while two 5.08 mm radius cylindrical pads and flat pad type 2 (FP2), type 3 (FP3) show more decreased values than the result at d_c = 0 μm. Although the averaged MSSR values from the two 5.08 mm radius cylindrical pads and flat pad type 2 (FP2), type 3 (FP3) show decreased values within the short length of the critical distance, i.e. d_c = 50 μm, these values remain fairly constant as the critical distance is increased to a relatively long distance from d_c = 100 μm to 500 μm. However, the data points from the cylindrical pads with radii of 50.8 mm, 101.6 mm and 304.8 mm are continuously decreasing as the critical distance increases up to 500 μm. These two different features of rate of decrease generate the smaller scatter band as increasing the critical distance between average MSSR values from those pad configurations. However, even at d_c = 500 μm, the averaged MSSR values show a greater scatter band than do contact surface results in Figure 52 due to the data points from flat pad type 1 (FP1).

Appendix G illustrates end point MSSR values at various critical distances from 50 to 500 μm. For the end point value, the difference between the cylindrical pads with radii of 50.8 mm, 101.6 mm, 304.8 mm cases, two of 5.08 mm cylindrical pads and flat pads type 2 (FP2) and type 3 (FP3) is greater than the averaged values. As was

mentioned before, this increased difference is due to the different stress gradients between pad geometries. From the figures in Appendix G, it can be seen that the scatter band is narrowed as similar to those from the averaged values, as the critical distance is increased. At d_c = 500 μm, the smallest scatter band of the end point MSSR parameter is also found. However, even at d_c = 500 μm, the end point MSSR values also show a greater scatter band than do contact surface results in Figure 52. The difference between averaged and endpoint MSSR values at d_c = 500 μm is however negligible.

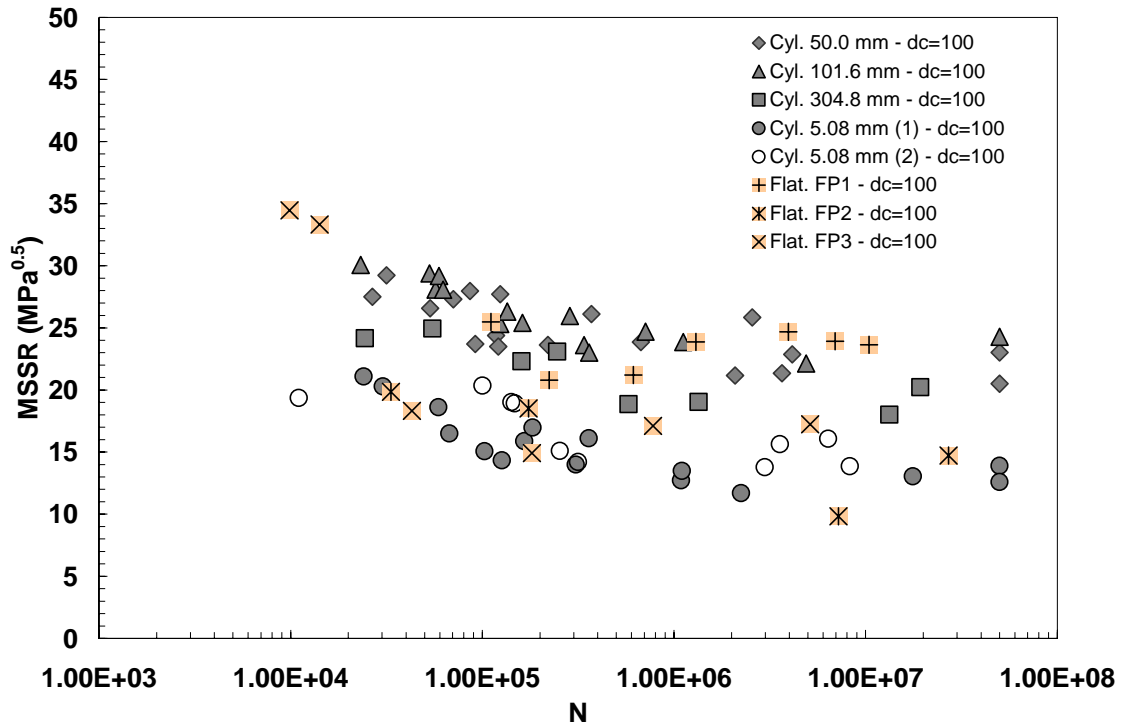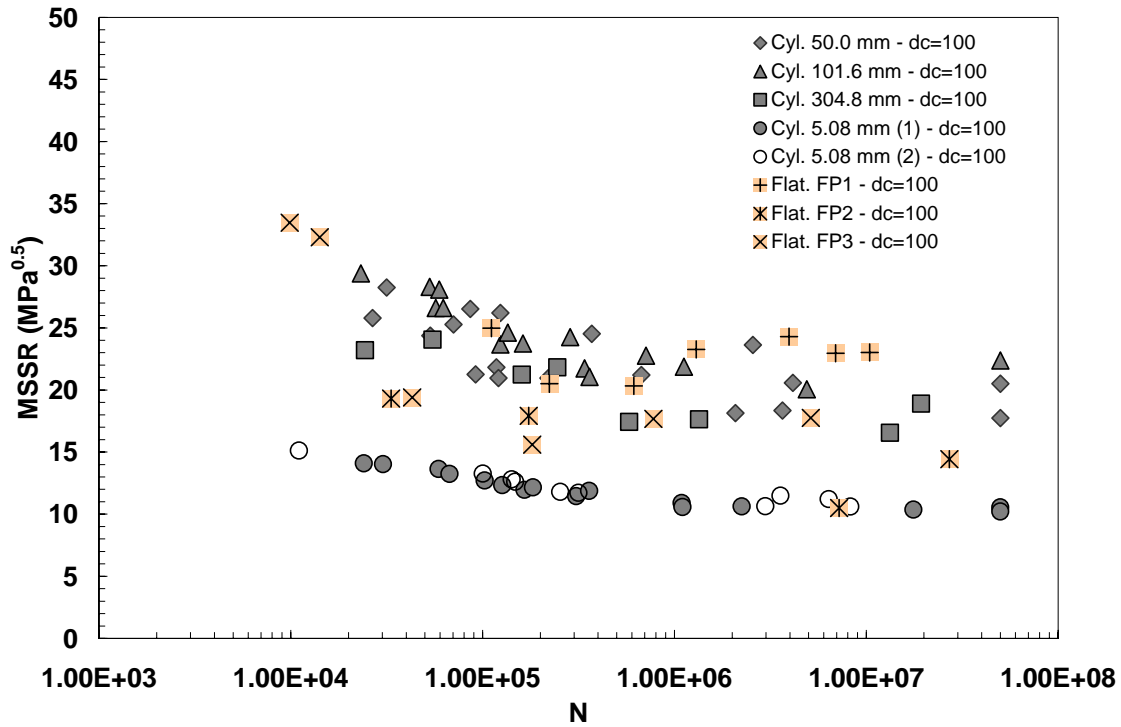Figure 71. Averaged Value of MSSR at d_c = 100 μm

Figure 72. Point Value of MSSR at $d_c = 100$ μm

The same arbitrary critical distance method is utilized to evaluate the SMSSR on the test data including elastic and elastic-plastic fretting fatigue conditions. Figure 73 shows the averaged value of the SMSSR at the critical distance $d_c = 100$ μm. From Figure 73, it is seen that the data points from five cylindrical pads fall within a narrow scatter band. As mentioned previously, the two 5.08 mm radius cylindrical pads produced large plastic deformations while cylindrical pads with radii of 50.8 mm and 101.6 mm did not. As shown in Figure 52, which was calculated using contact surface stresses, the same pad configurations showed the separated data points between cylindrical pads with radii of 50.8 mm, 101.6 mm and 5.08 mm. From these improved results for the cylindrical pads with radii of 50.8 mm, 101.6 mm and 5.08 mm in Figure 73, the arbitrary critical distance could be regarded as a feasible approach to generate a narrow scatter band between data points from elastic and elastic-plastic fretting

conditions. However, the scatter range from all data points is still too wide to establish the equivalence between all tested pad configurations including cylindrical and flat pads tested in this study. Figure 74 shows the end point values of the SMSSR at the same critical distance, i.e. $d_c = 100$ μm. The result shows the scatter between the 304.8 mm radius cylindrical pad and that of the other pad geometries is smaller than the averaged values of Figure 73. However, similar to the averaged values in Figure 73, the global scatter range from all data points is still too wide to establish the equivalence among all tested pad configurations due to the result from 304.8 mm radius cylindrical pad and flat pads.

Appendices H and I illustrate the result of SMSSR parameter using the different values of arbitrary critical distances ranging from 20 μm to 500 μm. Appendix H shows the averaged SMSSR, while Appendix I illustrates the point values of SMSSR. From Appendix H, it is seen that the averaged values of SMSSR have better equivalence as the critical distance increases. Similar results were found in the point values of SMSSR as shown in Appendix I. From the figures in Appendices H and I, it can be seen that only small differences exist between averaged and point values of SMSSR parameter at the relatively long critical distance, i.e. $d_c = 500$ μm.

From the above comparison of the MSSR and SMSSR results, it is to be noted that better equivalent data were found on the contact surface values of MSSR whereas, for the SMSSR parameter, better equivalent results were found by increasing the critical distance. However, once the arbitrary critical distances are applied, both MSSR and SMSSR show better equivalent data points at the longer critical distance. Although, from the application of the arbitrary critical distance method, a smaller scatter band is observed as the critical distance increases, the scatter bands from MSSR and SMSSR parameters did not show equivalence among all test data (i.e. from all pad geometries) even at a long critical distance, i.e. 500 μm. Therefore, different critical distance methods from the

observation of the stress/strain distributions along the critical plane would be more efficient approaches as will be discussed in following sections.
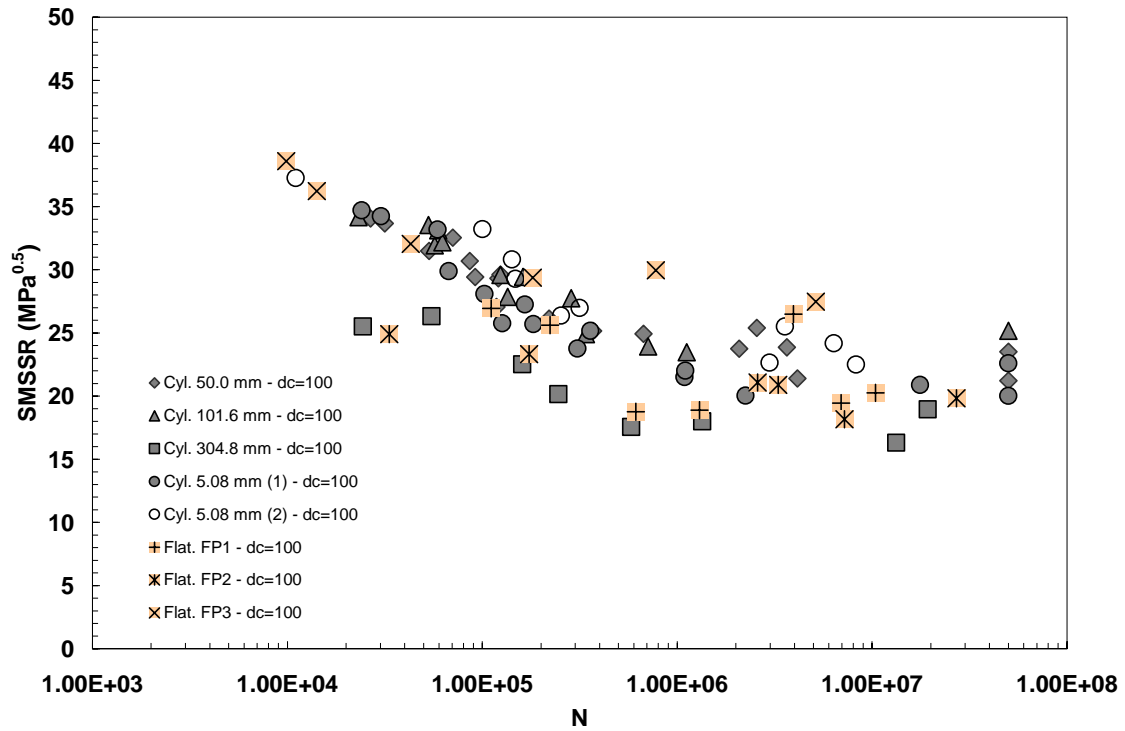

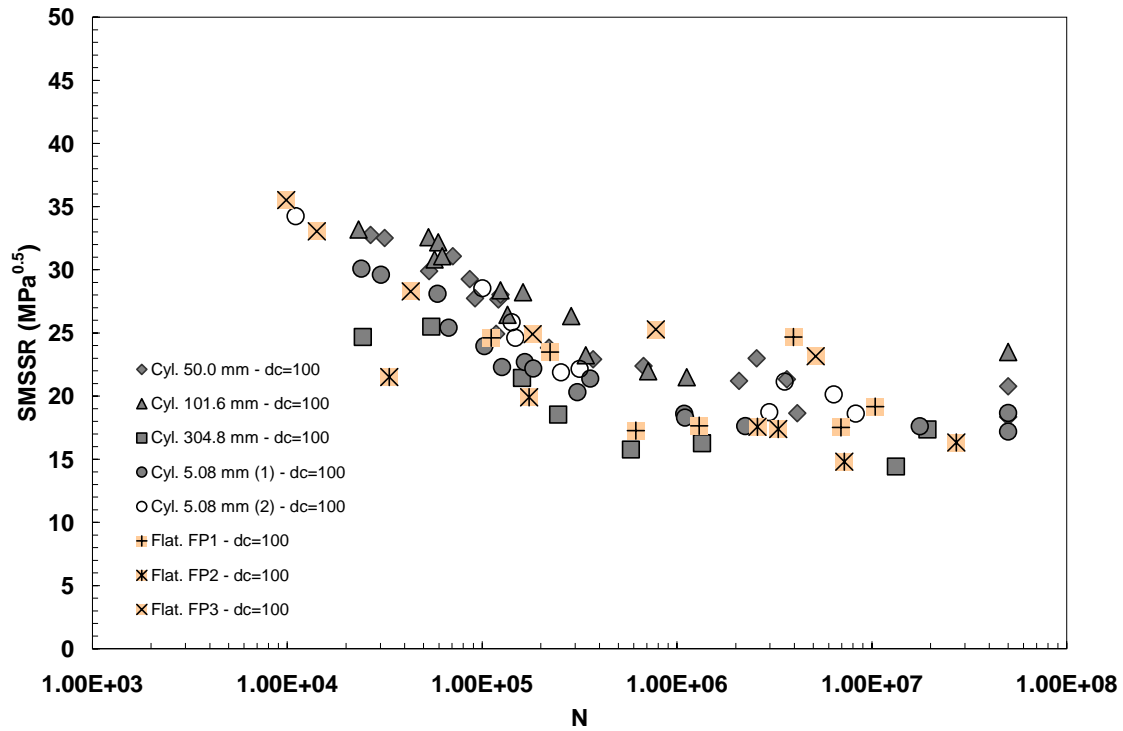Figure 73. Averaged SMSSR at $d_c = 100$ μm

Figure 74. End Point SMSSR at $d_c = 100$ μm

7.2. Results of the Effective Stress Range Method

In order to determine the critical distance that can account for the stress distribution near the contact surface, the variation in the effective stress range (i.e. von Mises stress range) will be evaluated. Once the effective stress range has been calculated, two different methods will be utilized: the von Mises stress range method and the modified relative stress gradient method. The results from these applications will be discussed for the MSSR and SMSSR parameters seperately.

7.2.1. Results of the von Mises Stress Range Method

The von Mises stress range, ΔV, method has been evaluated to determine its potential as a criterion for fretting fatigue analysis. In this approach, the method to find crack initiation and orientation is similar to that which was used in the MSSR parametric approach on the contact surface by Namjoshi et al. [10]. In order to predict the crack initiation location and angle, the shear stress range, $\Delta\tau_{critical}$, values from FEA were utilized. The information of the crack initiation location and orientation were also utilized to determine the critical plane. The crack initiation location was used as an origin of the critical plane while the crack orientation was used as an inclination of the critical plane. Once the critical plane was determined, the variation of the von Mises stress range, ΔV, was calculated along the critical plane. This procedure was conducted for each pad configuration under various applied loading conditions which have been measured from the experimental works. Therefore, the calculated von Mises stress ranges, Δvon Mises, curves are dependent on the pad configurations and applied loading conditions.

In the von Mises stress range method, the effective critical distances is determined by measuring the location that has the minimum value of the von Mises range, Δvon Mises. Due to the difference among the von Mises range curves under various loading conditions, the effective critical distances varied by the pad configurations and applied loading conditions. Figure 75 shows the calculated critical distances versus number of cycles to failure for all pad configurations tested in this study. As shown in Figure 75, most of the critical distances increase as the number of cycles to failure increase. If only the cylindrical pad configurations involving elastic deformation (three cylindrical pads with radii of 50.8, 101.6 and 304.8 mm) are considered, it can be noted that the critical distances decreased as the Hertzian peak pressure increased. Further, the scatter ranges

of effective critical distances among these cylindrical pad configurations narrowed in the high cycle fatigue regime. In other words, small differences of effective critical distances are found at the lower applied loading level. This is because the lower levels of the applied loads lead to the smaller decrease of the stress value for the cylindrical pad configurations involving elastic deformation. Further, the smaller gradient of stress values caused the longer effective critical distance that was measured from the origin to the location of the minimum value of von Mises stress. However, for the higher levels of the applied loading conditions, as in low cycle fatigue regime, the minimum value of von Mises stress range, Δvon Mises, was observed at the shorter distance from the contact surface. The two cylindrical pad configurations involving plastic deformation (5.08 mm radius cylindrical pads with different normal loads) also show similar features to cylindrical pads involving elastic deformation. If distance between elastic and elastic-plastic fretting fatigue are compared, the effective critical distances of pad configurations involving elastic-plastic deformation have shorter critical distance than the pad configurations involving elastic deformation. This is because the two 5.08 mm cylindrical pads have higher Hertzian peak stress on the contact surface than elastic deformation pad configurations and generate faster decrease of stress.

In the flat pad configurations (type 1 (FP1), type 2 (FP2) and type 3 (FP3)), the calculated effective critical distances also increased as the number of cycles to failure increased. However, the flat pads show that a big variation in effective critical distance from low to high fatigue life regime. Further, data points from these geometries did not follow the order of Hertzian peak pressure. As an example, one of the flat pad cases, type 2 (FP2) was expected to have the longest effective critical distance since it has the lowest Hertzian peak pressure among the tested pad configurations. However, the result shows that the FP2 has a shorter critical distance than the two 5.08 mm cylindrical pads, which have the highest Hertzian peak pressure. There are two possible explanations for this

result. First, in flat pad cases, the predicted crack initiation orientations were different than the cylindrical pad configurations. In cylindrical pad the crack angles were determined as -45±2° while, in flat pad configurations, the crack angles were calculated as -45±11°. Further, some of flat pad conditions had the positive angles instead of negative angles for the critical plane. Two factors may have contributed to these predictions of the crack initiation angles for flat pad configurations. First, the highly intensive small region of stress concentration at the end of flat pads may have played a role in these grater variations on the predicted crack initiation angles of flat pad configurations. Second, the narrow and wide shapes of the stress distributions near the contact surface could also be the reason that increased variations of the predicted crack initiation angles of flat pad configurations than variations from the cylindrical pad configurations.

Among the flat pad configurations, the flat pad type 3 (FP3) configuration involving elastic-plastic deformations shows the greatest variations of the effective critical distances. This is because the flat pad type 3 (FP3) has greater Hertzian peak pressure than the other flat pads (flat pad type 1 (FP1) and type 2 (FP2)). From effective critical distances resulting from flat pad geometries, it can be concluded that the increased Hertzian peak pressure induces bigger elastic-plastic deformation and thereby produces increased fluctuation of the effective critical distances.
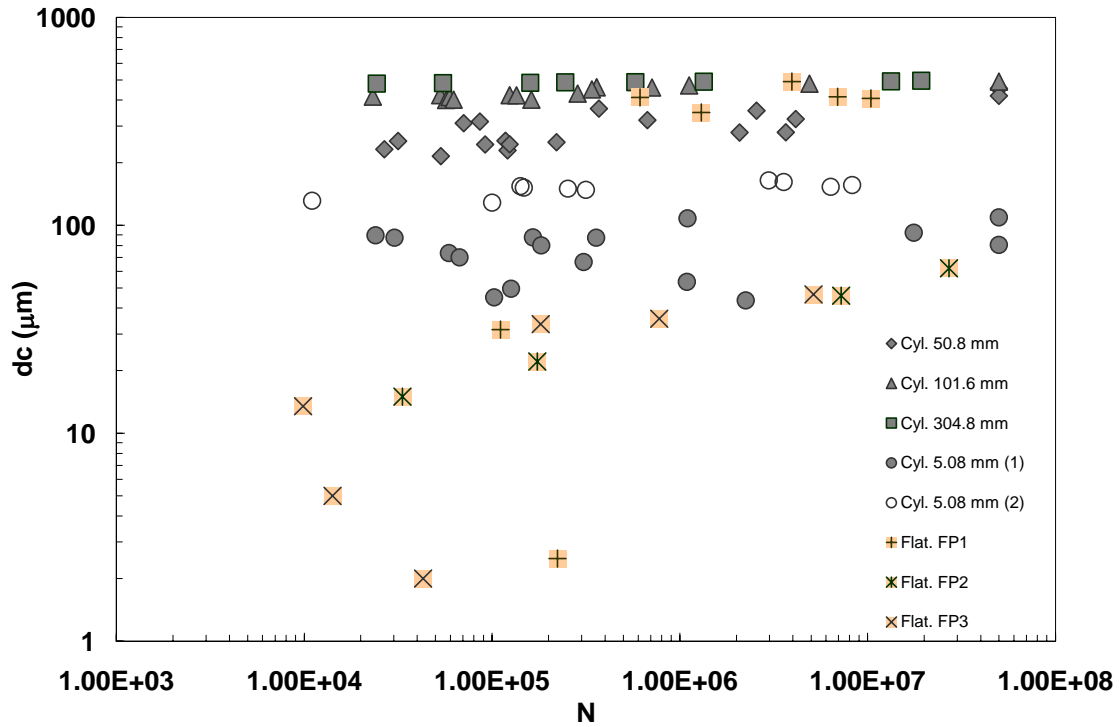
Figure 75. Effective Critical Distances (d_c) using von Mises Stress Range Method

Figure 76 shows the result of MSSR parameter based on the von Mises stress range method. The MSSR values were calculated using averaged stress along the critical plane up to the effective critical distances as given in Figure 75. From the figure, it can be noted that the result of the averaged MSSR using von Mises stress range method has a wider scatter range than does the result using only contact surface stresses in Figure 52. This wider scatter band is due to difference in results among cylindrical pads configurations after applying the von Mises stress range method. As shown in Figures 76 and 52, the data points from two 5.08 mm radius cylindrical pads have shown much lower values than those from same pad configurations using contact surface stresses. However, the cylindrical pads with radii of 50.8, 101.6 and 304.8 mm show almost the same values as the surface result. As mentioned previously, the two 5.08 radius cylindrical pads involved elastic-plastic deformation while the cylindrical pads with radii

of 50.8, 101.6 and 304.8 mm had elastic deformation only. Therefore, the differing stress gradients from elastic and elastic-plastic fretting fatigue conditions cause the increased scatter range in the von Mises stress range method.

The MSSR formula contains the maximum normal stress, σ_{max}, as the one of factors. In general, the σ_{max} values decrease as the critical distance from the surface increases. The amount of this decrease is dependent on the Hertzian peak pressure on the contact surface. As mentioned previously, the larger Hertzian peak pressure produces faster decrease of stress from the contact surface. The pad configurations involving elastic-plastic conditions (two 5.08 mm radius cylindrical pads) have shown higher Hertzian peak pressure than pad configurations involving elastic deformations (pad configurations with radii of 50.8 mm, 101.6 mm and 304.8 mm). Therefore, the values of the MSSR from pad configurations involving elastic-plastic deformations have shown smaller values than MSSR values from pad configurations involving elastic deformations.

For flat pad cases, these decreases did not occur in a regular manner. The results of the flat pads using the von Mises stress range method had the wider scatter band than contact surface results as shown in Figure 52. The larger scatter band can be found from the flat pad type 3 (FP3) which involved the elastic-plastic deformation. These irregular variations of the MSSR on the flat pad cases are due to the irregular pattern of the critical distance which was determined by von Mises stress range method in Figure 75.

Figure 77 shows the end point values of the MSSR which have been calculated at the critical distance. From the figure, the result of the end point MSSR show larger scatter band than the result of the averaged MSSR between pad configurations involving elastic and elastic-plastic deformations as shown in Figure 76. The scatter band increases as the number of cycle to failure decreases. In general, a larger Hertzian peak stresses occurs in the low cycle fatigue regime than the high cycle fatigue regime. The higher

151

Hertzian peak stresses also generate larger differences between stresses calculated at the contact surface and at the certain depth from the surface. Therefore, the bigger differences were present between average and end point values in the low fatigue life regime.

However, flat pads (flat pad type 1 (FP1), type 2 (FP2) and type 3 (FP3)) show smaller differences between averaged and end point MSSR values. This is because the flat pads have relatively shorter critical distances than do cylindrical pads and thereby these small distances did not generate noticeable difference between averaged and end point values of MSSR parameter.
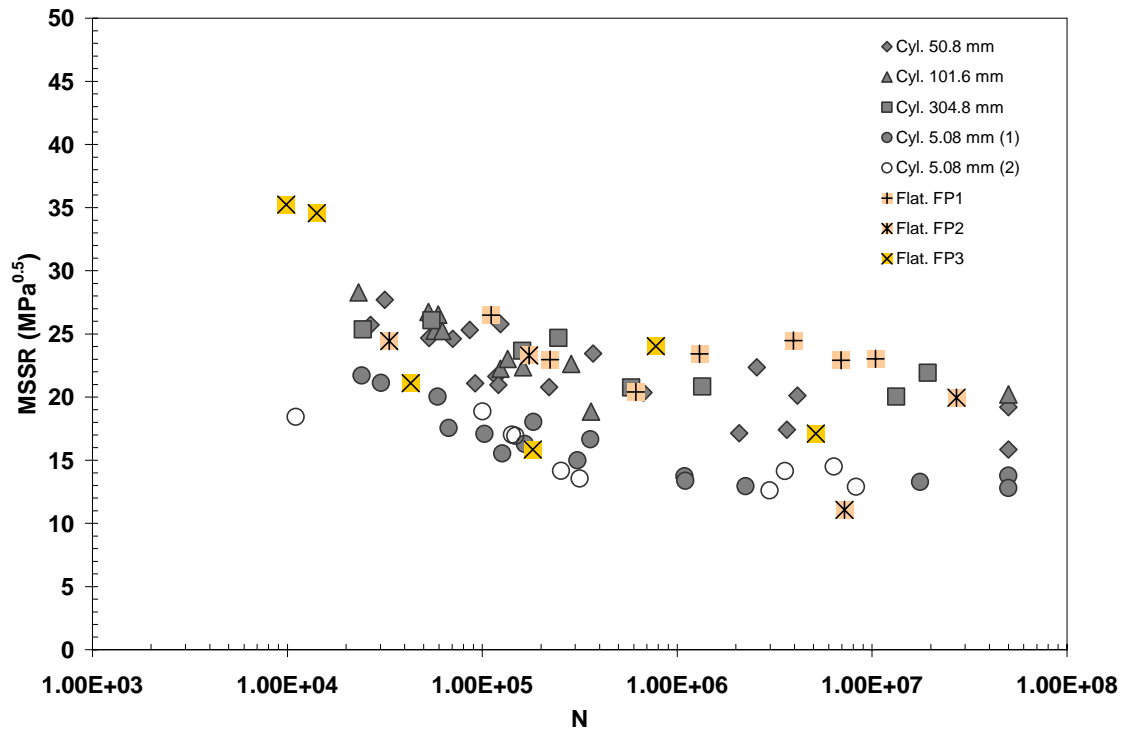
Figure 76. The Averaged MSSR Values at $d_c = \Delta$von Mises$_{min}$
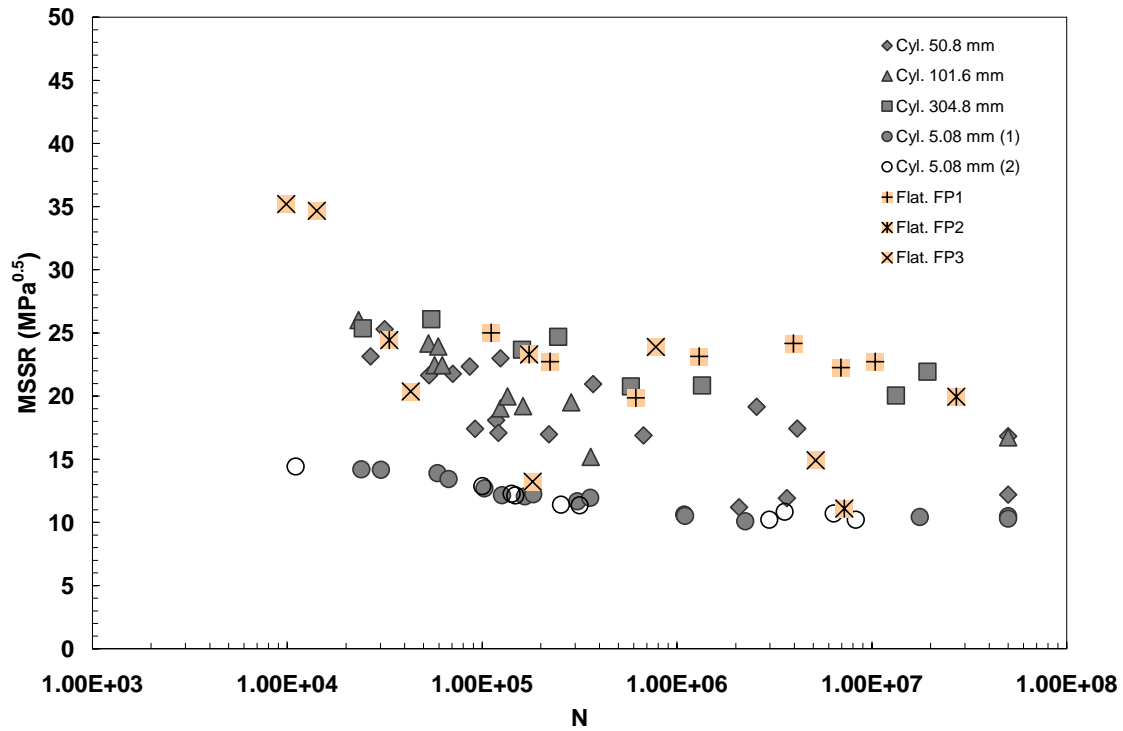
Figure 77. The End Point MSSR Values at $d_c = \Delta$von Mises$_{min}$

The critical distances calculated by von Mises stress range approach, in Figure 75, has been also utilized to compute the SMSSR parameter. Figures 78 and 79 show the results of the SMSSR parameter along the critical plane with these critical distances. Figure 78 have been plotted by the averaged value of MSSR while Figure 79 shows the end point values of the same parameter. As illustrated in Figure 54, the result of SMSSR parameter using contact surface stresses has shown the dependence on the pad configuration and wide scatter band, and it could not be used for establishing the equivalence between tested pad configurations. However, Figure 78, which is calculated using von Mises range method, shows smaller scatter band in comparison to the result using the contact surface stresses in Figure 54. Notably, the data from the cylindrical pads did appear to fall into a narrow scatter band, thus indicating that equivalence was established between the test data. In the SMSSR parameter, the normal stress range,

$\Delta\sigma_{normal}$, values have been utilized instead of the normal stress amplitude, σ_{max}, in MSSR parameter. This was done to account for the effects of the normal load on the critical plane at both maximum and minimum applied loading conditions. Figure 78 indicates that the dependency of the $\Delta\sigma_{normal}$ values on the pad configurations on the contact surface has decreased after applying the von Mises stress range method. From these collapsed data points in a narrow scatter band, it can be assumed that the critical distance determined by using von Mises stress range approach, in Figure 75, provide the proper approach for the cylindrical pad configurations involving both elastic and elastic-plastic deformations. As it has been seen from the result of the MSSR parameter in Figure 76, the critical distances resulting from von Mises stress range method, in Figure 75, acted to increase the scatter in the collapsed data points of MSSR parameter using contact surface stresses, in Figure 52. However, the same critical distances caused to improve the equivalence among SMSSR data points from the different pad configurations.

Although the critical distances resulting from von Mises stress range act to improve the equivalence data points among the cylindrical pad configurations, these critical distances were not very effective in the flat pad cases. A similar instability of the flat pad data points shows in the results of the SMSSR parameter. This means that the instability of the critical distance calculated from flat pad configurations has also affected the SMSSR parameter. Figure 79 shows the end point values of the SMSSR using the same critical distances. For the cylindrical pad configurations, results show a smaller scatter band than do the averaged SMSSR values in Figure 78. This result is due to the two 5.08 mm cylindrical pads involving elastic-plastic deformations. The end point SMSSR values of the two 5.08 mm cylindrical pads have shown decreased values as compared to the averaged value of same parameter and, therefore, data points from cylindrical pads fall into a narrower scatter band than do the averaged values. However, for the flat pads, an almost identical same scatter band to the averaged vales is seen and,

therefore, the equivalence among data points from all tested pad configurations was not achieved.

The results from the von Mises stress range method can be summarized as follows:

1. For cylindrical pads, the critical distance calculated by von Mises stress range method has shown the inverse relationship to the Hertzian peak pressure. However, for the flat pad, the relationship is not consistent.

2. The MSSR values, calculated using the von Mises stress range method, show wider scatter band than the results using contact surface stresses only when all tested pad geometries are considered.

3. The data points of cylindrical pads resulting from the SMSSR parameter using the von Mises stress range method show narrower scatter band than those using the contact surface stresses. However, the data from the flat pad configurations did not appear to collapse into a narrow scatter band. Therefore, the equivalence among all tested pad configurations could not been established using this approach. These results were caused by the inconsistent pattern of the predicted crack initiation angles of the flat pad conditions.
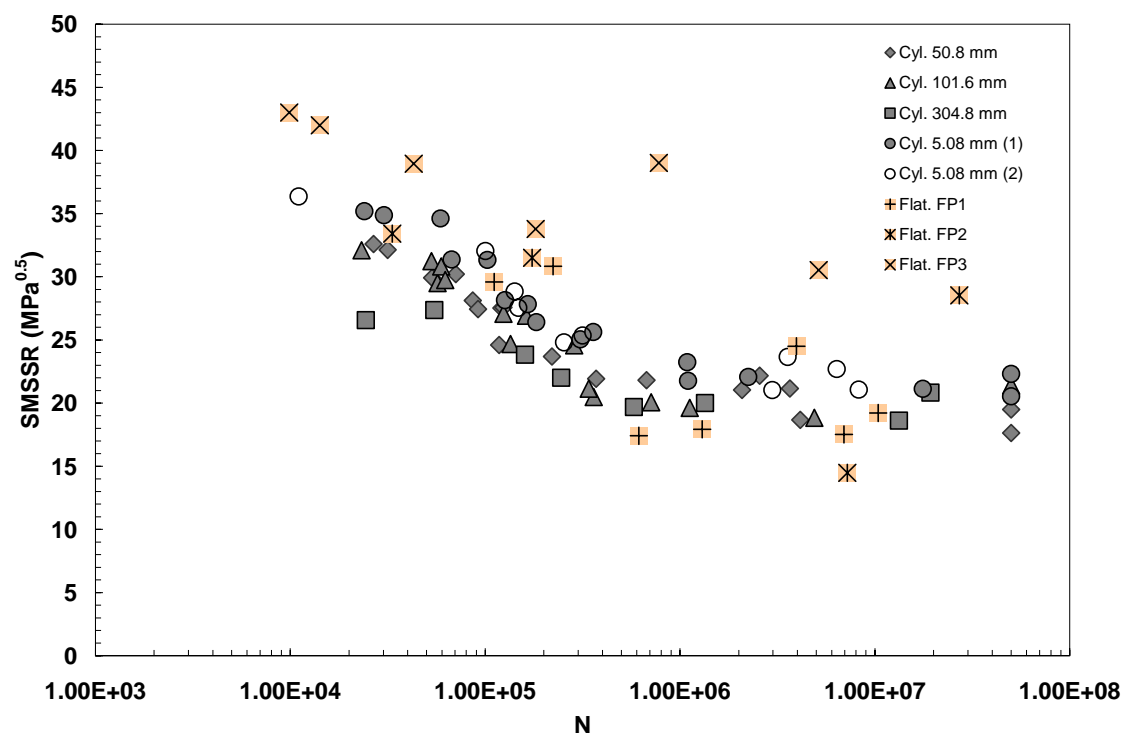
Figure 78. The Averaged result of SMSSR at d_c = min of Δvon Mises
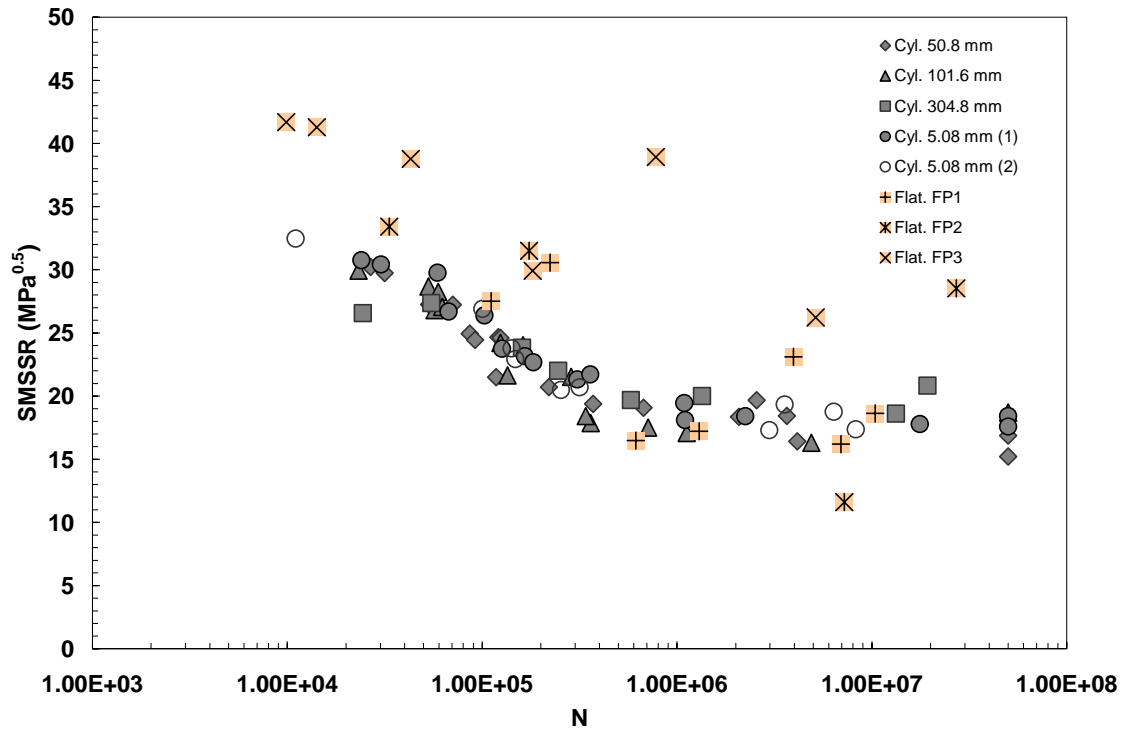
Figure 79. The End Point Result of the SMSSR at d_c = min of Δvon Mises

7.2.2. Results of the Relative Stress Gradient Method

Qylafku et al. [13] has applied the critical distance approach to the notch problem involving elastic-plastic deformation. Their efforts were concentrated on the analyzing the fatigue life of notch problem involving elastic-plastic deformation from elastic fatigue condition. In order to determine the effective critical distance, they used the relative stress gradient method. For measuring the stress gradient, they selected the normal stress, σ_{yy}, values along the critical plane since the loading condition of the notch is the one dimensional state. In this section, a similar approach will be attempted on the fretting fatigue condition with a little modification. The Δvon Mises values will be utilized instead of σ_{yy} values to measure the stress gradient due to the multi-axial stress state

condition of the fretting fatigue problem. In this approach, the crack initiation location and orientation were determined by using the same method with MSSR parametric approach on the contact surface by Namjoshi el al. [10]. After calculating $\Delta\tau_{critical}$ values for the all locations and angles under the contacted surface, the location and angle which generated maximum value of $\Delta\tau_{critical}$ was selected as a crack initiation location and orientation. Figure 80 shows the result of the calculated effective critical distances using relative stress gradient method for entire pad configurations included in this study. The critical distances were plotted against the number of cycle to failure, N, for all pad configurations tested in this study. As shown in Figure 80, the effective critical distances show decreased values as the number of cycle to failure increased. In other words, the critical distances were decreased as the size of plastic deformation zone was decreased. Similar results were found in Qylafku et al. [13]'s work. In the notch problem, shorter critical distances were also obtained as the size of plastic deformation decreased. All of the effective critical distances calculated by relative stress gradient method have smaller values than those from the von Mises stress range method in Figure 75. From the relative stress gradient method, the effective critical distances were determined where the slopes of stress curve are increased. For the elastic-plastic deformation conditions, these increases in slopes occurred at a certain distance from the crack initiation location. However for the elastic deformation condition, these slopes occurred near the contact surface.

In low cycle regime, two 5.08 mm cylindrical pads involving plastic deformations show longer critical distance than do other tested pad configurations. Also, longer critical distances occurred as the Hertzian peak pressure increased. However, these relationships did not exist at the high cycle fatigue regime. This is because the sizes of the plastic deformations were decreased in the high cycle fatigue regime for all cylindrical pad configurations.

For the flat pad cases, the variations in the effective critical distances were obtained as the number of cycle to failure increased. The similar irregular effective critical distances from flat pad configurations were seen in the effective critical distances calculated by von Mises stress range method in Figure 75. As mentioned previously, this is because the flat pads have shown the larger variation of the calculated angle of the critical planes than the cylindrical pad configurations.
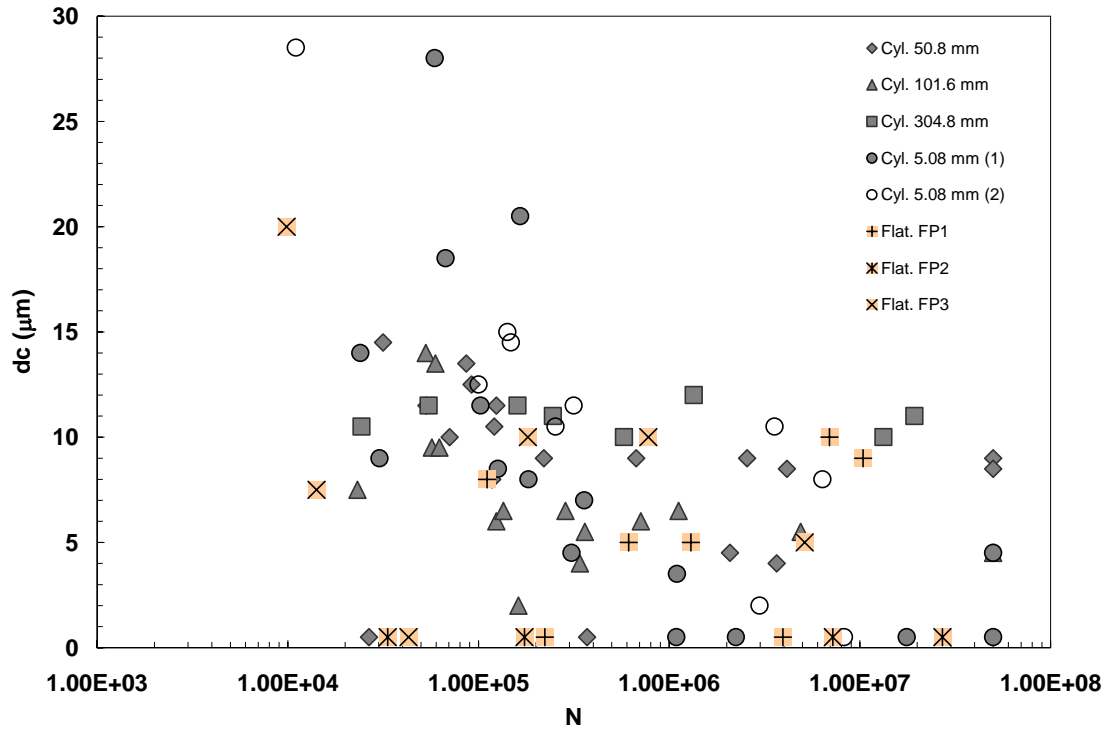

Figure 80. Effective Critical Distances using χ

Figure 81 illustrates the result of the MSSR parameter calculated by using effective critical distances from Figure 80. The values of the MSSR were calculated by using mean value of the stresses, i.e. $\Delta\tau_{cirtical}$ and σ_{max} along the critical plane up to the effective critical distance. As evident from the figure, the scatter band generated by

stress gradient approach is increased due to the large scatter band in the flat pad data points. The cylindrical pad configurations involving elastic deformation (cylindrical pads with radii of 50.8, 101.6 and 304.8 mm) have similar data points to those using contact surface stresses in Figure 52. However, the cylindrical pad configurations involving elastic-plastic deformation (two 5.08 mm radius cylindrical pad with different normal loads) show smaller values than those using the contact surface stresses. In cylindrical pad configurations involving elastic-plastic deformations, the greater decrease occurred at the lower cycle fatigue regime and thereby flatter data curves are seen than the results using the contact surface stresses. These differences depending on the number of cycle to failure were due to the longer critical distance at the low cycle fatigue regime than in the high cycle fatigue regime.

The flat pad configurations have shown greater variations than those from the cylindrical pads configurations. These wide scatter data points from the flat pad configurations increased the total scatter band of the MSSR values. These variations of the flat data point are due to the inconsistent variation of the critical distance of the flat pad cases. The similar phenomenon has been observed from the result of the MSSR parameter using the von Mises stress range method in Figure 76.

Figure 82 shows the end point value of the MSSR using same effective critical distance calculated by relative stress gradient method. From the figure, it can be seen that the increased scatter band for the cylindrical pad configurations than the averaged values of the MSSR in Figure 81. However, the flat pad cases show similar results with averaged results. This is because the short effective critical distances are calculated from flat pads than cylindrical pads and thus flat pads did not make distinct difference between averaged and end point values of MSSR parameter.
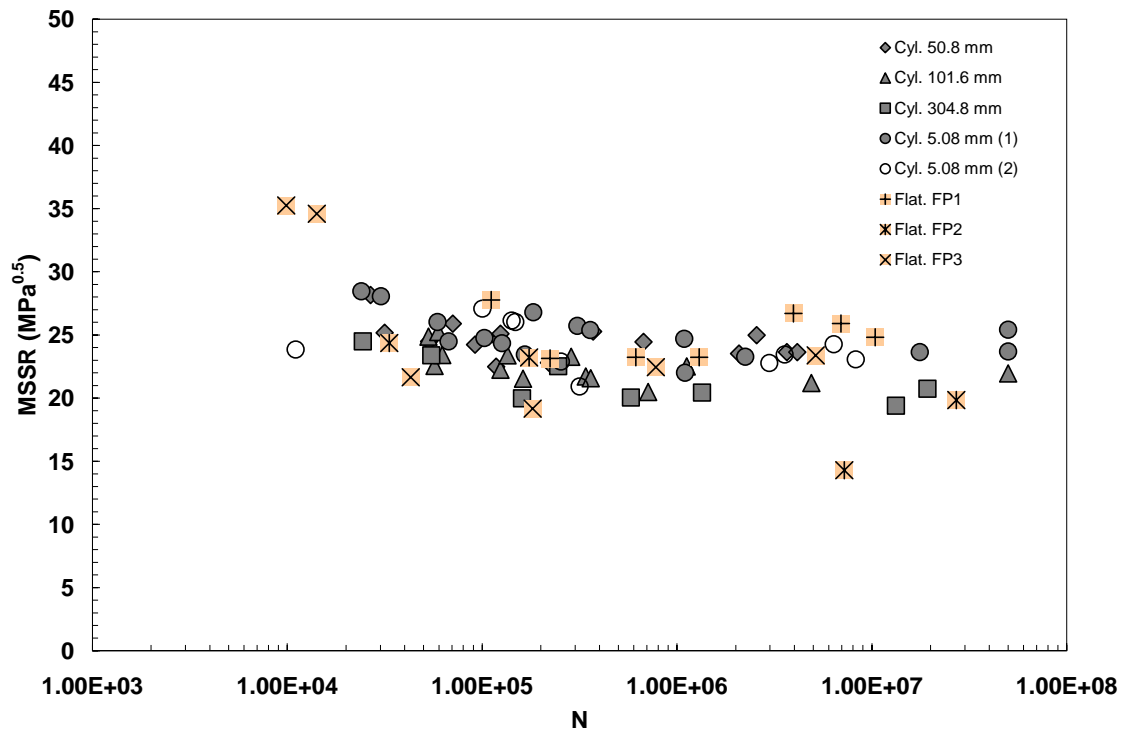
161

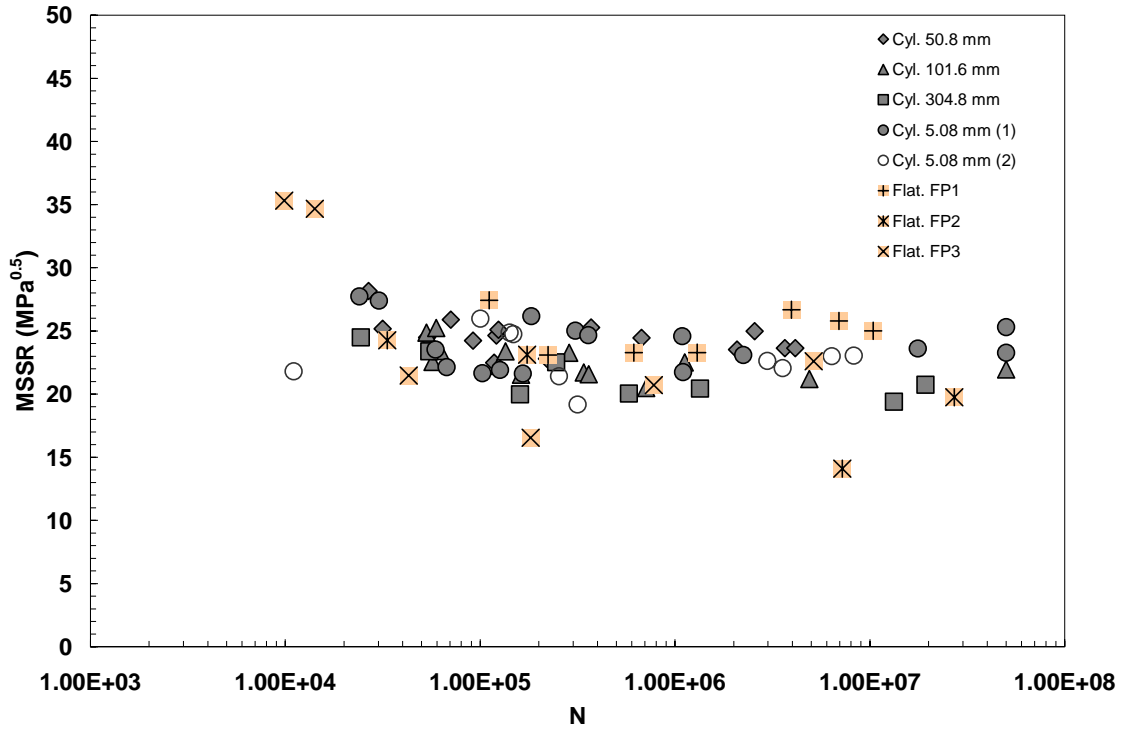Figure 81. The Averaged Result of MSSR at $d_c = \chi_{min}$

Figure 82. The End Point MSSR Values at $d_c = \chi_{min}$

Figure 83 shows the results of the SMSSR parameter using critical distance calculated by the relative stress gradient method. The figure shows the similar dependent phenomenon on the tested pad configurations as with the results using the contact surface stresses in Figure 52. This is because the short critical distances calculated from stress gradient approach do not improve the dependency of the results using contact surface stress as shown in Figure 52; thus only small changes occur for both results from cylindrical and flat pad configurations. Figure 84 shows the end points results of the SMSSR parameter using the same effective critical distances. As can be seen from Figures 83 and 84, the difference between the end point and averaged values of the SMSSR parameter is negligible. This similar behavior of the end points and averaged SMSSR parameter is due to the short lengths of the effective critical distances which were calculated from relative stress gradient method.

163

The results from stress gradient approach method can be summarized as follows:

1. The critical distances were decreased as the number of cycle to failure is increased. The shorter critical distances were calculated than those from by von Mises stress range method.

2. For the MSSR parameters, the difference in the flat pad data points acts to increase the scatter band than the result using the contact surface stresses.

3. The results from the SMSSR show similar dependency on pad configurations to those using the contact surface stresses.
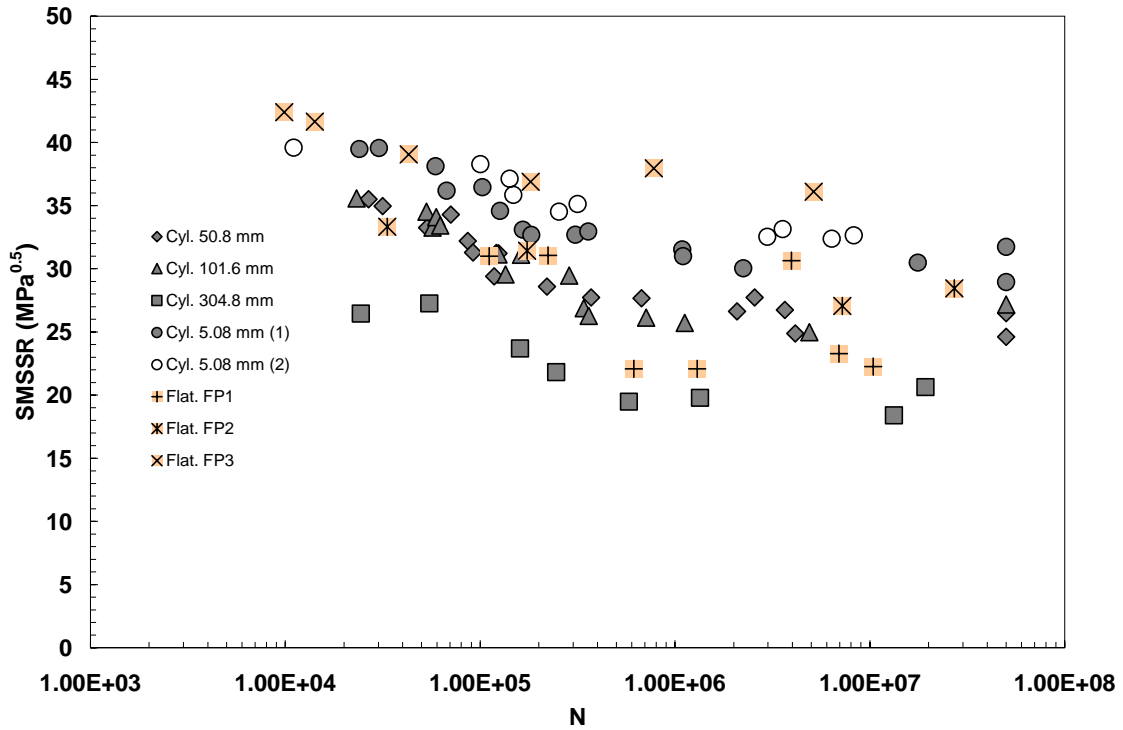
Figure 83. The Averaged SMSSR at d_c = min of χ
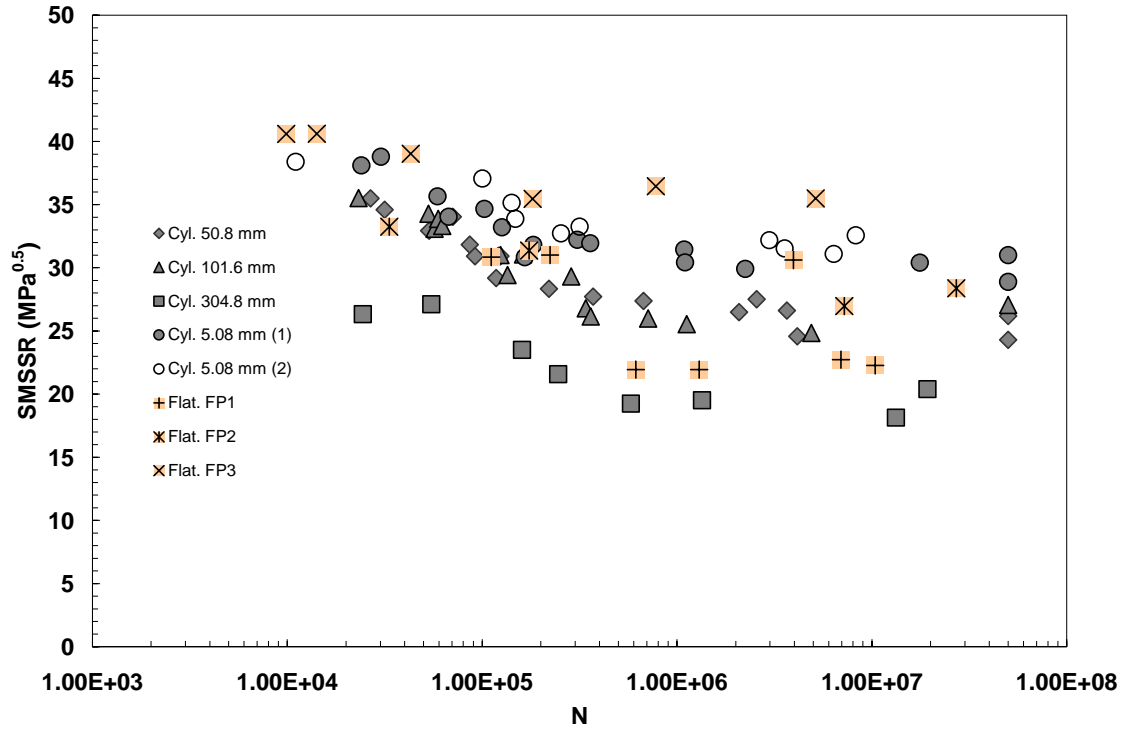
Figure 84. The End Point SMSSR at d_c = min of χ

7.3. Result of the Effective Strain Range Method

In the previous section, the two effective stress range methods, i.e. the von Mises stress range method and the relative stress gradient method, were utilized for the analysis of fretting fatigue. The results of the von Mises stress range method have shown that an equivalence could be established between the cylindrical pad configurations involving elastic and elastic-plastic deformations. However, for flat pad configurations, it has been shown that the data points did not appear to fall into a narrow scatter band, thus indicating that equivalence was not established. In the von Mises stress range approach, the critical plane angles were determined from the $\Delta\tau_{critical}$. Thereby, the different critical

plane orientations were obtained calculated for each pad configuration and applied loading condition. Further, from this method, a large variation in the critical plane angle was obtained for pad configurations of in this study. It is particularly notable that these variations caused a wide scatter band in flat pad cases. To reduce the large scatter band caused by the various angles of the flat pads, the effective strain range method was then evaluated in this study. In the effective strain range method, the crack initiation locations are determined by the maximum value of effective strain range, $\Delta\varepsilon_{effective}$, along the contact surface. Since the effective strain range values are independent of the angles, the crack initiation angles are assumed as -45° for entire pad configurations tested in this study. This is based on the experimental results from pad configurations included in the study. The experimentally observed primary crack orientations angles were either –45° or 45° with a variation of ±15° from a perpendicular to the loading direction [10]. By assuming the crack initiation angle as -45° for all pad configurations, it can be expected that the variation in calculated angles using stress distribution will be eliminated. Furthermore, this fixed crack initiation orientation can also reduce the fluctuation of the effective critical distances versus number of cycles to failure for all pad configurations.

As mentioned above, in the effective strain range method, the crack location was determined where the effective strain range has minimum value. This effective strain range criterion predicts the crack initiation location at the contact surface and near the trailing edge of contact. This is in agreement with the observation from experimental work [10]. Figure 85 shows the results of the effective critical distances determined by effective strain range method. The effective critical distances have been determined by the distance from the crack initiation location to the point where the minimum value of effective strain range, $\Delta\varepsilon_{effecitve}$, occurs along the critical plane. The result shows increased effective critical distances as the number of cycles to failure increases. This phenomenon is similar to the result shown by von Mises stress range method in Figure 75.

From the Figure 85, it can also be seen that the cylindrical pads have similar length of effective critical distances as those calculated by von Mises stress range method in Figure 75. For the cylindrical pads involving elastic deformations (cylindrical pads with radii of 50.8 mm, 101.6 mm and 304.8 mm), the effective critical distances decreased as the Hertzian peak pressure increased. Also the effective critical distances were decreased as the number of cycle to failure decreased. The small difference in the effective critical distances between cylindrical pads can be found in the high cycle fatigue regime. This is because the cylindrical pads with radii of 50.8 mm and 101.6 mm have more increase of effective critical distances than that in the 304.8 mm radius cylindrical pad cases as the number of cycles to failure increases. The cylindrical pad configurations involving elastic-plastic deformations (two 5.08 mm radius cylindrical pads with different loading conditions) have shorter critical distance than the cylindrical pad configurations involving elastic deformations (three cylindrical pads with radii of 50.8 mm, 101.6 mm and 304.8 mm). This is because two 5.08 mm radius cylindrical pads have higher Hertzian peak pressure than do cylindrical pad configurations involving elastic deformations.

While cylindrical pad configurations show similar results to those from the von Mises stress range method and effective strain range method, the effective critical distances from flat pads have shown different results between these two methods. The effective critical distances of flat pads from effective strain range method have shown stable increments in comparison to those using von Mises stress range method in Figure 75. The two flat pads (flat pad type 1 (FP1) and type 2 (FP2)) show similar critical distances as three cylindrical pads configurations (cylindrical pad with radii of 50.8, 101.6 and 304.8 mm). This is because the pad configurations mentioned above have elastic deformation, and therefore, relatively longer effective critical distances than have elastic-plastic fretting conditions.

The flat pad involving plastic deformations, flat pad type 3 (FP3), shows longer critical distance only in the high cycle fatigue regime. This is because, in this regime, the FP3 configurations produce elastic deformations due to the lower level of applied stresses. From Figure 85, it can be also noted that the large fluctuation of effective critical distances of the flat pad, which has been also shown in the results using the von Mises stress range method in Figure 75, improved by applying the effective strain range method. These improved results were due to removal in the variations of the critical plane orientations of the flat pad configurations.
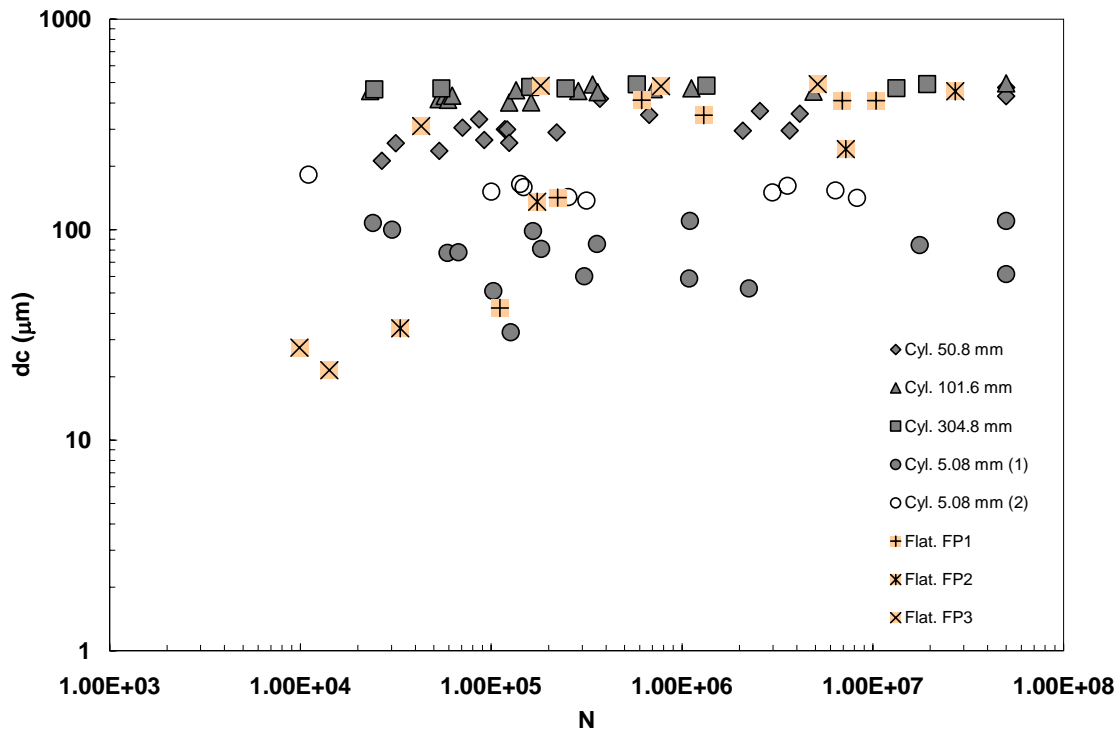
Figure 85. Effective Critical Distances using Effective Strain Range Method

Figure 86 shows the result of the MSSR parameter using critical distances determined by effective stress range method in Figure 85. The MSSR values were calculated using averaged stresses up to the given effective critical distances on the

critical plane. In Figure 86, a smaller scatter band can be seen than those from von Mises stress range method in Figure 76. Further, these improved results from effective strain range have been obtained over the entire fatigue life. This is because shorter effective critical distances have been calculated than those resulting from the von Mises stress range method for cylindrical pads involving elastic-plastic deformation (the two 5.08 mm radius cylindrical pads). However, cylindrical pads involving elastic deformation show almost the same results as are shown by the von Mises stress range method. As shown in Appendixes D and E, the von Mises stress range, Δvon Mises stress, and effective strain range, $\Delta\varepsilon_{effective}$, distributions near the contact surface show similar shapes for the pad configurations involving elastic deformations. However, for the pad configurations involving the elastic-plastic deformation conditions, both results have different distributions. These different stress distributions between pad configurations involving elastic versus elastic-plastic deformations lead to improve the equivalence between cylindrical pads with and without plastic deformation. Another reason for the smaller scatter band can be found from the data points of the flat pad configurations. The results of the flat pad configurations are much more stable than are the results from the von Mises stress range method in Figure 76. These increased stabilities resulting from the flat pad configurations also act to decrease the global scatter band. However, the result of the MSSR parameter using the effective strain method is dependent on the pad configurations involving elastic and elastic-plastic deformations and thereby the equivalence between elastic and elastic plastic deformation was not established.

Figure 87 shows the end point values of the MSSR using the same effective critical distances. The end point values of the MSSR show wider scatter band in comparison to the result from averaged MSSR values as shown in Figure 86. The distance between layered data points resulting from the pad configurations involving elastic deformation (cylindrical pads with radii of 50.8 mm, 101.6 mm and 304.8 mm)

and elastic-plastic deformation (two 5.08 mm radius cylindrical pads) is enlarged, thereby increasing the overall scatter band. For the cylindrical pads involving elastic deformations, the difference between averaged and end point values is small. However, for the cylindrical pads involving elastic-plastic deformations, the difference between averaged and end point values is increased. This is because the end point values for the two 5.08 mm radius cylindrical pads have shown greater decreased values than have the averaged values. The flat pads (flat pads type1 (FP1), type 2 (FP2) and type 3 (FP3)) also show an enlarged scatter band for the end point MSSR values. The wider scatter band also occurred in the high cycle fatigue regime where the longer effective critical distances are calculated.
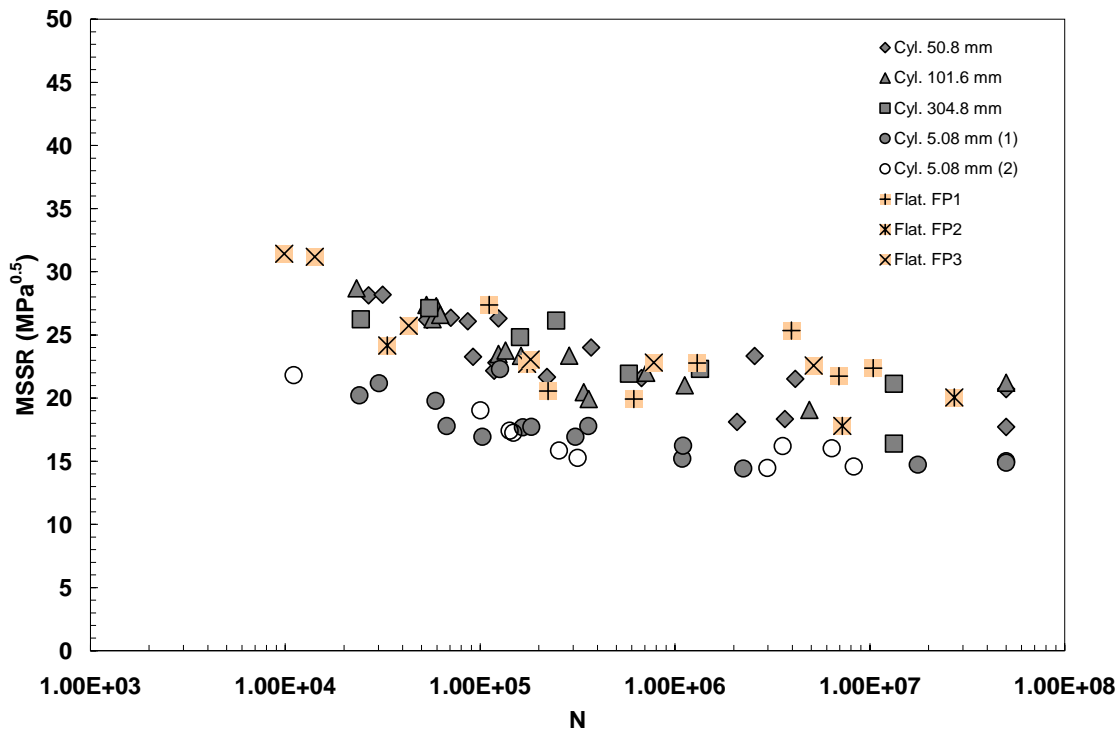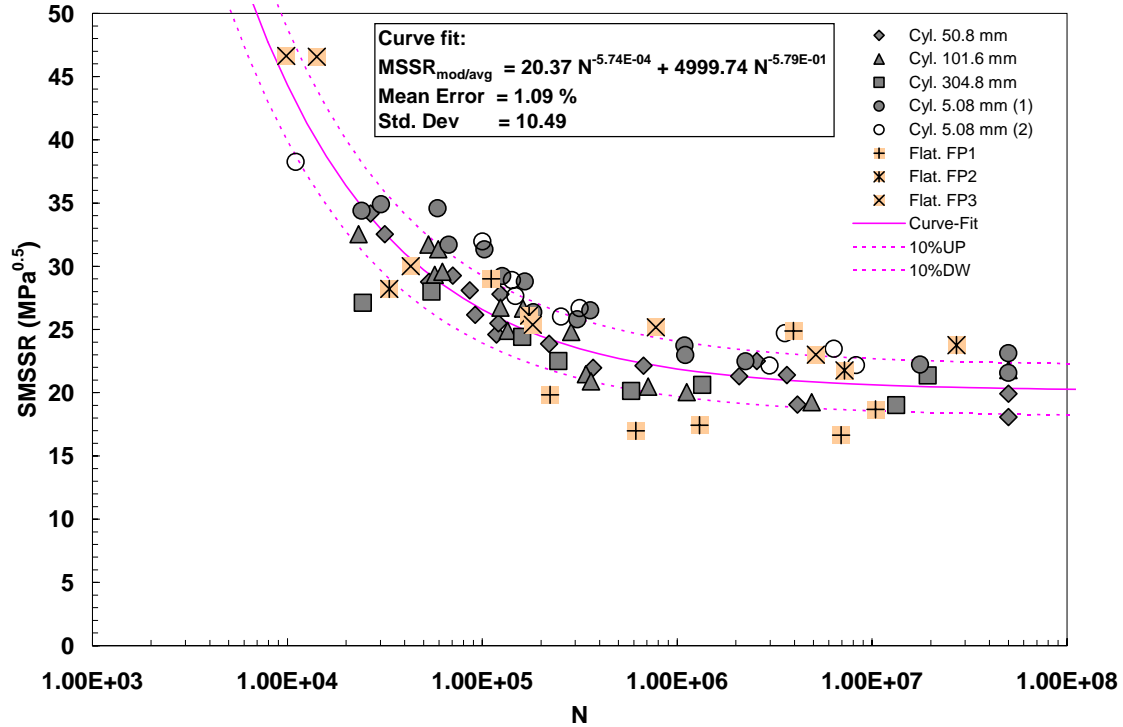

Figure 86. The Averaged MSSR Values at d_c = Min $\Delta\varepsilon_{effective}$

170
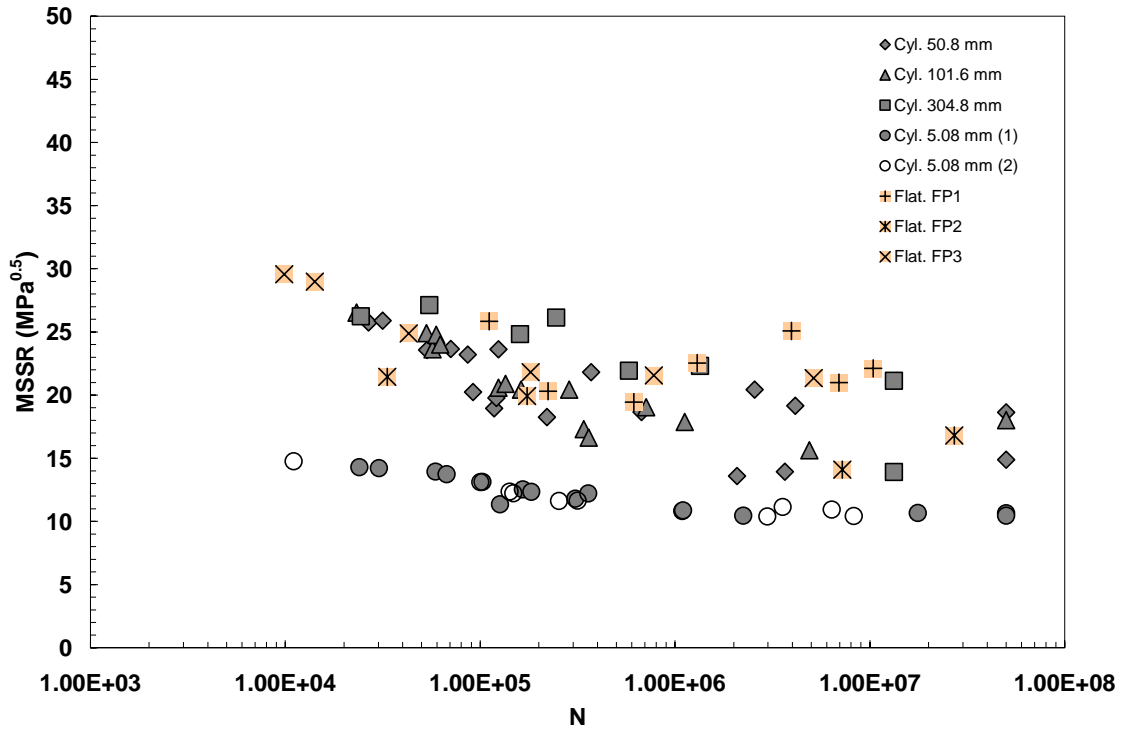
Figure 87. The End Point MSSR Values at $d_c = \text{Min } \Delta\varepsilon_{\text{effective}}$

Figure 88 shows the data points of the SMSSR parameter using the effective

critical distances, as shown in Figure 85, which were calculated by effective strain range

approach. These SMSSR values were calculated using averaged stresses up to the

effective critical distance in Figure 85. Figure 88 shows correlation of data points from

all pad configurations tested in this study. The curve fitted line which can be determined

from data points is also plotted in the figure. In order to measure the scatter band, the

10% upper and lower error line is also illustrated in the figure. Both the curve fit data

and fretting fatigue data lie in a narrow scatter band with a mean error of 1.09 % and a

standard deviation of 10.49. In the figure, the cylindrical pads show a good correlation of

data points between the pad configurations involving elastic and elastic plastic

deformations. The result of the cylindrical pads using effective stain range method has

shown similar results with the data points using the von Mises stress range method in Figure 78. However, the flat pads showed different values from both the effective strain range method and the von Mises stress range method. The data points of flat pads using the effective strain range method show a smaller scatter band than is seen from the von Mises stress range method. However, most of the data points of flat pad type 1 (FP1) were located out of the 10% error line and caused an increased total mean error.

Figure 89 shows end point values of the SMSSR parameters using the same critical distance. The results also show equivalence between the elastic and elastic-plastic fretting fatigue data. By comparing the end point values of the SMSSR to the averaged result of same parameter in Figure 88, it can be seen that the mean error decreased from 1.09% to 0.69%. Also, most of the data points fall within the narrow scatter range by 10% error. For the end point values, it can be noted that very small difference of data points occurred between elastic and elastic plastic cases. Also, very small difference occurred for cylindrical and flat pad configurations. However, the flat pads data were smaller than the cylindrical pads. These small differences in end point SMSSR parameters between cylindrical and flat pad configurations generated a narrower scatter band than did the averaged SMSSR results.

The result of the SMSSR parameters using effective strain range method can be summarized as follows:

1.   The von Mises stress range method and, the effective strain range method provided the different effective critical distance for the flat pads while similar effective critical distances were obtained for the cylindrical pads.

2.   The result of the MSSR shows smaller scatter band as compared to the von Mises stress range method. However, its dependency on the elastic and elastic plastic fretting fatigue conditions was found.

3.   The result of the SMSSR parameter shows an equivalence in data point for all pad configurations tested in this study. This result has been due to the reduced variation of the flat pad data points compared to those from von Mises method.

Figure 88. Averaged SMSSR Values at $d_c = \text{Min } \Delta\varepsilon_{\text{effective}}$
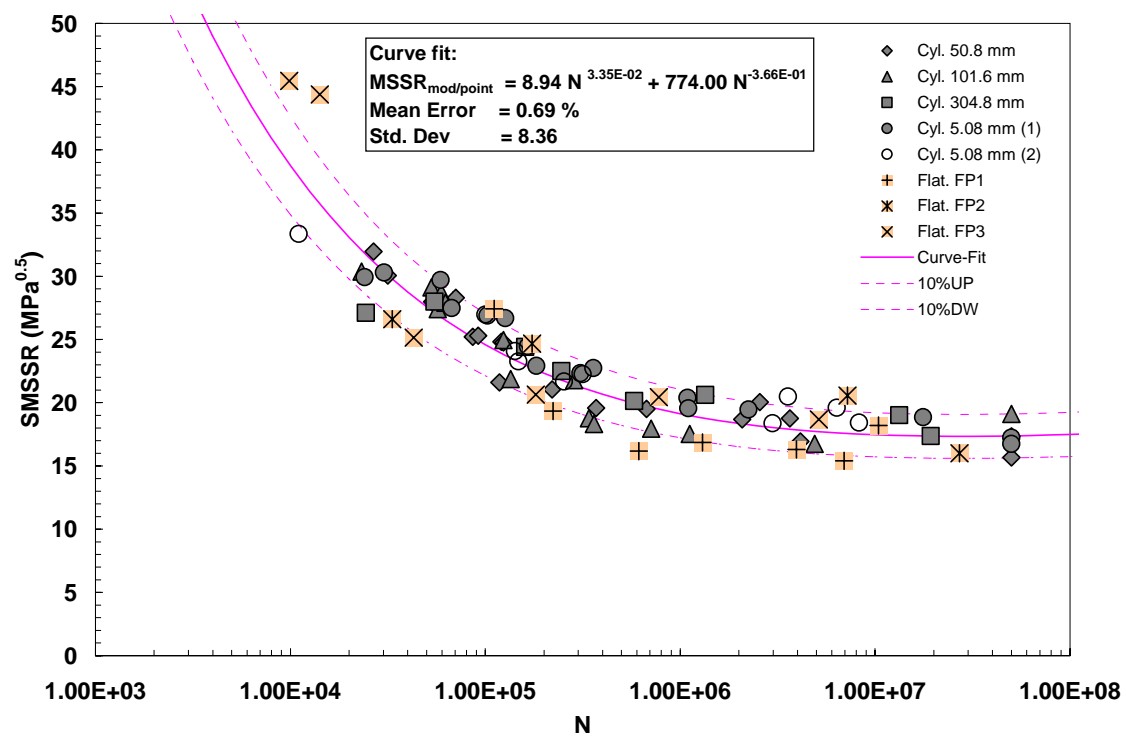
Figure 89. End Point SMSSR Values at d_c = Min $\Delta\varepsilon_{effective}$

VIII. Summary, Conclusion and Recommendations

Fretting is the surface damage that occurs when two contacting surfaces experience an oscillatory motion of small amplitude. When fretting occurs under cyclic loading conditions, the process is termed fretting fatigue. Fretting fatigue increases the tensile and shear stresses at the contact surface producing surface defects which can act as stress concentration sites. Fretting fatigue cracks can nucleate at these sites leading to an overall reduction in the fatigue strength of the material. The subject of fretting fatigue is important to the United States Air Force because the failure of turbine engines has been attributed to fretting fatigue. Specifically, fretting fatigue has been found to occur in dovetail joints where the turbine blade and turbine rotor interface. While many studies have evaluated the fretting fatigue behavior under elastic stress and strain environment, few studies have focused on the fretting fatigue behavior in elastic-plastic condition. However, plastic deformation is an essential part of the crack nucleation mechanism in general fatigue including fretting fatigue. In fretting fatigue, stress and strain concentrations arise near the trailing edge in the contact region. The stresses in this location are generally very close to the yield point of the material. However, when large normal and tangential forces are present, they generate a significant plastic deformation and this deformation plays a major role in crack nucleation. The aim of this study is to characterize the fretting fatigue life of Ti-6Al-4V under both elastic and elastic-plastic conditions.

8.1. Summary

Experimental Work

A total of eight different configurations of fretting pads were used in this dissertation. Five of the eight geometries were cylindrical pads with end radii of 50.8 mm, 101.6 mm, 304.8 mm and two 5.08 mm radius pads with normal load of 1334 N, 2224 N, 4003 N, 1334 N and 1779 N respectively. The other three pad geometries had a flat center section with edge radii. Three different flat pad configurations were used with edge radii of 5.08 mm for the Flat Pad type 1 (FP1), 2.54 mm for the Flat Pad type 2 (FP2) and 2.54 mm for the Flat Pad type 2 (FP2) with normal load of 1334 N, 4003 N and 4003 N respectively. In order to replicate the elastic-plastic deformation conditions, the decreased radii of the cylindrical pads, i.e. 5.08 mm radius pads, and flat pad type3 (FP3) were included in this study. Two different contact loads were applied for the 5.08 mm radius cylindrical pad, i.e. 1,334 and 1,779 N. The flat pad was included for the understanding of the behavior of the fretting fatigue under the turbine blades configuration.

The fretting fatigue tests were conducted on a 22.2 kN servo-hydraulic uniaxial test machine at ambient temperature in a laboratory environment. A load cell, attached to the servo-hydraulic load frame above the specimen, measured the axial load above the pads. Once the pads were aligned with the specimen, the normal load was applied. Four lateral springs, two on each side of the specimen, maintained contact with the pads and the specimen under a constant normal load. This system allowed the user to vary the axial load by controlling the displacement in the axial direction. Constant amplitude fretting fatigue tests were conducted over a wide range of applied axial force by controlling the servo-actuator on bottom of the specimen. Higher normal loads were applied to generate large plastic deformations, i.e. 4003 N for flat pad type 3 (FP3).

176

The results from this experiment were analyzed by examining the crack initiation location and crack initiation orientation. The crack initiation location was found near the trailing edge area between specimens and pad configurations under both elastic and elastic-plastic fretting fatigue conditions. The crack initiation orientation was also measured having similar angles for all pad configurations involving both elastic and elastic-plastic deformation. In experiments, the primary crack orientation angles under elastic and elastic-plastic fretting conditions were observed to be either $-45°$ or $45°$ with a variation of $\pm15°$ from a perpendicular to the loading direction.

Finite Element Analysis

The finite element analysis (FEA) was performed to generate stress and strain distributions under the experimental cyclic fretting conditions. Since this study has concentrated on the effect of the large plastic zone in fretting conditions, the elastic-plastic analysis was performed during the finite element analysis. In order to obtain accurate stress and strain results, the mesh size was determined through comparison with FEA and analytical solution, i.e. Ruiz Program. The applied loading conditions measured during experimental works were applied to the FEA models.

Some of previous studies reported that the range of coefficient of friction (COF) could vary under fretting fatigue test conditions. In this study, the effects of the COF on the FEA results were also investigated for elastic and elastic-plastic conditions. A summary of the effects of the COF on FEA results are as follows:

1. For both elastic and elastic-plastic fretting conditions, the transverse normal stress on contact surface, σ_{yy}, values were independent of variation in the COF. However, different distributions of σ_{yy} on the contact surface are found in each condition. For the elastic deformation condition, the change of distribution along the contact surface of σ_{yy} values showed a smooth variation

while, for the elastic-plastic deformation condition, the irregular variation of σ_{yy} values was shown along the contact surface. This is due to the accumulated stress caused by the large plastic deformation during the three times cyclic applied loadings.

2. For elastic condition, the normal stress on the contact surface, σ_{xx}, values at the maximum loading conditions were increased as the COF increased. However, for elastic-plastic condition, the maximum value of σ_{xx} did not change as the value of the COF increased. This is because the maximum σ_{xx} values were limited by yield stress value, σ_Y.

3. For elastic condition, the maximum values of the von Mises stress were increased as the COF value was increased similar to σ_{xx} values. In elastic-plastic analysis condition, the maximum values of the von Mises stresses were limited by the yield stress value, σ_Y, at trailing edge. However, in elastic-plastic analysis condition, the von Mises values also increased at the leading edge where the plastic deformation did not occur for both elastic and elastic-plastic conditions.

FEA were conducted to calculate the stress and strain distributions along and near the surface of the fretting fatigue specimen. The comparison of the stress and strain distributions resulting from each pad configuration was performed under same applied loading condition. A summary of the comparison of the stress and strain distributions are as follows:

1. The peak σ_{xx} stresses were increased as the maximum normal pressure, Po, increased.

2. For all pad configurations, the maximum peak σ_{xx} stress occurred at the trailing edge.

3. Near the contact surface, the rate of decrease of the σ_{xx} stresses was faster along the depth of the specimen as the maximum peak stress increased.

4. The maximum shear stresses, τ_{xy}, also increased as the Hertzian peak pressure increased.

5. Maximum von Mises stresses increased as Hertzian peak pressure increased, and two 5.08 mm radius cylindrical pad and flat pad type 3 (FP3) had the plastic deformation at the trailing edge.

6. In the equivalent plastic strain distribution plot, the large plastic zone near the contact surface for 5.08 mm radius cylindrical pads and the flat pad type 3 (FP3) also showed the plastic zone. However, in the other pad configurations, no plastic zones were found.

7. For elastic fretting condition, similar distributions were found between the total effective strain and the von Mises stress distribution. However, for elastic-plastic deformation conditions, different shapes were found between these two conditions. This is because the effective strain can determine the magnitude of the plastic deformation within the plastic zone while the von Mises stress cannot.

Fretting Fatigue Life Based on Contact Surface Stresses

The stress-life and strain-life approaches have been evaluated as a parameter of fatigue life using contact surface stresses since these approaches are commonly used in analysis of fatigue life. Due to the multi-axial nature of the fretting fatigue condition, in the fretting fatigue problem, the critical plane parameters have been commonly utilized to predict fretting fatigue life. Of the many multiaxial parameters available, Namjoshi et al. [10] have shown the modified shear stress range (MSSR) to be effective at predicting the fretting fatigue life of Ti-6Al-4V for elastic deformation condition. The MSSR

incorporates a combination of shear and maximum normal stress that are encountered in multiaxial fatigue loading condition. In addition to the MSSR parameter, the second modified shear stress range (SMSSR) was also suggested in this dissertation for both elastic and elastic-plastic deformations. The SMSSR incorporates a combination of shear and normal stress range instead of the maximum normal stress in MSSR formulation. In this study, the stress-life, strain-life, MSSR and SMSSR parametric approaches are investigated based on contact surface stresses. The summary of the results follows:

1. The stress-life and strain-life approaches using contact surface stresses did not appear to collapse data points into a narrow scatter band, thus indicating that the equivalence between test pad geometries is not established from these approaches.

2. The MSSR parametric approach using contact surface stresses has shown better converged data points for all tested pad configurations than have stress or strain versus life approaches. However, data points approximately layered by elastic and elastic-plastic fretting conditions. Further, the data from elastic-plastic fretting fatigue conditions increased the scatter band thereby weaken its accuracy in utilizing data points resulting from elastic fretting conditions to predict the fatigue life under elastic-plastic fretting conditions.

3. The SMSSR approach using contact surface stresses has shown a strong dependence on pad geometry thereby the equivalence among pad configurations tested in this study was not established from this approach also.

Use of Critical Distance Method

In notch problem, the various critical distance methods have been used to account for the effect of the stress gradient in fatigue life prediction. In this study, similar methods were evaluated for the fretting fatigue. In order to find the effective critical

distances, various approaches were evaluated with critical plane parameters, i.e. MSSR and SMSSR, in this study. The critical distance methods used in this study can be categorized into three methods: arbitrary critical distance method, effective stress range method and effective strain range method. Further, the effective stress range procedure was applied with two methods such as von Mises stress range method and relative stress gradient method. The result of the each critical method can be summarized as follows:

Arbitrary Critical Distance Method

1. The crack initiation location and orientation were determined by the maximum shear stress value at the contact surface.

2. The different effective critical distances were applied for all pad configurations

3. From the results, it was observed that a smaller scatter band has been found on the contact surface for the MSSR while, for the SMSSR parameter, better equivalent results were found with increased the critical distance. However, the scatter bands from the MSSR and SMSSR parameters did not show the equivalence of data points among all pad configurations tested in this study.

von Mises Stress Range Method

1. The crack initiation location and orientation were again found by maximum shear stress values at the contact surface.

2. For cylindrical pads, the effective critical distances calculated by von Mises stress range method showed an inverse relationship to the Hertzian peak pressure. However, for the flat pad, this relationship was not clear and consistent.

3. The MSSR parameter results showed a wider scatter range than the results using contact surface stresses. With the von Mises stress range method, the results of the SMSSR showed better results than those using contact surface stresses for the cylindrical pads. However, the data from the flat pad configurations did not appear to collapse into a narrow scatter band. Thereby the equivalence among entire group of tested pad configurations could not be established by this approach.

Relative Stress Gradient Method

1. The crack initiation location and orientation were found by maximum shear stress values within the contact surface.

2. The critical distances decreased as the number of cycles to failure increased. Shorter critical distances were obtained from this method than those calculated by the von Mises stress range method.

3. For the MSSR parameters, the variation of the flat pad data increased the scatter band more than do the results using contact surface stresses. The results from the SMSSR show similar dependency on pad configurations to those using contact surface stresses.

Effective Strain Range Method

1. The crack initiation location was determined by maximum effective strain range, $\Delta\varepsilon_{effective}$, value and the orientation was assumed to be $-45°$ for entire pad configurations which matched with the experimental observations.

2. For all pad configurations, the effective critical distances calculated by the effective strain range method showed an inverse relationship to the applied Hertzian peak pressure.

3. The results of the MSSR show a smaller scatter band than those from the von Mises stress range method. However, dependency on the elastic and elastic plastic fretting fatigue condition was found in this approach. The results of the SMSSR parameter showed equivalence of data points for the all tested pad configurations. This was due to the decreased variation of the flat pad data points compared to those from the von Mises method. Most importantly, the end point value of the SMSSR provided a more accurate prediction of fretting life among test data than did the averaged value of SMSSR along the critical plane from this approach.

8.2. Conclusion

The main conclusion that can be drawn from this study can be expressed as follows:

1. Establishing of an equivalence among fretting fatigue life data obtained from different pad geometries is always desirable since it would eliminate or reduce the fretting fatigue experiments which are significantly time consuming and relatively expensive to conduct.

2. In this study, various parameters, i.e. the stress, strain, MSSR and SMSSR, were utilized using contact surface stresses to determine its potential as a fretting fatigue parameter.

3. However, the results indicated that equivalence was not established between elastic and elastic plastic fretting fatigue conditions.

4. In order to account for the stress gradient near the contact surface, the various critical distances commonly used in notch problem are introduced.

5. As a result, the effective strain range method when used in conjunction with the SMSSR parameter demonstrated as an approach that can predict the fretting fatigue life for both elastic and elastic-plastic conditions.

8.2. Recommendations for Future Works

In this study, various critical distance methods were evaluated to predict fretting fatigue life, including elastic and elastic-plastic deformations. In conclusion, the effective strain range method, when used in conjunction with the SMSSR parameter, was demonstrated to be an approach that can predict the fretting fatigue life for both elastic and elastic-plastic conditions. However, the results from this study also lead to several recommendations for future work which may help further the development of improved approaches for predicting fretting fatigue life.

This dissertation was concentrated principally on the critical distance methods to predict fretting fatigue life for both elastic and elastic-plastic deformation conditions. Nevertheless, it should be noted that there is another method commonly used to predict fatigue life in notch problem, i.e. the critical area method. In the notch problem, the critical area has been determined from a notch root as shown in Figure 9. For the fretting fatigue condition, some modified critical area methods can be suggested due to its multi-axial stress nature. Figures 90 and 91 show the schematics of the critical area methods which could be utilized for predicting fretting fatigue life, i.e. square and semicircle area methods. As seen in Figures 90 and 91, in the fretting fatigue condition, the crack initiation point should be determined before applying critical area methods.
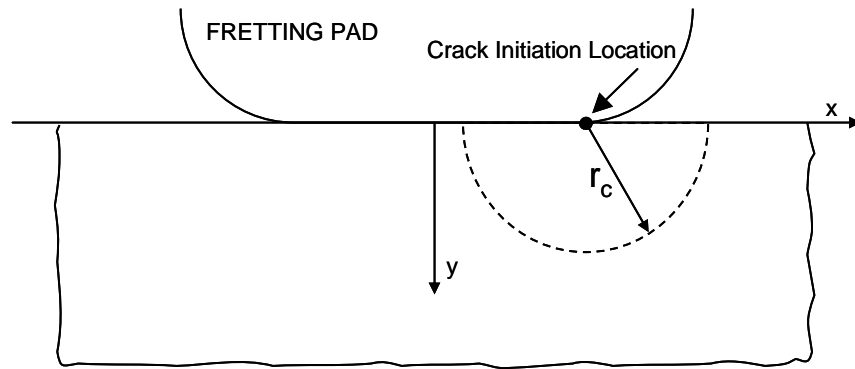
Figure 90. Suggested Semicircular Area Method for the Fretting Fatigue Condition
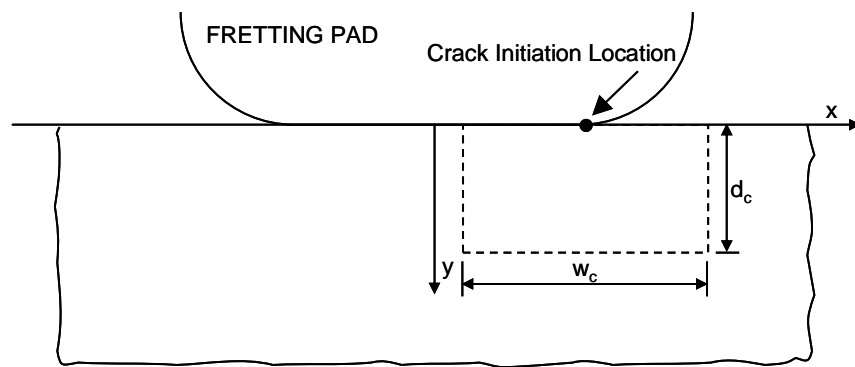
Figure 91. Suggested Square Area Method for the Fretting Fatigue Condition

185

The advantage of using the critical area method will be that this method is independent from the orientation of the critical plane. Based on observations made during the research for this dissertation, the critical distance methods were dependent on the predicted angle of critical plane. In contrast, the area method could be used without predicting the angle of critical plane. Araujo and Nowell [15] have evaluated the area method in fretting fatigue with square type area shape. Although their work was foundational, they presented a simple solution that involves the search for a dimension of area that could generate the best fit among a set of experimental data. Furthermore, their study was limited to the elastic fretting fatigue condition only. However, in order to reveal the relationship between the dimensions of the area and fretting conditions, it is necessary to determine the size of the area based on the contact and loading conditions. For the application of the critical area method, the averaged parameters over the critical area could be used as the criteria for the predicted fretting fatigue life.

In this dissertation, two critical plane parameters, i.e. MSSR and SMSSR, were evaluated with critical distance methods to predict fretting fatigue life. From the results of this study, it can be seen that the variations of these parameters are comparatively small as the critical distance is increase. Due to the comparatively small variations of the applied parameters, the effective critical distance, which can generate equivalence among test pad configurations, was determined at a relatively long distance. If there are more sensitive parameters to the distance near the contact surface, the length of the critical distance can be reduced.

For the critical distance method, the magnitude of the stress on the contact surface was dependent on the contact conditions, i.e. pad geometries. The different magnitude of the stress on the contact surface leads to the calculation of the effective critical distance based on given pad geometries and loading conditions. However, the stress intensity factor, i.e. K_I, K_{II} and K_{III}, also could be considered to represent the differences among

186

various contact conditions. Therefore, the stress intensity factor could be used to determine the effective critical distance or critical area for predicting fretting fatigue life involving elastic and elastic-plastic deformations.

Much more work could still be done using the critical distance and area methods utilized in this dissertation. This study has shown that the critical distance method could be used to correlate the fatigue life data obtained from elastic-plastic fretting fatigue with those from elastic fretting fatigue conditions. It is important to note that, in this study, the critical distance method was applied on specimens with no residual stress. In general, in order to improve strength and durability, the Shot Peening process is commonly used in the aircraft industry. Therefore, the prediction of the fretting fatigue condition including residual stress will be necessary.

APPENDIX A. Summary of Experimental Data

The purpose of this Appendix is to provide test results for the experiments. A load cell, attached to the servo-hydraulic load frame on the top side of the specimen, measured the axial load above the pads. A lightweight pressure transducer was also used to measure the applied axial load at the bottom of the specimen. During the test, the magnitudes of upper and lower loads were monitored by using these two load cells. The tangential load, Q, could be determined by the difference between magnitude of two axial loads from upper and lower load cells. In this study, the applied axial load was applied at a frequency of 50 Hz.

Table 3. Experimental Data for the 50.8 mm Cylindrical Pad (P = 1.334 kN)

Pad	N_f	σ_{max}	σ_{min}	$\Delta\sigma$	σ_{eff}	Q_{max}	Q_{min}
Cyl. 50.8 mm	Cycles	MPa	MPa	MPa	MPa	kN	kN
1	26700	635.8	-39.6	675.4	653.3	0.629	-0.629
2	31600	699.6	43.9	655.7	679.5	0.498	-0.316
3	53400	551.9	18.1	533.8	543.7	0.427	-0.294
4	70600	566.1	53.0	513.1	541.6	0.649	-0.574
5	86200	686.9	291.4	395.5	535.8	0.458	-0.494
6	91900	424.6	35.2	389.4	408.4	0.547	-0.445
7	118000	537.8	233.3	304.5	416.3	0.280	-0.254
8	121000	416.2	28.7	387.5	403.0	0.467	-0.512
9	124000	685.5	293.6	391.9	533.0	0.405	-0.209
10	220000	528.7	232.2	296.5	407.5	0.191	-0.214
11	371000	686.6	455.8	230.8	420.4	0.472	0.120
12	672000	581.7	350.5	231.2	384.0	0.203	-0.203
13	2080000	412.6	185.8	226.8	315.2	0.173	-0.173
14	2560000	685.8	441.6	244.2	430.9	0.171	-0.171
15	3660000	419.8	190.9	228.9	319.5	0.175	-0.175
16	4140000	540.3	372.3	168.0	319.4	0.601	0.427
17	50000000	506.6	330.6	176.0	314.8	0.618	0.196
18	50000000	410.1	273.2	136.9	250.3	0.467	0.125

Table 4. Experimental Data for the 101.6 mm Cylindrical Pad (P = 1.779 kN)

Pad	N_f	σ_{max}	σ_{min}	$\Delta\sigma$	σ_{eff}	Q_{max}	Q_{min}
Cyl. 101.6 mm	Cycles	MPa	MPa	MPa	MPa	kN	kN
1	23200	718.9	16.0	702.9	711.7	1.116	-0.552
2	53000	647.7	10.9	636.8	642.8	0.983	-0.649
3	57000	594.8	41.4	553.4	575.8	0.934	-0.418
4	59400	651.7	26.9	624.8	639.5	0.832	-0.601
5	62400	601.6	29.4	572.2	588.2	0.925	-0.498
6	124000	457.2	25.8	431.4	445.4	0.578	-0.512
7	135000	584.2	266.7	317.5	444.0	0.903	0.098
8	162000	456.1	34.1	422.0	440.4	0.623	-0.423
9	286000	559.9	243.1	316.8	433.3	0.667	-0.147
10	340000	446	210.1	235.9	334.9	0.485	-0.049
11	361000	428.5	203.9	224.6	320.4	0.436	-0.021
12	710000	587.9	401.3	186.6	350.8	0.976	0.516
13	1120000	537.4	357.8	179.6	328.2	0.767	0.311
14	4890000	416.9	246.4	170.5	278.8	0.440	-0.009
15	50000000	505.8	268.2	237.6	360.0	0.956	0.418

Table 5. Experimental Data for the 304.8 mm Cylindrical Pad (P = 4.003 kN)

Pad	N_f	σ_{max}	σ_{min}	$\Delta\sigma$	σ_{eff}	Q_{max}	Q_{min}
Cyl. 304.8 mm	Cycles	MPa	MPa	MPa	MPa	kN	kN
1	24376	441.2	136.0	305.2	373.8	0.336	-0.224
2	54850	494.6	178.3	316.2	404.4	0.577	-0.373
3	160201	413.7	231.7	182.0	285.9	0.380	-0.245
4	245686	577.3	481.7	95.6	257.0	0.300	-0.300
5	580000	321.7	248.9	72.8	164.9	0.260	-0.185
6	1344333	336.4	257.4	79.1	175.3	0.300	-0.190
7	13300000	287.5	224.3	63.2	145.5	0.163	-0.117
8	19300000	382.4	290.5	91.9	201.3	0.306	-0.204

Table 6. Experimental Data for the 5.08 mm Cylindrical Pad (P = 1.334 kN)

Pad	N_f	σ_{max}	σ_{min}	$\Delta\sigma$	σ_{eff}	Q_{max}	Q_{min}
Cyl. 5.08 mm (1)	Cycles	MPa	MPa	MPa	MPa	kN	kN
1	24014	630.0	53.2	576.8	605.5	0.323	-0.323
2	30260	618.6	49.6	568.9	595.7	0.322	-0.322
3	58963	512.8	49.6	463.1	489.8	0.322	-0.307
4	67231	503.3	37.6	465.7	486.0	0.188	-0.198
5	102625	377.2	33.6	343.6	361.7	0.228	-0.157
6	126467	373.3	46.7	326.6	351.5	0.173	-0.077
7	165437	577.1	272.4	304.8	433.0	0.196	-0.236
8	182890	608.8	288.1	320.7	456.3	0.077	-0.094
9	307819	435.8	205.8	229.9	326.8	0.105	-0.108
10	358818	559.2	266.4	292.8	418.0	0.184	-0.035
11	1090047	352.6	163.5	189.1	266.4	0.179	0.004
12	1100046	500.3	335.4	164.9	303.7	0.285	0.038
13	2241330	345.5	156.7	188.8	263.2	0.109	-0.007
14	17620086	447.5	301.2	146.2	270.5	0.183	0.001
15	50000000	489.9	347.8	142.1	280.7	0.247	-0.036
16	50000000	417.8	278.2	139.6	255.1	0.071	-0.071

Table 7. Experimental Data for the 5.08 mm Cylindrical Pad (P = 1.779 kN)

Pad	N_f	σ_{max}	σ_{min}	$\Delta\sigma$	σ_{eff}	Q_{max}	Q_{min}
Cyl. 5.08 mm (2)	Cycles	MPa	MPa	MPa	MPa	kN	kN
1	11032	686.2	-19.6	705.8	695.0	0.852	-0.852
2	100185	651.4	273.6	377.8	509.7	0.565	-0.369
3	141802	566.8	272.2	294.7	422.3	0.725	0.022
4	147906	565.4	279.4	286.0	416.0	0.694	0.142
5	253662	452.9	231.9	221.0	327.9	0.725	0.276
6	315886	427.1	212.7	214.5	313.3	0.707	0.156
7	2978944	448.2	311.7	136.4	262.4	0.743	0.436
8	3572462	554.5	368.0	186.5	339.6	0.721	0.267
9	6368523	547.6	373.0	174.5	327.4	0.667	0.325
10	8268218	448.5	311.7	136.8	262.9	0.698	0.405

Table 8. Experimental Data for the FP1 Flat Pad (P = 1.334 kN)

Pad	N_f	σ_{max}	σ_{min}	$\Delta\sigma$	σ_{eff}	Q_{max}	Q_{min}
Flat. FP1	Cycles	MPa	MPa	MPa	MPa	kN	kN
1	29300	691.6	36.7	654.9	674.8	0.628	-0.628
2	54000	691.3	36.3	655.0	674.7	0.621	-0.621
3	55900	566.4	33.0	533.4	551.3	0.607	-0.607
4	71600	574.4	32.3	542.1	559.6	0.625	-0.625
5	111000	695.6	326.2	369.4	523.2	0.538	-0.400
6	124000	406.8	-10.9	417.7	411.7	0.615	-0.615
7	138000	704.0	337.1	366.9	525.1	0.565	-0.369
8	198000	564.6	231.9	332.7	445.0	0.396	-0.440
9	223000	422.0	15.2	406.8	415.1	0.503	-0.534
10	260000	484.1	173.5	310.6	396.5	0.632	-0.632
11	614000	423.8	178.2	245.6	331.5	0.440	-0.236
12	1300000	613.3	381.0	232.3	396.2	0.520	-0.111
13	1890000	555.9	356.7	199.2	350.3	0.569	0.049
14	3950000	607.5	390.8	216.7	382.0	0.569	0.049
15	6930000	534.5	356.0	178.5	326.3	0.423	0.049
16	10400000	546.1	242.8	303.3	419.1	0.454	-0.356
17	16500000	394.4	180.7	213.7	299.3	0.543	0.071

Table 9. Experimental Data for the FP2 Flat Pad (P = 4.003 kN)

Pad	N_f	σ_{max}	σ_{min}	$\Delta\sigma$	σ_{eff}	Q_{max}	Q_{min}
Flat. FP2	Cycles	MPa	MPa	MPa	MPa	kN	kN
1	33369	478.0	246.4	231.7	345.0	0.180	-0.640
2	174106	422.9	248.2	174.7	284.0	0.440	-0.360
3	7214618	205.9	121.3	84.6	138.0	0.340	-0.120
4	27091735	310.7	215.8	94.9	182.2	0.304	-0.196

Table 10. Experimental Data for the FP3 Flat Pad (P = 4.003 kN)

Pad	N_f	σ_{max}	σ_{min}	$\Delta\sigma$	σ_{eff}	Q_{max}	Q_{min}
Flat. FP3	Cycles	MPa	MPa	MPa	MPa	kN	kN
1	9864	682.9	-25.9	708.8	694.4	1.251	-1.642
2	14158	692.3	88.6	603.7	650.9	1.024	-1.581
3	42951	636.1	270.0	366.1	496.1	1.735	-0.228
4	181424	532.2	283.5	248.7	377.9	1.445	0.065
5	777532	520.4	277.2	243.2	369.5	1.412	0.064
6	5140602	546.7	360.0	186.7	337.1	1.475	0.373

APPENDIX B. FEA Models for Each Pad Configurations

In this study, the finite element solutions were generated by using the commercial code ABAQUS. 4-node, plane strain elements were used for finite element model. The FEA models have fine mesh near the contact surface for the purpose of analyzing local stresses and strains within the contact region. In order to save the CPU time required to analyze the model, coarse meshes were applied in the regions where the values of stresses were not of interest in this study. The MPC was applied to the boundary between regions where the mesh size of the elements differed. On the contact surface of the specimen, the length and height of the contacting elements for cylindrical and flat with rounded edge pads are 6.35 μm and 1.59 μm respectively. The mesh sizes within the fine mesh area were determined by comparison of the results between the FEA and analytical solutions.
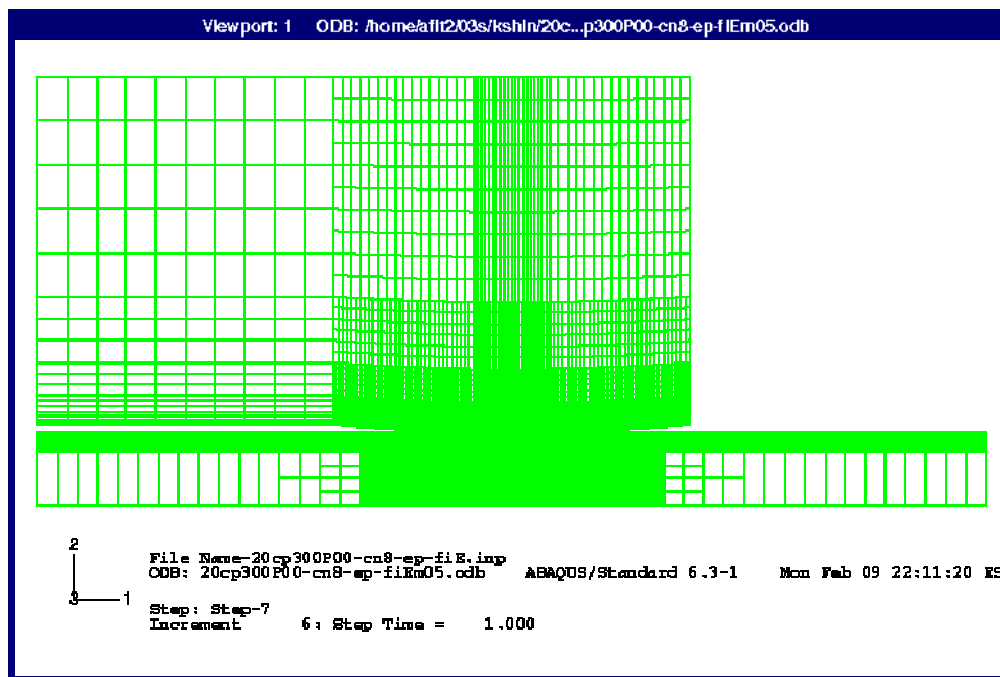
Figure 92. FEA Model for the 50.8 mm Radius Cylindrical Pad
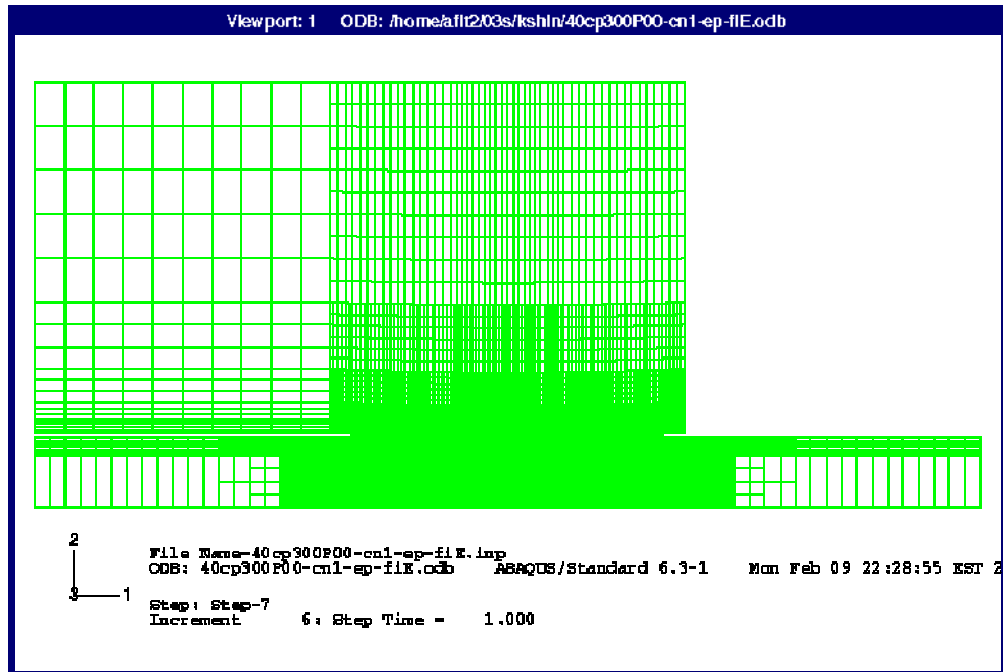
Figure 93. FEA Model for the 101.6 mm Radius Cylindrical Pad
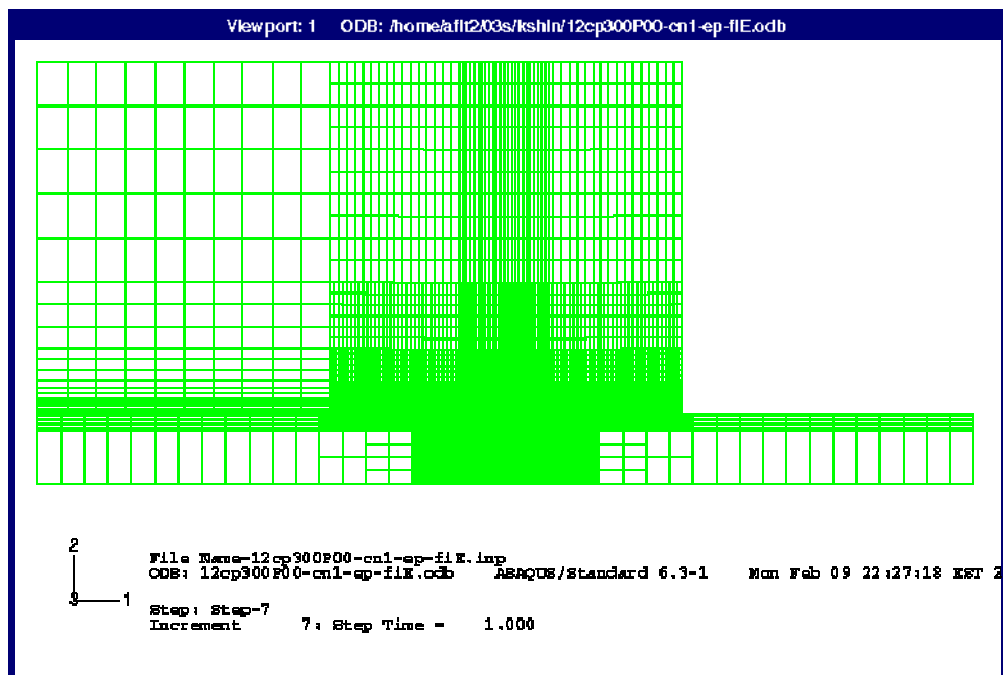
Figure 94. FEA Model for the 304.8 mm Radius Cylindrical Pad
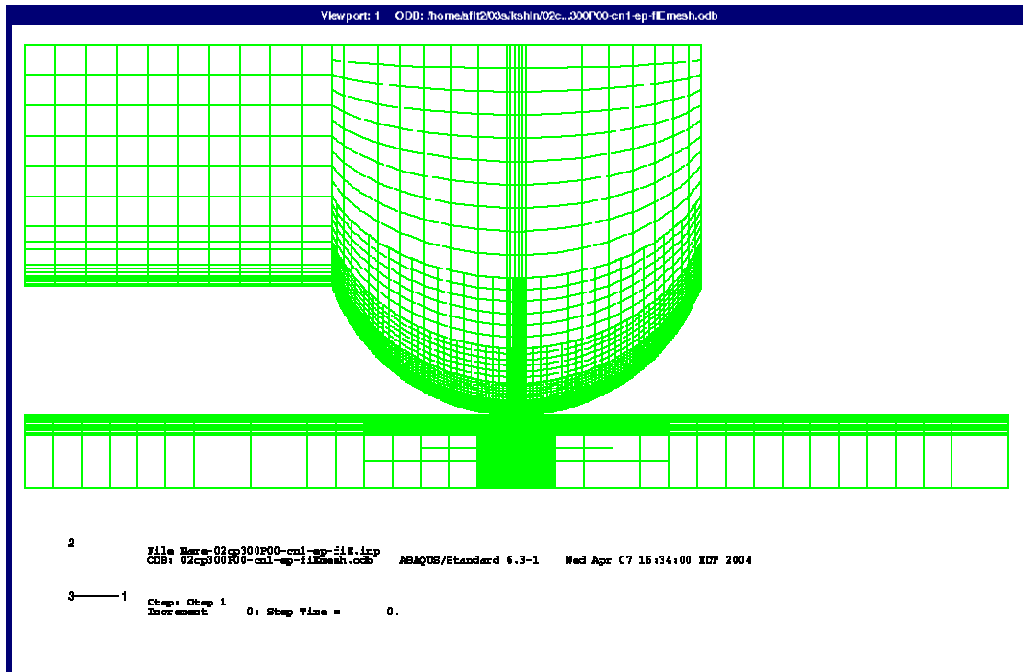
Figure 95. FEA Model for the 5.08 mm Radius Cylindrical Pad
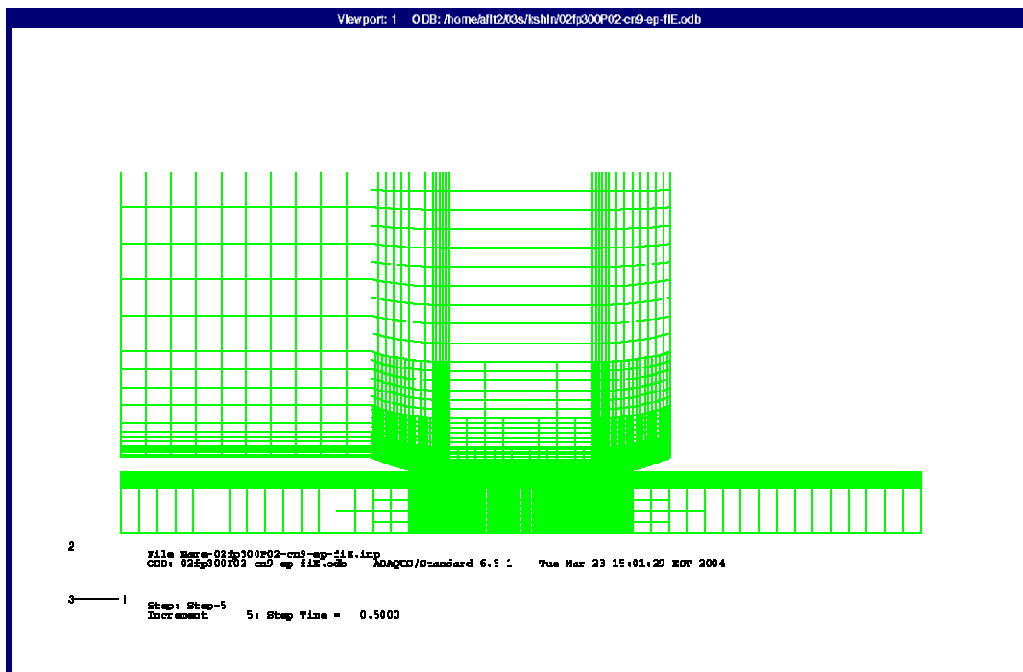
Figure 96. FEA Model for Flat Pad Type 1 (FP1)
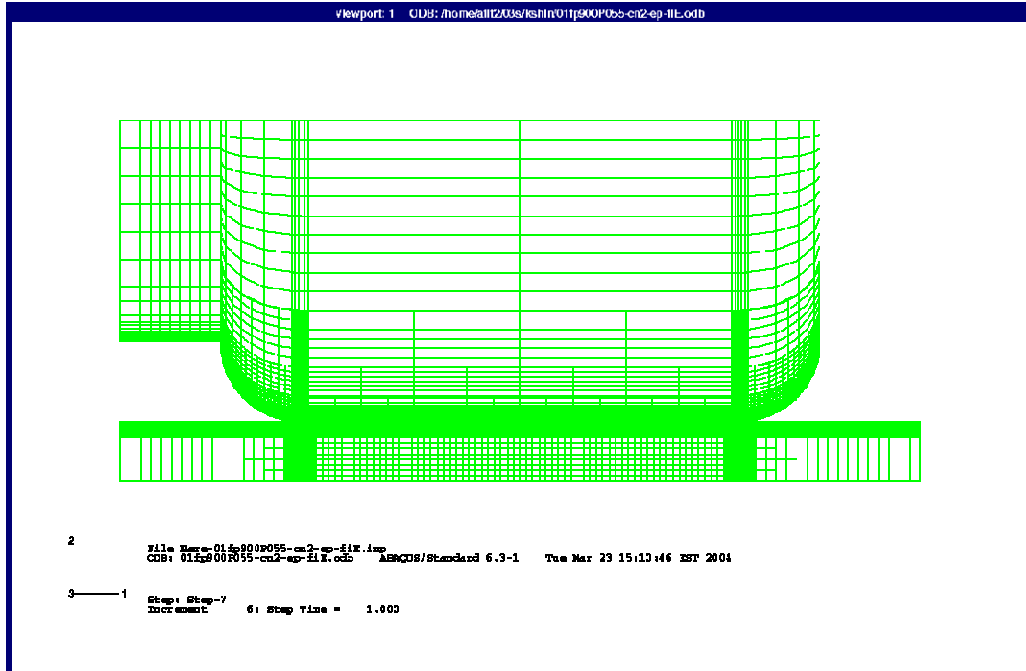
Figure 97. FEA Model for Flat Pad Type 2 (FP2)
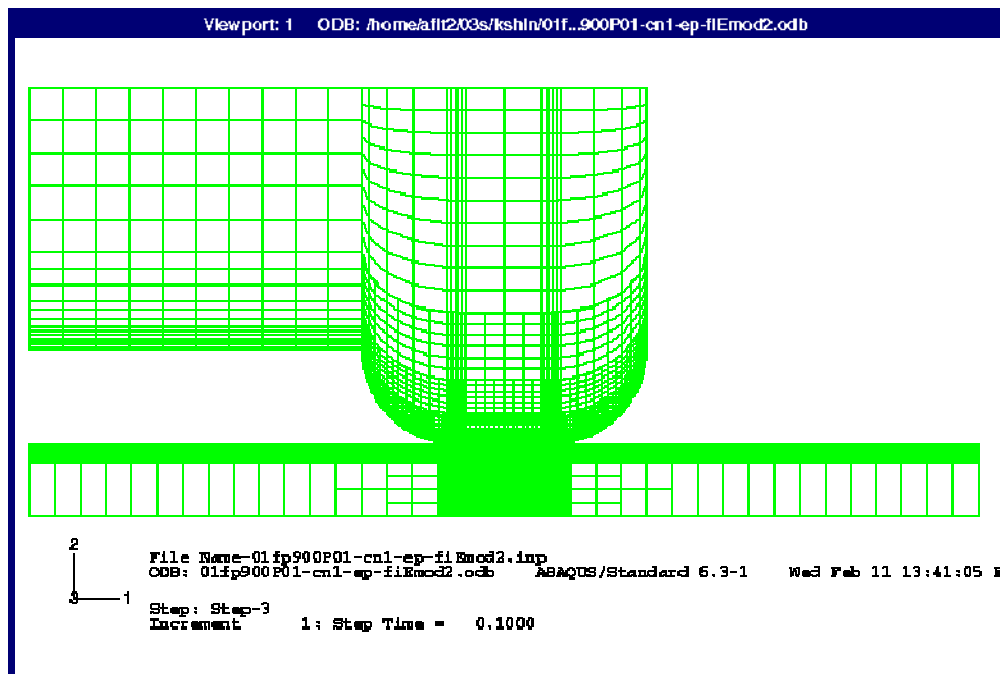
Figure 98. FEA Model for Flat Pad Type 3 (FP3)

APPENDIX C. Axial Stress Near the Contact Surface

This Appendix contains the 3-dimensional plots for the axial stress, σ_{xx}, states near the contact surface for all pad configurations included in this study. The stress states are obtained by finite element analysis (FEA) with same loading condition. The coordinates, x and y, of the stress field used in these plots can be seen in Figure 99. The distance x and y are normalized by half of contact width, a. The axial stress values are also normalized with maximum Hertzian peak stress value, P_o, which is dependent on the each pad configuration and coefficient of friction which is determined as 0.5.
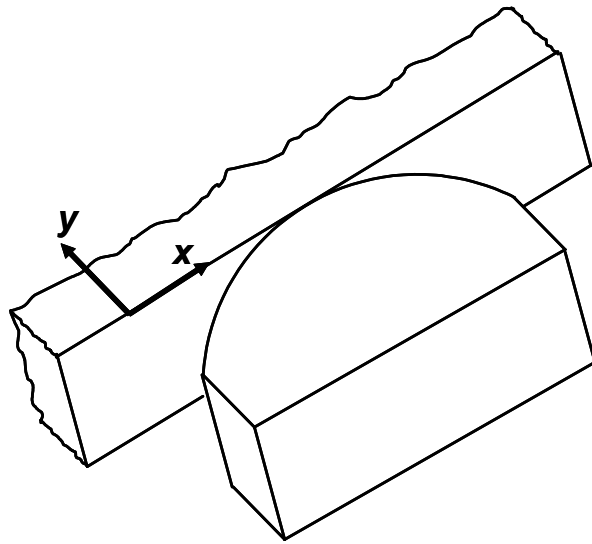
Figure 99. The Coordination of the Stress State Near the Contact Surface
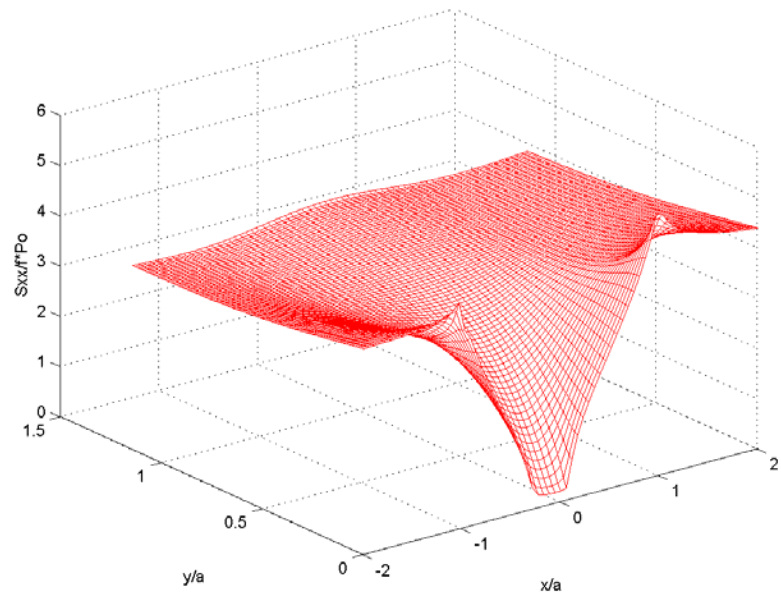
Figure 100. σ_{xx} Near the Contact Surface for the 50.8 mm Radius Cylindrical Pad
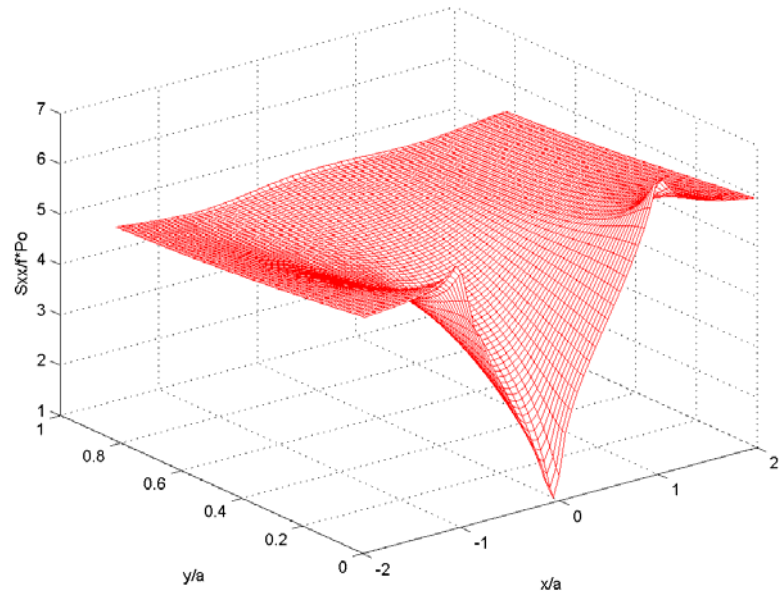
Figure 101. σ_{xx} Near the Contact Surface for the 101.6 mm Radius Cylindrical Pad
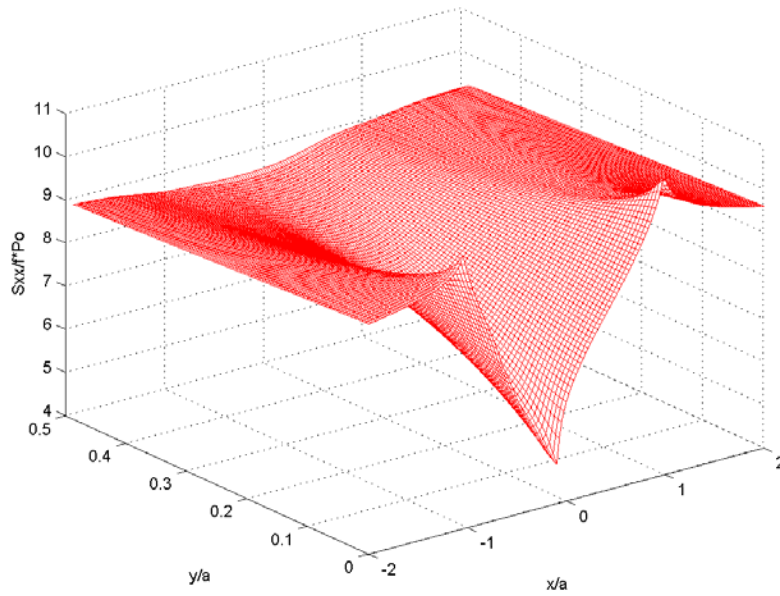
Figure 102. σ_{xx} Near the Contact Surface for the 304.8 mm Radius Cylindrical Pad
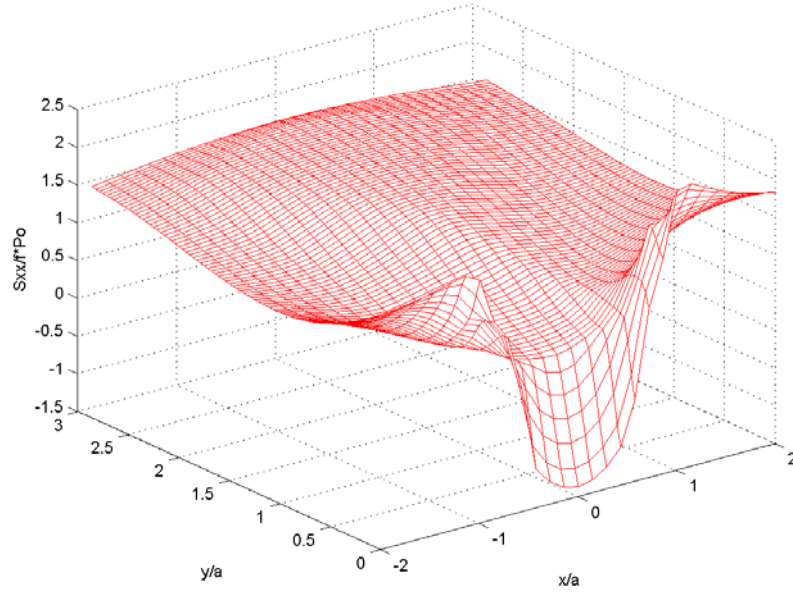
Figure 103. σ_{xx} Near the Contact Surface for the 5.08 mm Radius Cylindrical Pad Under
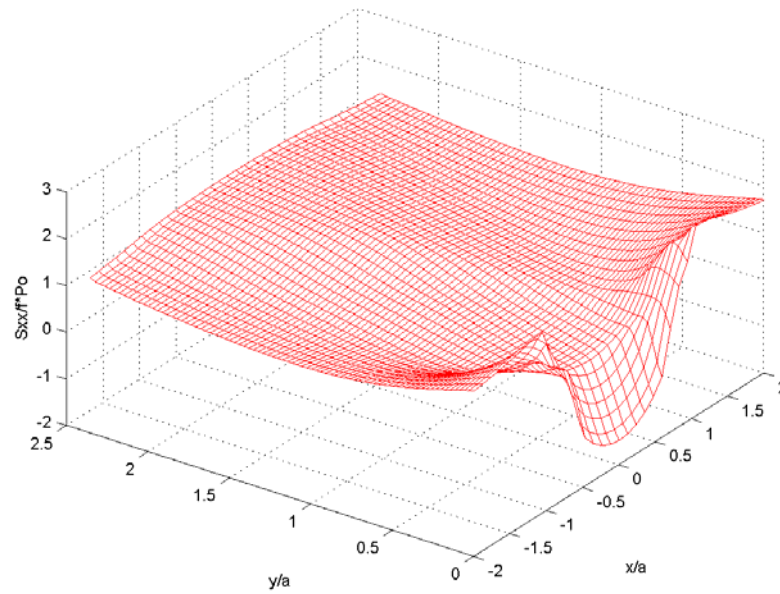
1334 N Normal load

Figure 104. σ_{xx} Near the Contact Surface for the 5.08 mm Radius Cylindrical Pad Under

1779 N Normal load
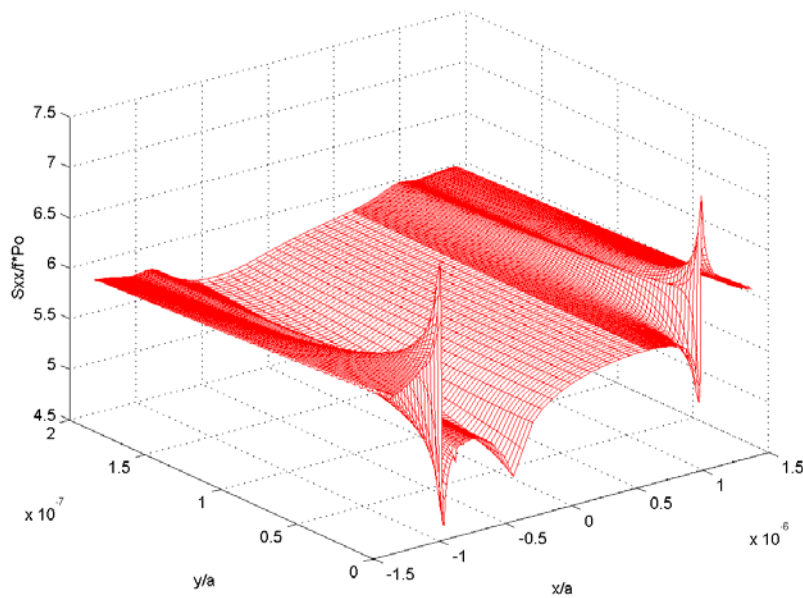
Figure 105. σ_{xx} Near the Contact Surface for the Flat Pad Type 1 (FP1)

200
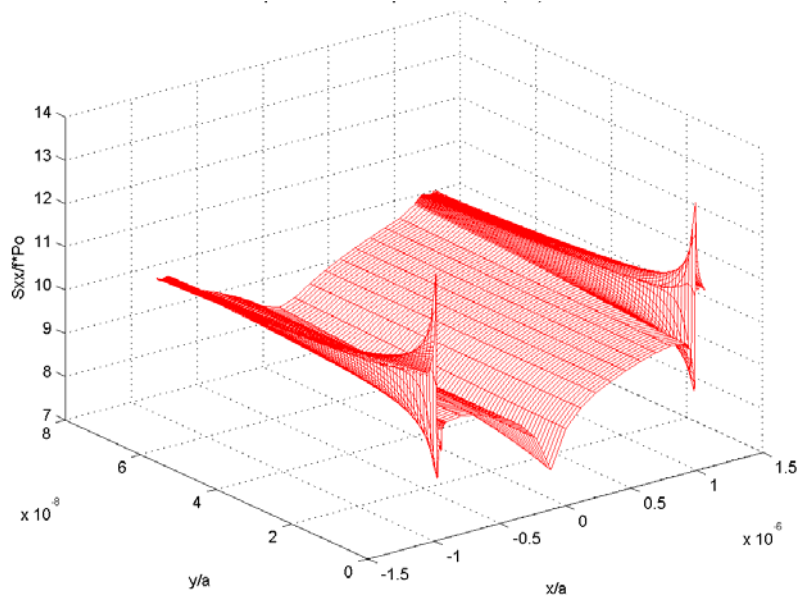
Figure 106. σ_{xx} Near the Contact Surface for the Flat Pad Type 2 (FP2)
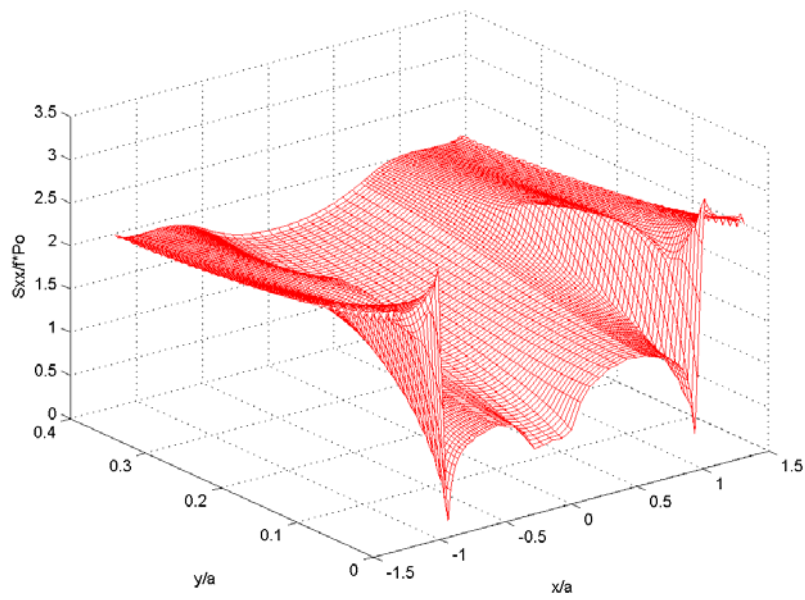
Figure 107. σ_{xx} Near the Contact Surface for the Flat Pad Type 3 (FP3)

APPENDIX D. von Mises Stress Near the Contact Surface

This Appendix contains the 3-dimensional plots for the von Mises stress states near the contact surface for all pad configurations included in this study. The stress states are obtained by finite element analysis (FEA) with same loading condition. The coordinates, x and y, of the stress field used in these plots can be seen in Figure 99. The distance x and y are normalized by half of the contact width, a. The axial stress values are also normalized with the coefficient of friction, which is determined as 0.5, and maximum Hertzian peak stress value, P_o, which is dependent on each pad configuration.
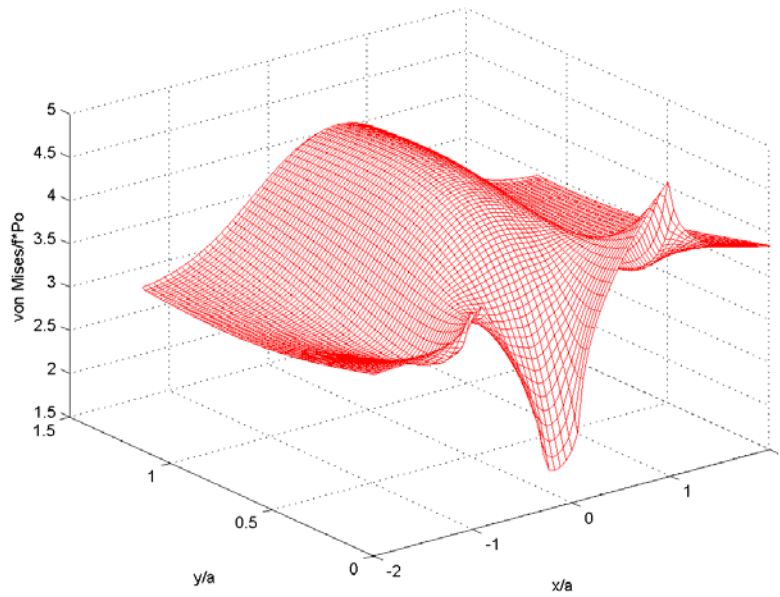
Figure 108. von Mises Stress for 50.8 mm Circular Pad
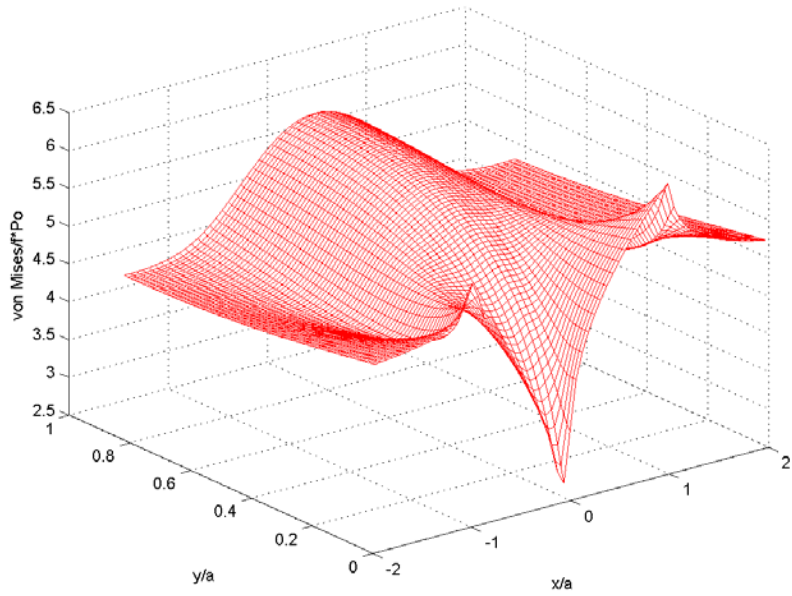
Figure 109. von Mises Stress for 101.6 mm Circular Pad
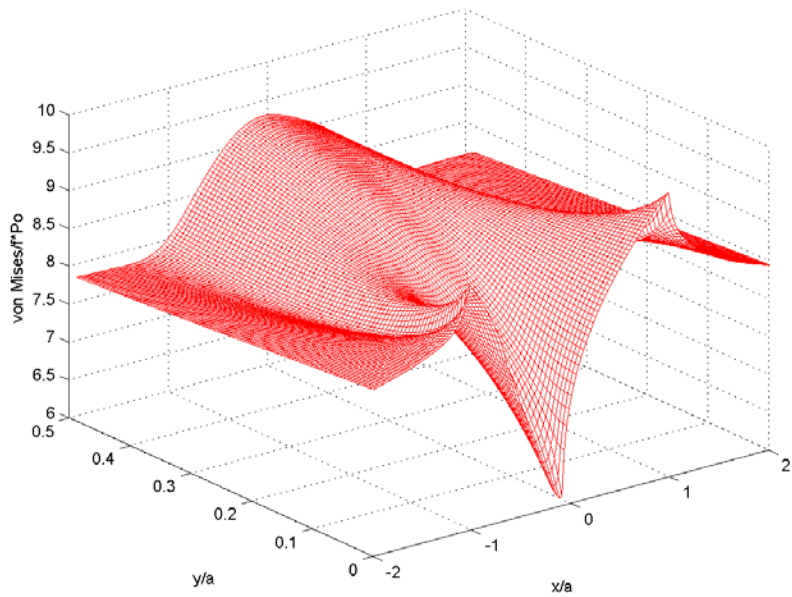
Figure 110. von Mises Stress for 304.8 mm Circular Pad
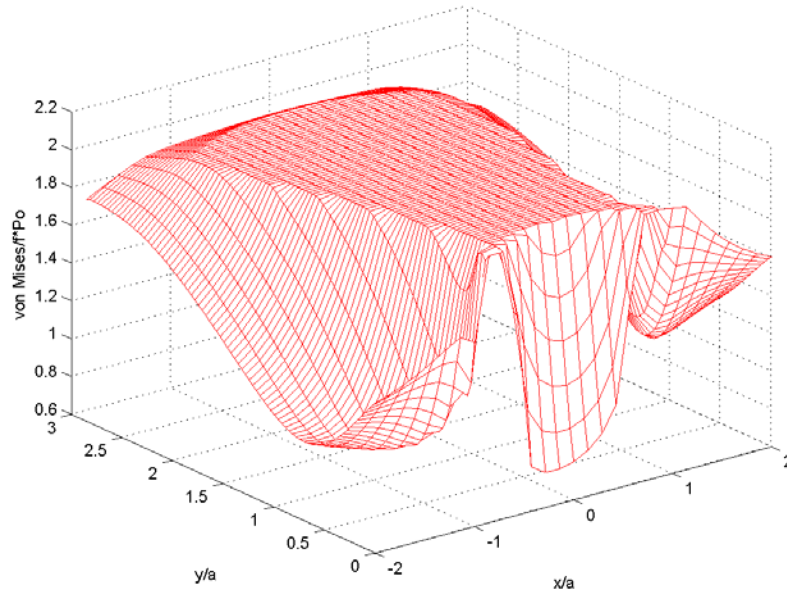
Figure 111. von Mises Stress for 5.08 mm Circular Pad with 1334 N Normal Load
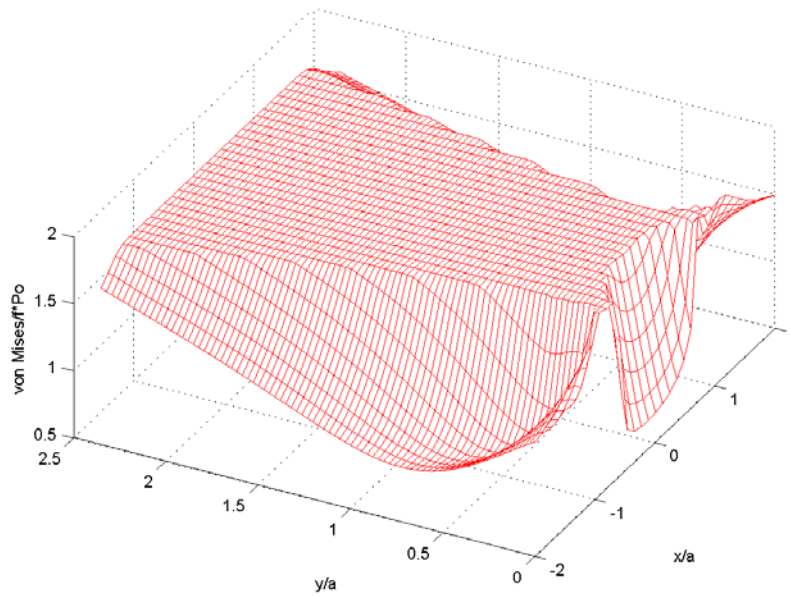
Figure 112. von Mises Stress for 5.08 mm Circular Pad with 1779 N Normal Load
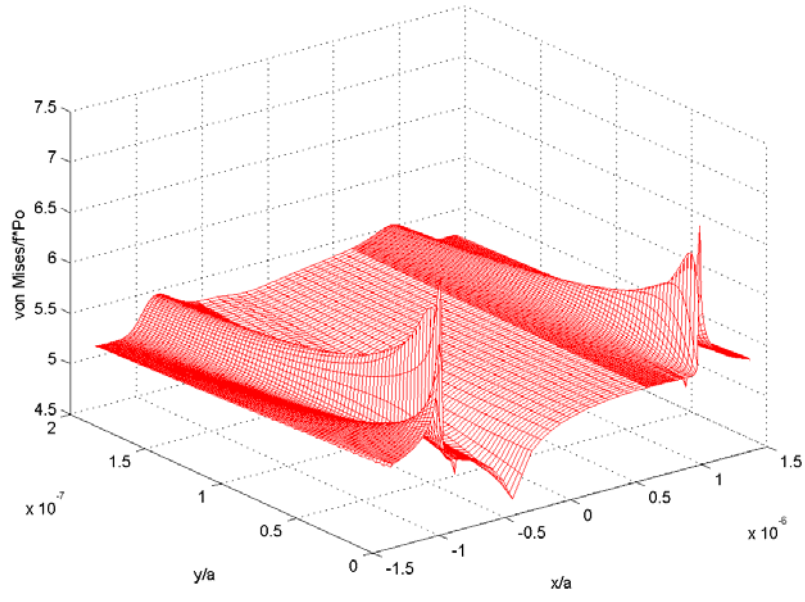
Figure 113. The von Mises Stress for Flat Pad Type 1 (FP1)
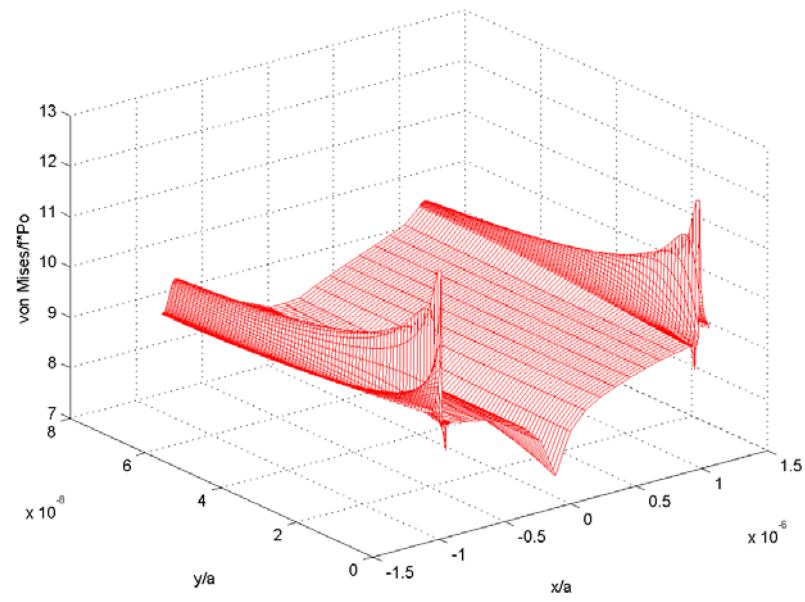
Figure 114. The von Mises Stress for Flat Pad Type 2 (FP2)
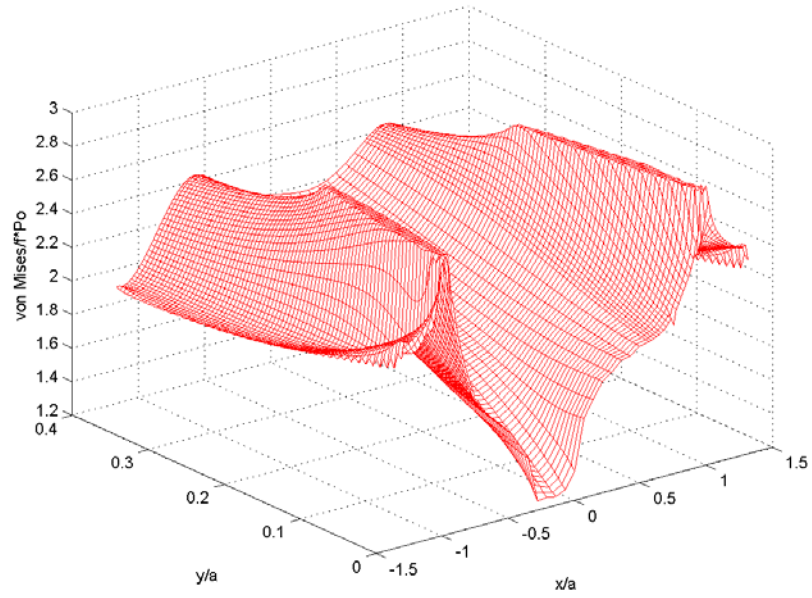
Figure 115. The von Mises Stress for Flat Pad Type 3 (FP3)

APPENDIX E. Effective Strain under the Contact Surface

This Appendix contains the 3-dimensional plots for the effective strain states near the contact surface for all pad configurations included in this study. The strain states are obtained by finite element analysis (FEA) with same loading condition. The coordinates, x and y, of the strain field used in these plots can be seen in Figure 99. The distance x and y are normalized by half of the contact width, a. The axial stress values are also normalized with the coefficient of friction, which is determined as 0.5, and yield strain value, ε_Y.
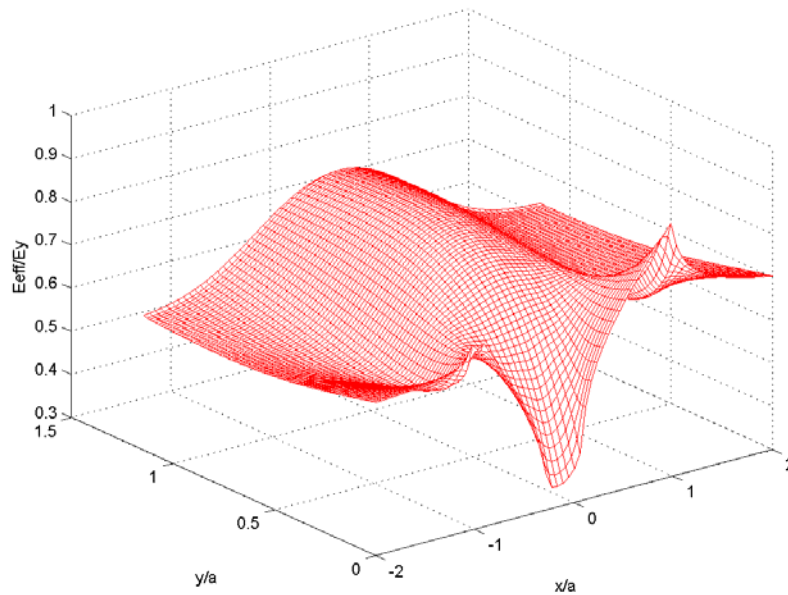
Figure 116. Effective Strain for 50.8 mm Circular Pad
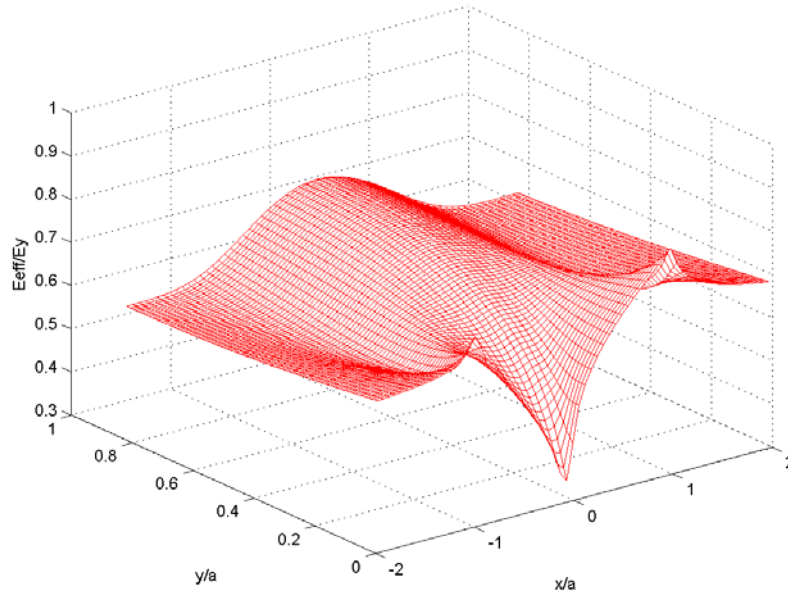
Figure 117. Effective Strain for 101.6 mm Circular Pad
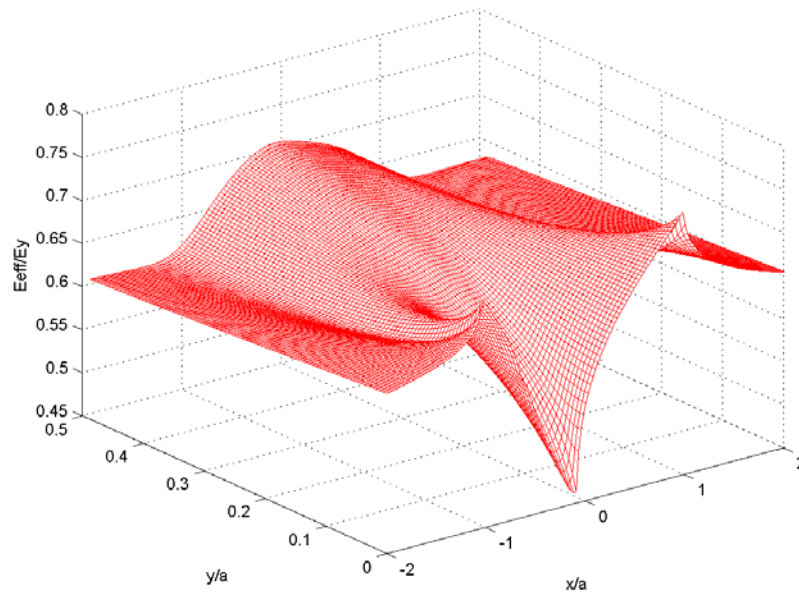
Figure 118. Effective Strain for 304.8 mm Circular Pad
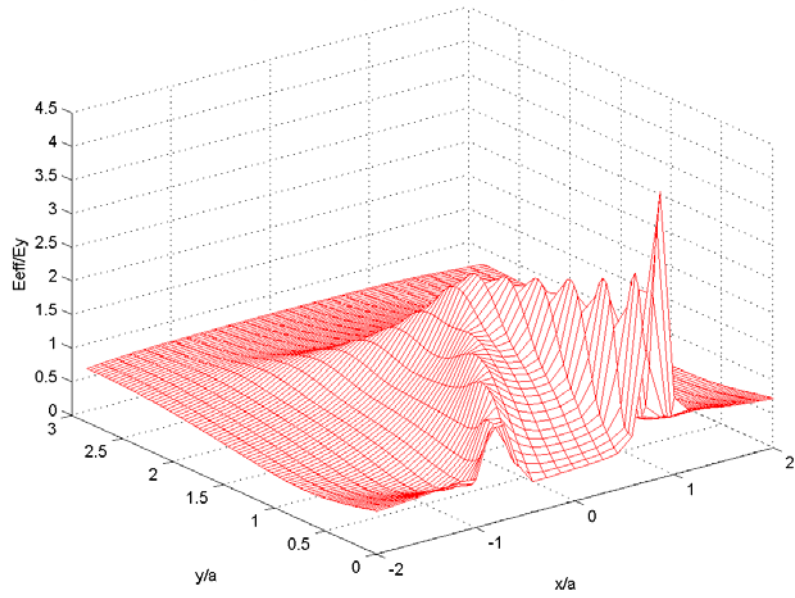
Figure 119. Effective Strain for 5.08 mm Circular Pad with 1334 N Normal Load
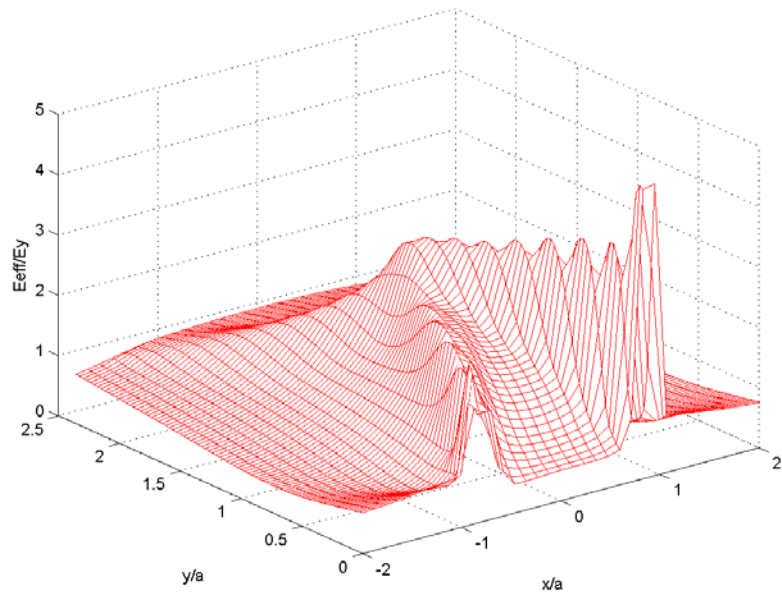
Figure 120. Effective Strain for 5.08 mm Circular Pad with 1779 N Normal Load
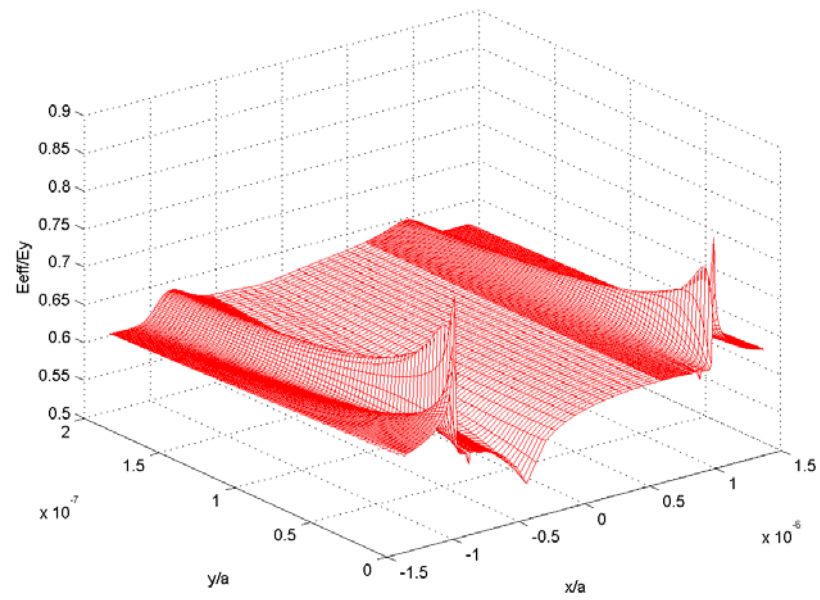
Figure 121. Effective Strain for Flat Pad Type 1 (FP1)
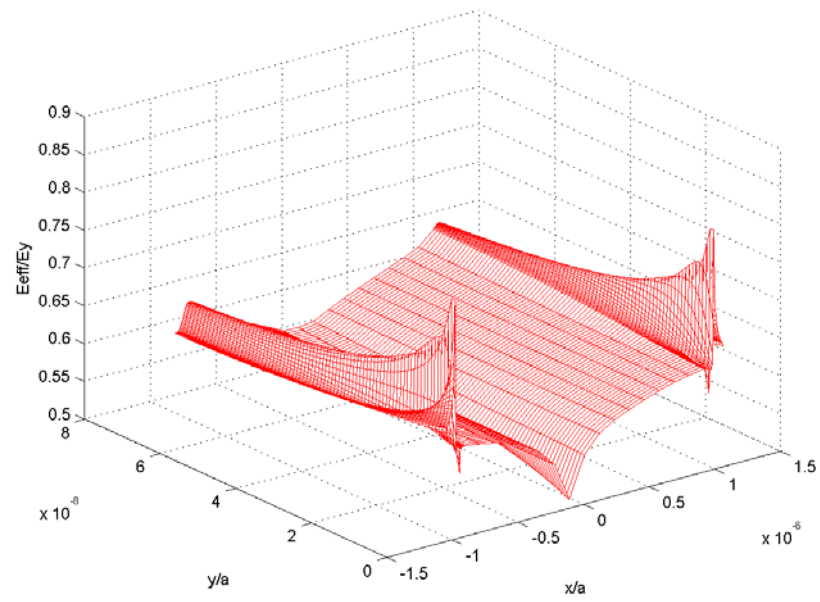
Figure 122. Effective Strain for Flat Pad Type 2 (FP2)
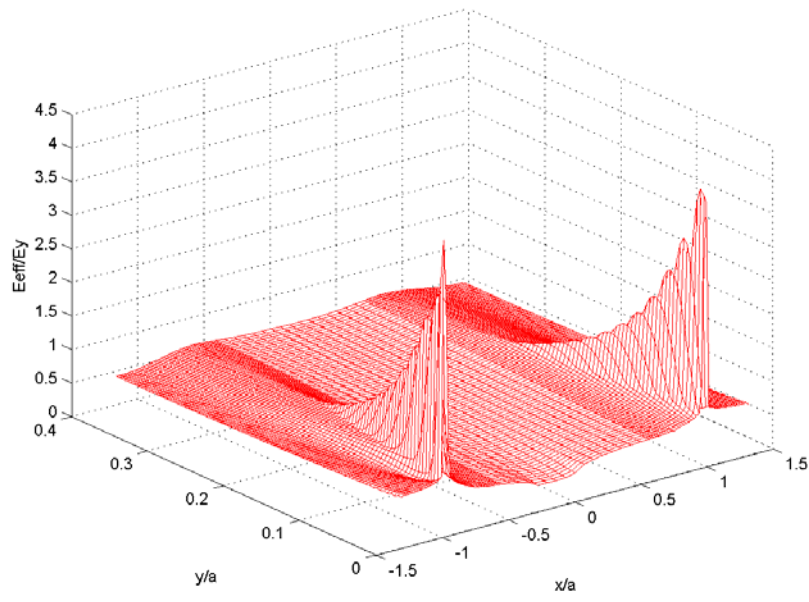
Figure 123. Effective Strain for Flat Pad Type 3 (FP3)

APPENDIX F. Averaged MSSR at Arbitrary Critical Distance

This Appendix contains the averaged MSSR parameters resulting from arbitrary critical distance for all pad configurations included in this study. In order to investigate the variation of the scatter band as critical distance increased, the results were plotted from 50 μm to 500 μm.
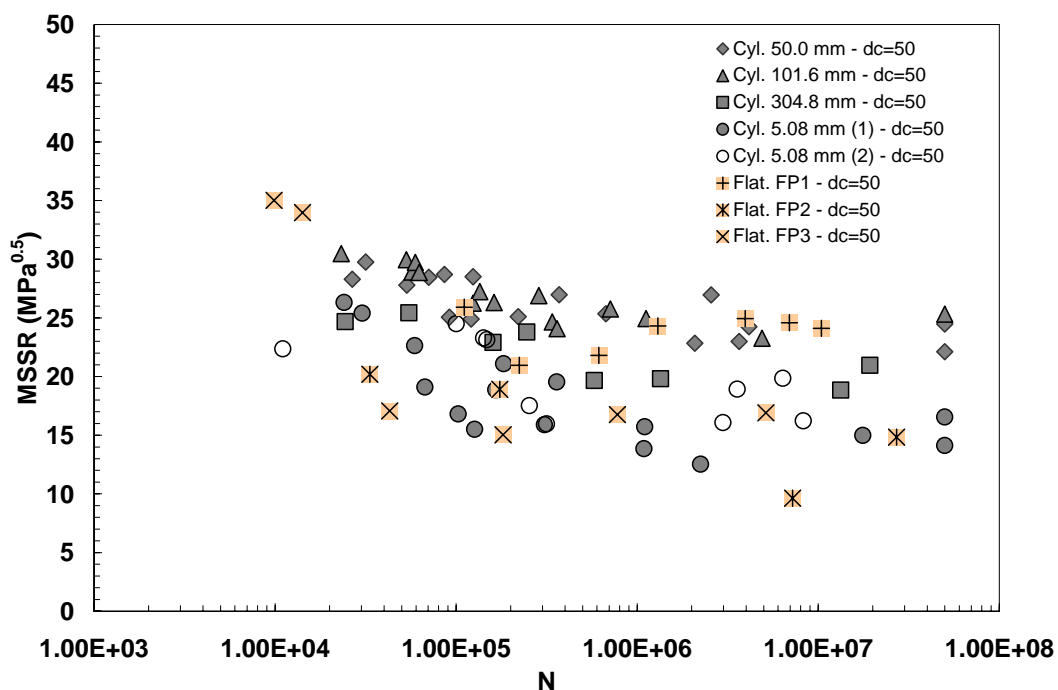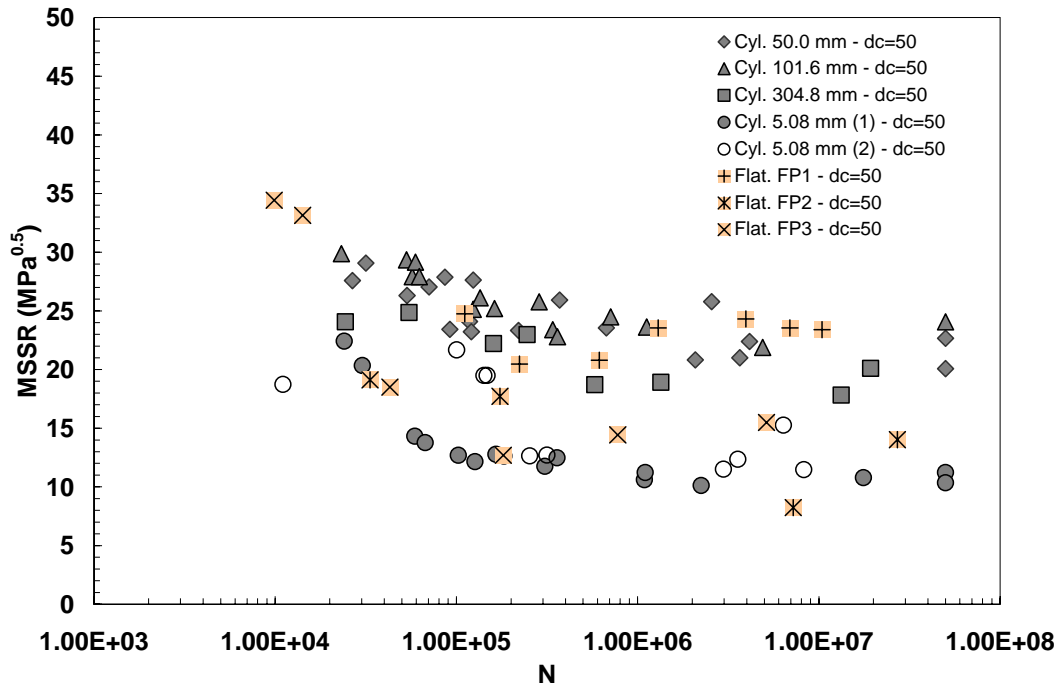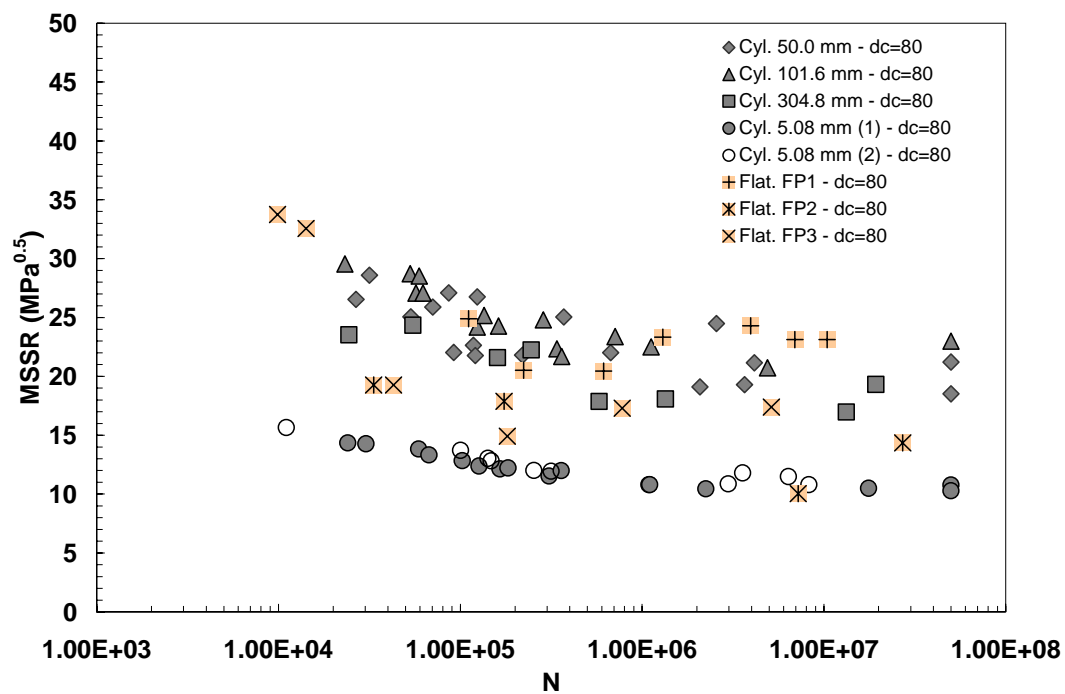

Figure 124. Averaged MSSR at $d_c = 50$ μm
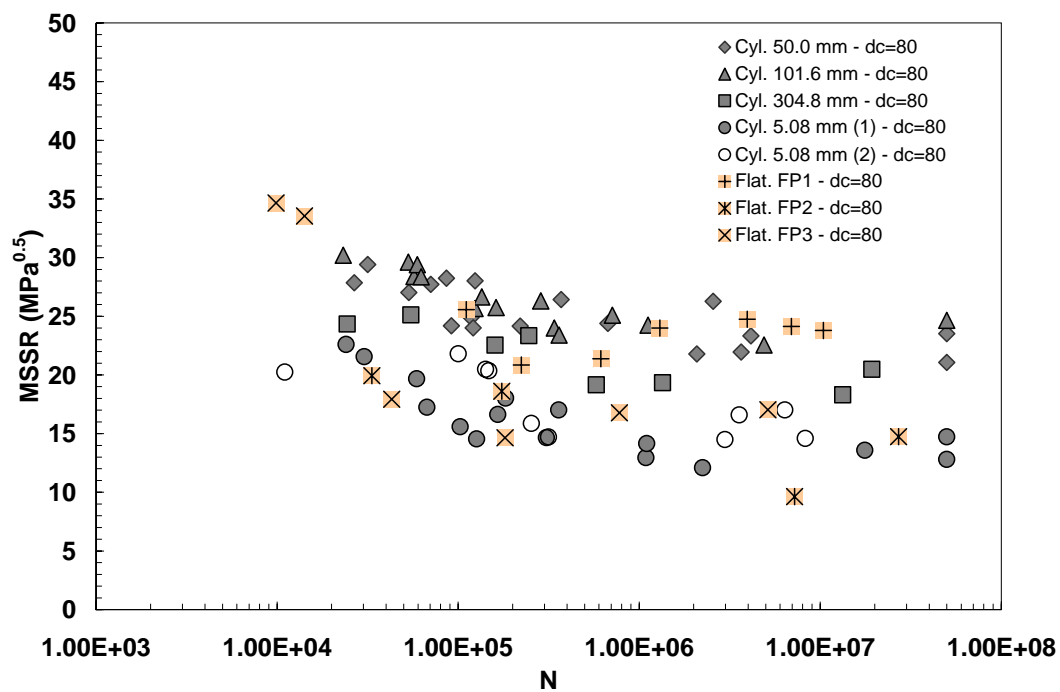
Figure 125. Averaged MSSR at d_c = 80 μm
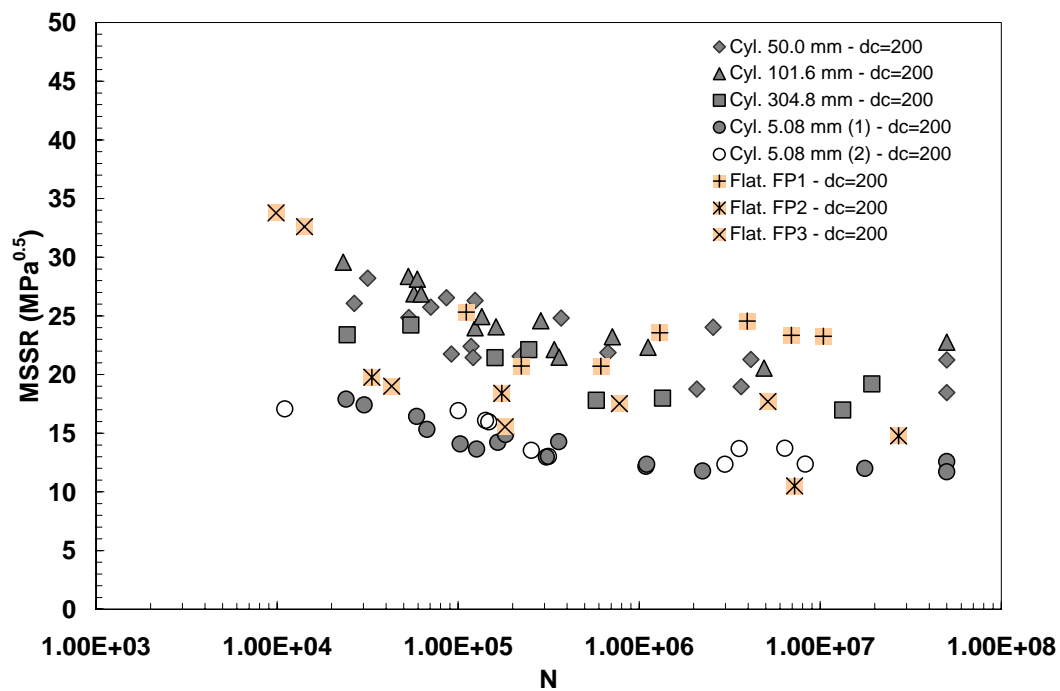
Figure 126. Averaged MSSR at d_c = 200 μm
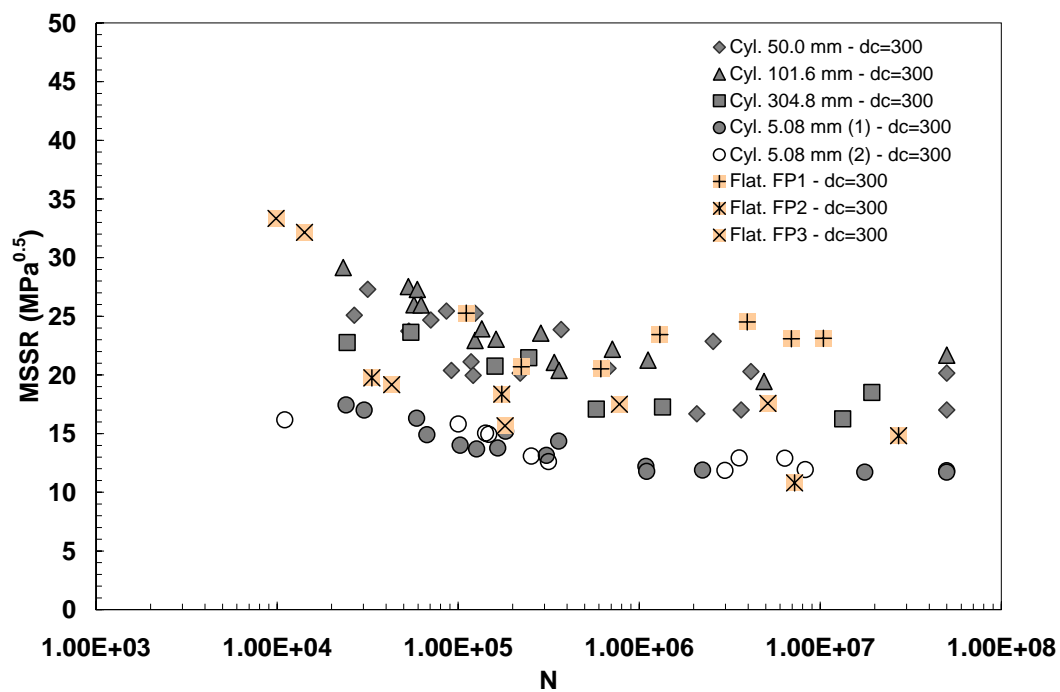
Figure 127. Averaged MSSR at d_c = 300 µm
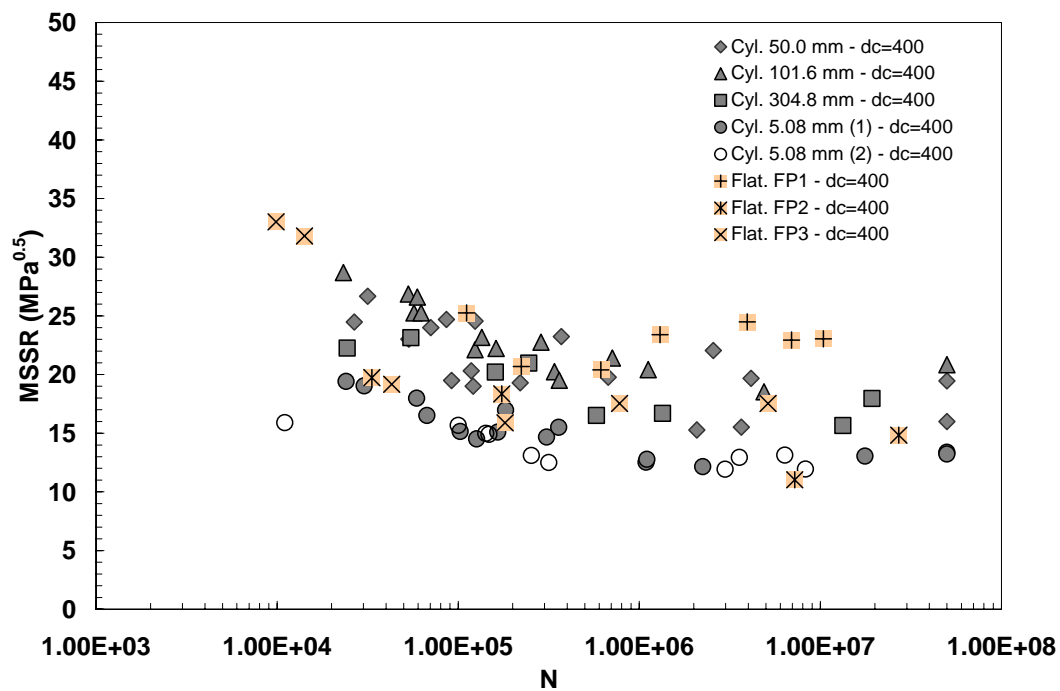
Figure 128. Averaged MSSR at d_c = 400 µm
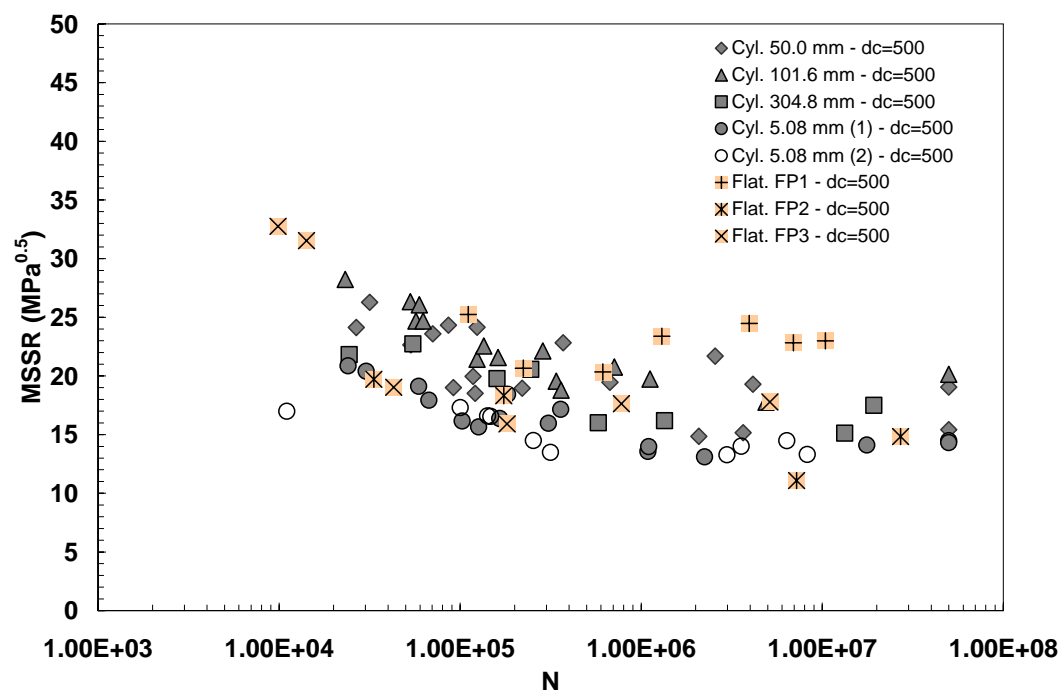
Figure 129. Averaged MSSR at d_c = 500 μm

APPENDIX G. Point MSSR at Arbitrary Critical Distance

This Appendix contains the point MSSR parameters resulting from arbitrary critical distance for all pad configurations included in this study. In order to investigate the variation of the scatter band as critical distance increased, the results were plotted from 50 μm to 500 μm.

Figure 130. Point MSSR at d_c = 50 μm

Figure 131. Point MSSR at $d_c = 80$ μm
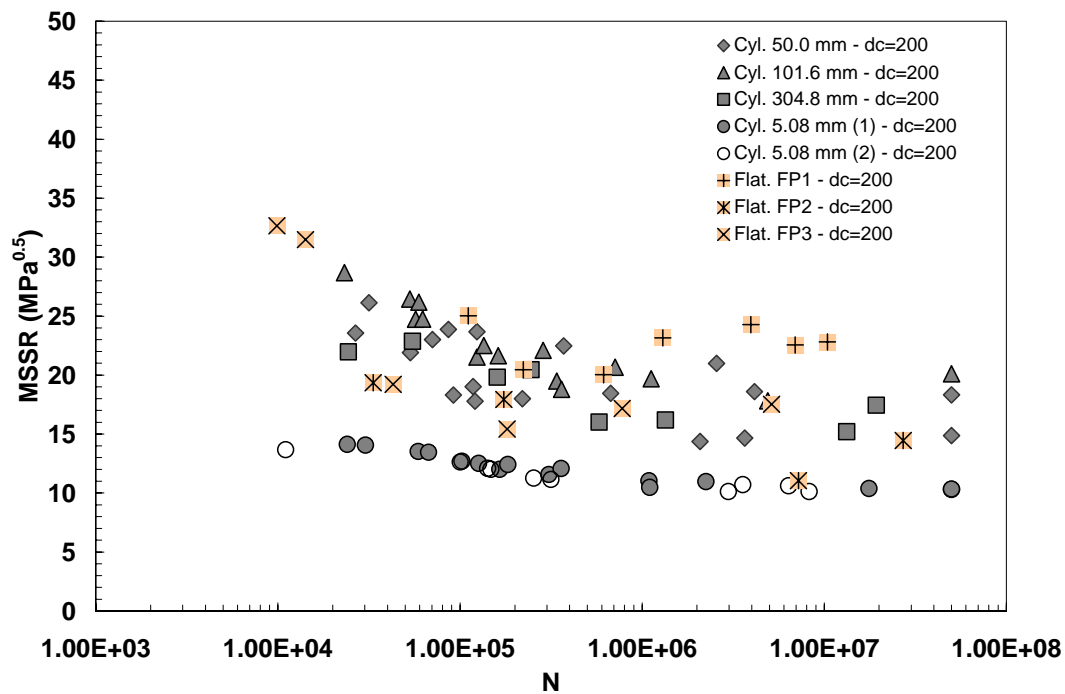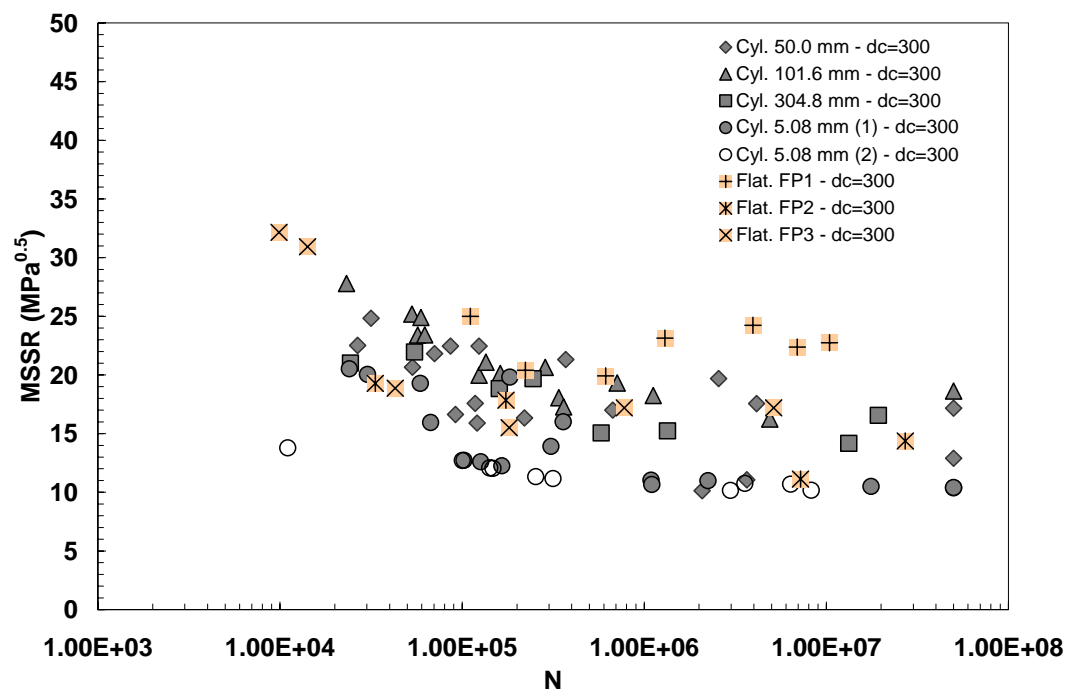

Figure 132. Point MSSR at $d_c = 200$ μm
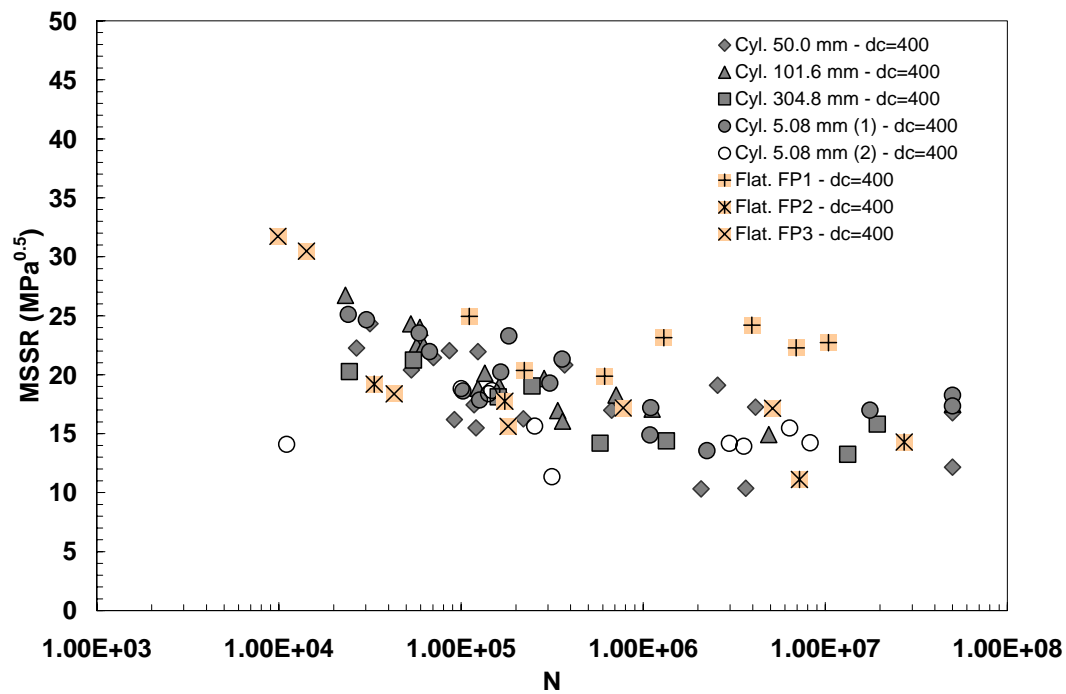
Figure 133. Point MSSR at dc = 300 μm
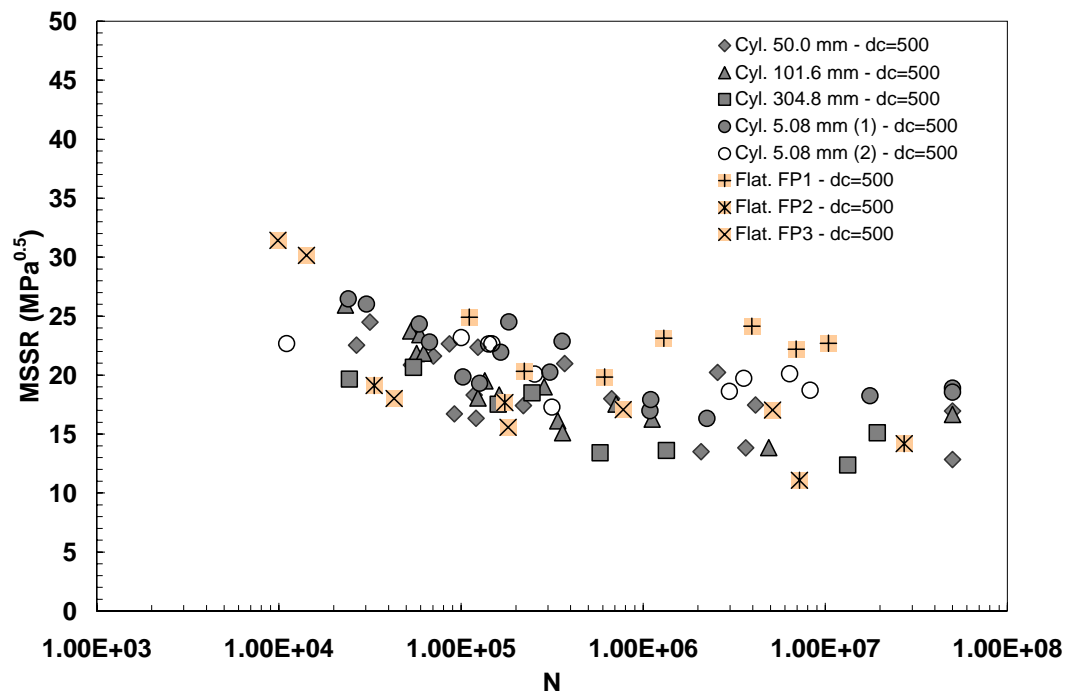

Figure 134. Point MSSR at dc = 400 μm

218

Figure 135. Point MSSR at d_c = 500 µm

APPENDIX H. Averaged SMSSR at Arbitrary Critical Distance

This Appendix contains the averaged SMSSR parameters resulting from arbitrary critical distance for all pad configurations included in this study. In order to investigate the variation of the scatter band as critical distance increased, the results were plotted from 20 μm to 500 μm.
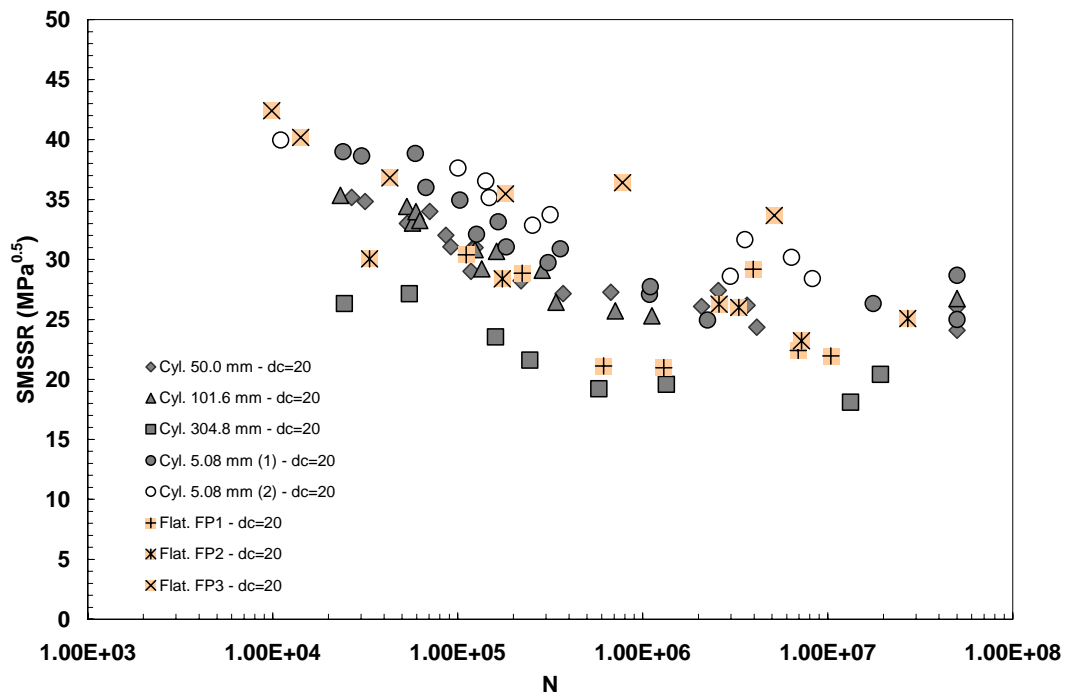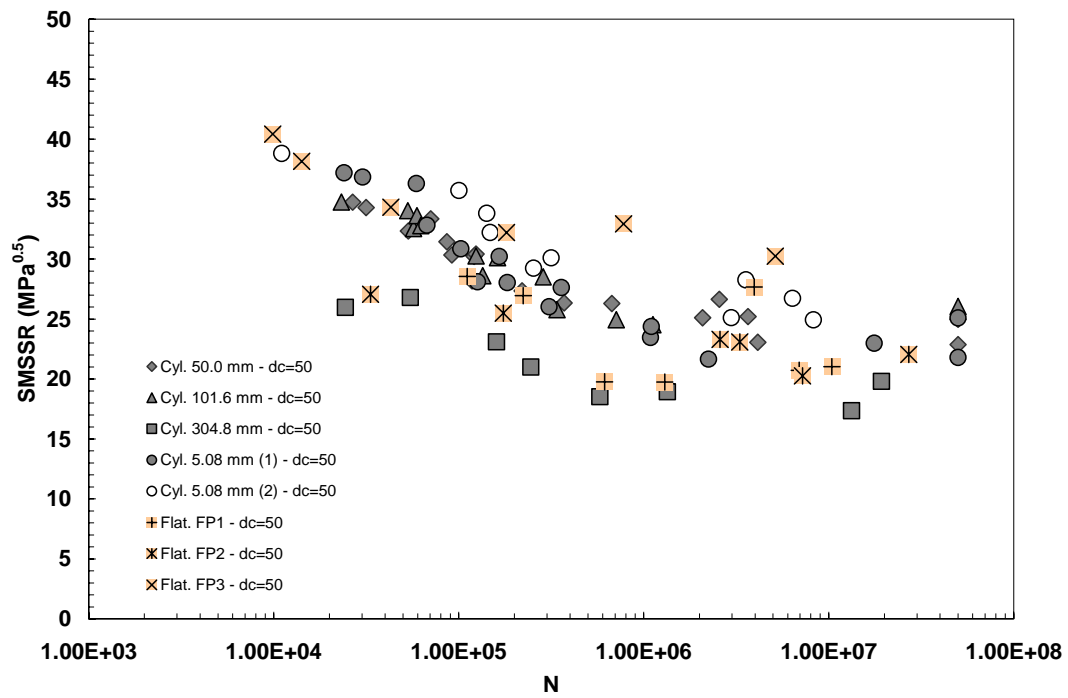

Figure 136. Averaged SMSSR at $d_c = 20$ μm

Figure 137. Averaged SMSSR at $d_c = 50$ μm

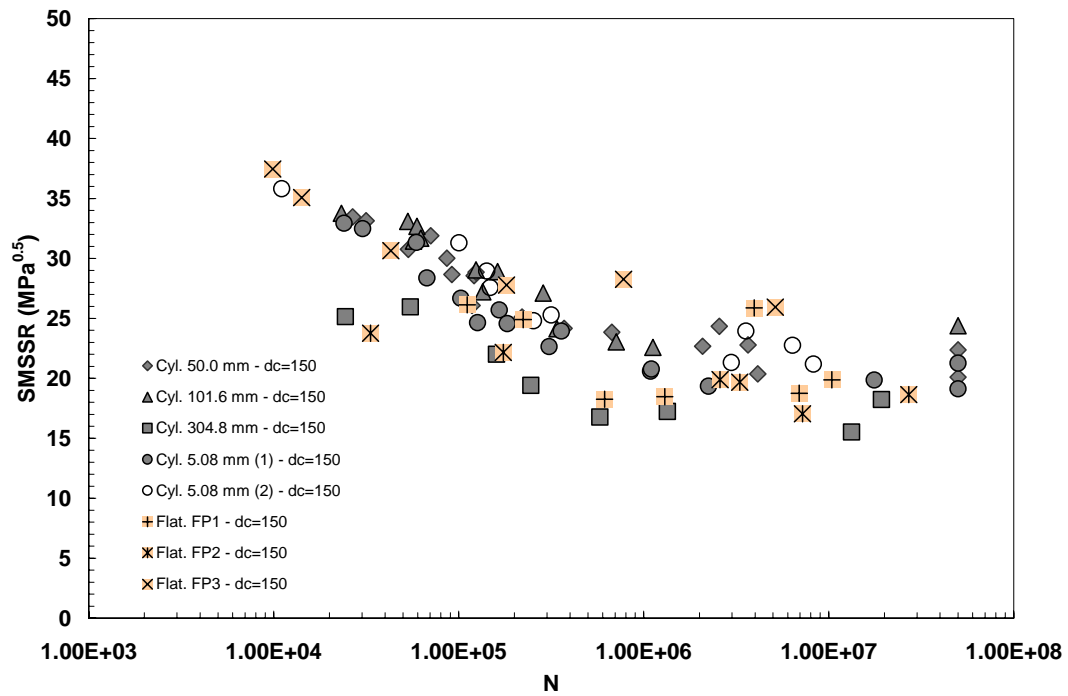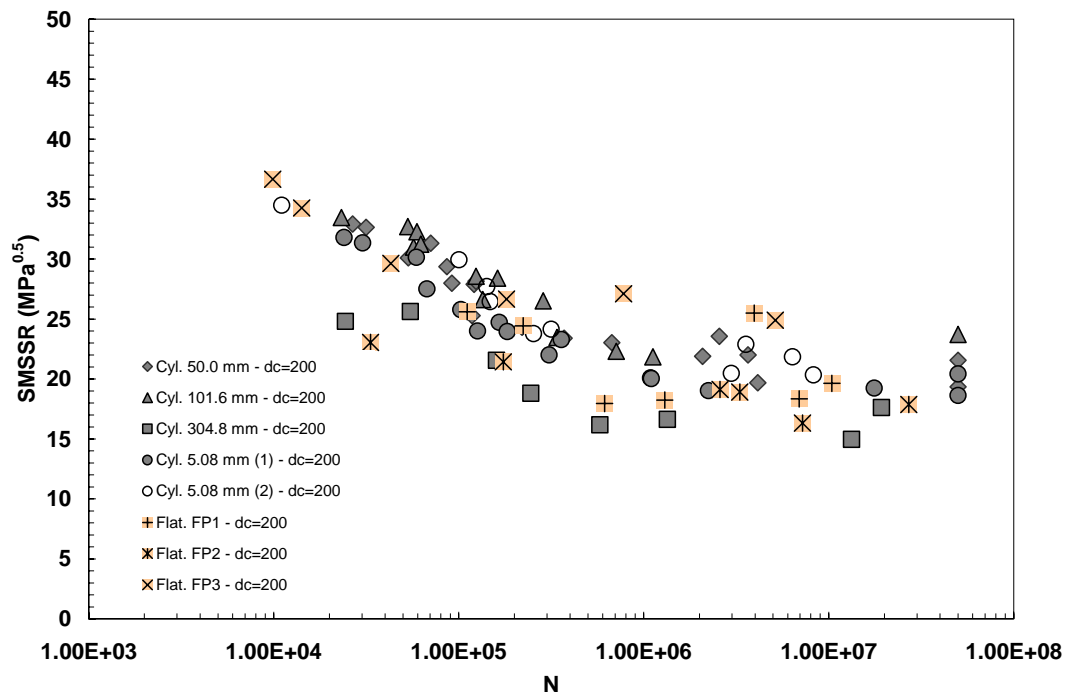Figure 138. Averaged SMSSR at $d_c = 150$ μm
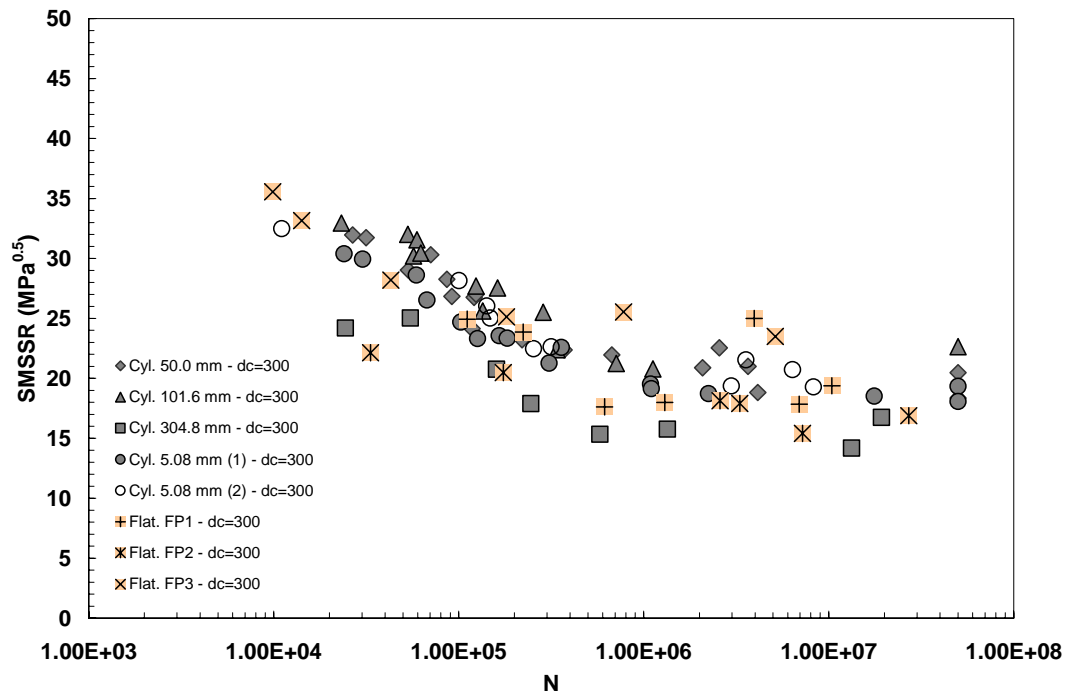
Figure 139. Averaged SMSSR at d_c = 200 μm

Figure 140. Averaged SMSSR at d_c = 300 μm
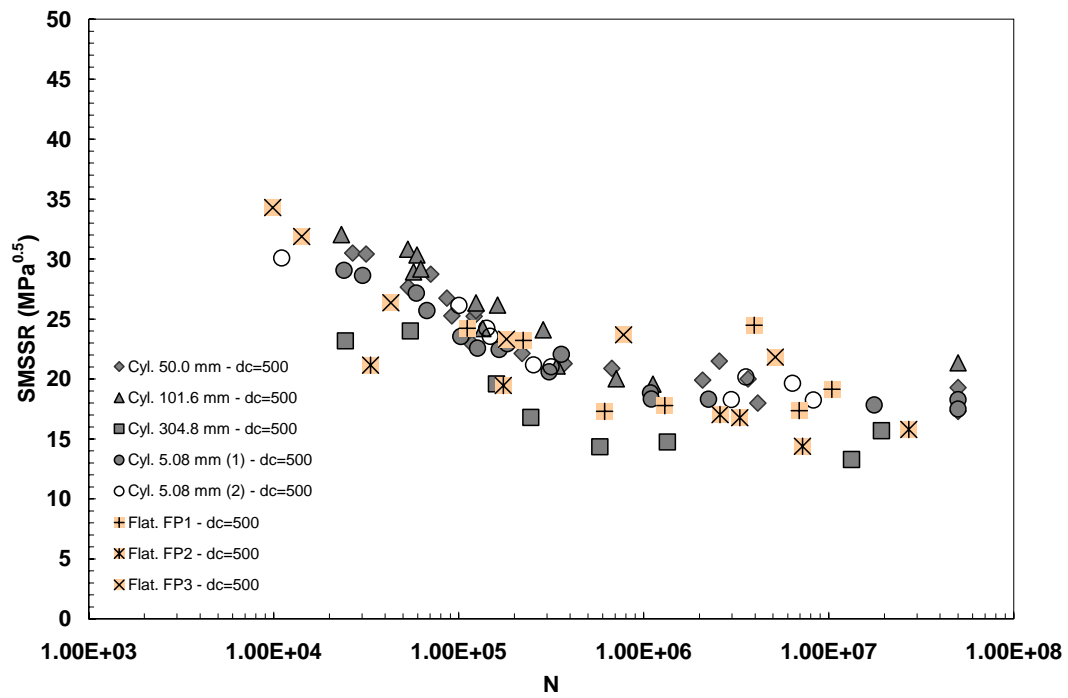
Figure 141. Averaged SMSSR at $d_c = 500$ μm

APPENDIX I. Point SMSSR at Arbitrary Critical Distance

This Appendix contains the point SMSSR parameter resulting from arbitrary critical distance for all pad configurations included in this study. In order to investigate the variation of the scatter band as critical distance increased, the results were plotted from 20 μm to 500 μm.

Figure 142. Point SMSSR at d_c = 20 µm

Figure 143. Point SMSSR at $d_c = 50$ µm

Figure 144. Point SMSSR at $d_c = 150$ µm

Figure 145. Point SMSSR at $d_c = 200$ μm

Figure 146. Point SMSSR at $d_c = 300$ μm

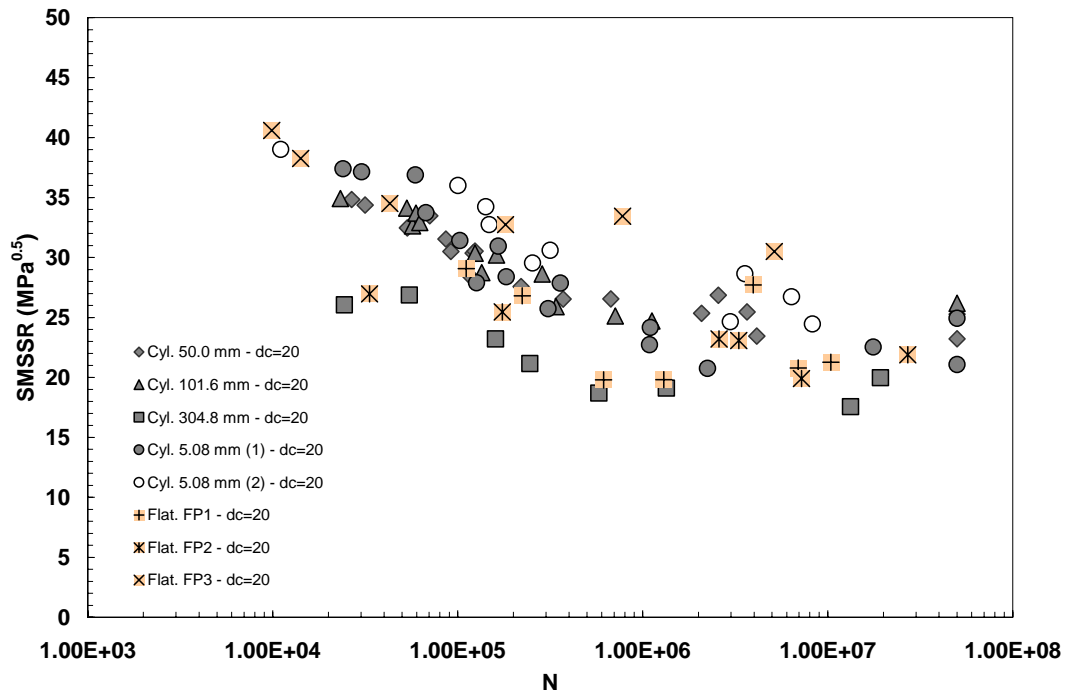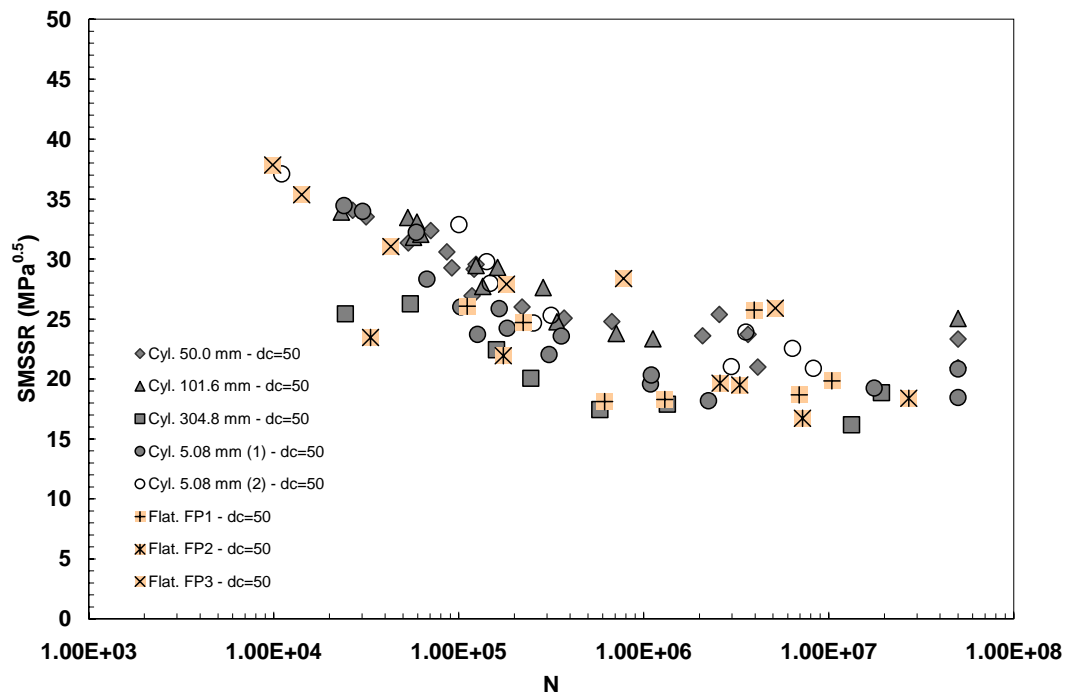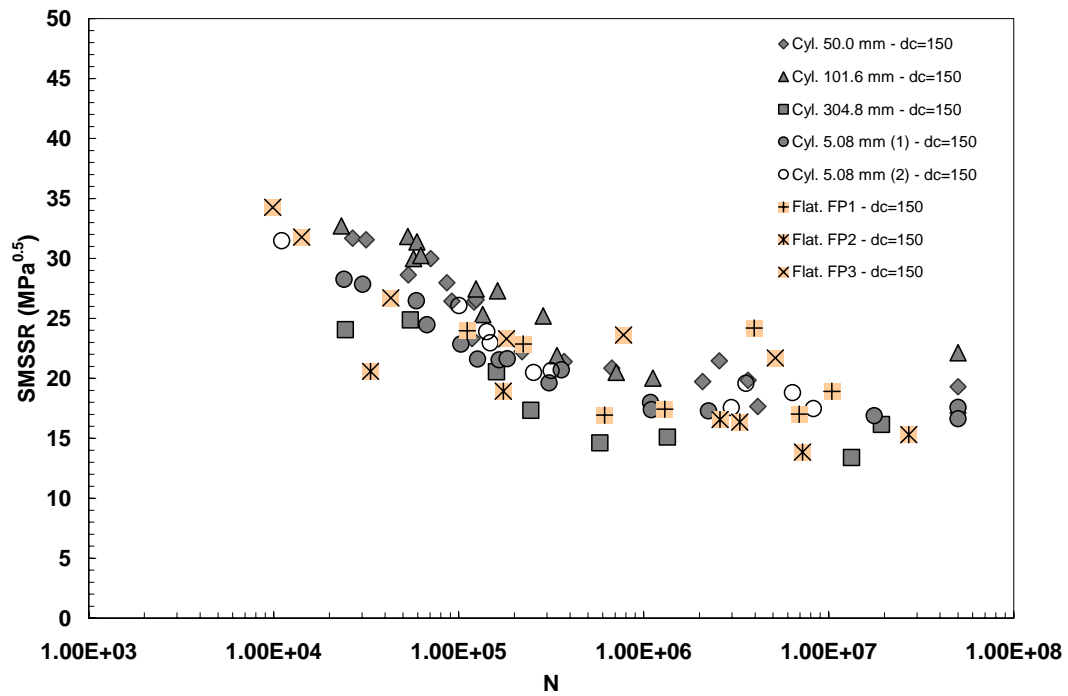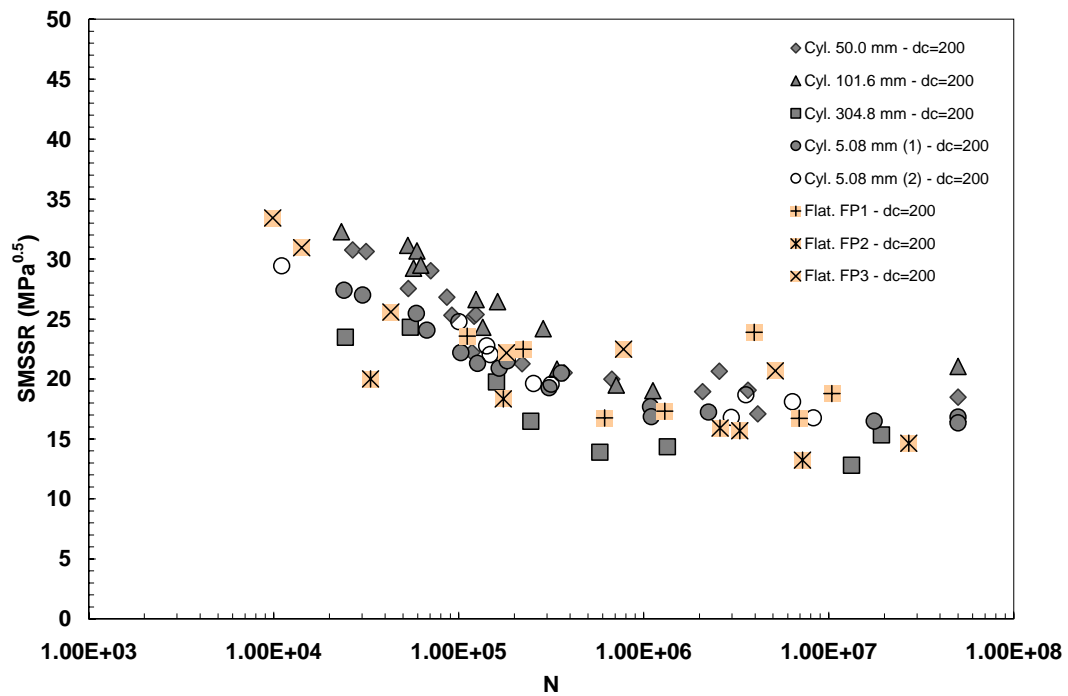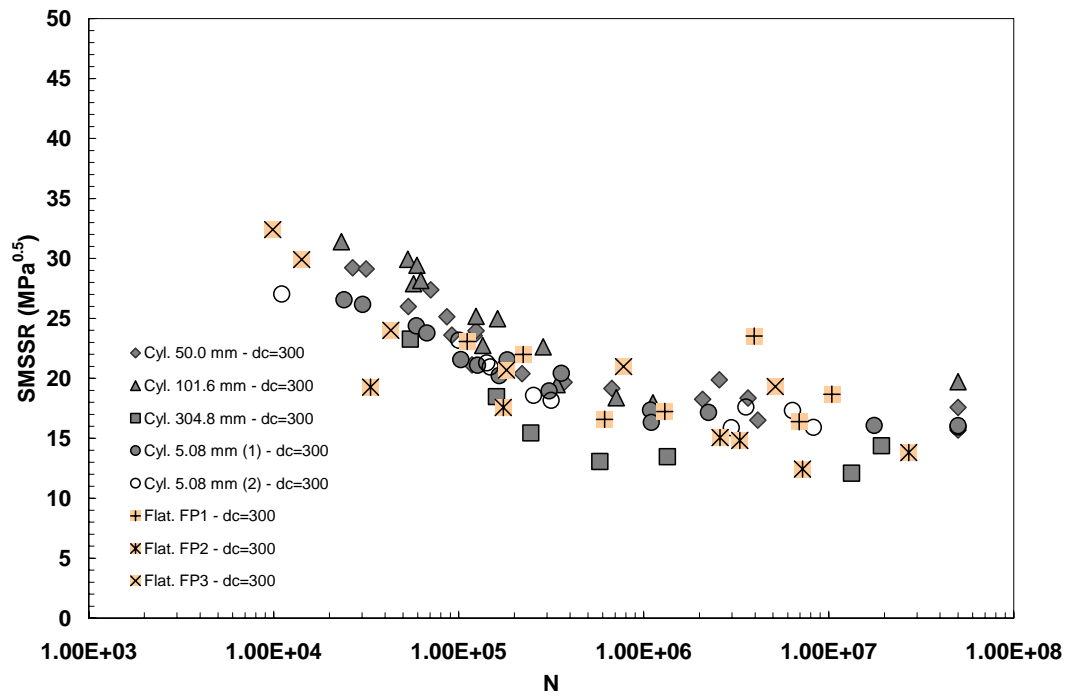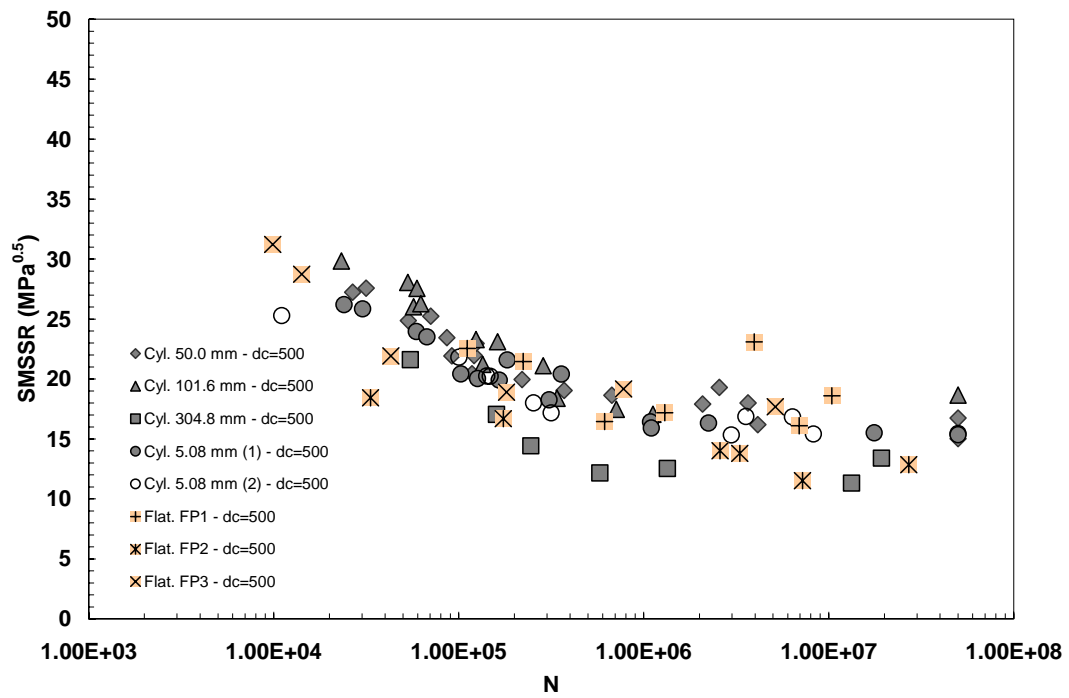Figure 147. Point SMSSR at d_c = 500 μm

Bibliography

1. D. W. Hoeppner, V. Chandrasekaran and C. B. Elliot, Eds. "Fretting-fatigue; Current Technologies and Practices", ASTM STP 1367, American Society for Testing and Materials, Philadelphia, 2000.

2. D. Rayaproula, R. Cook. "A Critical Review of Fretting-fatigue Investigations at the Royal Aerospace Establishment," Standardization of Fretting-fatigue Test Methods and Equipment, ASTM STP 1159, M. Helmi and R. Waterhouse, Eds. American Society for Testing and Materials, Philadelphia, 129-152, 1992.

3. T. Lindley, K. Nix. "Fretting Fatigue in the Power Generation Industry: Experiments, Analysis, and Integrity Assessment," Standardization of Fretting Fatigue Test Methods and Equipment, ASTM STP 1159, M. Helmi and R. Waterhouse, Eds. American Society for Testing and Materials, Philadelphia, 153-169, 1992.

4. M. Szolwinski, T. Farris. "Mechanics of fretting fatigue crack formation", *Wear*, 198: 93-107, 1996.

5. R. N. Smith, P. Watson and T. H. Topper. "A Stress-Strain Function For the Fatigue of Metals," *Journal of Materials*, JMLSA, 5: 767-778, 1970.

6. A. Fatemi, D. Socie. "A critical plane approach to multiaxial fatigue damage including out of phase loading," *Fatigue and Fracture of Engineering Materials and Structures*, 11: 149-165, 1988.

7. R. Neu, J. Pape and D. Swalla-Michaud. "Methodologies for Linking Nucleation and Propagation Approaches for Predicting Life Under Fretting Fatigue," *Fretting Fatigue: Current Technology and Practices*, ASTM 1367, D. Hoeppner, V. Chandrasekaran and C. Elliot, Eds. American Society for Testing and Materials, 1999.

8. C. D. Lykins, S. Mall and V. K. Jain. "Combined experimental-numerical investigation of fretting fatigue crack initiation," *International Journal of Fatigue*, 23: 703-711, 2001.

9. A. Krgo, A. R. Kallmeyer, and P. Kurath. "Evaluation of HCF Multiaxial Fatigue Life Prediction Metrologies for Ti-6Al-4V," *Proceeding of the 5th National Turbine Engine High Cycle Fatigue Conference*, Arizona, 2000.

10. Namjoshi, S., Mall, S., Jain, V., and Jin, O. "Fretting Fatigue Crack Initiation Mechanisms in Ti-6Al-4V," *Fat. & Fract. Engng. Mater. Struct*, 25: 955-964, 2002.

11. Peterson, R. E. *Metal Fatigue* (Ed. G.Sines & J.L.Waisman). 293-306. New York: McGraw-Hill, 1959.

12. Neuber, Heinz. *Theory of Notch Stresses: Principles for Exact Stress Calculation*. Ann Arbor, Michigan: J. W. Edwards, 1949.

13. G. Qylafku, Z. Azari, N. Kadi, M. Gjonaj and G. Pluvinage. "Application of a new model proposal for fatigue life prediction on notches and key-seats," *International Journal of Fatigue*, 21: 753-760, 1999.

14. Kadi N. "Notch effect in high cycle fatigue," NATO Sciences Series II, Kluwer, 207-220, 2001.

15. J. A. Araujo, D. Nowell. "The effect of rapidly varying contact stress fields on fretting fatigue," *International Journal of Fatigue*, 24: 763-775, 2002.

16. D.R. Swalla, R.W. Neu. "Characterization of Fretting Fatigue Process Volume Using Finite Element Analysis," Fretting Fatigue: Advances in Basic Understanding and Application, STP 1425, American Society for Testing and Materials, West Conshohocken, PA(in press)

17. Namjoshi, Mall, Jain and Jin. "Effects of Process Variables on Fretting Fatigue Crack Initiation in Ti-6Al-4V," (in press)

18. J.M. Ambrico, M.R. Begley. "Plasticity in Fretting Contact", *Journal of the Mechanics and Physics of Solids*, 48: 2391-2417, 2000.

19. J.M. Ambrico, M.R. Begley. "The Role of Macroscopic Plastic Deformation in Fretting Fatigue Life Predictions," *International Journal of Fatigue*, 23: 121-128, 2001.

20. D. Hills, D. Nowell. *Mechanics of Fretting Fatigue*. Netherlands: Kluwer Academic Publishers, 1994.

21. Muskhelishvili, N.I. "Some Basic Problems of the Mathematical Theory of Elasticity," Noordhoff, Groningen, 1953.

22. K. Chan, Y. Lee. "Ruiz Program," South West Research Institute, Personal Communication, 1998.

23. C. Ruiz, P. H. B. Boddington and K. C. Chen. "An Investigation of Fatigue and Fretting In A Dovetail Joint," *Experimental Mechanics*, 24: 208-217, 1984.

24. Walker K. "The effect of stress ration during crack propagation and fatigue for 2024-T3 and 7075-T6 Aluminum Effects of Environment and Complex Load

History on Fatigue life," *American Society for Testing and Materials*, West Conshohocken, PA. STP 462, pp. 1-14, 1970.

25. W. N. Findley. "Fatigue of Metals Under Combinations of Stresses," *ASME*, 79: 1337-1348, 1957.

26. Bannantine, Comer and Handrock. *Fundamentals of Metal Fatigue Analysis*. New Jersey: Prentice-Hall, Inc., 1990.

27. D. Taylor. "Stress Concentrations in High Cycle Fatigue," Fatigue 2002, 1849-1856, 2000.

28. Mitchell MR. SAE/SP-79/448. USA: Publ. Society of Automotive Engineers, 1979.

29. Kuhn, P., Hardraht, H. F. "An Engineering Method For Estimating Notch-Size Effect In Fatigue Tests On Steel," NACA Technical Note, No 2805, 1952

30. R. C. Juvinall. *Engineering Consideration of Stress, Strain and Strength*. New York: McGraw-Hill, 1967.

31. El Haddad MH, Dowling NF, Topper TH and Smith KN. "J integral applications for short fatigue cracks at notches," *International Journal Fracture*, 1980, 16:15-24, 1980.

32. Weixing Y. "Stress field intensity approach for predicting fatigue life," *International Journal of Fatigue*, 15: 243-245, 1993.

33. M.R. Begley, J.W. Hutchinson. "Plasticity in fretting of coated substrates", *Engineering Fracture Mechanics*, 62: 145-164, 1999.

34. C-H. Goh, J.M. Wallace, D.L. McDowell. "Polycrystal plasticity simulations of fretting fatigue", *International Journal of Fatigue*, 23: S423-S435, 2001.

35. K. Iyer, S. Mall. "Analysis of contact pressure and stress amplitude effects on fretting fatigue life," *ASME Journal of Engineering Materials and Technology*, 123: No 1: 85-93, 2001.

36. S. Suresh. *Fatigue of Materials*. United Kingdom: Cambridge University Press, 2001.

37. ABAQUS Standard User's Manual. Vol. 2. Hibbit, Karlsson and Sorensen Inc, Providence RI, 1995.

38. Stereoscan 360FE Scanning Electron Microscope Operating Instructions. Leica Cambridge Ltd, Cambridge UK, 1992.

Vita

Major Kisu Shin was born in Seoul, South Korea. He graduated from Chung-Buk High School in Cheong-Ju. He was admitted into South Korea Air force Academy in March 1984, where he graduated with Bachelor of Science degree in Mechanical Engineering in March 1988. After graduate from Air Force Academy, his first assignment was at 153th Maintenance Squadron, 17th AFB, Cheong-Ju where he led the maintenance team responsible F-4 aircraft maintenance.

In August 1993 he attended the Wichita State University in Kansas where he received a Master of Science degree in Aeronautical Engineering in September 1995. He was then assigned to Air force Technology Research Institute (ATRI) in Dae-Gu where he worked for the aircraft structure integrity program (ASIP). In August 2000, he entered the Unite State Air Force Institute of Technology as a candidate for a Doctor of Philosophy degree in Aeronautical Engineering. Upon graduation, he will be again assigned to Air force Technology Research Institute in Dae-Gu.

<table>
<tr><td colspan="3" align="center">REPORT DOCUMENTATION PAGE</td><td colspan="2" align="center">Form Approved
OMB No. 074-0188</td></tr>
</table>

REPORT DOCUMENTATION PAGE	*Form Approved* *OMB No. 074-0188*

The public reporting burden for this collection of information is estimated to average 1 hour per response, including the time for reviewing instructions, searching existing data sources, gathering and maintaining the data needed, and completing and reviewing the collection of information. Send comments regarding this burden estimate or any other aspect of the collection of information, including suggestions for reducing this burden to Department of Defense, Washington Headquarters Services, Directorate for Information Operations and Reports (0704-0188), 1215 Jefferson Davis Highway, Suite 1204, Arlington, VA 22202-4302. Respondents should be aware that notwithstanding any other provision of law, no person shall be subject to an penalty for failing to comply with a collection of information if it does not display a currently valid OMB control number.
PLEASE DO NOT RETURN YOUR FORM TO THE ABOVE ADDRESS.

1. REPORT DATE (DD-MM-YYYY) 03-09-04	**2. REPORT TYPE** PhD's Dissertation	**3. DATES COVERED** (From – To) Sep 2000 – Sep 2004

4. TITLE AND SUBTITLE

ROLE OF PLASTICITY ON FRETTING FATIGUE BEHAVIOR OF Ti-6Al-4V

5a. CONTRACT NUMBER

5b. GRANT NUMBER

5c. PROGRAM ELEMENT NUMBER

6. AUTHOR(S)

Kisu Shin, Major, ROKAF

5d. PROJECT NUMBER

5e. TASK NUMBER

5f. WORK UNIT NUMBER

7. PERFORMING ORGANIZATION NAMES(S) AND ADDRESS(S)
Air Force Institute of Technology

Graduate School of Engineering and Management (AFIT/EN)

2950 Hobson Way

WPAFB OH 45433-7765

8. PERFORMING ORGANIZATION REPORT NUMBER

AFIT/DS/ENY/04-05

9. SPONSORING/MONITORING AGENCY NAME(S) AND ADDRESS(ES)
AFOSR/NA
801 N. Randolph St. Rm. 732
Arlington, VA 22203-1977 Tel: 703-696-8523

10. SPONSOR/MONITOR'S ACRONYM(S)

11. SPONSOR/MONITOR'S REPORT NUMBER(S)

12. DISTRIBUTION/AVAILABILITY STATEMENT
APPROVED FOR PUBLIC RELEASE; DISTRIBUTION UNLIMITED.

13. SUPPLEMENTARY NOTES

14. ABSTRACT
Fretting fatigue generally leads to the degradation of the fatigue strength of a material due to cyclic micro-slip between two contacting materials. Fretting fatigue is regarded as an important issue in designing aerospace structures. While many studies have evaluated fretting fatigue behavior under elastic deformation conditions, few studies have focused on fretting fatigue behavior under elastic-plastic deformation conditions. The primary goal of this study was to characterize the fretting fatigue crack initiation behavior in the presence of plasticity. Experimental tests were performed using pad configurations involving elastic-plastic deformations. In order to calculate stress distributions under elastic-plastic fretting fatigue conditions, FEA was also performed. Several parametric approaches were used to predict fretting fatigue life along with stress distribution resulting from FEA. However, those parameters using surface stresses were unable to establish an equivalence between elastic fretting fatigue data and elastic-plastic fretting fatigue data. Based on this observation, the critical distance methods, which are commonly used in notch analysis, were applied to the fretting fatigue problem. In conclusion, the effective strain range method when used in conjunction with the SMSSR parameter showed e SMSSR parameter showed a good correlation of data points between the pad configurations involving elastic and elastic plastic deformations.

15. SUBJECT TERMS
Fretting Fatigue, Fatigue Life, Elastic-Plastic Deformation, Titanium Alloys, Fatigue Tests, Finite Element Analysis

16. SECURITY CLASSIFICATION OF:			**17. LIMITATION OF ABSTRACT**	**18. NUMBER OF PAGES**	**19a. NAME OF RESPONSIBLE PERSON** Prof. Dr. Shankar Mall, AFIT (ENY)
REPORT U	**ABSTRACT** U	**c. THIS PAGE** U	**UU**	252	**19b. TELEPHONE NUMBER** (Include area code) (937) 255-3636, ext 4587; e-mail: Shankar.Mall@afit.edu

Standard Form 298 (Rev: 8-98)
Prescribed by ANSI Std. Z39-18